

AD-A042 189

MINNESOTA UNIV MINNEAPOLIS DEPT OF ELECTRICAL ENGIN--ETC F/G 20/8
A STUDY OF ELECTRON SCATTERING FROM GERMANIUM (100).(U)
APR 77 R L ERICKSON

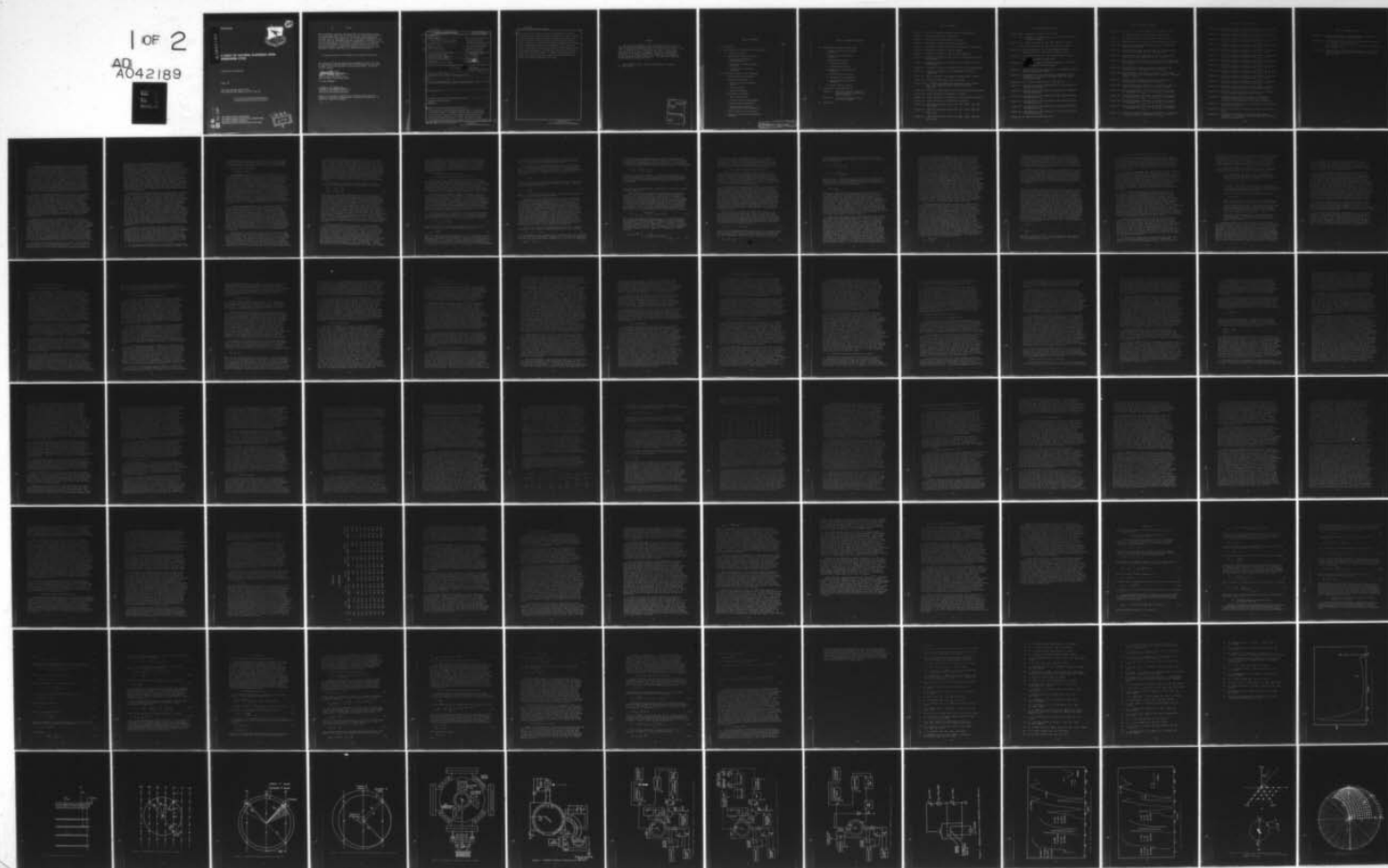
UNCLASSIFIED

AFAL-TR-76-36

F33615-72-C-2105

NL

1 OF 2
AD
A042189



AD A042189

AFAL-TR-76-36



A STUDY OF ELECTRON SCATTERING FROM GERMANIUM (100)

UNIVERSITY OF MINNESOTA

APRIL 1977

TECHNICAL REPORT AFAL-TR-76-36
FINAL REPORT FOR PERIOD JULY 1972 - MAY 1975

Approved for public release; distribution unlimited

AD No. _____
DDC FILE COPY

AIR FORCE AVIONICS LABORATORY
AIR FORCE WRIGHT AERONAUTICAL LABORATORIES
AIR FORCE SYSTEMS COMMAND
WRIGHT-PATTERSON AIR FORCE BASE, OHIO 45433

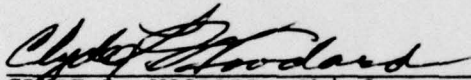


NOTICE

When Government drawings, specifications, or other data are used for any purpose other than in connection with a definitely related Government procurement operation, the United States Government thereby incurs no responsibility nor any obligation whatsoever; and the fact that the Government may have formulated, furnished, or in any way supplied the said drawings, specifications, or other data, is not to be regarded by implication or otherwise as in any manner licensing the holder or any other person or corporation, or conveying any rights or permission to manufacture, use, or sell any patented invention that may in any way be related thereto.

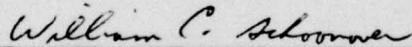
This technical report has been reviewed and is approved for publication.

This report has been reviewed by the Information Office (OI) and is releasable to the National Technical Information Service (NTIS). At NTIS, it will be available to the general public, including foreign nations.



CLYDE L. WOODARD, Chief
Electro-Optic Detectors Group
Electro-Optics Technology Branch

FOR THE COMMANDER



WILLIAM C. SCHOONOVER, Chief
Electro-Optics Technology Branch
Electronic Technology Division

Copies of this report should not be returned unless return is required by security considerations, contractual obligations, or notice on a specific document.

UNCLASSIFIED

SECURITY CLASSIFICATION OF THIS PAGE (When Data Entered)

REPORT DOCUMENTATION PAGE		READ INSTRUCTIONS BEFORE COMPLETING FORM
1. REPORT NUMBER AFAL-TR-76-36	2. GOVT ACCESSION NO.	3. RECIPIENT'S CATALOG NUMBER
4. TITLE (and Subtitle) A STUDY OF ELECTRON SCATTERING FROM GERMANIUM (100)	5. TYPE OF REPORT & PERIOD COVERED Technical Report 7-1-72 - 5-31-75	6. PERFORMING ORG. REPORT NUMBER
7. AUTHOR(s) Robert Leon Erickson	8. CONTRACT OR GRANT NUMBER(s) F33615-72-C-2105	
9. PERFORMING ORGANIZATION NAME AND ADDRESS University of Minnesota Dept of Electrical Engineering Minneapolis, Minn. 55455	10. PROGRAM ELEMENT, PROJECT, TASK AREA & WORK UNIT NUMBERS 2001-03-31	
11. CONTROLLING OFFICE NAME AND ADDRESS AFAL/DHO-3 Wright-Patterson AFB, OH 45433	12. REPORT DATE Apr 77	13. NUMBER OF PAGES
14. MONITORING AGENCY NAME & ADDRESS (if different from Controlling Office) 152	15. SECURITY CLASS. (of this report) UNCLASSIFIED	15a. DECLASSIFICATION/DOWNGRADING SCHEDULE n/a
16. DISTRIBUTION STATEMENT (of this Report) Approved for public release; distribution unlimited.		
17. DISTRIBUTION STATEMENT (of the abstract entered in Block 20, if different from Report) Technical rept. 1 Jul 72 - 31 May 75,		
18. SUPPLEMENTARY NOTES		
19. KEY WORDS (Continue on reverse side if necessary and identify by block number) Secondary electron emission Plasmon Auger LEED		
20. ABSTRACT (Continue on reverse side if necessary and identify by block number) Low energy electron scattering measurements were made on an atomically clean Ge(100) surface as a function of primary energy, scattering angle and surface order. Analysis of the elastically diffracted electrons indicated the probable existence of a Ge(100) 4x2 surface structure. With appropriate inner potential corrections, most elastic intensity maxima		

DD FORM 1 JAN 73 1473

EDITION OF 1 NOV 65 IS OBSOLETE

UNCLASSIFIED

SECURITY CLASSIFICATION OF THIS PAGE (When Data Entered)

233 520

UNCLASSIFIED

SECURITY CLASSIFICATION OF THIS PAGE(When Data Entered)

→ were found to satisfy either kinematical Bragg conditions or secondary Bragg conditions associated with maxima of another beam. Inelastic electron energy distributions displayed numerous characteristic loss peaks due to interband electron excitation in addition to bulk and surface plasmon loss peaks. Measurements of the energy and angular distributions of the inelastic electrons showed the existence of strong inelastic electron diffraction effects. Measurements of the low energy secondary electron energy distributions produced observations of secondary peaks which could be attributed to diffraction of secondary electrons. In addition, secondary peaks were observed which are felt to be due to direct electron emission from local maxima in the conduction band density of states. ↗

UNCLASSIFIED

SECURITY CLASSIFICATION OF THIS PAGE(When Data Entered)

PREFACE

The research described in this report was carried out in the Physical Electronics Laboratory of the University of Minnesota under Contract No. F33615-72-C-2105 - Project No. 2001, Task 03, Work Unit 31, between July 1, 1972 and May 31, 1975. The work was supervised by W. T. Peria, Professor of Electrical Engineering, University of Minnesota, Minneapolis, Minnesota. The project monitor is W. H. Nelson, AFAL/TEO, Air Force Avionics Laboratory, Wright-Patterson Air Force Base, Ohio. The report was submitted by the authors on October 8, 1975.

This technical report has been reviewed and is approved for publication.

ACCESSION for	
NTIS	White Section <input checked="" type="checkbox"/>
DDC	Buff Section <input type="checkbox"/>
UNANNOUNCED	<input type="checkbox"/>
JUSTIFICATION	
BY	
DISTRIBUTION/AVAILABILITY CODES	
SPECIAL	
A	

TABLE OF CONTENTS

	<u>Page</u>
I. Introduction	1
II. Basic Concepts of Electron Solid Interactions	3
1 Secondary Electrons	3
2 Backscattered Primary Electrons	5
a Inelastically Scattered Primary Electrons	5
b Elastically Scattered Primary Electrons	8
c Inelastically Diffracted Electrons	12
III. Experimental Apparatus and Techniques	15
1 Vacuum System and Processing	15
2 Measurement Apparatus	16
a Electron Gun and Scattering Chamber	16
b Energy Analyzer	17
c Apparatus Alignment	18
3 Measurement Procedures	19
a Sample Positioning	19
b Secondary Electron Measurements	19
c Auger Electron Measurements	21
d Electron Diffraction and Characteristic Loss Measurements	22
4 Target Preparation and Cleaning	22
5 Coordinate Systems and Experimental Variables	23

TABLE OF CONTENTS (continued)

	<u>Page</u>
IV. Experimental Results and Discussion	24
1 Characterization of the Sample Surface	24
2 Elastic Electron Intensity Analysis	25
3 Characteristic Losses	30
a Plasmon Excitations	31
b Interband Excitations	32
4 Inelastic Low Energy Electron Diffraction	38
a Inelastic Energy Profiles	38
b Characteristic Loss Spectra	39
c Inelastic Angular Intensity Profiles	43
5 Secondary Electron Spectra	48
V. Conclusions and Recommendations	52
Appendix A: Some Relationships Between the Complex Dielectric Constant and Energy Absorption	54
Appendix B: Inelastic Low Energy Electron Diffraction (ILEED)	59
VI. References	66

LIST OF FIGURES

- Figure 1 - Typical secondary electron energy distribution
- Figure 2 - Possible bulk Auger transitions
- Figure 3 - Ewald sphere construction in K-space
- Figure 4 - Inelastic electron diffraction diagram
- Figure 5 - Inelastic electron diffraction diagram for IE process
- Figure 6 - Schematic diagram of vacuum chamber
- Figure 7 - Schematic diagram of experimental apparatus
- Figure 8 - Schematic diagram of apparatus for secondary electron measurements
- Figure 9 - Schematic diagram of apparatus of secondary electron measurements
- Figure 10 - Schematic diagram of apparatus for Auger measurements
- Figure 11 - Schematic diagram of ion bombardment cleaning apparatus
- Figure 12 - Auger spectrum from carbon contaminated Ge surface
- Figure 13 - Auger spectrum from clean Ge surface
- Figure 14(a) - Primary electron beam orientation with crystal axes. (b) Experimentally controlled angular variables
- Figure 15 - Graphical construction for determining scattering angles
- Figure 16 - Auger spectrum of oxidized Ge surface
- Figure 17 - Auger spectrum of oxidized Ge surface after sputtering
- Figure 18 - LEED patterns for clean Ge(100) surface
- Figure 19 - LEED beam intensity plots for (00), (10), (11) and (01) beams
- Figure 20 - LEED beam intensity plots for (21), (02), ($\frac{1}{2}0$) and ($0\frac{1}{2}$) beams
- Figure 21 - LEED beam intensity plots for ($\frac{1}{2}1$), ($1\frac{1}{2}$), ($0\frac{3}{2}$) and ($\frac{3}{2}1$) beams

LIST OF FIGURES (CONT'D)

- Figure 22(a) - Reciprocal lattice for Ge(100)
(b) - Example of point plotting in K-space for elastic intensity maxima
- Figure 23(a) - Point plotting of (00) beam intensity maxima
(b) - Point plotting of (01) beam intensity maxima
- Figure 24 - Point plotting of (10) beam intensity maxima
Point plotting of (11) beam intensity maxima
- Figure 25 - (a) Point plotting of (02) beam intensity maxima
(b) Inner potential curve for Ge
- Figure 26 - Low energy elastic intensity plots for (00), (01), and $(\frac{1}{2}0)$ diffraction beams
- Figure 27 - Characteristic loss spectra for (a) annealed surface and (b) sputtered surface
- Figure 28 - Characteristic loss spectra vs. scattering angle transverse to plane of incidence about the (100) diffraction beam
- Figure 29 - High energy characteristic loss spectra
- Figure 30 - Typical low energy characteristic loss spectrum for specular scattering
- Figure 31 - Characteristic loss spectra obtained with improved energy resolution
- Figure 32 - Characteristic loss spectra in (00) beam direction as function of E_p
- Figure 33 - Characteristic loss spectra in (01) beam direction as function of E_p
- Figure 34 - Characteristic loss spectra in (10) beam direction as function of E_p
- Figure 35 - Characteristic loss spectra in (11) beam direction as function of E_p
- Figure 36 (a) Optical reflectivity for Ge

LIST OF FIGURES (CONT'D)

- Figure 36 - (b) $\epsilon_1(\omega)$, $\epsilon_2(\omega)$ and energy loss function, $\text{Im } \frac{1}{\epsilon}$, vs. photon energy for Ge (from reference 62).
- Figure 37 - Calculated electron energy bands (from ref. 63)
- Figure 38 - Characteristic loss spectra from oxidized Ge surface
- Figure 39 - Elastic and inelastic intensity plots in specular scattering direction
- Figure 40 - Characteristic loss spectra for (11) beam direction (curve A) and 2° off of (11) beam curve (B)
- Figure 41 - Characteristic loss spectra vs. E_p for scattering direction of (01) LEED beam at $E_p = 36$ eV
- Figure 42 - Characteristic loss spectra measured in (00) LED beam direction and 2° either side in plane of incidence for $E_p = 120$ eV
- Figure 43 - K-space plots showing scattering conditions for characteristic loss spectra of Figure 42
- Figure 44 - Characteristic loss spectra measured in (00) LEED beam direction and 2° either side in plane of incidence for $E_p = 130$ eV
- Figure 45 - K-space plots showing scattering conditions for characteristic loss spectra of Figure 44
- Figure 46 - Characteristic loss spectra vs. scattering angle in plane of incidence about (00) diffraction beam
- Figure 47 - Inelastic angular intensity distributions in plane of incidence for $E_{\text{Loss}} = 10$ eV and $E_p = 70-100$ eV
- Figure 48 - Inelastic angular intensity distributions in plane of incidence for $E_{\text{Loss}} = 10$ eV and $E_p = 105-140$ eV
- Figure 49 - Inelastic angular intensity distributions in plane of incidence for $E_{\text{Loss}} = 16$ eV and $E_p = 70-100$ eV
- Figure 50 - Inelastic angular intensity distributions on plane of incidence for $E_{\text{Loss}} = 16$ eV and $E_p = 105-140$ eV
- Figure 51 - Inelastic angular intensity distribution as function of E_p , for plane of incidence and $E_{\text{Loss}} = 10$ eV

LIST OF FIGURES (CONT'D)

- Figure 52 - Inelastic angular intensity distributions as function of E_p , for plane of incidence and $E_{loss} = 12$ eV
- Figure 53 - Inelastic angular intensity distributions as function of E_p , for plane of incidence and $E_{loss} = 14$ eV
- Figure 54 - Inelastic angular intensity distributions as function of E_p , for plane of incidence and $E_{loss} = 16$ eV
- Figure 55 - Inelastic angular intensity distributions as function of E_p , for plane of incidence and $E_{loss} = 18$ eV
- Figure 56 - Inelastic angular intensity distribution as function of E_p , for plane of incidence and $E_{loss} = 20$ eV
- Figure 57 - Inelastic angular intensity distributions as function of E_p , for plane of incidence and $E_{loss} = 10$ eV
- Figure 58 - Inelastic angular intensity distributions as function of E_p , for plane of incidence and $E_{loss} = 12$ eV
- Figure 59 - Inelastic angular intensity distributions as function of E_p , for plane of incidence and $E_{loss} = 14$ eV
- Figure 60 - Inelastic angular intensity distributions as function of E_p , for plane of incidence and $E_{loss} = 16$ eV
- Figure 61 - Inelastic angular intensity distributions as function of E_p , for plane of incidence and $E_{loss} = 18$ eV
- Figure 62 - Inelastic angular intensity distribution as function of E_p , for plane of incidence and $E_{loss} = 20$ eV
- Figure 63 - Secondary electron energy distributions as function of E_p , measured in specular scattering direction
- Figure 64 - Secondary electron energy distribution as function of E_p , measured normal to sample surface
- Figure 65 - Secondary peak energy variation as function of scattering angle for diffraction of secondary electron; with descriptive wave vector diagrams
- Figure 66 - Secondary electron energy distributions for sputtered and annealed surfaces
- Figure 67 - Idealized inelastic intensity plots as function of E_{loss}
- Figure 68 - Idealized wave vector plots describing angular variation of inelastic intensity; depicting sideband diffraction conditions

LIST OF FIGURES (CONT'D)

- Figure 69 - Idealized inelastic angular intensity variation as function of E_p near a Bragg energy
- Figure 70 - (a) Changes in wave vector for sideband diffraction with changes in detector angle
(b) Changes in wave vector for sideband diffraction with changes in E_p
- Figure 71 - Idealized wave vector diagrams depicting changes in inelastic angular intensity as function of E_p near Bragg energy

I. Introduction

An understanding of the electronic and structural properties of solid surfaces has become increasingly important, both because of the troublesome aspects of surfaces, such as encountered in semiconductor integrated circuit fabrication, and because surface properties play such an important role in areas such as catalysis and electron emitting devices. Basically, despite the large amount of work devoted to them, surfaces remain as a poorly understood aspect of solid state physics. To a great extent this is due to the fact that surfaces are not easily studied either theoretically or experimentally. Theoretical treatments are difficult because much of the symmetry that simplifies the theory of bulk properties is lost when the surface is considered. Experimental difficulties stem partly from the requirement that the measurements be carried out under ultrahigh vacuum conditions using specialized techniques to insure clean and well characterized surfaces; however, much of the problem lies in the fact that none of the measurement techniques are able to completely separate bulk from surface effects.

Ideally, an external, nondestructive probe which only interacts with the first one or two atomic layers of the solid is required. Although such an ideal probe is not available, the requirements of nondestruction and small penetration are reasonably well satisfied by a low energy electron beam. Despite this fact, low energy electron scattering from surfaces has received little attention. It was the main thrust of this experiment, therefore, to explore the possibilities of low energy electron scattering as a technique for investigating solid surfaces. Long range interests in such measurements are concerned with studying adsorbates on surfaces, but as a first step the clean surface itself must be understood and this study was restricted to that goal. It was felt that new and useful information could be obtained through a complete characterization of the low energy electron scattering from a clean, atomically ordered surface.

Although low energy electron beams have been neglected to a large extent, electron beams in general have been used extensively for studying solids and solid surfaces. Most of these investigations, however, have been done with relatively high primary energies (> 100 eV), and those measurements at lower primary energies have almost exclusively dealt with the elastically scattered electrons. Further, the measurements have primarily been made with large solid angle detectors or small solid angle detectors at a fixed scattering angle, usually the specular angle. Restrictions such as these have limited the available information. Thus, in the present study an apparatus was constructed in which both the energy and angular distributions of the electrons could be studied. Measurements were concentrated on primary energies of 5-100 eV, although the apparatus was not restricted to this range and occasional measurements at higher energies (100-1000 eV) were made.

As mentioned, the principal study of low energy electron beams has been that of elastic scattering from surfaces in the form of low energy electron diffraction (LEED) measurements. From atomically ordered surfaces, the low energy elastically scattered electrons are

predominantly contained in diffracted beams, and their geometrical arrangement forms a LEED pattern which is usually displayed on a phosphor screen. Analysis of the LEED pattern allows the size and symmetry of the two-dimensional surface atomic structure to be determined. Measurements of these LEED patterns are qualitatively useful in assessing the degree of order of a surface, but by far the most common application of LEED has been in monitoring the changes in surface periodicity during adsorption of foreign atoms or molecules on the surface. In some instances such measurements can lead to predictions of likely bonding schemes at the surface but in general this is not possible. Despite the qualitative nature of LEED, such studies have been useful and a number of recent review papers¹⁻⁶ cover the applications and shortcomings of the technique. At energies lower than those used for LEED (< 20 eV) elastic electron reflection measurements have been shown to be quite sensitive to chemical and structural changes in the surface,^{7,8,51} but the interpretation of these measurements is quite complex and at present there is disagreement on interpretation.

Investigations of the inelastically scattered primary electrons, although rather few in number, have also shown pronounced surface effects. It has been shown, for example, that oxidation of metal surfaces causes the energy of the surface plasmon peak to shift in energy,⁹ indicating the changed electronic environment at the surface. Propst and Piper¹⁰ have observed surface effects in the inelastic scattering of 4.5 eV electrons from W(100). Energy loss peaks observed when the clean sample was exposed to controlled amounts of gases were attributed to the excitation of vibrational modes of the adsorbed species that are related to the bonding arrangement to the surface. In a similar experiment, Ibach has recently measured the low energy inelastic spectrum and found multiple surface phonon losses on ZnO¹¹ and Si.¹² These last two experiments were carried out with better energy resolution than available in the present study but they serve to point out the sensitivity of a low energy electron beam to surface interactions. Interband electron transitions have also been identified in the inelastic spectrum of low energy electrons^{13,14} and, in principle, electron transitions involving surface electronic states should also be observed but have not as yet been reported; however, photon-induced transitions of this kind have been observed.^{15,16}

In addition to the information contained in the elastic and inelastic spectra, peaks have also been observed in electron energy distributions which remain at fixed secondary energies as the primary energy is varied. Two recent experiments^{17,18} conducted at low primary energies have yielded secondary peaks which could be correlated quite well with energies and directions of high densities of states in the conduction band. Peaks fixed in secondary energy are also obtained through an Auger process, and Harrower,¹⁹ as well as Scheibner and Tharp,^{13,14} have attributed the low energy peaks in their secondary electron spectra to such a process.

In the foregoing discussion some of the possible interactions of a low energy electron beam with a solid have been reviewed. From

this discussion it is clear that the surface plays a strong role in the scattering of low energy electrons and this has provided the motivation for this present study. In the following section the electron-solid interactions will be developed in more detail.

II. Electron-Solid Interactions

1 Secondary Electrons

The distribution in energy of electrons leaving a target due to its bombardment with primary electrons is referred to as a secondary electron energy distribution (SED). For primary energies of about 50 eV or greater, a typical SED can be illustrated as shown in fig. 1, and by common convention is broken up into the three regions indicated by the Roman numerals I to III. Region I is referred to as the region of true secondary electrons and extends from $E_s = 0$ to a somewhat arbitrary upper limit of $E_s = 50$ eV. Electrons in regions II and III are referred to as backscattered primary electrons, region III containing the elastically and quasi-elastically scattered electrons while region II contains the inelastically scattered primary electrons. It should be pointed out that these distinctions are made only as a matter of convenience, since regions I and II have a certain amount of overlap, where true secondary electrons cannot be distinguished from inelastically scattered primary electrons. The backscattered primary electrons will be the subject of the next section and the rest of this section will be devoted to the secondary electrons in regions I and II of the SED.

Virtually all materials display the same general shape of the SED with the characteristic large broad peak at low energies. These electrons originate from a cascade process in which the primary electrons scatter inelastically from lattice electrons, exciting the latter to higher energies. These excited electrons then are considered to diffuse through the solid, scattering from other lattice electrons and thus multiplying in number. Those whose energy and momentum are proper can escape into vacuum over the surface barrier of the solid and it is these which give rise to the true secondary peak. Many experiments have been carried out dealing with various aspects of the true secondaries and this work is adequately reviewed elsewhere.^{20,21} With the exception of some Auger spectroscopy measurements, which will be discussed below, this present study dealt only with SED's at low primary energies where regions I and II cannot be distinguished and the cascade process is minimized.

Superimposed on the generally smooth secondary spectrum there is a certain amount of fine structure as depicted in fig. 1. These are peaks which remain fixed in secondary energy, E_s , as the primary energy is varied. Such peaks have been observed for many years and were first explained by Lander²² in 1953 as being due to an Auger process. The Auger process can be explained by using the energy level diagram of fig. 2 showing two different possible combinations of electronic transitions. Consider for the moment the transitions indicated by the solid arrows. For sufficiently high primary energies,

an electron can be removed from the M shell of the solid. This state can then be refilled by a higher lying electron, in this case a valence electron, with energy being given up in one of two ways. Either the energy can be given off in the emission of a photon, giving the usual x-ray lines, or the energy can be given up in a nonradiative process where another electron receives the energy and is excited up to a higher electron state. This latter process is called an Auger process and for this particular example is depicted by an excitation from the valence band; this would be termed an MVV Auger process. A second example is indicated by the dashed arrows. Here the L shell is initially emptied and is neutralized by an electron from the M shell with energy being transferred to a valence electron; this is labelled an LMV Auger process.

The energies at which these electrons appear in the SED, using the vacuum level, E_{vac} , as a zero reference are given as

$$E_{MVV} \approx |E_M - E_V| - |E_V| \quad (1)$$

$$E_{LMV} \approx |E_L - E_M| - |E_V| \quad (2)$$

As can be seen from these expressions, aside from the broadening of the atomic levels, especially the valence band levels, the energy transfers available are characteristic of the elements from which the solid is made up. Similarly, if there were contaminants on the surface, the same type of Auger processes could take place, the energy levels then being characteristic of the contaminants present. A measurement of the energies of these small peaks in the SED then provides a determination of atomic species present near the surface of a solid. Such measurements have led to a form of spectroscopy called Auger electron spectroscopy (AES) which has been the subject of intensive work since 1967; much of it being covered in review papers by Chang²³ and Riviere.²⁴ Auger spectroscopy measurements are generally made with high primary energies and the peaks measured involve transitions where a core state is ionized; however, the same considerations can be applied to electron transitions involving only the conduction and valence bands, and such processes have been used to explain structure in photo-emission energy distributions.²⁵

Other processes which lead to structure in the secondary electron spectrum have also been proposed. In a manner similar to that involved in the Auger process, plasmons may de-excite by transferring their energy to valence or conduction electrons from a preferred narrow range of initial states. These excited electrons may then, if energetic enough, escape into vacuum and cause fine structure in the SED. It has also been shown by Kane²⁶ that secondary electrons occupy the conduction band according to the local density of states, so that at specific energies and directions in K-space the electron densities should display relative maxima. These would show up in the SED as angularly dependent structure. Such effects have been observed in Si by Best.¹⁷ Peaks related to the band structure have also been observed in the SED's from graphite

using a hemispherical detector.¹⁸ One additional process that leads to structure in the secondary spectrum is the diffraction of secondary electrons. Secondary electrons that are created with the proper energy and direction may satisfy a Bragg diffraction condition and give enhanced intensity to the SED in the diffraction direction. Effective separation of these various processes requires that both energy and angular distribution measurements be made.

2 Backscattered Primary Electrons

a Inelastically Scattered Primary Electrons

Region II of fig. 1 contains the inelastically scattered primary electrons. The most prominent structure in this region is the group of characteristic loss peaks which occur within 30 eV of the elastic peak. Each of these peaks contains primary electrons which have lost a discrete amount of energy in causing some excitation of the solid; they are termed characteristic loss peaks because in general their energy separation from the elastic peak is characteristic of the material and independent of primary energy.

Two types of characteristic losses are commonly observed, those due to interband electron transitions and those due to the excitation of collective oscillations of the valence electrons, called plasma oscillations. A plasmon, which is the quasi-particle terminology for a plasma oscillation, is often what one refers to in scattering problems. Plasmon loss peaks are usually the dominant peaks in the inelastic spectrum at high energies and have received a great deal of interest, both experimentally and theoretically. Several reviews of the subject^{9,27,28} have been written covering both the theoretical aspects and experimental work; the latter has dwelt mainly on high primary energies (> 10 KeV).

Two different types of plasmons have been distinguished; one is the bulk plasmon and corresponds to a longitudinal oscillation of the valence electrons of the solid. The excitation energy of the bulk plasmon, in the free electron approximation, is given by

$$\hbar\omega_p = \hbar\omega_{po} + \frac{3}{5} E_f \frac{\hbar K^2}{m\omega_{po}} \quad (3)$$

where K is the wave vector of the plasma oscillation, E_f is the Fermi energy and ω_{po} is the plasma frequency given by

$$\omega_{po} = \left[\frac{e^2 n}{\epsilon_0 m} \right] \quad (4)$$

where n is the valence electron density, m is the free electron mass, and ϵ_0 is the permittivity of vacuum. It may be noted from this expression that the plasma frequency is dependent only upon properties of the material. For a number of metals and some semiconductors, including Ge, good agreement is obtained between the measured plasmon energy and that calculated by using the full number of valence electrons

per atom to determine the electron density. However, in general good agreement is not obtained since interband transitions can shift the plasmon peak considerably⁹ (Appendix A).

The second type of plasmon excitation, the surface plasmon, is one in which the oscillation is associated with a surface wave that is propagating parallel to the surface but whose amplitude falls off in directions normal to the surface. Excitation energies of surface plasmons are related to the bulk plasmon for thick samples by⁹

$$\hbar\omega_s = \frac{\hbar\omega_p}{\sqrt{2}} \quad (5)$$

if the surface is clean, planar and bounded by vacuum. Should the surface not be clean, such as when oxidized for example, then the excitation energy is given by

$$\hbar\omega_s = \frac{\hbar\omega_p}{\sqrt{1+\epsilon}} \quad (6)$$

where ϵ is the static relative dielectric constant of the bounding material on the surface, e.g. the oxide.

Calculation of the characteristic loss spectrum is possible if the primary electron energy is relatively large. For the case of electrons in the energy range of 10^3 - 10^5 eV the inelastic scattering is reasonably well described by the dielectric theory of solids, certain aspects of which are described in appendix A. In this theory the response of the electron system of the solid to the Coulomb forces of the fast charged particle is described by the dielectric constant, $\epsilon(\vec{k}, \omega)$, where $\hbar\omega$ and $\hbar\vec{k}$ are the electron energy and momentum respectively of the electron belonging to the solid. In principle this function can be calculated from the band structure of the solid; however, it is found that the function $\epsilon(0, \omega)$ describes the scattering of fast electrons quite well and is easily obtained from optical reflectivity measurements. The reason that $\epsilon(0, \omega)$ is adequate, is that the excitations produced with significant probability, for high energy electrons, have small momenta (e.g. plasmons) or are associated with essentially zero momentum change, as for direct interband transitions.²⁹

From optical reflectivity measurements the real and imaginary components of the complex, frequency-dependent dielectric constant

$$\epsilon(\omega) = \epsilon_1(\omega) + i \epsilon_2(\omega) \quad (7)$$

can be determined. The principal direct interband electron transitions are indicated by strong peaks in either ϵ_2 or $\omega^2\epsilon_2$ since the transition rate per unit volume for direct transitions is given by (see Appendix A)

$$W_{vc}(\omega) \propto \omega^2 \epsilon_2(\omega) \quad (8)$$

For the case of fast charged particles, the Coulomb interaction of the fast particle with the electron system of the solid replaces the plane wave interaction of optical measurements. As indicated in Appendix A, the probability of an energy loss $\hbar\omega$ by a fast charged particle in producing bulk excitations is proportional to the function

$$-\text{Im} \frac{1}{\epsilon(\omega)} = \frac{\epsilon_2(\omega)}{\epsilon_1(\omega)^2 + \epsilon_2(\omega)^2} \quad (9)$$

termed the energy loss function. Using this function, with the optically determined $\epsilon_1(\omega)$ and $\epsilon_2(\omega)$ functions, the characteristic loss spectrum can be fit reasonably well for high energy electrons. In this theory, the energy of the bulk plasmon is determined by the condition

$$\epsilon_1(\omega) = 0 \quad (10)$$

which for free electron behavior yields equation (4) for the plasma frequency (Appendix A).

Bauer²⁹ has attempted a theoretical analysis of low energy inelastic scattering of electrons in which he concludes that the function $\epsilon(0, \omega)$ may not be suited to describing the inelastic scattering. He draws this conclusion on the basis that low energy electrons have a scattering probability that is less sharply peaked in the forward direction than that for the high energy electrons. If there is significant large angle scattering ($\theta \sim 20^\circ$), then the excitation wave vector may become comparable to the dimensions of the reciprocal lattice, meaning that non-direct transitions become significant. In his analysis he derives an expression for the scattered current associated with a given energy loss, ΔE , given by

$$I(\Delta E) = \sum_{u,v} \sum_{\Delta \vec{K}} \frac{j_{\text{muv}}(\vec{K}_0, \Delta \vec{K})}{j_0} J_{\text{mluv}}(\Delta E, \Delta \vec{K}) \quad (11)$$

where j_0 is the incident current and j_{muv} is the scattered current for a particular interband excitation which involves a momentum transfer $\Delta \vec{K}$ in going from branch u of band ℓ to branch v of band m separated by energy ΔE ; this latter term also includes in it the inelastic scattering factor. The term J_{mluv} is termed a generalized joint density of states function, in analogy with its counterpart in optical absorption theory, where $\Delta \vec{K} = 0$ (Appendix A), and is given by

$$J_{\text{mluv}}(\Delta E, \Delta \vec{K}) = \int_s \frac{dS}{|\nabla_{\vec{K}} E_{\text{mu}}(\vec{K} + \Delta \vec{K}) - E_{\ell v}(\vec{K})|} \quad \begin{matrix} E_{\text{mu}} - E_{\ell v} = \Delta E \end{matrix} \quad (12)$$

As in the case of optical absorption, when the two bands are parallel for a given ΔE and $\Delta \vec{K}$, the term $J_{m\ell uv}$ is large. It is Bauer's conclusion that $\Delta \vec{K} \neq 0$ will be the rule rather than the exception. However, experiments^{18,40} have indicated that small angle scattering is often obtained even for large losses; therefore, Bauer's conclusion may not be fully warranted.

b Elastically Scattered Primary Electrons

Region III of fig. 1 contains electrons which have been either elastically or "quasi-elastically" scattered. "Quasi-elastic" electrons are those primary electrons which as well as being elastically scattered have suffered small energy losses or gains (~ 10 meV) by phonon scattering. Since the apparatus used in this experiment was not able to resolve the "quasi-elastic" electrons from the elastic electrons, all electrons in region III will be considered as elastically scattered.

In general there are elastically scattered electrons at all angles of scattering, but their number at any given angle is strongly dependent upon the degree of atomic order of the solid. For completely disordered solids the elastic intensity varies smoothly with angle of scattering showing little or no structure. Atomically ordered solids, in contrast, give rise to diffraction of electrons from the "atomic grating", leading to intense beams at specific scattering angles, depending upon the primary energy and angle of incidence. For "perfect" crystals there would only be the coherent scattering leading to the diffraction beams, but real crystals yield some elastic intensity between the diffraction beams with the relative intensity dependent upon the degree of crystalline order, temperature, defect density, etc. The amount of background scattering gives a rough measure of the degree of crystalline order.

When low energy electrons are elastically scattered, the diffraction beams observed are governed by the two dimensional surface periodicities of the atoms. This is because the elastic and inelastic collision cross sections are so large for low energy electrons that the primary electrons only penetrate the solid to an estimated depth of $3-10\text{\AA}$ ³⁰ before being scattered. The propagation directions of the resulting LEED beams are governed by the two dimensional Laue condition given as

$$\vec{K}_{||} - \vec{K}_{0||} = \vec{g} \quad ; \quad |\vec{K}| = |\vec{K}_0| \quad (13)$$

where \vec{K}_0 is the incident electron wave vector, \vec{K} is the wave vector of the diffracted beam and \vec{g} is a surface reciprocal lattice vector. The surface reciprocal lattice vector is defined in analogy with the three dimensional reciprocal lattice vector by the relation

$$\vec{g}_{\ell m} = \ell \vec{b}_1 + m \vec{b}_2 \quad (14)$$

where the basis vectors, \vec{b}_1 and \vec{b}_2 , of the reciprocal lattice are determined from the basis vectors, \vec{a}_1 and \vec{a}_2 , of the surface mesh of the solid as

$$\begin{aligned}\vec{b}_1 &= 2\pi \frac{\vec{a}_2 \times \hat{n}}{\hat{n} \cdot (\vec{a}_1 \times \vec{a}_2)} \\ \vec{b}_2 &= 2\pi \frac{\hat{n} \times \vec{a}_1}{\hat{n} \cdot (\vec{a}_1 \times \vec{a}_2)}\end{aligned}\tag{15}$$

where \hat{n} is a unit vector in the direction of the outward normal to the surface. Any given reciprocal lattice vector, $\vec{g}_{\ell m}$, is perpendicular to the surface grating line identified by the Miller indices (ℓ, m) and satisfies the property

$$|\vec{g}_{\ell m}| = \frac{2\pi}{d_{\ell m}}\tag{16}$$

where $d_{\ell m}$ is the distance between adjacent grating lines (ℓm) . It should be pointed out that the basis vectors are defined for a surface mesh where the atoms have the bulk spacings. In general, however, the outer one or two surface layers may have unit meshes that are different than the bulk. This is found for clean surfaces of some materials where the surface is reconstructed and is often found when other atomic species are adsorbed on a solid surface. This outermost surface structure when it differs from the bulk atomic arrangement is termed the superstructure and the first atomic layer which has the bulk atomic configuration is termed the substrate surface layer. It is quite often found that the unit mesh of the superstructure has dimensions which are integer multiples of the substrate mesh and this fact gives rise to fractional order beams in the LEED pattern.

Without multiple scattering, a simple two dimensional grating will not produce any change in LEED beam intensity as the energy is varied, but in practice the beam intensities are strongly modulated. This effect can partly be described by a kinematical model in which the third Laue condition is used to account for constructive and destructive interference between parallel two dimensional gratings. The kinematical model assumes that the electron wave field incident on any atom is equal to the primary wave field and only single weak scattering events are allowed as governed by the atomic scattering factor. Such models are useful in explaining some of the intensity structure but are generally inadequate because the large collision cross sections violate the kinematical approximation of single weak scattering events. An improvement in the model can be achieved by assuming the primary wave field is attenuated as it penetrates the surface; the attenuation partially accounts for the large collision cross sections. What is needed, however, is a multiple-scattering model which takes

into account the inelastic damping of the electron waves. Such dynamical calculations have been attempted and have explained experimental results with varying degrees of success, but they are difficult and as yet not readily applicable to explaining experimental results. In dynamical calculations the wave field incident upon an atom is made up of the primary wave field and the scattered wave fields from all other atoms in a self consistent manner; inelastic damping of the elastic wave field is sometimes included. This means that aside from determining the surface periodicities and the unit cell size it is usually not possible to determine positions of atoms within the unit cell. These considerations are described thoroughly in a number of review articles¹⁻⁶ and will not be pursued further here. One additional theoretical advance does bear some mention at this point; this is the intensity averaging technique employed by Duke and Tucker^{31,32} for determining surface structure from LEED measurements. This technique relies on the observation that above about 100 eV the effect of multiple scattering is to add fine structure and energy shifts to the intensity curves predicted by a kinematical model. However, suitable energy averages of the intensity around a strong reflection in the intensity profile lead to averaged intensity profiles which are in good agreement with kinematical calculations and are independent of the substrate. This then gives a method by which experimental intensity profiles with a large number of multiple scattering peaks can be averaged to yield intensity profiles which only have peaks corresponding to the kinematical peaks. Comparisons of this profile to assumed kinematical model calculations can then give the surface structure. This is a new and so far little tested approach but has shown promise in explaining some simple structures.

For the purposes of this work, a convenient representation of the diffraction process, which will lend itself nicely to the later discussion of inelastic diffraction is the Ewald sphere construction in reciprocal space. An example of such construction is shown in fig. 3. This diagram shows the reciprocal lattice of a simple cubic crystal with lattice spacing, a , for a plane corresponding to one of the cube faces. This is also taken to be the plane of incidence of the electron beam. The dots represent reciprocal lattice points of the three-dimensional reciprocal lattice while the rods which run normal to the surface of the crystal are the two dimensional diffraction rods used for LEED. The rods are generated by keeping the surface periodicities of the crystal fixed while separating the atom layers parallel to the surface to infinity. Because the dimension in reciprocal space are inversely related to the dimensions in direct space, this causes the reciprocal lattice points in the direction normal to the surface to merge together and form a rod. In an Ewald construction the incident electron wave vector, \vec{k}_0 , is drawn such that its end is on a reciprocal lattice point and it is oriented at its proper angle of incidence with respect to the diffraction rods. The wave vector length is given by the free electron relation

$$\vec{k}_0 = \left[\frac{2m E}{\hbar^2} \right]^{1/2} \quad (17)$$

A circle of radius $|\vec{k}_0|$ is drawn about, 0, the origin of the incident vector and each intersection of this circle with a reciprocal lattice rod defines the end point of the wave vector of a diffracted beam; a number of such vectors are shown with their beam notations indicated as subscripts. Also shown is a surface reciprocal lattice vector, \vec{g}_{10} , and it can be seen that the condition of equation (13) governing the parallel components of the wave vectors is satisfied.

Whereas the diffraction angles are determined by the intersection of the Ewald sphere with the reciprocal lattice rods the intensity variations cannot be understood in terms of the rods alone. From a kinematical viewpoint an intensity maximum occurs for a particular diffraction beam when the intersection point of the Ewald sphere with the reciprocal lattice rod coincides with a reciprocal lattice point. Such intensity maxima are called Bragg peaks and occur when the three dimensional Laue conditions are satisfied, i.e.

$$\vec{k} - \vec{k}_0 = \vec{G} \quad (18)$$

where \vec{G} is a three dimensional reciprocal lattice vector. For the conditions shown in fig. 3 this is only satisfied for the (00) diffraction beam. As mentioned already, due to strong multiple scattering the kinematical model is not sufficient to describe the low energy elastic intensity variation; however, much of the multiple scattering can still be accounted for on this diagram. A multiple scattering theory accounts for the coupling between the set of beams produced by the interaction of the primary beam with the lattice. Because the scattering factor is peaked primarily in the forward direction, two beams that make a small angle with one another are most strongly coupled. Therefore, a strong reflection condition for one of the beams can lead to an increased intensity of the other beam. Such peaks in the intensity profile are called secondary Bragg peaks (SBP's) and tend to occur as fractional order intensity maxima whereas the Bragg peaks are integer order maxima. In fig. 3 the order numbers of the (00) beam maxima are indicated along the (00) rod by $n=1-5$, and as an example a secondary Bragg peak might occur in the ($\bar{1}$ 0) beam due to coupling with the fourth order Bragg scattering in the (00) beam, giving approximately a $9/2$ order intensity maximum for the ($\bar{1}$ 0) beam. General conditions for SBP's are given by,

$$\vec{k}_0 - \vec{k}^1 = \vec{G} \quad (19)$$

and

$$\vec{k}^1 - \vec{k} = \vec{G} \quad (20)$$

where \vec{k}^1 is the wave vector of a diffracted beam other than the one being observed, \vec{k}_0 is the incident beam wave vector and \vec{G} is a reciprocal lattice vector.

c Inelastically Diffracted Primary Electrons

Most inelastic scattering events of interest involve small energy losses with respect to the primary energy and correspondingly small momentum changes. In order that the inelastically scattered electron be backscattered out of the solid, then requires that it also undergo one or more elastic scattering events. This relationship between elastic and inelastic scattering in backscattering measurements gives rise to pronounced diffraction effects in the inelastic spectra.

In the simplest processes, the backscattered electron undergoes one of each type of scattering event before being detected. Davisson and Germer were the first to propose such a model in 1927.³³ Their experimental results were explainable by assuming that some of the elastically scattered electrons suffered inelastic collisions before escaping the solid. This process will be called an EI (elastic-inelastic) scattering process. Since the elastic scattering precedes the inelastic scattering, the intensities of the loss peaks will reach maxima at primary energies where the elastic intensity is maximized. Also, since the momentum transfer is relatively small, the loss peaks will maximize near the LEED beam directions.

In 1938 Turnbull and Farnsworth³⁴ obtained results which indicated a reversed two-step process was taking place, i.e. the inelastic scattering preceded the elastic scattering; this sequence is called an IE (inelastic-elastic) process. In such a process, primary electrons inelastically scattered within some cone about the forward direction are elastically scattered out of the solid. Some of these may have the right energy and momentum to satisfy a Bragg scattering condition whereupon they will be strongly scattered leading to an intensity maximum. Again, since the scattering angle is small, the intensity maximum for any particular loss, W , occurs approximately when the primary energy is $E_B + W$, where E_B is the Bragg energy. The scattering angle for which the maximum occurs is nearly the same as the angle at which the elastically scattered maximum with energy E_B is found. This process, therefore, unlike the EI process is dispersive in nature with only one particular loss peak being maximized for a given primary energy.

Reichertz and Farnsworth³⁵ found both EI and IE processes present in some measurements made in 1949, but that ended the interest in the subject until the last few years when a renewed effort has been made to understand inelastic low energy electron diffraction (ILEED) behavior. A number of experimental studies³⁶⁻⁴² have been carried out recently which complement a series of theoretical studies by Duke and coworkers⁴³⁻⁴⁸. These theoretical studies have been successful in qualitatively explaining most of the experimental results obtained to date and a quantitative application has been made in obtaining a dispersion relation for the surface plasmon for aluminum.⁴⁷

Calculations of ILEED behavior require that the elastic and inelastic scattering parameters be fairly well understood. To begin such a calculation the measured elastic intensity profiles

(intensity vs E_p) must be fit by a multiple scattering calculation, such that trends in the intensity profiles with changing angle of incidence are preserved. Once reliable fits are obtained, the added complexity of combined inelastic and elastic scattering events can be considered. So far aluminum has been the only suitable material for such calculations since the inelastic and elastic scattering parameters have been extensively studied.

A discussion of some of the theoretical considerations given by Duke and Laramore^{45,46} is contained in Appendix B. The basic concepts and conclusions of the theory are the following:

1. As in the case of low-energy elastic scattering, the large elastic and inelastic collision cross sections require that only the parallel component of momentum for the double scattering event be conserved, i.e.

$$\vec{k}_{o||} - \vec{k}_{||} + \vec{g} = \vec{p}_{||} \quad (21)$$

where $\vec{k}_{o||}$, $\vec{k}_{||}$ and $\vec{p}_{||}$ are the parallel components of the wave vectors for the primary electron, scattered electron, and inelastic excitation (e.g. plasmon) respectively and \vec{g} is a surface reciprocal lattice vector.

2. Energy is conserved in the double scattering process:

$$E_p - E_s = w(\vec{p}) \quad (22)$$

where E_p is the primary energy, E_s is the energy of the scattered electron and w is the energy of the excitation.

3. Each Bragg peak in the elastic intensity profile will lead to two "energy-tuned" peaks in the inelastic intensity profile occurring at primary energies of E_B and $E_B + w$. These are the two cases of diffraction before (EI) and after (IE) energy loss respectively.
4. Besides the "energy-tuned" peaks, the theory predicts "momentum-tuned" or "sideband-diffraction" peaks for bulk loss modes as a result of momentum conservation normal to the surface.

As mentioned above, one of the predictions of this theory is that each Bragg peak in the elastic intensity profile can lead to four peaks in the inelastic intensity profile. In practice, however, the "momentum-tuned" peaks are not usually observed because the dispersion relations of the excitation (e.g. plasmons) are rather "shallow"; this effect is discussed in Appendix B. In the angular profiles (intensity vs scattering angle) of the inelastic electrons, however, the "momentum-tuned" peaks should nearly always be observed, when the primary energy is near E_B or $E_B + w$, since by scanning the collector an angle can be found at which the normal momentum conservation is satisfied. These basic concepts and predictions are more easily grasped by using modified Ewald constructions in reciprocal

space. Two types of excitations must be considered; volume excitations where the excitation momentum has both parallel and normal components with respect to the surface, and surface excitations where momentum is restricted to lie parallel to the surface. In each case the excitation dispersion relation will be considered isotropic, i.e. $w(\vec{p})$ depends only $|\vec{p}|$.

In fig. 4 a diagram is shown for an EI scattering process. On the right hand side of the figure a volume excitation is illustrated while on the left hand side a surface excitation is considered. The two large circles represent the intersection of the Ewald spheres with the plane of incidence for wave vectors corresponding to the primary momentum \vec{k}_0 and secondary momentum \vec{k} . On the right, a Bragg condition is shown⁰ satisfied for the (00) diffraction beam and at the end of this wave vector a small sphere is indicated which defines the possible values of $-\vec{p}$ for the volume excitation. For a given reciprocal lattice vector, in this case $\vec{G} = 0$, and a given $w(\vec{p})$ the possible secondary wave vectors, \vec{k} , can be determined from equations (21) and (22). The end points of these vectors lie on the circle of secondary \vec{k} vectors and the parallel momentum conservation requirement limits \vec{k} to lie within the shaded region. Within the shaded region two secondary wave vectors are shown which satisfy both the parallel and normal momentum conservation conditions ("momentum-tuned" condition) and peaks would be obtained in the inelastic angular profiles at these two angles.

On the left hand side of fig. 4 the EI conditions are shown for a surface excitation about the (02) diffraction beam. Since surface excitations have no normal momentum there are only two possible values of \vec{k} which satisfy equations (21) and (22). Ideally, then, rather narrow doublets should always be observed in the angular profiles for surface excitations.

An IE scattering process is illustrated in fig. 5 for a bulk excitation. The vector, \vec{k} , shown represents the condition for obtaining a "momentum-tuned" peak in the inelastic angular profile. Because of the small angle scattering, this will occur for a primary energy near $E_p + w$. It should be noted that for non-normal incidence, as illustrated, at any given primary energy and $w(\vec{p})$ there is only one value of \vec{k} which satisfies the "momentum-tuned" condition. A more detailed discussion is given in Appendix B.

III. Experimental Apparatus and Technique

1 Vacuum System and Processing

A basic requirement of surface measurements is that the surface of interest must be kept free of contamination for the duration of the measurement. In order to allow measurement times of several hours experiments were conducted in ultrahigh vacuum of about 1.0×10^{-10} Torr, requiring special procedures and apparatus. The ultra-high vacuum system used was a non-commercial system built especially for this study and is shown schematically in fig. 6 along with some of the major components inside. The main chamber itself is 22 cm in diameter and has four 10 cm side ports and four 5 cm side ports alternated every 45° around it. All the parts of the vacuum system were made of 304 stainless steel and gold gaskets were used for flange seals. A 50 liter/sec. sputter-ion pump was used as the main pump and was connected to one of the 10 cm side ports by about 1 meter of 10 cm pipe in order to minimize the effect of the pump magnets on the experiment. A titanium sublimation pump, positioned inside the pipe going to the sputter-ion pump, was used to provide additional pumping of active gases. For rough pumping, two zeolite sorption pumps were used with liquid nitrogen cooling and were connected to the system by a Granville-Phillips 2.5 cm ultrahigh vacuum valve.

Two windows were mounted on the system; one, a 10 cm window, was used as a viewing port for observing sample and energy analyzer positions, and the other was a 5 cm quartz window which provided a direct view of the sample face for visual checks of sample temperature and was available should photoelectric measurements be desired. A gas admission system was coupled to the vacuum system by a 1/2 inch Granville-Phillips type C valve and was used to admit pure argon for ion bombardment cleaning of the sample.

Because the measurements involved low energy electrons, magnetic fields were a serious problem. To minimize magnetic fields from the sputter-ion pump, the entire pump was enclosed in a case made up of two layers of high permeability metal separated by a layer of aluminum. The Earth's magnetic field was compensated by a set of Helmholtz coils five feet in diameter, centered around the main chamber of the vacuum system. These coils allowed the magnetic field to be nulled to within 10 milligauss over the region of electron traversal.

Vacuum processing started with ultrasonic cleaning of every part in methyl alcohol or boiling Freon prior to assembly. After assembly the system was rough-pumped to about 1.0×10^{-3} Torr. At this pressure the titanium getters were outgassed and the ion pump was baked into the sorption pumps for several hours. The sorption pumps were then valved off and the sputter-ion pump was started with the aid of the titanium sublimator. Once the pressure reached about 1.0×10^{-8} Torr a brief outgassing was given to all the filaments in the system and the entire system was baked at 275°C . When the pressure reached about 5×10^{-7} Torr while hot the system was cooled slowly and a thorough outgassing was given all the filaments

and the titanium sublimators. To remove gases readsorbed on the walls during this outgassing the system was rebaked at 275°C. This procedure typically produced total pressures of about 1.0×10^{-10} Torr or less, as measured with a Bayard Alpert gauge.

2 Measurement Apparatus

a Electron Gun and Scattering Chamber

A schematic view of the electron gun and scattering chamber is shown in fig. 7; also shown is the energy analyzer and related biasing configurations. The electron gun is a three-electrode device machined from 304 stainless steel where focusing is controlled primarily by the voltage between the second and third anode. The first anode voltage has almost no effect on the focus but acts mainly to control the amount of current. A tungsten ribbon filament was used as the electron source and was heated by direct current flow. At the emitting point of the filament, the .040 inch by .001 inch ribbon was etched to about half its initial size to permit smaller filament currents to be used. This was desirable because magnetic fields needed to be minimized and the smaller volt drop that occurred decreased the energy spread of the primary beam. About 1.0A of filament current was used and this gave beam currents of about 1.0×10^{-8} A for 10 eV primary energy and about 1.0 μ A at 100 eV.

To obtain good focusing properties and a stable beam position for electron energies in the range 5-1000 eV, it was necessary to vacuum anneal the electron gun at 1050°C and then quench it with a flow of argon. This procedure removed residual magnetization induced in the gun parts by machining. Regions where the metal was machined to small dimensions, such as near the apertures of the electrodes, had magnetizations of up to several gauss. Spot welding also caused excessive localized magnetization in the stainless steel. A beam size of about 1.5 mm was obtained at the target and its position was stable with changes in energy when good cancellation of the Earth's magnetic field was provided by Helmholtz coils.

A 3.0 inch spherical scattering chamber was formed from two hemispheres of 304 stainless steel. From these were supported the internal grids and collector plates. Surrounding the target, which during measurements was positioned at the center of the scattering chamber, was a spherical grid, g_1 , constructed from 100 line/inch chromium plated stainless steel woven mesh. This grid was kept at target potential thus maintaining a field free region about the target to minimize trajectory distortion. A battery in the target lead, allowed for correction of a contact potential difference between the target and g_1 . A hemispherical collector was placed behind g_1 on the back half of the scattering chamber and was biased at 22 1/2 to remove electrons which scattered in this direction.

On the other half of the scattering chamber, a second hemispherical grid, g_2 , was mounted concentric to the first grid with 0.1 inch spacing and was used as a retarding grid for energy analysis

of the scattered electrons. This grid was connected to a nearly complete hemispherical collector used for large solid angle measurements. To permit measurements of energy distributions at specific angles a slot was cut in this collector and a drift channel was welded in to provide an electrically shielded drift space, extending beyond the outer hemisphere, in which an entrance tube for the energy analyzer moved. All these parts were also chromium plated.

b Energy Analyzer

Figure 7 shows a schematic view of the 127° cylindrical, electrostatic energy analyzer that was used in the experiment. The analyzer was mounted on a cart which rode in a slotted track providing 60° rotation about the scattering chamber in the horizontal plane. A vacuum rotary feedthrough coupled to the cart by a radial arm served as the driver.

The energy analyzer was constructed from 304 stainless steel and as in the case of the electron gun it was necessary to vacuum anneal the entrance and exit aperture plates to eliminate magnetization caused by machining. Chromium plated stainless steel grids with about 75% transmission (100 lines/inch) formed the deflecting electrodes inside the energy analyzer. These were used in conjunction with cylindrical collectors placed directly behind them to prevent the creation of secondary electrons inside the analyzer which could reach the exit aperture. On the exit plate a knife edge circular aperture .020 inch in diameter was used, while on the entrance plate a .020 inch by .20 inch knife edge slit was used. A slit was necessary because this type of analyzer does not have refocusing properties along the direction of the cylindrical axis. With a circular aperture instead of the slit, small misalignment of the transmitting plane of the analyzer with the trajectory of the electrons entering the analyzer caused loss of signal. A slit provided enough leeway to eliminate this problem.

An analysis of the properties of this type of electrostatic velocity analyzer was given by Hughes and Rojansky.⁴⁹ They showed that 127° 17' was the optimum deflection angle for a cylindrical condensor; however, recently Roy and Carotte⁵⁰ have shown that slight variations on the geometry of the analyzer can improve its performance. The resolution of the analyzer is approximately given by

$$\frac{\Delta E}{E} = \frac{\Delta R}{R_0} + \frac{4}{3} \alpha^2$$

where ΔR is the aperture width, R_0 is the mean radius of the analyzer and α is the angular acceptance of the analyzer. For the analyzer as used, ΔR was .020 inch and $R_0 = .886$ inch. The angular acceptance, α , is defined as the maximum angular deviation an electron can have from normal entrance and still pass through the analyzer, if it originates from a point source at the entrance slit. A value of about 5° was estimated for α from the approximate orbit equations given by Hughes and Rojansky. Using these values gives a resolution for the

analyzer of $\Delta E/E = 3\%$. With respect to the angular acceptance of the analyzer, it should be pointed out that this is for electrons emanating from a point source at the entrance aperture whereas the geometrical angle of acceptance, for a point source at the target and radial electron trajectories, is less than 0.4 degree. The operating characteristics of the analyzer were in good agreement with calculations, the energy passing relationship, $E_{\text{pass}} = 3.52 \Delta V$ where ΔV is the potential between the deflecting grids was measured to be less than 3% in error for pass energies from 1.0 eV to 60 eV.

There are two modes of operation for this analyzer. In the first mode, the pass energy is fixed and the electrons are retarded by grid g_2 before they enter the analyzer. Since the resolution is a fixed percentage of the pass energy, this mode leaves the resolution of the analyzer fixed over the entire energy range of the measurement; this method was used almost exclusively. The second mode of operation consisted of setting g_1 , g_2 and the analyzer case at the same potential and then obtaining the energy distribution by sweeping ΔV . Energy distributions obtained this way had to be corrected by a resolution factor to give their true shape. The true energy distribution is related to the measured distribution by a factor proportional to E^{-1} . Energy distribution measurements taken by the two different modes of operation were compared, and the E^{-1} proportionality was verified.

c Apparatus Alignment

Mechanical alignment of the parts of the apparatus was a critical factor for obtaining reliable energy and angular distributions. A procedure, utilizing a laser beam, was developed to align the parts accurately. A jig was constructed that supported a front surface mirror at the sample position such that it could be rotated about the same axis as the energy analyzer with accurate control of the angle. With the mirror set for normal incidence the laser beam was directed down the axis of the electron gun and reflected back from the mirror to the laser and back again. If there was some misalignment, the reflected beam back to the gun could be seen displaced from the originally transmitted beam. The electron gun position was then adjusted until all the beams were coincident; this was the condition for having the electron gun properly aligned. Next the mirror was rotated so that the laser beam was reflected onto the energy analyzer. A mirror was mounted on the entrance plate of the analyzer and the aperture position was marked with cross hairs. The reflected laser beam from the target mirror was kept between the cross hairs of the analyzer mirror and the analyzer position was adjusted until the laser beam doubled back upon itself. When this condition was reached the electron gun and energy analyzer were in mutual alignment with the proper target position. A final check was made by allowing the laser beam to pass through the entrance aperture and reflect off the back wall of the analyzer onto the exit aperture. When this reflected beam was at the same height as the exit aperture then the analyzer was mounted properly on its movable cart.

3 Measurement Procedures

a Sample Positioning and Orientation

The target was mounted at a fixed 45° angle to the incident beam on the end of a manipulator shaft as shown schematically in fig. 6. The main rotary axis of the manipulator was coincident with the electron beam axis, so that rotations of the target left the incident angle unchanged; such rotations are equivalent to rotating the energy analyzer about the electron beam axis. Besides the rotary motion, the manipulator allowed the crystal to be translated 6 mm in two directions perpendicular to the rotary axis and the rotary axis itself could be tipped.

When the sample was cleaned by ion bombardment it had to be withdrawn from the scattering chamber. This necessitated some means of accurately repositioning the sample in order to continue measurements. An axial translation stage on the manipulator allowed the target to be withdrawn 7 cm where it could then be tipped in front of the ion bombardment unit. To reposition the sample, the manipulator shaft was adjusted to be coaxial with the electron beam and the target was then reinserted into the scattering chamber as accurately as possible with external measurements. Final adjustments were made by monitoring the specularly scattered electron beam. With the energy analyzer positioned to receive the 45° specular beam, the sample was adjusted until a maximum signal was obtained. This proved to be a very reliable way to reproduce target position. In addition the target could be translated in directions perpendicular to the electron beam until the beam missed the target. In this way the sample edges could be defined and the sample could easily be centered.

Prior to mounting the sample manipulator, the conditions for cancelling the magnetic field were determined. A remote probe from a gaussmeter was inserted into the center of the scattering chamber such that it was perpendicular to the axis of one set of the Helmholtz coils. The current was then adjusted through those coils until a null reading was obtained. Each set of coils was adjusted in that way until the best cancellation was achieved. The fields were reduced to the order of 10 milligauss or less by this procedure.

b Secondary Electron Measurements

In making these low energy measurements, it was important to maintain a field free region between the target and the inner grid, g_1 , so that the electron trajectory distortions were minimized. This meant that contact potential differences had to be cancelled out. The condition for no potential difference between the target and g_1 could be established by measuring the low energy cutoff of the SED. If there is no potential difference between the target and g_1 , then an electron that originates at the target with zero kinetic energy will pass through the analyzer when the sweep voltage, V_s , as defined in fig. 7 is given by $V_s = -V_{pass}$, where V_{pass} is defined by $V_{pass} = eE_{pass}$. In other words a zero energy electron must

be accelerated up to the selected passing energy of the energy analyzer. However, if there is a contact potential difference, ϕ_{Tg} , such that g_1 is positive with respect to the target, then the zero kinetic energy electron at the target will be accelerated by this potential and will pass through the analyzer when $V_s = -V_{pass} + \phi_{Tg}$. This will be evident in the measured energy distribution as a shift in the low energy cutoff along the energy axis. In fact, the entire energy distribution will be shifted by an amount ϕ_{Tg} toward higher energy. If on the other hand, the contact potential is such that the target is positive with respect to g_1 by some amount ϕ_{Tg} then this will act as a potential barrier to electrons which originate at the target. An electron leaving the target with kinetic energy, $e\phi_{Tg}$, will just reach g_1 with zero kinetic energy and electrons with lower energy will not be able to reach g_1 at all. Under these conditions the entire energy distribution will be shifted by an amount ϕ_{Tg} to lower energies while the low energy cutoff will occur when $V_s = -V_{pass}$. This premature cutoff makes the energy distribution narrower by the amount ϕ_{Tg} . Therefore the low energy cutoff is fixed for all conditions except those where the target is negative with respect to g_1 . This then provided a method of correcting for contact potentials by use of an external potential, V_{Tg} , between the target and g_1 . The external voltage, V_{Tg} , was adjusted until the target was sufficiently negative that a definite shift could be measured in the low energy cutoff towards larger sweep voltage. Then V_{Tg} was backed off carefully until the low energy cutoff just stopped shifting; this ideally was the condition for $V_{Tg} = -\phi_{Tg}$ and a field free condition between the target and g_1 . Since the clean Ge target was assumed to have a work function of 4.75 eV, the +0.6 eV value necessary for V_{Tg} means that the work function of the chromium plated grid, g_1 , was about 4.15 eV. This value agrees well with a value determined by photoemission measurements from similar grids using the Fowler technique.

Measurements of the secondary electron energy and angular distributions were carried out in two ways, the apparatus for the first method is shown schematically in fig. 8. In this technique, those secondary electrons which arrive into the solid angle accepted by the energy analyzer are retarded by grid g_2 prior to entering the energy analyzer and those whose kinetic energy is correct pass through the energy analyzer and reach the electron multiplier. A Channeltron electron multiplier was used in a pulse-saturated mode and the detection technique was one of pulse counting. The amplified pulses were fed into an integral discriminator whose output went to a ratemeter which provided an analog signal in counts/sec. By sweeping the target and inner grid potential a direct plot of the energy distribution of secondary electrons was obtained.

The second method of measurement was basically quite similar, but utilized a FabriTek model 1064 signal digitizer for data accumulation and manipulation; the schematic is shown in fig. 9. In this type of measurement, an output ramp which was synchronized to the memory advance of the signal digitizer was amplified and

used as the retarding voltage. Pulses from the integral discriminator were then fed directly into the signal digitizer where the information was stored. Typically, counts from about a thousand sweeps were accumulated in the memory for a single energy distribution. Only one fourth of the memory was used to accumulate an energy distribution so that the rest of the memory could be used to store other distributions or for the purposes of scaling, adding or subtracting distributions or integrating the data.

In addition to the secondary electron energy distribution (SED) measurements made at specific angles using the 127° energy analyzer, SED's and the first derivative of the SED's were obtained for nearly hemispherical collection. These measurements were made by a modulation technique that will be described in the next section. Useful contrasting information was provided through comparisons of these measurements with those obtained with the 127° energy analyzer at various scattering angles.

Angular distributions of the secondary electrons were obtained with the apparatus as shown in fig. 8. With the sweep voltage set to detect electrons with a particular energy, angular distributions could be obtained by rotating either the energy analyzer or the target with motor drives connected to the respective rotary feedthroughs. The angular motion was detected by coupled potentiometers and this signal was used to drive the x-axis of an x-y recorder for direct plotting.

c Auger Measurements

As mentioned in Section 1, Auger spectroscopy is a method of determining the atomic species present near the surface of a solid. Because of the short escape depth for an Auger electron, it has been shown that only the first few atom layers are analyzed by this technique,⁵¹ making it ideal for measurements of surface contamination. Figure 10 shows the schematic of the apparatus as used to measure Auger spectra. The ac modulation technique for differentiation of the collector signal has been described elsewhere.⁵¹ Briefly, the target, third anode and grid, g_1 , are modulated with a small sinusoidal voltage in series with the retarding voltage. The modulation produces an ac signal at the collector which is proportional to the energy distribution of the secondary electrons. For this apparatus the collector was connected to the retarding grid, g_2 , resulting in a large capacitive signal due to the capacitance between g_1 and g_2 that was sufficient to overdrive the detection apparatus. To correct this, a capacitance bridge circuit was formed by the variable capacitor, C_p , and a center-tapped modulation transformer. By tuning C_p it was possible to effectively null out the capacitive signal. After preamplification, the ac signal went to a lock-in amplifier where the second harmonic was measured. It can be shown⁵¹ that this is proportional to the derivative of the energy distribution. This is more desirable than the energy distribution itself, because small peaks and shoulders on a large background in the energy distribution show up as quite prominent features in the differential curve making observation and identification much easier.

d Electron Diffraction and Characteristic Loss Measurements

Measurements of low energy electron diffraction (LEED), characteristic losses and inelastic diffraction were taken with the apparatus as shown in fig. 8. To measure the LEED patterns or beam intensities, the retarding voltage was set so that elastic electrons passed through the energy analyzer, and by rotating the target and energy analyzer it was possible to map out the LEED pattern (i.e. to obtain an elastic intensity profile). Measurements of the elastic intensity versus primary energy were taken in a point by point fashion since the LEED beam positions changed with primary energy, requiring that the energy analyzer also be moved to track the beam.

Characteristic losses were measured by sweeping the retarding voltage through a range of energies near the elastic peak and plotting the energy distribution; these were done at specific scattering angles. Variation in the loss peak intensities with angle and primary energy were also measured and gave information about inelastic diffraction events. Either a series of energy distributions were taken at increments in scattering angle, or the retarding voltage was set to allow electrons from a particular loss peak to pass through the energy analyzer while the angle of scattering was varied with a motor drive, thus yielding direct plots of angular profiles of particular losses.

4 Target Preparation and Cleaning

A (100) face of Ge was chosen as the surface to be studied because Ge has been well studied in this laboratory by other techniques and the (100) face gives a simple LEED pattern thus making inelastic diffraction measurement simpler. The sample was cut from a commercial single crystal of 45 Ω -cm germanium to a square face 0.7 cm on a side. This sample was oriented to within $\pm 0.5^\circ$ by a technique using a preferential etch and optical reflection patterns.⁵² After orientation it was mechanically polished to an optically flat mirror finish. The Ge crystal was mounted on a tantalum block machined to fit the crystal. Tantalum tabs, which fit into slots cut in the sides of the crystal, were welded to the tantalum block, holding it in place. A 150 watt projection lamp filament, mounted inside the tantalum block, was used to heat the block and sample by radiation.

An ion bombardment method was used for cleaning the target and a schematic of the apparatus is shown in fig. 11. This method consists of bombarding the surface to be cleaned with ions which "sputter" the surface away, i.e. surface atoms are ejected due to the impact of the ions; in this experiment argon ions were used. This apparatus is nothing more than an ionization chamber from which the ions can be drawn to the target surface. It consists of a cylindrical tantalum enclosure with a square opening at one end where the target is positioned. Inside a double filament of .005 inch tungsten wire provides a source of electrons and a sinusoidally shaped .030 inch tungsten wire forms the anode used for accelerating electrons to ionize the argon.

This apparatus was used at a pressure of 1.0×10^{-3} Torr of argon which had been cataphoretically cleaned⁵³ prior to admission to the vacuum system. A gas discharge was struck inside the ion bombardment chamber by running the filament at about 5.0 A and setting the anode voltage at about 30 V. Ions were drawn to the target by applying a negative potential to the target with respect to the anode. Two modes of discharge were encountered with this apparatus, one was characterized by low target currents and uniform sputtering and the other by large target currents and nonuniform sputtering. The high current mode was the one used and was obtained by raising the anode voltage up to about 80 volts momentarily, thus striking the high current mode, and then reducing the anode voltage to the desired operating voltage of about 27-30V. At an anode voltage of about 25 V the discharge usually reverted to the low current mode. The anode voltage was kept as low as possible to minimize sputtering of the filament and tantalum enclosure. For typical operating conditions, i.e. using 4.8 A filament current, 30 V anode potential and 50 V target potential, an ion current density of about $100 \mu\text{A}/\text{cm}^2$ was obtained.

Initial sputter cleanings removed about one thousand atom layers; these were followed by lengthy heatings at about 600°C. At first, this procedure left the surface with some carbon contamination as determined by Auger spectroscopy; however, after several sputter-anneal cycles this carbon contamination disappeared and it is suspected that the carbon was migrating onto the surface from the sample holder and sample edges during the anneal stage of the treatment. After a clean surface was established the sample was annealed each day prior to making measurements, in order to desorb any CO or other contaminants that may have been adsorbed on the surface. Periodically a significant amount of carbon could be detected by measurement of an Auger spectrum as shown in fig. 12; this seemed to be accompanied by some degradation of the LEED beam intensities as well. This build up of carbon was felt to be the result of electron beam cracking of CO molecules on the surface. A light sputtering of the surface (~ 100 atom layers) was sufficient to reestablish a clean surface as demonstrated by the Auger spectrum of fig. 13. In the figure, each section of the Auger spectrum is labeled with the relative attenuation, A , the time constant used, τ , the peak to peak modulation voltage, V_m and the primary electron current, I_p ; where they have been omitted they are the same as the previous section of the spectrum. To reduce the depth of damage during sputtering and make annealing easier, the ion energy was kept at 80 eV for all but the initial sputtering when 200 eV ions were used.

5 Coordinate Systems and Experimental Variables

Throughout the measurements it was necessary to reference the experimentally measured angles to the crystallographic orientation of the sample. Figure 14a shows the orientation of the incident electron beam with the primary crystallographic directions in a (100) plane of the Ge crystal. The primary beam was incident on the (100) face of the sample at an angle of 45° such

that its projection onto the surface was in the [110] direction. Also shown in the figure are the surface unit net vectors, \hat{a}_1 and \hat{a}_2 , that are used for LEED pattern specification.

In fig. 14b the experimentally, allowed angles are shown. The two allowed rotations, θ_A and θ_m , are not the usual θ , φ coordinates of a spherical coordinate system since the angle of incidence is non-normal. This complicated the measurements, as a scan along a particular crystal axis in general required changing the target angle, θ_m , as well as the analyzer angle, θ_A . Curves of constant θ_A and θ_m were calculated and plotted as a function of the spherical coordinates θ and φ in a polar plot as shown in fig. 15. The crystallographic directions are defined by the θ, φ coordinates and some of the low index directions are indicated in the figure. The superimposed curvilinear net of constant θ_A and θ_m lines was used to graphically transform the angular coordinates based on the crystal axes to the experimentally determined angles, thus allowing any crystal direction to be located for measurements. LEED beam positions were also easily determined using this plot.

IV. Experimental Results and Discussion

1 Characterization of the Sample Surface

Since the goal of this experiment was to assess the low energy electron scattering from as near an ideal Ge(100) surface as possible, great care was taken during the course of experimental measurements to insure that the sample surface was clean and well ordered. Surface cleanliness was checked periodically by Auger spectroscopy while surface order was checked continuously by LEED measurements. Argon ion bombardment and annealing procedures used to obtain clean ordered surfaces are described in section III-4.

The Auger spectrum from the Ge(100) surface before its initial sputtering is shown in fig. 16; as expected for the oxidized surface a large KLL oxygen peak was observed and the KLL carbon peak was quite large while all the Ge Auger peaks were small. After sputtering the sample with Argon ions at energies of 135 eV so that about 600 monolayers of Ge would be removed, the Auger spectrum of fig. 17 was obtained. Although this sputter treatment removed all traces of carbon, the oxygen contamination was still severe. Sputtering alone was not sufficient for removal of this oxygen; however, by heating the sample to about 550°C subsequent to sputtering all traces of the oxygen disappeared. Apparently whatever oxygen remains on the surface after sputtering is quite loosely bound and is perhaps mobile enough to move about the surface rather than be ejected during argon ion bombardment.

Once the oxygen was removed the Auger spectrum appeared as shown in fig. 13, and is the Auger spectrum of clean Ge. However, after periods of prolonged measurements a buildup of carbon contamination was observed to take place; a severe case of such a buildup is shown in fig. 12. This carbon presumably resulted from

CO molecules being cracked on the surface by the electron beam. As a general rule, whenever the carbon peak amplitude became greater than one twentieth the peak to peak amplitude of the 106 eV Ge peak, the sample was given a fresh sputter-anneal treatment.

Measurements of the LEED pattern and elastic electron intensity were used to determine the relative state of surface ordering of the Ge(100) surface. Several previous studies of the Ge(100) LEED patterns have been made, yielding two different results. Jona⁵⁴ cleaned his samples by heating alone and observed integral and 1/2-order diffraction spots giving a Ge(100) 2x1 pattern. Lander and Morrison⁵⁵ using ion bombardment and annealing procedures to clean their Ge, observed in addition to the integral and 1/2-order spots, streaks through the lowest 1/2-order spots which at low energies could be partially resolved into 1/4-order spots. They postulated a Ge(100) 4x2 model for the surface structure where the top atomic layer, with a 4x2 unit cell, was partially disordered leading to streaking. Chen⁵⁶ also cleaned his sample by ion-bombardment and annealing and observed the streaks but could not resolve any 1/4-order spots.

In this study the streaking as well as the 1/4-order spots were readily observed for energies below about 30 eV. Complete streaking was not observed, presumably because of the non-normal incidence; instead the streaks were only apparent parallel to the plane of incidence. Besides the usual 1/2-order spots, other spots were observed in the (1/2 1/4), (1/2 1/2), (1/2 3/4) and (3/4 1/2) positions with the streaking between the (1/2 1/4) and (1/2 3/4) spots. A second Ge(100) sample was also examined in a visual display LEED apparatus, where both the streaking and the 1/4-order spots were clearly observed leading to the conclusion that the clean Ge(100) surface quite likely does possess a 4x2 surface structure. Figure 18 shows illustrations of the observed LEED patterns for three different energies at normal incidence. In panel (a) the pattern at 40 eV shows only integral and 1/2-order beams and this pattern has often been considered as the complete clean Ge(100) pattern but at 20 eV (panel (b)) the streaks through the lowest 1/2-order spots are very evident and spots can be resolved in the 1/2 1/2 positions. When the primary energy is lowered to about 4 eV the 1/2 1/2 spots fade away but the 1/4-order spots emerge distinctly as shown in panel (c).

As a check on the diffraction conditions and electric and magnetic field cancellation, the angles of the LEED beams were measured with varying primary energy and very good agreement was obtained with those theoretically calculated over the energy range 5-150 eV. This suggests that there was little trajectory distortion of the scattered electrons in the experiment.

2 Elastic Electron Intensity Analysis

Although a detailed study of the elastic electron intensities was not an intended part of this investigation, the influence of the

elastic scattering on the inelastic electron and secondary electron spectra made it necessary to investigate the elastic intensities rather extensively. The main problem with elastic intensity studies is the complexity of the analysis problem, where usually anything short of a multiple scattering analysis is found to be unsatisfactory; this is especially true at lower primary energies such as used in this experiment. Although a complete analysis of the elastic scattering is an ominous task, it is possible to identify certain features and trends by simpler analytical methods used in this study.

Elastic intensity profiles of twelve LEED beams were measured for energies below 150 eV and are shown in figs. 19-21, corrected for primary current variation with energy. Each of these plots has the correct relative intensity scale for direct comparison of intensities among profiles. It is apparent from the large amount of structure that more than primary Bragg scattering is involved. A method for examining this data, described by Seah,⁵⁷ that will be followed here, consists of representing each peak in the elastic intensity profile by a dot on the plane of incidence in K-space. Each dot represents one end of the incident wave vector and therefore corresponds to the center of the Ewald sphere, with the wave vector length being determined from the free electron relationship (eq. (17)) with suitable inner potential correction. The relative size of the dot gives a qualitative relationship to the strength of the peak it represents. Only peaks for a given LEED beam are plotted on any given diagram. On the same diagram are plotted relevant lines of intersection of Brillouin zone planes with the plane of incidence. These lines of intersection are called Bragg zone lines and define the locus of the Ewald sphere center for a given Bragg reflection as energy is varied.

These diagrams can be useful in determining whether an intensity peak for a given LEED beam is a Bragg peak or is a secondary Bragg peak (SBP) due to coupling with another beam. If it is a Bragg peak, then the dot in K-space should fall on a Bragg zone line associated with the beam of interest. However, if it is an SBP then the dot should fall on a Bragg zone line associated with a different beam.

Figure 22a shows the plane of incidence in K-space for the Ge(100) sample used in this study. The dots represent the reciprocal lattice points of the crystal and are labelled according to the usual assumed cubic unit cell of the face centered cubic Bravais lattice. Also shown are the diffraction rods used for LEED specification with the indices shown above each rod. In fig. 22b an illustrative plot of the type described above is shown for the (00) diffracted beam. A very superficial intensity plot is also shown superimposed on the point plotting in K-space, for electrons incident on a surface at angle θ . The first through the fourth order Bragg peaks are indicated along with some half integral secondary Bragg peaks. The dots along the (00) diffraction rod are reciprocal lattice points.

In the actual K-space plots there should be Bragg zone lines corresponding to each reciprocal lattice point both in and out of the plane of incidence; however, often only a few of these are important. It is not clear how the electron flux is shared between various propagating waves in the crystal, but Bauer² proposes that because forward scattering is preferred, diffracted beams along adjacent diffraction rods are the ones which are strongly coupled. If this is the case, the number of Bragg zone lines that need to be considered is reduced considerably.

In preparing the K-space plots, each peak in the intensity profile of a given LEED beam was qualitatively assessed as being weak or strong, thus determining the size of the dot in K-space. Shoulders on the side of a large peak such as the ones at 61 eV and 100 eV for the (00) beam are considered as weak peaks. The wave vector length was then determined from the energy of the peak along with an appropriate inner potential correction according to the relation

$$K = \left[\frac{2m(E+eV_I)}{\hbar^2} \right]^{1/2} \quad (23)$$

where V_I is the inner potential. Assuming an idealized step potential change at the surface and conservation of the wave vector parallel to the surface, the angle of the wave vector inside the solid, θ_i , was determined from the angle of incidence, θ_o , by applying a refractive correction given as

$$\frac{\sin^2 \theta_o}{\sin^2 \theta_i} = \frac{E+eV_I}{E} \quad (24)$$

Plots of the peaks in K-space for the (00), (10), (01), (11), and (02) LEED beams are shown in figures 23, 24 and 25a for data obtained in two different ways. One set of dots was obtained from the intensity profiles shown in figs. 19-21, measured at 45° angles of incidence using the apparatus described in section III. The normal and near normal incidence data shown in the K-space plots was obtained on a second Ge(100) sample using a visual display LEED apparatus. Energies of intensity maxima in the latter case were obtained by visual inspection of the LEED spot brightness and could easily be determined to within one eV. For the case of the (00) beam, normal incidence could not be used since the beam returns directly back to the electron gun; therefore a 5° angle of incidence was used for most of this data with the exception of some normal incidence data obtained from the work of Chen.⁵⁶

The normal incidence data was used to determine an inner potential correction for the analysis. An inner potential correction is used to account for the change in the average potential which the

electron encounters when going from vacuum into the crystal and depends on the penetration of the solid. An assumption was made that the inner potential rises from a value equal to the work function at zero kinetic energy and saturates at some average value for higher energies; a typical value used being about 15 eV. By fitting the strong intensity maxima of the normal incidence data to calculated Bragg conditions, the data points of fig. 25b were obtained. The solid curve shown drawn through these points was then used as the inner potential relationship and corrections to all the data in the K-space plots were based on this curve.

As shown by the K-space plots of figs. 23-25 the normal incidence data gives a good fit of the strong elastic intensity maxima to the predicted Bragg conditions. The scale on the right of fig. 23a gives the wave vector length as a function of energy. There is also a good fit of most of the weaker maxima to Bragg zone lines for other beams, suggesting strongly that these are SBP's (see eq. (19)). This is reinforced by comparing the five plots and noting the correlation between strong beams and weak maxima in other beams. Visual inspection of the LEED spots shows this quite graphically, in that nearly simultaneous maxima occur in different beams while only one of them satisfies a Bragg condition, suggesting that there is a sharing of the electron flux giving rise to SBP's.

A proper analysis of the LEED intensity profiles would include data for many angles of incidence instead of just the two available here, and studies of this kind have been carried out by Seah⁵⁷ and Reid⁵⁸ on Ag and Cu respectively. A trend indicated in both studies was that many of the intensity maxima remained nearly fixed in energy as the angle of incidence was varied. In the K-space plots this means that the dots representing the maxima tend to fall along circular arcs rather than follow Bragg zone lines; this is especially true for low energies. A true Bragg peak, in contrast, would shift in energy as the angle of incidence was changed so that in K-space the dots would follow the particular Bragg zone line involved. Calculations by Tucker and Duke⁵⁹ have reproduced the behavior observed by Seah and Reid. In their calculations they determine that most of the peaks in a low energy elastic intensity profile are interlayer multiple scattering peaks which remain relatively fixed in energy as the angle of incidence is changed but whose magnitudes vary greatly. These calculations also show that the multiple scattering peaks are usually only strong in the vicinity of a kinematical Bragg energy, and as the angle of incidence is changed the multiple scattering peak nearest the Bragg energy tends to be enlarged, so that the behavior is as though an intensity envelope following the kinematical Bragg energy passes through the background of multiple scattering peaks, varying their amplitudes. They also conclude that it is very difficult, except possibly at normal incidence, to label any peak in the elastic intensity profile as a Bragg peak; instead they contend there are clusters of multiple scattering peaks around the kinematical Bragg peak positions, some of which are quite strong.

In fig. 23a the (00) beam maxima are shown for normal incidence, 5° angle of incidence and 45° angle of incidence. The normal incidence and 5° angle of incidence data fit low index zone lines very closely. Three Bragg conditions are satisfied by strong peaks while the weak peaks fall upon the set of zone lines for the (01) and equivalent LEED beams. Comparison with fig. 23b shows that the (01) beam does have strong maxima for these Bragg conditions, leading to the conclusion that these peaks are SBP's caused by (01) beam maxima. At 45° angle of incidence the (00) beam data does not show any definite trends toward following specific zone lines although some of the peaks do fall near degeneracies of zone lines as observed by Seah.⁵⁷ The large dot representing the 120 eV peak for the (00) beam does fall close to a (00) Bragg zone line so it is likely that this is a Bragg peak. Additional evidence in support of this interpretation will be presented in the later discussion of inelastic diffraction. The (01) beam is more consistent in having the strong maxima lie along Bragg zone lines of the (01) beam and weak maxima corresponding to regions of degeneracy in zone lines of other beams. Three strong peaks in the 45° data appear to satisfy Bragg relations while the weaker peaks are most likely SBP's.

The K-space plots for the (10) and (11) beams are shown in fig. 24a and 24b respectively and are similar in behavior to those for the (00) and (01) beams. Again the normal incidence data shows a close correspondence between strong maxima and Bragg conditions. Weak maxima for the (10) beam do not fall as near to zone lines as for the other beams but those of the (11) beam are on zone lines. At 45° angle of incidence there is fairly good correspondence between zone lines and intensity maxima; as before this is especially true near regions of degeneracy in the zone lines.

Figure 25a shows data for the (20) diffracted beam. As for the other beams the normal incidence data fits the main Bragg zone lines very well with the exception of the second strong peak which does not fit any zone lines. At 45° angle of incidence little data was available because of the limited swing of the energy analyzer, but the three maxima shown follow the trend of lying near degeneracies of zone lines.

All of this data is in general agreement with the results obtained by Seah⁵⁷ and is in keeping with a multiple scattering explanation. The correspondence of weak peaks to Bragg zone lines and regions of Bragg zone line degeneracy seems to indicate that electron flux is directed into one diffraction beam at a given energy through a coupling with one or more other beams which are strong at or near the same energy.

Some very low energy elastic intensity profiles were also measured and are shown in fig. 26. Two major peaks are seen in this figure; the 21 eV peak for the (01) beam satisfies a (01) beam Bragg condition and is considered a true Bragg peak. It can be seen from fig. 26 that there is a correspondence between some

minima in one beam and maxima in another beam. This correspondence could very well be due to flux conservation between the beams, where one beam becomes stronger at the expense of another beam. This effect would be especially evident at these low energies where there are only a few allowed diffraction beams. Another explanation for structure in elastic intensity curves, which has been proposed¹, is that it is due to emergence of new beams from the surface. Peaks, dips and combinations of the two have been measured by others that seem to be correlated in many instances to the grazing emergence of a new beam from the surface. These peaks and dips have been interpreted^{1,60} as being due to interference between singly and doubly scattered beams. In this interpretation a beam parallel to the surface is most likely to give rise to interference since it encounters a nearly perfect periodic structure and, therefore, should scatter strongly. In the present experiment the emergence energies of some beams are 3.3, 5.0, 7.5, 12.5 and 19 eV for the (01), (1/2 0), (0 3/2), (02) and (10) beams respectively. There is some correlation between these energies and peaks and dips in the intensity profiles and it could well be that these are due to the emergence of new beams.

It is quite probable that the steep rise in (00) beam intensity at about 1 eV is due to potential reflection of electrons from the surface barrier. Because of the 45° angle of incidence a 1 eV electron would only have 0.7 eV normal component to the surface and errors in the potential differences between the target and the tungsten filament may well have caused the energy to be lower yet by several tenths of an electron volt. One possible source of error was the reference potential of the electron gun which was the center tap potential on a potentiometer across the filament. This potential may easily have been several tenths of a volt different than the actual electron source potential.

3 Characteristic Losses

Extensive measurements of the characteristic loss spectra of Ge(100) were made for a wide range of energies and angles, and in this section their general behavior will be discussed and the various losses will be identified as much as possible. In discussing the characteristic losses it is very difficult not to involve inelastic diffraction effects, but since they will be covered thoroughly in the next section such effects will be involved here only as much as necessary.

One of the general observations that can be made about the characteristic losses at low primary energies is that they are usually strong only for ordered surfaces and then only in close proximity to the LEED beams. The effect of the ordering is illustrated in fig. 27 where the characteristic loss spectra are shown for specular scattering from a lightly sputtered (80 eV ions) surface and the subsequently annealed surface. Along with the very sizeable increase in elastic current in the (00) LEED beam for the annealed surface, the characteristic loss region of the spectrum was greatly enhanced and additional losses appeared. The bulk plasma loss peak at about 16.5 eV was relatively unaffected by the

surface disorder caused by sputtering but the lower lying surface plasma loss and the interband losses were virtually eliminated by the sputtering damage. With the sample in its sputtered state the only characteristic loss peaks found were the bulk plasma loss and a peak at 7.5 eV, the latter being of questionable origin. It is possible that the 7.5 eV loss is due to excitation of a surface plasmon since energy loss values of 8 eV have been measured in high energy transmission measurements on evaporated films⁶¹ and are presumed to be surface plasma losses. Arguing against this interpretation, however, is the fact that the 7.5 eV loss for sputtered samples is fairly strong even at primary energies as low as 15-20 eV, while in the case of an annealed sample there is no noticeable surface plasma loss peak at these energies and in general the losses are enhanced on ordered samples.

A second interpretation stems from the fact that as well as being disordered, the sputtered surface has argon embedded in it. It is conceivable that the 7.5 eV loss could be due to excitation of an electron from an argon atom to the conduction band of the Ge. A free argon atom has a first ionization potential of 15.7 eV; but if the argon level when embedded in Ge should be altered to occur about 12.2 eV below the vacuum level or 7.5 eV below the conduction band edge, then excitation of the kind proposed could account for the observed loss.

Localization of the loss peaks to the vicinity of the LEED beams is a result of the apparent small angle scattering of electrons. Elastically scattered electrons emerging in a diffraction beam can undergo inelastic collisions through small angles resulting in an increase in the inelastic signal near the LEED beam. Similarly, electrons which lose energy and are contained in a narrow cone of inelastic electrons about the incident beam, may be diffracted out of the sample and appear near to a LEED beam. Figure 28 shows the behavior of the loss spectrum about the (00) diffraction beam for angular variation in a direction perpendicular to the plane of incidence. As can be seen, except for the bulk plasma loss peak, the inelastic intensity in general but particularly the low energy loss peaks are very much degraded within a few degrees of the LEED beam. This behavior is very characteristic of all the losses, and it is found that the equivalent of a diffraction pattern exists for each inelastic loss, as will be discussed in the section on ILEED.

a Plasmon Excitations

In identifying the characteristic losses, measurements were made over a wide range of primary energies. The interband and surface plasmon losses were most prominent at low primary energies, while the bulk plasmon and multiple plasmon losses were stronger at high primary energies. In order to study the plasmon losses, therefore, a number of high energy measurements were taken for specular scattering of the electrons; a sampling of the loss spectra is shown in fig. 29. At a primary energy of 120 eV the 10 eV loss, which is tentatively identified as the surface plasmon loss, dominates the bulk plasmon loss and the interband losses are relatively strong.

In part, this is because at 120 eV the elastic intensity has a strong maximum which leads to inelastic diffraction enhancement of the losses, especially the smaller losses, but this distribution of relative intensities is generally true in this energy range. For the higher primary energies, the interband transitions become diminished, while the bulk plasma loss, at about 16.5 eV, dominates the spectra, and multiple losses become more pronounced.

Measurements made with increasing primary energy indicated a gradual increase in the value of the bulk plasma loss from about 16.0 eV at primary energies around 100 eV to 16.5 eV at primary energies of 700-1000 eV. Values from 16.0 to 16.5 eV have been measured by many other workers^{9,27} using high energy electrons, with the larger value being favored for single crystals. According to free electron calculation the bulk plasmon energy, $\hbar\omega_{po}$, is found from equation (4) to be 15.6 eV; however, if the influence of the d-bands in Ge are considered, as discussed in Appendix A, then a calculated value of 16.2 eV is obtained, which is in good agreement with the measured values. Also, one expects to measure a somewhat higher value than $\hbar\omega_{po}$ since the angular divergence of the detected electrons allows plasma losses further out on the dispersion relation (see eq. (3)) to be measured. In this regard, measurements made for electrons scattered into a hemispherical collector gave values for the bulk plasmon ranging from 16.0 eV to about 17.0 eV. Again because of the large range of angles allowed, the dispersion relation favors a larger value for the bulk plasmon loss energy.

Accurate measurements of the surface plasma loss energy at primary energies of 150-1000 eV were difficult since no distinct peak occurred due to the overlap with the large bulk plasma loss. Careful decomposition of the two losses into two superimposed peaks, however, yielded values between 10.5-11.5 eV for the surface plasmon. This compares quite well with other measured values^{9,27} as well as with the theoretical value of 11.0 eV calculated from equation (5) in the free electron approximation. A value of about 11.0 eV is also determined from the energies of the multiple loss peaks at 27 eV and 43 eV corresponding to a surface plasma loss coupled with one and two bulk plasma losses respectively.

b Interband Excitations

At lower primary energies the loss peaks due to interband electron excitations become much more evident as shown by fig. 30 for specular scattering at a primary energy of 70 eV. In this figure, three definite interband peaks are indicated. These three peaks were almost always observed in the loss spectra, with energies of 5.0-5.5, 2.8-3.0 and 1.4-1.7 eV. Also shown are the first and second bulk plasma losses at about 16.0 eV and 32 eV as well as a tentatively identified surface plasma loss peak at 10 eV. In addition to the three main interband peaks, others are sometimes observed at about 7.5-8.0 eV, 9.0 eV, 13.0-13.5 eV and 14.5 eV; but often they are only apparent as a somewhat increased intensity in the

vicinity of these values. As will be pointed out later, these interband losses may lead to erroneous assignment of the plasmon loss peak energies because of the overlap of the losses and for this reason the word tentative is used in regard to the surface plasmon loss at 10 eV. All of these peaks are relatively weak and often poorly resolved due to the large background of multiple losses and limited experimental energy resolution.

The limiting factor on resolution in this experiment was the energy spread of the primary electron beam. For usual current levels the width of the elastic peak at half maximum was about 0.5 eV; while at the base of the elastic peak the edge extended to about 1.2 eV, making measurements of losses less than this impossible. Improved resolution could be obtained by decreasing the electron gun filament current, but only at a drastic reduction in beam current, necessitating extremely long measurement times. By making a few of these measurements, however, peaks were observed at about 1.2 eV and 1.6-1.7 eV, suggesting that the single peak ordinarily found around 1.5 eV may actually be the result of poor resolution. Figure 31 shows two spectra, for specular scattering, where somewhat improved resolution was obtained by decreasing the filament current. In both, the interband losses at 1.2, 1.7, 3.0, 5.0 and 7.5 are clearly distinguished while those at 13.0 and 14.6 in fig. 31b are weaker and their energies not as well established. The broad peak at 10 eV could be the surface plasma loss, but the occasional appearance of a peak at 9.0 eV raises the possibility that it is due to a combination of a loss around 9.0 eV and a surface plasmon nearer to 11.0 eV.

In addition to measurements in the specular direction, characteristic loss spectra were obtained for scattering in the directions of several other LEED beams with varying primary energy. Such measurements for the (00), (01), (10) and (11) LEED beams are illustrated in figs. 32-35. Zero levels for the various curves are indicated along the right hand side of each figure. In all of these spectra, the three basic interband peaks at about 1.5, 3.0 and 5.0-5.5 eV are observed without significant changes in energy and, in a number of the spectra, peaks at about 7.5, 13.0 and 14.6 eV can be seen. It is also found that due to inelastic diffraction enhancement the interband structure is strongest at primary energies where the elastic intensity is large (see figs. 19-21). It can be seen from these four figures that at such primary energies there tends to be significant changes in the spectra for the 8.0-11.0 eV energy loss region. This observation seems to add weight to the idea that the peak near 10.0 eV is actually the result of interband losses from 7.5 eV to 9.0 eV combined with a surface plasma loss centered somewhat higher than 10 eV. For example, the 70, 80 and 100 eV spectra of the (00) beam indicate more than one peak in this region as do the 60 and 70 eV spectra of the (01) beam, the 60 eV spectrum of the (10) beam and the 50, 70, 80, and 90 eV spectra of the (11) beam. Similarly, shifts in the apparent position of the bulk plasma loss could be related to the enhancement of overlapping loss peaks in the 13.0-15.0 eV region, although an inelastic diffraction effect will be discussed in the next section that may also account for such shifts.

Interband losses on Ge have been observed previously in high energy scattering measurements by Zeppenfeld and Raether,⁵⁶ where a 5 eV peak and a partially resolved doublet structure centered about 3 eV were found. It is usual in these high energy scattering measurements to compare the characteristic loss spectrum to the calculated energy loss function, $-\text{Im } 1/\epsilon$, as derived from the optically determined components of the complex dielectric constant, $\epsilon_1(\omega)$ and $\epsilon_2(\omega)$ (see Appendix A). Such data for Ge was obtained by Philipp and Ehrenreich⁶² and is shown reproduced in fig. 36. The measured reflectivity is given in fig. 36a and the $\epsilon_1(\omega)$ and $\epsilon_2(\omega)$ curves deduced from the reflectivity are shown in fig. 36b. Also in the latter figure the calculated energy loss function $-\text{Im } 1/\epsilon$ is plotted. As shown by Raether,⁵ this loss function must be multiplied by $(1/\Delta E)^2$ (eq. A.17) in order to compare it directly to the characteristic loss spectrum. Zeppenfeld and Raether made this comparison with their measurements and found excellent agreement for the interband losses, indicating that the same direct transitions are involved as with optical excitation.

While fitting the data to $\text{Im } 1/\epsilon$ is acceptable for high energy electron scattering, Bauer²⁹ contends that it is not an acceptable method of analysis for low energy scattering since the momentum transfers may be comparatively large. In his analysis of low energy electron scattering from Si he chose to compare losses directly with the $\epsilon_2(\omega)$ data. Strong structure in $\epsilon_2(\omega)$ is interpreted as due to direct transitions and weak structure to indirect transitions. It was his conclusion that most peaks correlated with weak structure in the $\epsilon_2(\omega)$ function indicating that indirect transitions were predominant. He also observed some loss peaks, however, that were in fairly good agreement with direct optical transitions.

The characteristic losses obtained in this present study will also be compared with optical data and the band structure. For Ge the optical data has been studied extensively and the particular electron transitions involved are felt to be understood in terms of the electron energy band structure. A band structure diagram as calculated by Herman et. al.⁶³ is shown in fig. 37 and the principal direct gaps, determined from $\epsilon_2(\omega)$ are given in Table I.

Table I

	Ref	$\Gamma_{25}' - \Gamma_2'$	$\Gamma_3' - L_1$	$A_3 - A_1$	$\Gamma_{25}' - \Gamma_{15}$	$X_4 - X_1$	$L_3' - L_3$
Theory	64	0.8	1.8	2.0	2.7 or 3.6	3.6 3.8	5.4
	63	1.1	2.1	-	3.0	4.1	5.4
Expt.	64	0.8	1.74	2.10	3.2	4.5	5.9
		0.9	1.94	2.29	3.4		6.1

In Appendix A the $\epsilon_2(\omega)$ function is shown to be directly proportional to the joint density of states for direct transitions, $J_{vc}(\omega)$, which is large when the relation

$$|\nabla_{\vec{K}} (E_c(\vec{K}) - E_v(\vec{K}))|_{E_c - E_v = \hbar\omega} = 0 \quad (25)$$

is satisfied. For the case of low energy electron scattering, Bauer²⁹ arrives at a similar expression (eq. (12)) where the joint density of states for indirect transitions is large when the relation

$$|\nabla_{\vec{K}} [E_c(\vec{K} + \Delta\vec{K}) - E_v(\vec{K})]|_{E_c - E_v = \hbar\omega} = 0 \quad (26)$$

is satisfied, i.e. when the bands are parallel for an energy separation, $\hbar\omega$, and a wave vector separation $\Delta\vec{K}$. Depending on the allowed $\Delta\vec{K}$ values there can be any number of $(\hbar\omega, \Delta\vec{K})$ combinations which satisfy eq. (26) but for limited $\Delta\vec{K}$ the problem becomes nearly comparable to the optical problem. By inspection of the band diagram it can be seen that indirect transitions around symmetry points like the Γ point will increase the energy of the loss compared to direct transitions, while at positions along the symmetry directions where the bands have the same curvature, indirect transitions can cause a lowering of the energy loss value; but for small $\Delta\vec{K}$ values a correspondence with the energies of Table I might be expected.

In the scattering process, the primary electron loses an amount of energy ΔE and its wave vector is approximately reduced, for small losses, by the amount

$$\Delta K = \frac{m}{\hbar^2 K} \Delta E \quad (27)$$

The actual wave vector transfer to the lattice electron depends upon the nature of the scattering and the momentum conservation rules assumed to hold. It is usual to impose conservation of total momentum, but Duke⁴³⁻⁴⁸ contends that it is only the momentum parallel to the surface that need be conserved. In either case, if the electron is scattered through a large angle, large momentum transfers are possible; however, Seah⁴⁰ has found that the inelastic scattering in silver occurs with negligible angular deflection. This observation is in general agreement with the experimental results of this study as indicated in fig. 4.13 and as will be shown more specifically in the next section. Some deflection toward the surface normal was generally observed but at most the angular deviation for well defined inter-band losses was about 3°.

If total momentum is assumed conserved and the scattering is considered to occur without angular deflection, then equation (27) gives the wave vector transfers shown in Table II for various primary energies and energy losses. If only the

momentum parallel to the surface is conserved, the momentum transfer would depend upon the scattering direction. As an example, for the particular case of specular scattering, the values given in Table II would be reduced by a factor of .707.

Table II

$\Delta E(\text{eV})$	$\Delta K(\text{\AA}^{-1})$								
	$E_p=25$	50	75	100	125	150	500	10^3	10^4
1.5	.078	.055	.045	.039	.035	.032	.017	.012	.004
3.0	.156	.110	.090	.078	.070	.064	.035	.025	.008
5.0	.260	.184	.150	.130	.116	.106	.058	.041	.013
7.5	.390	.276	.225	.195	.174	.159	.087	.062	.020
9.0	.468	.331	.270	.234	.209	.191	.105	.074	.023
13.0	.676	.478	.390	.338	.302	.276	.151	.107	.034

For the purposes of discussion, a pseudo-direct transition will be defined as one in which the wave vector transfer to the lattice electron is less than one tenth the smallest Brillouin zone dimension. For Ge the smallest zone dimension is along the [111] zone direction and establishes a maximum wave vector transfer for pseudo-direct transitions at about 0.1\AA^{-1} . It can be seen from Table II that the 1.5 and 3.0 eV losses satisfy the pseudo-direct requirement rather well but the larger losses involve momentum transfers that are a significant percentage of the zone dimension. For high energy scattering ($E_p \sim 10^4$ - 10^5 eV) it can be seen that very small momentum transfers are involved; this means that direct interband transitions occur, thus accounting for the good correspondence with optical measurements. In general, however, at low primary energies the electron transitions will be indirect and this fact will have to be taken into account in attempting to analyze the electron transitions in terms of the band structure.

In view of inadequate theoretical information on low energy electron scattering, the interband transitions involved for the observed loss peaks can only be guessed at, using the wave vector transfers given in Table II as a guide. Since the scattering involved small angular deviations these values are probably close to correct. For the pseudo-direct losses, the loss energy will not deviate greatly from the optically measured gap energies so that a correlation with the gap energies of Table I should be expected. It is also likely that because of the lack of resolution and indirect nature of the transitions, most of these peaks contain contributions from more than one point in the Brillouin zone. In this regard, Kane⁶⁵ has shown specifically for Si that extended regions of the zone contribute to a single peak in $\epsilon_2(\omega)$.

As discussed earlier, the peak which typically is observed around 1.5-1.7 eV is considered to represent two peaks at around 1.2 eV and 1.6-1.7 eV. The 1.2 eV peak is most likely a pseudo-direct transition from Γ_{25}' to Γ_2' and agrees rather well with the measured and calculated values in Table I. A pseudo-direct transition from near L_3' to L_1 is also consistent with a peak at 1.6-1.7 eV and is also in reasonable agreement with the values of Table I. The 3.0 eV peak is in good agreement with a Γ_{25}' - Γ_{15} transition, but because of its breadth it probably includes transitions along the nearly parallel Λ_3 and Λ_1 branches of the valence and conduction bands. In optical studies the Λ_3 - Λ_1 transition at about 2.2 eV is quite strong. A similar consideration probably applies to the peak at 5.0-5.5 eV, which on occasion has appeared to resolve itself into two peaks at 4.5 and 5.5 eV, e.g. see fig. 31b. A wave vector change of about 0.15 \AA^{-1} occurs for this loss and is consistent with a transition from the Λ_3 branch near L_3' to the nearly parallel region near L_3 in the conduction band. Another possible transition might be from Δ_5 to Δ_2' . The rather strong peak at 4.45 eV in the optical measurements associated with X_4 - X_1 transitions is very likely represented in this 5.0 eV loss peak as indirect transitions in the X_4 - X_1 region of the Brillouin zone.

The higher lying characteristic losses are also consistent with gap energies shown in the band structure diagram of fig. 37, but it must be kept in mind that the accuracy of such calculations is not very good so they must only be used as a rough guide. The loss peak at 7.5 eV could be attributed to indirect transitions from Γ_{25}' to the Γ_1 region, the energy separation being approximately right for a wave vector change of about 0.15 \AA^{-1} . The peak at 9.0 eV which has been alluded to several times is very consistent with a wide range of possible transitions. With a wave vector change of about 0.25 \AA^{-1} , transitions are reasonable from the Λ_3 branch of the valence band to the conduction band states along the [111] direction near 8.5 eV band energy. Also, indirect transitions from Λ_3 to L_2' would give the right energy loss, as would a transition from the deeper X_1 valence band region to the X_1 conduction band region. Although the energy band diagram does not go high enough to cover the losses from 13.0-15.0 eV, it is clear from crude extrapolation that there are a number of final states in this energy range at the L and X points of the Brillouin zone which could account for the observed losses.

Before leaving this section it is of interest to examine the low energy characteristic losses for an oxidized Ge surface. In fig. 38 the characteristic losses for primary energies of 5.5, 7.5, 12 and 16 eV are shown; the zero levels of intensity for each curve are indicated on the right hand edge of the figure. Energy loss peaks are found at 3.75, 5.1 and 7.5 eV. These spectra are included strictly as a point of interest and no interpretation has been attempted for these peaks. They are stronger than the low energy losses found on clean Ge and the loss spectrum is identical both on the initially oxidized surface and on the surface which has been sputtered but is still contaminated with oxygen (see section IV.1). It is unusual to see strong losses at

energies that are a large fraction of the primary energy, but these spectra were unique in this regard.

4 Inelastic Low Energy Electron Diffraction

In this section experimental results will be presented which demonstrate the strong role inelastic diffraction effects play in determining the intensity distributions in the inelastic electron spectra. The only theoretical work which can be used for comparison purposes is that of Duke and Laramore,^{45,46} but this must be treated somewhat cautiously since the theory only can provide a qualitative guideline and is best for small angles of incidence, whereas this experiment was done at the larger angle of 45° . Also, as was indicated in section IV.2 it is difficult to relate strong elastic maxima to Bragg maxima at this angle of incidence, making much of the simplified analysis described in section II.2c and Appendix B hard to justify. However, in much of the experimental data, qualitative behavioral agreement was obtained with the predictions of Duke and Laramore. In Appendix B, a summary of theoretical considerations is presented.

There are three categories of measurements in which the inelastic diffraction effects are observed. These are the inelastic intensity profiles, characteristic loss spectra and the inelastic angular intensity profiles. Characteristic behavioral patterns observed in each type of measurement will be discussed below and comparisons with the theory will be attempted as much as possible.

a Inelastic Intensity Profiles

As pointed out in section II.2c and in Appendix B, the inelastic intensity profile for a given loss energy should show at least two peaks for each corresponding elastic maximum. These two peaks represent electrons which have lost energy before and after the diffraction process and occur at energies E_{max} and $E_{\text{max}} + \Delta E$, where E_{max} is the energy of the elastic intensity maximum. In Appendix B the E_{max} term is called E_B but because it is not usually possible to assign the elastic maxima to Bragg maxima, E_{max} will be used in this discussion. Under proper conditions it was predicted by theory (Appendix B) that four peaks may be observed instead of two; the extra peaks, resulting from the total conservation of momentum, being called sideband diffraction peaks. This effect has been verified in a recent experiment on aluminum,⁴² but in general is not found or expected because of the slowly increasing dispersion relations for excitations such as plasmons.

Inelastic intensity profiles in this experiment were obtained by analysis of the angular profiles taken at 5 eV intervals in primary energy. Figure 39 shows inelastic intensity profiles obtained in the (00) diffraction beam direction with energy losses of 10 eV and 16 eV; also shown is the (00) beam elastic intensity for purposes of comparison. Two peaks are clearly observed in the inelastic profile for each of the elastic peaks as predicted by

theory; but the higher energy peaks for the 10 eV loss, that correspond to energy loss before diffraction (IE process), are not found at $E_{\text{max}} + 10$ as theory predicts. This is due to the fact that the non-normal incidence of the electron beam leads to highly unsymmetrical intensity distributions about the (00) beam causing the IE peaks for the 10 eV loss to occur higher than they would for normal incidence. The weak peak at about 110 eV may be the result of sideband diffraction and the angular profiles to be shown later will show evidence in support of this interpretation.

b Characteristic Loss Spectra

Inelastic electron diffraction effects are usually evident in the characteristic loss spectra as an increased intensity of a portion of the characteristic loss spectrum. This increased intensity occurs because electrons in that particular energy range satisfy a diffraction condition (IE process) causing them to scatter out of the solid with increased intensity. The particular portion of the spectrum which satisfies this IE scattering process is strongly dependent upon the angle at which the measurement is made as well as the primary energy used. Because the inelastic diffraction conditions change with primary energy and measurement angle, each characteristic loss spectrum measured will be affected differently, and this makes it difficult to make any conclusive statements about how characteristic loss spectra in general are affected. However, trends can be identified and in this section some examples of inelastic diffraction in characteristic loss spectra will be discussed.

Two types of scattering processes were discussed in section II.2c; these were termed EI (elastic-inelastic) and IE (inelastic-elastic) processes. In the EI process, the electrons lose energy after being diffracted so that in the diffraction directions all losses, independent of energy, should be increased in intensity when the diffracted intensity is large. This, of course, is strictly true only if the electrons inelastically scatter without angular deflection. An IE process is one in which the electrons lose energy before diffraction. For such a process the inelastic intensity will vary markedly with energy loss and scattering angle, depending upon whether strong or weak diffraction conditions are satisfied.

The characteristic loss spectra taken in the (00) beam direction, shown in fig. 32, can be analyzed by referring to the elastic intensity plot of the (00) beam, shown in fig. 19. A large elastic intensity maximum is found at about 76 eV so it would be expected that, for primary energies greater than 76 eV, IE scattering processes would lead to an enhanced intensity in the characteristic loss spectrum near a secondary energy of 76 eV. As seen in fig. 32, as the primary energy approaches 76 eV there is an overall increase of the loss spectrum due to the increased elastic intensity and the occurrence of EI scattering processes, as in the curve for $E_p = 70$ eV. When $E_p = 80$ eV, the elastic intensity is still large but decreasing so there is still an overall

enhancement of the loss spectrum, but there is in addition a strong peaking in the region of $\Delta E = 4$ eV from IE scattering. For $E_p = 90$ eV, the EI scattering is considerably reduced, but the IE contribution near 14 eV gives this region an increased intensity. When $E_p = 100$ eV, it can be seen that neither EI nor IE contributions are significant in the range of losses shown, and the overall intensity is reduced considerably.

A similar analysis of the loss spectra taken in the (01) LEED beam direction (fig. 33) can be made with the aid of the elastic intensity plot in fig. 19. For the energy range covered in fig. 33, there are two elastic intensity maxima, occurring at 60 eV and about 82 eV. The $E_p = 60$ eV loss curve shows the strong influence of combined IE and EI scattering processes on the low energy losses (0-4 eV) and the overall EI enhancement of most of the spectrum. The analysis of the rest of the spectra is more difficult, since unlike the (00) beam the diffraction angle changes with primary energy so that in general it is difficult to predict the energy losses that will be enhanced; however, a straightforward graphical analysis in K-space does account for most of the structure. The low energy losses for $E_p = 80, 90$ eV are increased over the $E_p = 70$ eV curve as expected due to the elastic intensity increase with the attendant EI scattering. The enhanced intensity at about 11 eV, in the curve for $E_p = 80$ eV, is predicted by plotting the K-wave vectors in a K-space diagram, where inner potential corrections have been applied. Similarly, this graphical procedure predicts an increased intensity at about $\Delta E = 18$ eV for the $E_p = 90$ eV curve. This agrees fairly well with the measured result, where it can be seen that the intensity enhancement is centered around $\Delta E = 17$ eV.

For the (10) diffraction beam direction the characteristic loss spectra are shown in fig. 34 and again the elastic intensity is given in fig. 19, where intensity maxima occur at 60 eV and 90 eV with a subsidiary maximum at 76 eV. For the low lying losses, an increased intensity is observed for primary energies of 60 eV and 90 eV as expected for the combined IE and EI processes; also the $E_p = 60$ eV curve shows the overall increase expected for EI scattering. In the $E_p = 70$ eV curve there appears to be enhanced intensity around 9-10 eV. This is expected for IE scattering, even though the 60 eV elastic maximum is not a Bragg maximum, since for forward scattering the 60 eV inelastic electron wave will behave very much like the 60 eV primary wave. The analyzer position has changed by about 1.5° , however, so it is expected that the energy loss required to satisfy the diffraction condition would be a little less than 10 eV, and this is observed. In the 80 eV curve, both IE and EI processes may be active, the latter increasing the losses overall and the former adding some intensity at higher energies around 18 eV. In the 90 eV curve there is a strong overall increase in the spectrum due to EI scattering, while in the 100 eV curve the significant overall decrease in intensity again reflects the large drop in elastic intensity, indicating the importance of the EI scattering process; some IE enhancement may be present around $\Delta E = 10$ eV in the $E_p = 100$ eV curve.

Figure 35 shows the characteristic loss spectra for the (11) beam direction, and the (11) beam elastic intensity is given by fig. 19. The 50 eV curve shows the overall increase in intensity from EI scattering and the region below $\Delta E = 4$ eV demonstrates the strong combined EI and IE scattering associated with the sharp elastic maximum at 48 eV. As the primary energy is increased as in the 60 and 70 eV curves there is a shifting of the enhanced region to higher losses somewhat indicative of IE scattering; however, it must be kept in mind that the excitation probability for a bulk plasmon is also increasing with primary energy, so some increase around 16 eV is expected even in the absence of inelastic diffraction effects. In the 90 eV curve, the lower energy losses are again increased due to the combination of IE and EI processes associated with the elastic intensity maximum at 90 eV.

Another effect which is predicted by the Theory of Duke and Laramore⁴⁶ (see Appendix B) is the shifting of loss peaks as the primary energy is varied near the energy of an elastic maximum. As the primary energy passes through the energy of the elastic intensity maximum, the wave vector length for the excitation that is needed to conserve momentum becomes less. Because of the dispersion relation for the excitation, e.g. plasmons, this decreases the value of the energy loss. So, at or slightly above the value of an elastic maximum the plasma loss peak should be at its minimum value. In fig. 33 such a shift of the bulk plasma loss peak near 16.0 eV may be present in the 60 and 70 eV curves. Similar shifts seem to be present in the 60 eV curve of fig. 34 and the 50, 60 and 90 eV curves of fig. 35.

Because of the inelastic diffraction effects, caution is required in interpreting peaks in a characteristic loss spectrum. Only those peaks which persist under a variety of primary energies and angles have significance as characteristic losses. It is quite common to measure strong peaks which are strictly due to diffraction and have no significance in terms of highly probable loss processes. As an example of the strong change in the characteristic loss spectrum with scattering angle due to ILEED effects, fig. 40 shows spectra taken at $E_p = 50$ eV in the (11) diffraction beam direction (curve A) and for about a 2° deviation toward a larger diffraction angle (curve B). At the larger diffraction angle, a large increase in intensity occurs for a loss of about 4.5 eV, also, the surface and bulk plasma losses have shifted to larger values. The peaking at 4.5 eV is found to be consistent with IE scattering as determined from a graphical analysis in K-space. The (11) beam has a Bragg peak at 48 eV (see fig. 24b) so in curve A of fig. 40 there is strong IE enhancement around $\Delta E = 2$ eV. When the analyzer is moved the Bragg energy becomes about 45.5 eV and the IE maximum occurs at $\Delta E = 4.5$ eV in curve B in accordance with this change in Bragg condition. The shift in the plasma loss peaks toward higher energy is consistent with an EI process in which scattering from the diffracted beam at larger angles requires a larger excitation wave vector and hence, from the dispersion relation, a larger loss energy (see fig. 68).

Inelastic diffraction effects corresponding to IE scattering processes are very clearly observed if the energy analyzer is left in position to receive a strong LEED beam and the primary energy is increased by ΔE . When this is done, those electrons which lose an energy ΔE in a small angle scattering event can satisfy the same diffraction conditions and gives rise to increased intensity in the loss spectrum at ΔE . Such behavior is clearly illustrated by fig. 41, where the analyzer was left in the position of the (01) LEED beam for $E_p = 36$ eV, which corresponds to the energy of an elastic intensity maximum. As the primary energy is increased, it can be seen that there is an increase in the inelastic intensity for a fixed secondary energy of about 36 eV (noted by the arrows) which clearly indicates IE scattering. Also shown in the figure is a series of peaks indicated by arrows which occur at a fixed energy of about 23 eV. These peaks represent secondary electrons which satisfy a Bragg diffraction condition for the (01) beam for electrons with 55° angle of incidence. Any electrons which scatter by an angle of 10° from the primary beam, having an energy of 23 eV, can satisfy this strong Bragg condition. This same Bragg condition for the usual 45° angle of incidence is shown in fig. 26 occurring at 21.5 eV. When the diffraction condition corresponds to the energy of a particular characteristic loss, the loss intensity becomes much stronger, as for the 1.5 eV loss in the 37 eV curve, the 3 eV loss in the 37 eV curve, and the bulk plasmon loss near 17 eV in the 41 eV curve. Very similar observations of diffraction enhancement have been made by Porteus and Faith³⁷ for tungsten.

Both calculations⁴⁶ and measurements³⁸ have shown that there is a strong asymmetry of the characteristic loss intensities in the plane of incidence when the primary electron beam is not at normal incidence. This asymmetry usually favors scattering towards the surface normal. Figure 42 shows characteristic loss spectra taken for the (00) beam direction and 2° to each side of the (00) beam in the plane of incidence; with a positive 2° being towards the surface normal. The primary energy used for these curves is 120 eV and corresponds to a strong elastic intensity maximum, which appears to be a Bragg maximum. In the (00) beam direction the low energy interband losses are strong due to the combination of EI and IE processes which can occur. As the analyzer is moved toward the normal by 2° , electrons whose energy is about 110 eV can satisfy the Bragg diffraction condition, and this is what is observed. When the analyzer is moved the opposite direction, none of the electrons are capable of satisfying the Bragg diffraction condition so the intensity is considerably less. Figure 43 shows the K-space diagrams representing conditions for the three spectra of fig. 42. Part B of fig. 43 represents the case where $\theta_A = 0$, and it is clear that any diffracted electrons which inelastically scatter in the forward direction will be detected independent of the amount of energy lost, and in addition electrons which lose small amounts of energy before diffraction will still nearly satisfy the Bragg condition and also be detected. This gives rise to the overall EI enhancement and the IE enhancement of the small losses. When the detector is moved toward the surface normal, the conditions shown in part C of the figure are set up. Under these conditions electrons inclined toward the surface normal from the primary beam

by 2° with an energy of 110 eV satisfy a Bragg scattering condition leading to a strong peak around $\Delta E = 10$ eV. For the condition where the detector is moved away from the surface normal, the conditions of part A of the figure hold. Here, it is impossible for electrons which have energy lower than 120 eV to satisfy the Bragg relation and so the spectrum is probably made up of electrons which are scattered by 2° from the diffracted (00) beam.

When the primary energy is raised to 130 eV, the three spectra shown in fig. 44 are obtained. The vertical intensity scales of the inelastic portions of this figure are the same as for fig. 42, so direct comparison can be made. When $\theta_A = 0$ so that the analyzer is measuring in the (00) LEED beam direction, there can be noted a significant drop in inelastic intensity in the region below 10 eV loss as compared to the $\theta_A = 0$ curve of fig. 42. This is expected since the primary energy is no longer equal to a Bragg energy; so that both EI and IE processes in this energy range are diminished. Electrons which have lost about 10 eV, however, can now satisfy the Bragg scattering condition and this accounts for the fact that the intensity around $\Delta E = 10$ eV is still quite large. The appropriate wave vector diagram is shown in fig. 45b. When the detector is moved toward the surface normal, the Bragg relationship is satisfied for electrons with energies of 117-118 eV, accounting for the IE enhancement of the characteristic loss spectrum in the 12-13 eV loss region. The conditions appropriate to this process are depicted in the wave vector diagram of fig. 45c. When the detector is moved 2° away from the surface normal, the energies of the electron are all too low to satisfy the Bragg relation so IE scattering is not present and the EI scattering is weak because the diffracted intensity is decreased. This causes the entire spectrum to be diminished in comparison to its counterpart in fig. 42.

A similar set of measurements for low primary energies is shown in fig. 46, where again as the analyzer is moved towards the normal the diffraction condition is satisfied for larger loss values; this is the condition depicted in part c of fig. 43. The peak at about $\Delta E = 7$ eV is felt to correspond to the elastic intensity peak at about 19 eV for the (00) beam and does not have any significance as a characteristic loss.

c Inelastic Angular Intensity Profiles

Inelastic angular intensity profiles have provided the best agreement with the theoretical predictions of Duke and Laramore^{45,46} since the sideband diffraction phenomena are expected to be clearly exhibited even when absent in the inelastic energy profiles. Experimental studies have been made by Porteus and Faith³⁸ on an Al(111) sample, and by Burkstrand and Propst⁴² for an Al(100) sample, which indicate qualitative agreement with theoretical studies^{45,46,48} and experimental results obtained by Porteus have also been used to obtain a surface plasmon dispersion relation for aluminum.⁴⁷

In this experiment extensive inelastic angular intensity measurements were made both in and out of the plane of incidence. Those made in the plane of incidence will be concentrated upon since they are the least complicated to analyze and compare to theory. Angular profiles were taken at 5 eV increments in primary energy and representative sets of data taken in the plane of incidence for loss values of 10 eV and 16 eV are shown in figs. 47-50. These plots show most of the basic patterns observed in all of the measurements and they demonstrate much of the qualitative behavior predicted by theory. However, it should be reemphasized that the theoretical predictions were made for angles of incidence of the order of 15° and so some of the behavior predicted is not seen in these experimental results because of the large angle of incidence.⁴⁶

These four figures are useful for obtaining a qualitative feel for the inelastic angular profiles and how they vary with primary energy. The dots on each curve indicate the angle of the LEED beams, the (00) beam being at 45° and the $(0\ 1/2)$, (01) and $(0\ 3/2)$ being at successively smaller angles. Formation of the inelastic counterpart of a LEED pattern is clearly evident in these diagrams, especially for the 10 eV loss. This is a result of the small angular scattering that accompanies inelastic scattering for small losses so that the combined two step ILEED process bunches the inelastic intensity close to the LEED beams.

In section 2.4 of Appendix B the expected variation of the inelastic intensity profiles with primary energy is described. In general, the angular profiles shown in figs. 47-50 display this type of behavior. Looking at the profiles about the (00) beam ($\theta = 45^\circ$), it can be seen that as the primary energy approaches an elastic maximum (77 eV and 120 eV) a peak is found on each side of the 00 beam with the high angle peak appearing as a shoulder. At higher primary energies the shoulder goes away with the formation of a single large peak toward the low angle side of the LEED beam. For a primary energy around $E_{\text{max}} + \Delta E$ the shoulder reappears and for primary energies beyond $E_{\text{max}} + \Delta E$ a small single peak is found. This behavioral pattern agrees with the predictions of Duke and Laramore's⁴⁶ theory. A similar observation can be made for the 10 eV and 16 eV losses about the (01) LEED beam for primary energies between 105 eV and 140 eV. The elastic maximum for the (01) beam occurs at 123 eV and the changing resonance conditions are readily apparent in the angular profiles around this energy. A peak begins on the high angle side of the LEED beam, but near the elastic maximum a peak on the low angle side begins to grow and becomes dominant at a primary energy near $E_{\text{max}} + \Delta E$. A somewhat similar behavior can be observed for the $1/2$ -order beams, but it is never as pronounced.

The data as shown in figs. 47-50 are useful in getting a qualitative feeling for how the angular profiles vary, but for a more quantitative description the angular profiles are plotted directly above one another so that angular shifts are emphasized. Measurements were made in the plane of incidence to obtain the angular profiles for energy losses of 10, 12, 14, 16, 18 and 20 eV

at primary energy intervals of 5 eV between 70 eV and 140 eV. This extensive collection of data is shown in figs. 51-62, where the open circles on the curves denote the LEED beam positions and zero intensity levels are indicated on the left hand edge of each figure.

Concentrating on the (00) beam, the trends described above are seen to be repeated for each of the losses shown here. The set of curves describing the angular profiles at primary energies below 105 eV are difficult to compare with theory, since the elastic maximum at 77 eV for the (00) beam does not correspond to a Bragg maximum and is not readily identified as being due to any other strong beam. This peak apparently arises from some complicated multiple scattering process. All that can be said, is that when $E_p \approx 77$ eV the EI process should be represented as an increased intensity, and the larger losses should give peaks displaced to larger angles, as is observed. Also, when $E_p \approx 77 + \Delta E$ the IE scattering should predominate and an intensity maximum should be obtained at this energy, since for forward scattering the inelastic wave should undergo the same scattering conditions as the original primary wave. This peaking at $E_p \approx 77 + \Delta E$ is observed for all the losses except possibly the 20 eV loss.

For the range of primary energies above 105 eV (figs. 57-62) the angular profiles are subject to analysis because the elastic maximum at 120 eV does correspond to a Bragg maximum. The low angle peak position due to IE scattering can be calculated, taking into account inner potential corrections to the electron energy and angle of incidence and assuming that the Bragg relation is satisfied, i.e.

$$2K = \frac{2\pi n}{d}$$

These calculated angles and the measured angular positions of the low angle peaks are shown in Table III. The measured angle of the peak for $E_p = 105$ eV has not been included because it overlaps the peak associated with the 1/2-order beam causing uncertainty in its position. Agreement between the measured and calculated angles is fairly good with the exception of those measured for $E_p = 115$ eV and $E_p = 120$ eV. This discrepancy results because the low angle peak for these energies is due to an EI scattering process that causes the peak to be much closer to the (00) beam than would be the case for IE scattering. In the curves for 16-20 eV losses at primary energies around 110 eV the EI scattered intensity can be seen around the (00) beam distinctly separated from the IE peak which is displaced toward the normal by a fairly large angle. This intensity due to EI scattering is weak because the elastic intensity of the (00) beam is relatively small. For primary energies of 115 eV and 120 eV, however, the onset of the Bragg maximum causes the IE intensity to become large, but also, in some of the curves, for example, the 115 eV curve of fig. 60 and the 120 eV curve of fig. 61, the IE peak is visible as a shoulder on the low angle side of the dominant EI peak.

Table III

 θ (degrees)

ΔE	10 eV		12 eV		14 eV		16 eV		18 eV		20 eV	
	Expt.	Calc.	Expt.	Calc.	Expt.	Calc.	Expt.	Calc.	Expt.	Calc.	Expt.	Calc.
105	-	37.3	-	36.4	-	35.8	-	34.7	-	33.6	-	32.6
110	39.7	39.0	38.6	38.2	37.7	37.5	36.3	36.7	-	35.8	-	35.0
115	42.3	40.3	41.7	39.8	41.1	39.1	39.7	38.3	37.3	37.7	36.4	27.0
120	43.0	41.7	43.2	41.3	42.6	40.4	41.3	40.0	41.2	39.4	39.0	38.7
125	43.2	43.1	42.7	42.5	41.7	42.0	41.5	41.4	41.0	40.8	40.8	40.1
130	43.4	44.2	43.4	43.7	43.4	43.2	42.9	42.8	42.1	42.2	41.4	41.5
135	44.5	45.3	44.6	44.9	44.2	44.3	43.4	43.9	42.5	43.4	41.7	42.9
140	45.2	46.3	45.3	45.8	45.3	45.4	44.3	45.0	43.0	44.5	42.9	44.0

The low angle peaks around the (01) beam for $E_p = 70, 75, 80$ eV and $\Delta E = 10, 12, 14$ eV are found from graphical analysis to correspond to IE scattering where the Bragg relation satisfied is the one which gives the 60 eV peak in the elastic intensity. For the higher losses the peak positions cannot be accounted for but could be due to some influence from the (0 3/2) beam. At higher primary energies, there is a relative intensity maximum at $E_p = 80 + \Delta E$ due to IE scattering conditions which correspond to the multiple scattering peak at 80 eV in the elastic intensity plot.

The angular profiles about the (01) beam for primary energies above 105 eV are partially accounted for by the graphical analysis in K-space. For primary energies of about 115-125 eV the EI processes dominate the angular profiles but above this primary energy IE scattering begins to take over in importance, causing the growth of a peak to the low angle side of the LEED beam. This peak becomes a maximum at about $E_p = 122 + \Delta E$, where $E_p = 122$ eV corresponds to the Bragg maximum for the (01) LEED beam. The angular position of this maximum amplitude peak is confirmed by graphical analysis. This exact behavior has been observed by Burkstrand⁴² in inelastic angular profiles measured around the (11) and (10) diffraction beams on an Al(100) sample with normal incidence of the primary beam. Bagchi⁴⁸ has analyzed this data using the theory of Duke and Laramore^{45,46} and gets qualitative agreement between theory and experiment.

In general, the 1/2-order peaks have a maximum in inelastic intensity at a primary energy of $E_{\max} + \Delta E$, where E_{\max} is an elastic intensity maximum for the particular 1/2-order diffraction beam. This again is the result of having a forward scattered inelastic wave satisfying the same conditions which led to a maximum in the elastic intensity. For the (0 1/2) beam, elastic maxima occur at 83 eV and 127 eV as shown in fig. 20. It can be seen that for the various losses, maxima do occur at about $E_p = 83 + \Delta E$ and $E_p = 127 + \Delta E$. Similarly for the (0 3/2) beam with an elastic maximum^p at 80 eV and a second weaker maximum at 95 eV the increase in elastic intensity begins suddenly at $E_p = 80 + \Delta E$ and dies off for energies above about $E_p = 95 + \Delta E$.

Porteus and Faith³⁸ have attempted to extract dispersion relations for the surface and bulk plasmons in Al from their inelastic angular intensity data but the results were rather unsatisfactory. Some attempts were also made in this present study to determine the dispersion relations for the surface and bulk plasmons but they were unsuccessful. The measured angles of the peaks, as shown in Table III, appear to be controlled by the diffraction conditions and are not significantly influenced by any excitation wave vectors. This may be due to the fact that there are no dominant loss peaks and the background of multiple inelastic losses is quite large.

5 Secondary Electron Spectra

Secondary electron energy distributions (SED's) were measured over a wide range of angles and primary energies with the observation of a number of secondary peaks, i.e. peaks which remain fixed in secondary energy when the primary energy is changed. Mechanisms for the production of such peaks have been mentioned already in section II.1; these will be considered here in more detail in attempting to account for the observed structure in the low energy SED's.

Most of the structure in the SED's was observed in the specular scattering direction ($\theta_A = 0$) and in the direction of the crystal normal ($\theta_A = 45^\circ$). Figures 63 and 64 illustrate SED's for various primary energies in these two directions. The specular direction SED's (fig. 63) show the existence of secondary peaks at energies of about 3.5, 5.7, and 11.5 eV and the SED's measured in the direction of the crystal normal (fig. 64) have secondary peaks at about 4 eV, 8.7 eV and 21.5 eV. These peaks remain fixed in secondary energy with increasing primary energy but become less pronounced.

One common process by which secondary peaks are produced is the Auger process, and this has been used by some^{13,14,19} to account for the existence of secondary peaks at low energies. In this experiment, however, most of the peaks occur at primary energies which are too low for ionization of a level sufficiently deep that the Auger process could account for the measured peaks. The peaks at 11.5 eV in the $\theta_A = 0$ curves and the peaks at 8.7 eV and 21.5 eV in the $\theta = 45^\circ$ curves would require an MVV Auger process, but the M level is 29 eV below the top of the valence band and these peaks occur at primary energies less than 29 eV. Therefore, the Auger process is ruled out for these peaks. Similarly, in the case of the lower energy peaks, one could construct a set of Auger transitions using the maxima in the valence band density of states as the levels. The two deepest maxima in the valence band density of states for Ge occur at about 7.5 eV and 10.5 eV below the top of the valence band. If the neutralizing electron and the Auger electron both come from the top of the valence band, then Auger peaks at 2.8 eV and 5.8 eV could occur. However, the secondary peak at 3.5 eV is found for primary energies below 7 eV and the 5.7 eV secondary peak occurs for primary energies of about 7 eV. The primary energy is, therefore, too low for ionization of the likely levels needed to account for the observed peaks as Auger peaks.

Chung and Jenkins⁶⁶ have proposed a characteristic gain process to account for secondary peaks. They propose that excited states of the crystal decay by transferring their energy to electrons at the vacuum level, resulting in secondary peaks at energies characteristic of the existing excitations. In their analysis they obtain a good correlation between the secondary peak energies and the characteristic loss energies. This process, despite the good correlation of peak energies, is hard to justify since it presumes

that secondary electrons at the vacuum level are favored over secondary electrons of any other energy, and this is very unlikely unless a large density of states should occur at the vacuum level. A similar correlation between secondary peak energies and loss energies can be found in the data of this experiment, but the secondary peaks are not felt to be due to a characteristic gain process, especially as there is not a large density of states peak at the vacuum level.

One process that does seem to fit most of the results is the diffraction enhancement of parts of the SED due to strong diffraction of some of the secondary electrons. If secondaries are created which have the correct energy and direction to satisfy a strong diffraction condition they will be elastically scattered out of the crystal in the diffraction direction with greater intensity than those electrons of other energy and direction. This leads to a peak in the SED for the diffraction direction at a secondary energy corresponding to a strong elastic maximum. This process has been used to explain secondary peaks in the SED's for tungsten⁶⁷ and silver⁶⁸ single crystals.

In the specular direction, it is expected that secondary peaks due to diffraction would correspond closely in energy to the (00) beam elastic intensity maxima. Also, for primary energies approaching the secondary peak energy the secondary peak should become sharper and more intense since the inelastically scattered electrons are more concentrated in the primary beam direction. The SED's of fig. 63 can be compared with the (00) beam intensity plot of fig. 26. It can be seen that there are elastic maxima at about 3.5 eV, 6.0 eV, 11.0 eV and 19.0 eV and these correspond very well with the energies of the secondary peaks. The energy range is not large enough in fig. 63 to show the 19.0 eV peak, but in fig. 46 there is a peak at $E_s = 19$ eV which is believed to be due to diffraction of secondary electrons. The relative intensities are qualitatively in agreement as well, with the 5.7 eV secondary peak being the strongest in accordance with the elastic intensities. It can also be seen that the secondary peaks are sharpest when the primary energy is near to the secondary peak energy; this is demonstrated for the 3.5 eV peak by the SED for $E_p = 7$ eV and for the 5.7 eV peak by the SED for $E_p = 9$ eV. These peaks are also localized near to the specular direction, as is expected if they are associated with the specular diffraction conditions.

In the direction of the crystal normal the two peaks at 8.7 eV and 21.5 eV shown in fig. 64 also are accountable to diffraction of secondary electrons. The secondary peak at 21.5 eV corresponds to the strong (01) beam elastic maximum at 21.5 eV (fig. 26), which appears at about $\theta_A = 45^\circ$. Since this (01) beam maximum appears to satisfy a Bragg condition (see fig. 23b), the variation of the secondary peak energy with angle in the plane of incidence should be predictable. The right hand side of figure 65 shows the calculated and measured peak energies with the K-space diagram below depicting the situation for two assumed wave vectors. In the calculations, inner potential correction is taken into account and the peak energy is given by

$$E_{\text{peak}} = \left[\frac{G/2}{.514 \cos\theta} \right]^2 - V_I$$

where G is the three dimensional reciprocal lattice vector expressed in \AA^{-1} and V_I is the inner potential given in eV. The agreement is reasonably good for about a 6° range from the surface normal but becomes poorer towards smaller θ_A . At these smaller angles the peak was becoming quite weak and broad, increasing the possibility of error, but more likely the discrepancy indicates the breakdown of kinematical behavior for anything more than a small range of angles. Also, there is the possibility that the strong wave set up normal to the crystal can cause a peak to appear that is characteristic of a normally incident beam. Elastic reflection measurements made at normal incidence⁵⁶ (see fig. 23) indicate a peak at about 20 eV which seems to be a SBP due to a Bragg condition for the {01} set of beams. If such a peak were present it would cause the measured peak energies to be lowered.

The energy value of this peak for a given θ_A did not change with angle when measured perpendicular to the plane of incidence, but the intensity did drop off to about half its initial value within about 7° from the plane of incidence, for the primary energies shown. This may be the cone angle over which the secondaries can undergo coherent scattering for this particular diffraction condition. If this is the case, then this could also explain why the measured peak energies diverge from the calculated Bragg energy for angles greater than about 7° .

The peak at about 8.7 eV in the SED's measured normal to the sample correlates rather well with the strong Bragg peak that occurs at this same energy for elastic reflection at normal incidence. Again the angular variation of the peak energy can be tested if this Bragg condition is responsible for the peak. Calculated and measured values are shown on the left side of fig. 65, along with the appropriate wave vector diagram, and reasonably good agreement is obtained. In this case secondary electrons with wave vectors directed nearly normal to the crystal are diffracted out giving rise to the peak.

Additional evidence in favor of a diffraction process is the fact that the secondary peaks are not present when the surface has been disordered by light sputtering. Figure 66 shows energy distributions taken in the specular direction, $\theta_A = 0$, and in the direction of the crystal normal, $\theta_A = 45^\circ$, for both a sputtered surface and the subsequently annealed surface. The sputtered surface SED's are found to be generally free of structure except for the loss peak at $\Delta E = 7.5$ eV which was discussed previously; also, there is a remnant of the 8.7 eV peak. This latter peak was also observed by Chen⁵⁶ for his sputtered surfaces and presumably remains because the sputtering damage is so shallow that the underlying atomic layers can still give rise to some peaking at this energy. When the sample is annealed a LEED pattern is re-established and the usual set of secondary peaks reappear. In fig. 66 it is only coincidental that the loss peaks in the sputtered

surface SED's appear at nearly the same energy as the secondary peaks in the annealed surface SED's. When the primary energy is increased these peaks separate and it is clear that there is no connection between them. It can be noted that there is a work function lowering when the sample is sputtered and this is evident by the shift in the elastic peak.

One other process that gives rise to secondary peaks in the SED is the direct emission of electrons from local maxima in the density of states of the conduction band. Such peaks have been reported for measurements on Si¹⁷ and graphite.¹⁸ Kane has shown that the density of secondary electrons in the conduction band is proportional to the local density of states. Since maxima in the density of states usually occur along symmetry directions and Brillouin zone boundaries it would be expected that a larger number of electrons would be emitted with momentum along the symmetry directions at energies characteristic of regions of the band structure where the density of states are large. The density of states is proportional to $(\nabla_{\mathbf{k}} E(\mathbf{k}))^{-1}$ so that flat regions in the conduction band structure curves are likely places for large densities of states.

Referring to the band structure diagram in fig. 37 and placing the vacuum level at about 4.7 eV, maxima in the density of states for the [100] branch might be expected for energies of about 2.5 eV and 4.5-5.0 eV above the vacuum level. As can be seen from the SED's of fig. 64 maxima do occur at these energies. Similarly for the [111] branch of the band structure, there is a flat region 4.0 eV above the vacuum level (8.7 eV band energy) which might be expected to give a large peak. Measurements made in the vicinity of the [111] direction did indeed show a strong peak at 4.0 eV in the SED.

Band structure calculations by Brust and Kane,⁶⁹ extending to higher energies, indicate that a large density of states might occur in the [100] direction at 7.0-8.0 eV above the vacuum level. If there is a peak in this energy range it is masked by the secondary electron diffraction peak at 8.5 eV. Their calculations also show a region of large density of states about 6.0-7.0 eV above the vacuum level in the [111] direction and measured SED's in this direction did have a peak at about 7.0 eV. Peaks were also observed for directions other than the symmetry directions but these cannot be compared directly to the band structure.

V. Conclusions and Recommendations

Low energy electron scattering measurements were conducted as a function of scattering angle and primary energy for an atomically clean Ge(100) sample. These measurements were carried out in an attempt to characterize the different types of electronic processes that occur under low energy bombardment and to assess the role the surface plays in these scattering processes. Although none of the observed effects were found to be peculiar only to Ge, such low energy electron scattering data has not been obtained previously for Ge.

Measurements of the LEED pattern for the clean, annealed surface indicate the probable existence of a Ge(100) 4×2 surface structure. This conclusion is based on the existence of a set of $1/4$ -order diffraction beams that have been in question from previous experiments. Analysis of the LEED beam intensity maxima was accomplished by plotting the incident electron wave vector, corrected for inner potential, on a K-space diagram for the plane of incidence. An inner potential of 14 eV was obtained for primary energies greater than 30 eV. Through such an analysis, most elastic maxima were determined to be Bragg peaks or secondary Bragg peaks due to multiple scattering. This method of analysis showed the potential for easily identifying the diffraction beams that are coupled in the multiple scattering process.

Inelastic electron energy distribution measurements showed the existence of a number of energy loss peaks that are attributed to interband excitations of lattice electrons. These losses were only observed when the sample surface was clean and well ordered. Some of these losses were in fair agreement with band gaps determined by optical measurements and with band structure calculations; however, positive assignment of some electron transitions was not possible. In addition to the interband losses, both surface and bulk plasmon losses and combinations of these losses were observed and their energies were in good agreement with reported values. Future measurements of the inelastic spectra should be made with improved energy resolution for the primary electron beam in order to separate the losses more effectively. In principle it is possible, with better energy and angular resolution, to obtain the E vs. K dependence of the energy bands by careful measurement of the indirect excitations.

Inelastic electron diffraction effects were observed in measurements of both the energy and angular distributions of the inelastic electrons. Results were obtained corresponding to processes where the primary electrons were diffracted before and after energy loss. The qualitative behavior observed in these measurements is in agreement with current theoretical models and for certain instances, where particular Bragg relations could be identified, quantitative evaluations of peak energies and angles were possible. Any additional work done in this area should be carried out on an Al(100) sample to complement the theoretical work being done.

Results of the secondary electron energy distribution measurements indicate the existence of secondary peaks due to two mechanisms. In one, peaks are formed by secondary electrons that satisfy strong diffraction conditions. These peaks were found to correlate very well with the energies and directions of elastic intensity maxima. Variations of the peak energy with scattering angle were calculable in the cases of two peaks where the particular Bragg relations involved could be determined. Over a limited angular range, kinematical Bragg scattering was found to describe the measured peak variation. The second possible mechanism giving rise to secondary peaks is one in which secondary electrons are directly emitted from regions of local maxima in the conduction band density of states. Correlations were obtained between the energies of secondary peaks measured in the [100] and [111] crystal directions and predicted energies of density of states maxima obtained from band structure calculations. Such measurements show promise as a method for determining the shape of the conduction bands and are worth pursuing in more detail. For both mechanisms a well ordered surface was necessary for observation of structure.

A future experiment that could be done with this apparatus is the measurement of secondary electron energy distributions for surfaces with overlayers, e.g. a cesium overlayer. The accompanying work function lowering would allow the deeper lying conduction bands to be examined. Also, by measuring shifts in the energy band peaks with overlayer coverage, the band bending could be determined directly. This latter measurement has importance in the study of negative electron affinity photocathodes. The advantage this method has over techniques like photoemission, is that where photons penetrate deeply into the solid, low energy electrons penetrate only the first few atom layers; thus, features in the electron scattering measurements reflect energy states near to the surface. In negative affinity photocathodes the space charge region at the surface is often very thin so that electrons, unlike photons, could be effective in measuring changes in the electron states of this region.

APPENDIX A

Some Relationships Between the Complex Dielectric Constant and Energy Absorption

A.1 Interaction of a Dielectric with an Electromagnetic Wave

A link between the macroscopic behavior of a dielectric material in an electric field and its microscopic or atomic properties is afforded by the frequency dependent, complex dielectric constant defined as

$$\epsilon(\omega) = \epsilon_1(\omega) + i \epsilon_2(\omega) \quad A.1$$

Macroscopically the dielectric constant acts as the coupling factor in a linear relationship between the electric field and the electric displacement function as specified by

$$D(\omega, t) = \epsilon(\omega) \epsilon_0 E(\omega, t) \quad A.2$$

From general electromagnetic theory, the rate of energy loss per unit volume from a periodic electric field is given by

$$W(t) = -\frac{1}{2\pi} \int_0^{2\pi} E(t) \frac{\partial D(t)}{\partial t} d(\omega, t) \quad A.3$$

where the electric field is assumed to be

$$E(t) = E_0 e^{i\omega t} \quad A.4$$

Combining these relationships and taking the real part gives $W(t)$ as

$$W(t) = -\frac{\epsilon_0 \epsilon_2(\omega) E_0^2}{2} \quad A.5$$

so that the rate of energy loss by the electric field is proportional to $\epsilon_2(\omega)$.

In optical absorption theory for solids, $\epsilon_2(\omega)$ can be related to the band structure and direct interband electron transitions. A transition rate per unit volume is derived from time dependent perturbation theory to be⁶⁴

$$W_{vc}(\omega) = -4\pi h(e/m)^2 A_0^2 \int \frac{d\vec{k}}{4\pi^3} |M_{vc}|^2 \delta(E_c - E_v - \hbar\omega) \quad A.6$$

where the matrix element M_{vc} is defined by

$$M_{VC} = \int_V d\vec{r} e^{-i\vec{k}' \cdot \vec{r}} u_C^*(\vec{k}', \vec{r}) \hat{e} \cdot \nabla e^{i\vec{k} \cdot \vec{r}} u_V(\vec{k}, \vec{r}) \quad A.7$$

where u_C and u_V are Bloch functions for the initial and final electron states and the wave vector of the photon has been neglected. Multiplying this transition rate by the energy, $\hbar\omega$, of the transition gives the rate of energy loss

$$W(t) = -W_{VC} \hbar\omega \quad A.8$$

Since the electric field in the absence of a scalar potential is given by the vector potential according to

$$\vec{E} = -\frac{\partial \vec{A}}{\partial t} = -\omega \vec{A}, \quad A.9$$

then by combining equations A.8, A.9 and A.5 gives the expression

$$\omega^2 \epsilon_2(\omega) = \frac{2 W_{VC} \hbar}{\epsilon_0 A_0^2} \quad A.10$$

relating the transition rate for direct interband transitions to the imaginary part of the dielectric constant. It is possible to associate maxima in the $\epsilon_2(\omega)$ function with specific interband transitions in many instances. In particular when the assumption is made that M_{VC} is a slowly varying function of the wave vector, the delta function property changes equation A.6 so that

$$\omega^2 \epsilon_2(\omega) = \frac{8\pi^2 e^2}{\epsilon_0 m} |M_{VC}|^2 J_{VC} \quad A.11$$

where the term J_{VC} , called the joint density of states, is given by

$$J_{VC} = \int_S \frac{1}{4\pi^3} \frac{dS}{|\nabla_{\vec{k}}(E_C - E_V)|} \quad E_C - E_V = \hbar\omega \quad A.12$$

with the surface of integration being the constant energy surface in \vec{k} -space, $E_C(\vec{k}) - E_V(\vec{k}) = \hbar\omega$.

A.2 Interaction Between a Dielectric and a Fast Charged Particle

Inelastic scattering of fast charged particles can be related to the dielectric constant by determining the response of the electron system of the solid to the coulomb force of the moving particle; this analysis was carried out by Frohlich and Platzman.⁷⁰

The electric displacement vector as a function of time is calculated for a general point, P, due to the moving charged particle. Fourier transforms of this function and the electric field vector are related by the complex dielectric constant as

$$\vec{D}_{(\omega)} = \epsilon(\omega) \vec{E}_{(\omega)} \quad \text{A.13}$$

Then the energy transfer to a unit volume at the point, P, is given by

$$W_P = \frac{1}{4\pi} \int_{-\infty}^{\infty} \vec{E}(t) \cdot \frac{\partial \vec{D}(t)}{\partial t} dt \quad \text{A.14}$$

which, when using the Fourier Transforms, is shown to give

$$W_P = \int_0^{\infty} \frac{\epsilon_2(\omega)}{\epsilon_1(\omega)^2 + \epsilon_2(\omega)^2} \omega \vec{D}_{(\omega)} \cdot \vec{D}_{(\omega)}^* d\omega \quad \text{A.15}$$

The total energy transfer is found by integrating over the entire volume. It has also been shown⁷¹ that a quantum-mechanical interpretation gives the probability of a charged particle losing energy between $\hbar\omega$ and $\hbar(\omega+d\omega)$, in a single "collision", as being proportional to the factor

$$-\text{Im } 1/\epsilon(\omega) = \frac{\epsilon_2(\omega)}{\epsilon_1(\omega)^2 + \epsilon_2(\omega)^2} \quad \text{A.16}$$

The cross section per energy interval, into an angle θ , in causing bulk excitations is given by⁹

$$\frac{d\sigma}{dE} \propto \left(\frac{1}{\Delta E}\right)^2 \text{Im } 1/\epsilon \quad \text{A.17}$$

when measured with an angularly selective energy analyzer. Using equation A-17 and the real and imaginary parts of the dielectric constant, obtained from optical measurements, good agreement has been obtained with characteristic loss spectra for fast electrons.⁹ From this it can be seen that there will be a close correspondence between energies of strong optical absorption (maxima of $\epsilon_2(\omega)$) and electron loss peaks but the loss peaks will be shifted somewhat due to the denominator terms of $\text{Im } 1/\epsilon$.

A.3 Relation of the Dielectric Constant to Atomic Properties of a Solid

A connection between the dielectric constant and the atomic properties of a solid can be developed according to a rather simplified model⁷² in which the atoms comprising the solid are considered independent. If the perturbing potential is considered to be

$$V = e \vec{E} \cdot \vec{r} \quad \text{A.18}$$

where

$$\vec{E} = E_x (e^{i\omega t} + e^{-i\omega t}) \hat{x}, \quad \text{A.19}$$

then the use of time-dependent perturbation theory gives an expression for the dipole moment for one atom of the solid as⁷²

$$\langle e x(t) \rangle = E_x \sum_j \frac{e^2}{\hbar} |x_{oj}|^2 \frac{\omega_j}{\omega_j^2 - \omega^2} (e^{i\omega t} + e^{-i\omega t}) \quad \text{A.20}$$

where $\hbar\omega_j = E_j - E_0$. This can be written as

$$\langle e x(t) \rangle = \alpha(\omega) E(t) \quad \text{A.21}$$

where a polarizability, α , has been defined by

$$\alpha(\omega) = \sum_j \frac{e^2}{\hbar} |x_{oj}|^2 \frac{\omega_j}{\omega_j^2 - \omega^2}. \quad \text{A.22}$$

It is usual to define an oscillator strength, f_j , by

$$f_j = \frac{2m}{\hbar} \omega_j |x_{oj}|^2 \quad \text{A.23}$$

which satisfies a sum rule

$$\sum_j f_j = 1 \quad \text{A.24}$$

Then the polarizability becomes

$$\alpha(\omega) = \frac{e^2}{m} \sum_j \frac{f_j}{\omega_j^2 - \omega^2}. \quad \text{A.25}$$

When all N atoms of the solid are considered then the dielectric constant is given by electric field theory as

$$\epsilon(\omega) = 1 + \frac{N \alpha(\omega)}{\epsilon_0} \quad \text{A.26}$$

which becomes

$$\epsilon(\omega) = 1 + \frac{Ne^2}{m\epsilon_0} \sum_j \frac{f_j}{\omega_j^2 - \omega^2}. \quad \text{A.27}$$

In the above treatment, damping was neglected, and a more general treatment would give an expression

$$\epsilon_1(\omega) + i \epsilon_2(\omega) = 1 + \frac{Ne^2}{m\epsilon_0} \sum_j \frac{f_j}{\omega_j^2 - \omega^2 - i \frac{\omega}{\tau}} \quad A.28$$

For $\omega\tau \gg 1$, this reduces to the expression of equation A.27, where now $\epsilon_1(\omega)$ is the proper term to use.

For free electrons all ω_j are zero so that

$$\epsilon_1(\omega) = 1 - \frac{\omega_{po}^2}{\omega^2} \quad A.29$$

where the free electron plasma frequency, ω_{po} , is given by

$$\omega_{po}^2 = \frac{Ne^2}{m\epsilon_0} \quad A.30$$

It is a result of the dielectric theory that the plasma frequency is determined by the condition $\epsilon(\omega) = 0$,⁷² which, when neglecting damping, is given by setting $\epsilon_1(\omega) = 0$. When this is done for equation A.29 the plasma frequency becomes $\omega_p = \omega_{po}$, the free electron plasma frequency. It can be seen from equation A.27, however, that if interband transitions are present that in general ω_p may not equal ω_{po} .

When considering an intrinsic semiconductor, like Ge, where valence, conduction and d bands are considered, a general expression can be given as⁹

$$\epsilon_1(\omega) = 1 - \frac{e^2}{m\epsilon_0} \sum \frac{f_{cv}}{\omega_{cv}^2 - \omega^2} - \frac{e^2}{m\epsilon_0} \sum \frac{f_{cd}}{\omega_{cd}^2 - \omega^2} \quad A.31$$

where now the sum rule on oscillator strengths is given by

$$\sum f_{cv} + \sum f_{dv} = N_v \quad A.32$$

with N_v being the density of valence electrons. In the case of Ge, the d bands are 30 eV below the top of the valence band so the last term of A.31 is weak at lower energies. Also, the oscillator strength, f_{cv} , is found to be exhausted above $\hbar\omega \approx 7$ eV; therefore, in the region between these two energies the behavior of $\epsilon_1(\omega)$ is nearly free electron like so that the plasma frequency for Ge is nearly equal to ω_{po} , the free electron value.

APPENDIX B

Inelastic Low Energy Electron Diffraction (ILEED)

The only comprehensive theoretical treatment of the topic of ILEED has been carried out by Duke and Laramore,^{45,46} and their model has been fairly successful in qualitatively describing the experimental results which have been obtained thus far. Some quantitative use of the theory has been made in the case of aluminum, but at present it is very difficult to apply the theory to other materials except in a qualitative manner. Aluminum was chosen as the material for initial theoretical studies because LEED beam intensity calculations have been obtained that predict the measured beam intensities, as a function of energy and angle of incidence, with reasonably good success. This is essential for their theory. In addition the inelastic scattering parameters for the plasmon losses have been studied extensively for aluminum and could be incorporated into the calculation. In what follows, an attempt is made to summarize some of the theoretical considerations of Duke and Laramore and supplement this with some additional interpretation in terms of modified Ewald diagrams.

B.1 Calculated Cross Section

The inelastic cross section, as calculated by Duke and Laramore, for bulk excitations takes the form

$$\frac{d^2\sigma}{dE d\Omega} = \left(\frac{E-w}{E}\right)^{\frac{1}{2}} \frac{1}{(2\pi)^3 A} \sum_g \rho(w, P_{\parallel}) \{M(K_{O\perp}, K_{\perp}, P_{\perp}, \vec{g}) [A_D(P_{\perp}) + A_C(P_{\perp})]^2 + M(K_{O\perp}, K_{\perp}, -P_{\perp}, \vec{g}) [A_D(-P_{\perp}) + A_C(-P_{\perp})]^2\} \quad B.1$$

where $\rho(w, P_{\parallel})$ is a density of states function given by

$$\rho(w, P_{\parallel}) = \left| \frac{\partial h \omega(\vec{P})}{\partial P_{\perp}} \right|^{-1}_{\hbar\omega=w} \quad B.2$$

In the theory, it is assumed that only the parallel components of the momenta need be conserved along with the energy conservation as given by

$$\vec{K}_{O\parallel} - \vec{K}_{\parallel} - \vec{P}_{\parallel} = \vec{g} \quad B.3$$

$$\hbar\omega(P_{\parallel}, P_{\perp}) = w$$

where P_{\parallel} is the parallel component of the excitation wave vector and w is the energy lost in the inelastic scattering event.

There are two types of resonances in the expression for the cross section, the A_b and A_c terms give rise to the so-called "energy-tuned" resonances and occur at energies E_B and $E_B + w$ respectively. These represent the cases of electron diffraction before and after energy loss and are essentially independent of P . The second type of resonance is governed by the envelope function $M(K_{O\perp}, K_{\perp}, P_{\perp}, \theta)$. Resonances in this term are called "momentum-tuned" resonances and lead to a phenomenon called sideband diffraction. These resonances are the result of "accidental" conservation of momentum normal to the surface.

B.2 ILEED for the (00) Diffraction Beam

B.2.1 Inelastic Energy Profiles for Bulk Excitations

Inelastic diffraction involving the (00) diffraction beam is the simplest to discuss and so the salient features will be developed around this beam. Also for simplicity the incident electron beam will be assumed to have normal incidence. For the bulk excitations a quadratic dispersion relation will be assumed and in particular the bulk plasmon will be considered to have a dispersion relation given as

$$W(p) = \hbar \omega_{po} + \alpha p^2. \quad B.4$$

Assuming that the electronic interaction is similar to the case of aluminum, then from reference 46 the form of the envelope function is given as

$$M(K_{O\perp}, K_{\perp}, P_{\perp}, 0) = \left(\frac{m}{2}\right)^{\frac{4}{A}} \frac{P_{\perp}^2}{A^2} [1 - e^{i(K_{O\perp} + K_{\perp} - P_{\perp})d}]^{-2}. \quad B.5$$

For intensity measurements in the (00) beam direction, the inelastic energy profile for a given energy loss, w , will ideally exhibit four resonance peaks for each Bragg peak in the elastic energy profile. A resonance in the A_b term occurs when

$$2 K_{O\perp}(E) = \frac{2\pi n}{d} \quad B.6$$

where d is the atomic layer spacing. This gives a resonance when the primary energy is equal to a Bragg energy, i.e. $E = E_B$. Similarly the A_c term gives a resonance when

$$2 K_{\perp}(E-w) = \frac{2\pi n}{d} \quad B.7$$

which is the condition for a Bragg resonance at $E = E_B + w$. The envelope function provides two additional resonances given by

$$K_{O\perp}(E) + K_{\perp}(E-w) + P_{\perp} = \frac{2\pi n}{d} \quad B.8$$

and

$$K_{0\perp}(E) + K_{\perp}(E-2) - P_{\perp} = \frac{2\pi n}{d} \quad B.9$$

which represent the sideband diffraction resonances.

The two resonances given by equations B.8 and B.9 tend to occur near E_B and $E_B + w$ respectively, but because P_{\perp} is usually different than the wave vector difference $K_{0\perp} - K_{\perp}$, the particular energies at which they occur will depend upon the energy loss value, w , and the dispersion relation. In particular, if the dispersion relation is "steep" (large α) then a large energy loss corresponds to a large value of P_{\perp} . Under these conditions the two sideband resonances occur at energies which are sufficiently removed from E_B and $E_B + w$ that they show up in the inelastic energy profile as distinct peaks separate from the "energy tuned" resonances. An illustration of this sort of behavior is shown in fig. 67 for an idealized case of an excitation with a "steep" dispersion relation. In this diagram the curve for the loss, w_1 , illustrates the case of a small loss and hence such a small value of P_{\perp} that the sideband resonance is not split from the "energy-tuned" resonance.

B.2.2 Angular Profiles for Bulk Excitation

Angular profiles are determined primarily by the product of the envelope function, M , with the density of states function, ρ . For quadratic dispersion relations the density of states is given by

$$\rho = \frac{1}{2\alpha P_{\perp}}$$

and this multiplied by the envelope function of equation B.5 gives

$$G_{\perp}(P_{\perp}) = \left(\frac{m}{\hbar}\right)^2 \frac{P_{\perp}}{2A^2\alpha} \{1 - e^{i(K_{0\perp} + K_{\perp} - P_{\perp})d}\}^{-2} \quad B.11$$

which is essentially the controlling term for the angular profile. It can be seen that as $P_{\perp} \rightarrow 0$ the angular distribution will go to zero and if the term in brackets is small, i.e. off resonance, then the angular distribution will be nearly proportional to P_{\perp} . For normal incidence with θ measured relative to the surface normal, the components of the secondary wave vector are given by

$$\begin{aligned} K_{\perp} &= K \cos \theta \\ K_{\parallel} &= K \sin \theta \end{aligned} \quad B.12$$

Using relations B.3 gives

$$P_{\parallel} = -K_{\parallel}$$

and

$$w = \hbar\omega + \alpha(P_{\parallel}^2 + P_{\perp}^2) \quad \text{B.13}$$

leading to the expression

$$P_{\perp} = \left[\frac{\omega - \hbar\omega}{\alpha} - K^2 \sin^2 \theta \right]^{1/2} \quad \text{B.14}$$

Since the intensity goes to zero when $P_{\perp} = 0$, a cutoff angle, θ_c , can be defined as

$$\theta_c = \sin^{-1} \left(\frac{w - \hbar\omega}{\alpha K^2} \right)^{1/2} \quad \text{B.15}$$

From the above relations, the angular distribution as a function of primary energy can be illustrated. When the primary energy is far from the energy tuned resonances, then the overall cross section is small and the angular distribution, as governed by G_{\perp} , gives a single symmetric peak which varies as P_{\perp} . When the primary energy is near a resonance the overall cross section is increased due to the A_b or A_c term but also the G_{\perp} term can resonate causing peaks symmetrically displaced about the (00) beam. Illustrative diagrams of angular profiles are shown in fig. 68, together with modified Ewald diagrams depicting the condition when $E = E_B$. Conservation of parallel momentum leads to the limited scattering cone shown by the shaded region. For small w the momentum vector \vec{P} is too small to allow a sideband resonance, but in the two cases of medium and large w the sideband resonances can be tuned and lead to peaks in the angular profile at angles where the normal momentum is also conserved.

If the energy loss, w , is fixed at a moderately large value and the primary energy is changed, then the behavior illustrated in fig. 69 is obtained for the angular profiles. When the primary energy is well below the Bragg energy, E_B , the angular profile is a small singlet but as the primary energy passes through E_B the cross section increases and the sideband resonances appear causing the angular distribution to become a doublet. When the primary energy passes beyond E_B a singlet is obtained again, but this changes again to a doublet near $E_B + w$ as the resonance conditions can again be satisfied. For primary energies beyond this a weak singlet is obtained again.

B.2.3 Energy Loss Profiles

Shifts of the characteristic loss peaks in energy are expected when energy loss profiles are measured at different scattering angles. In fig. 70a the cases of measurement in the (00) beam direction and slightly off this direction are illustrated for $E = E_B$. As the detector is moved off of the (00) beam direction, a large value of P and hence w is needed to satisfy the resonance condition and so the peak in the loss profile moves to a larger energy loss value.

Similarly if the detector is fixed in the (00) beam direction and the primary energy is varied around the Bragg energy, the loss peak will shift in energy as the resonance conditions change. Figure 70b illustrates the conditions when the primary energy is somewhat below E_B and somewhat above E_B . When the primary energy is below E_B then equation B.8 is satisfied for a large value of P_{\perp} and correspondingly large energy loss w . As the primary energy increases, the necessary values of P_{\perp} and w to cause resonance decrease and so the peak shifts in the loss profile towards smaller energy loss values. Ideally, this shifting continues until $P_{\perp} = 0$, but the intensity goes to zero when $P_{\perp} \rightarrow 0$ so the maximum shift is never observed.

B.2.4 Non-normal Angles of Incidence

When the primary electrons are incident on the sample at other than normal incidence the symmetric behavior about the (00) diffraction beam is lost. While G_{\perp} remains the same as given by equation B.11 the results are modified because $K_{O_{\parallel}}$ is no longer zero. Conservation of parallel momentum now is given by

$$K_{O_{\parallel}} = K_{\parallel} + P_{\parallel} \quad B.16$$

Using expression B.16 with the same sort of analysis as for equations B.12 - B.14, leads to the expression

$$P_{\perp} = \left[\frac{w - \hbar \omega}{\alpha} \frac{p_0}{K} - (K_O \sin \theta_O - K \sin \theta)^2 \right]^{1/2} \quad B.17$$

As before when the primary energy is far removed from the resonance energies then the angular distribution will be a singlet which is proportional to P_{\perp} . The maximum of this singlet will occur where $P_{\parallel} = 0$ which gives

$$\sin \theta_{\max} = \frac{K_O}{K} \sin \theta_O \quad B.18$$

This angle depends on both the primary energy and the energy loss value, w , so the angular behavior becomes more complicated but qualitatively it is similar to that discussed previously for normal incidence. A cutoff angle can also be defined as

$$\theta_c = \sin^{-1} \left[\frac{K_O}{K} \sin \theta_O + \left(\frac{w - \hbar \omega}{\alpha K^2} \frac{p_0}{K} \right)^{1/2} \right] \quad B.19$$

The resonance conditions of equations B.6-B.9 can be rewritten in terms of θ ; the A_D resonance becomes

$$2 K_O \cos \theta_O = \frac{2\pi n}{d} \quad B.20$$

while the A_c resonance becomes

$$2K \cos \theta = \frac{2\pi n}{d}, \quad \text{B.21}$$

The two sideband resonances are specified by

$$K_0 \cos \theta_0 + K \cos \theta + \left[\left(\frac{w - \hbar \omega}{\alpha} p_0 \right) - (K_0 \sin \theta_0 - K \sin \theta)^2 \right]^{1/2} = \frac{2\pi n}{d} \quad \text{B.22}$$

and

$$K_0 \cos \theta_0 + K \cos \theta + \left[\left(\frac{w - \hbar \omega}{\alpha} p_0 \right) - (K_0 \sin \theta_0 - K \sin \theta)^2 \right]^{1/2} = \frac{2\pi n}{d} \quad \text{B.23}$$

As pointed out in reference 46 the first resonance to occur in the angular profile as the primary energy is increased is due to equation B.22; this gives a low angle peak for $E < E_B$ as depicted in fig. 71a. As the energy is increased this peak moves toward lower angles and a second peak on the other side of the LEED beam occurs and moves toward larger angles. At the same time a resonance in the A_b term gives an overall increase to this doublet. This condition is shown in fig. 71b for the case where $E = E_B$. The loss before diffraction resonance given by equation B.23 is still not capable of being tuned; however, as the energy is raised above E_B a low angle peak begins due to this resonance. This new resonance combines with the low angle resonance of equation B.22 to form a large low angle peak as shown in fig. 71c. As the primary energy is increased further the resonances due to eq. B.22 and the A_b term die out but the low angle peak due to the resonance of eq. B.23 moves towards the LEED beam and the A_c resonance causes the intensity to grow. This condition is depicted in fig. 71d for a primary energy a little below $E_B + w$. For $E > E_B + w$ the low angle peak dies out and a high angle peak is allowed by eq. B.23, but the decrease in the A_c resonance causes this peak to be weak. When the primary energy is far above $E_B + w$ the angular distribution becomes a weak asymmetric singlet centered about the angle specified by equation B.18.

B.3 Surface Losses

ILEED involving surface losses differs from the bulk loss case in that the momentum of the surface excitation lies parallel to the surface and since there is no normal momentum the sideband resonances do not exist. Neglecting broadening effects there are only two angles for a given loss value, w , for which parallel momentum and energy can be conserved. This leads to two narrow

peaks in the angular distribution, for all primary energies, at the scattering angles which satisfy these conservation conditions; this is illustrated on the left hand side of fig. 4. The relative intensity of these peaks depends on the angle of incidence and excitation cross sections, also, since the A_B and A_C resonances still occur, they are expected to maximize near primary energies of E_B and $E_B + w$.

VI. References

1. P. J. Estrup and E. G. McRae, Surface Sci. 25, 1 (1971).
2. E. Bauer, in: Techniques of Metals Research, Vol. II part 2, ch. 16 (Wiley, New York, 1969).
3. P. J. Estrup, in: Modern Diffraction and Imaging Techniques in Material Science, Eds. S. Amelinckx et. al. (North-Holland, Amsterdam 1970) p. 377.
4. W. D. Robertson, J. Vac. Sci. Technol. 8, 403 (1971).
5. J. W. May, Ind. Eng. Chem. (I-Ec) 57 (1965).
6. J. J. Lander, in: Progress in Solid State Chemistry, Vol. 2 (Pergamon; New York 1965) p. 26.
7. P. A. Redhead, J. P. Hobson and E. V. Kornelsen, in: The Physical Basis of Ultrahigh Vacuum, (Chapman and Hall Ltd., London 1968) p. 139.
8. L. F. Cordes, Ph.D. Thesis, University of Minnesota, 1966.
9. H. Raether, Springer Tracts in Mod. Phys. 38, 84 (1965).
10. F. M. Propst and T. C. Piper, J. Vac. Sci. Technol. 4, 53 (1967).
11. H. Ibach, Phys. Rev. Lett. 24, 1416 (1970).
12. H. Ibach, Phys. Rev. Lett. 27, 253 (1971).
13. E. J. Scheibner and L. N. Tharp, Surface Sci. 8, 247 (1967).
14. L. N. Tharp and E. J. Scheibner, J. Appl. Phys., 38, 3320 (1967).
15. W. Müller and W. Mönch, Phys. Rev. Lett. 27, 250 (1971).
16. G. Chiarotti, G. Del Signore and S. Nannarone, Phys. Rev. Lett. 21, 1170 (1968).
17. P. E. Best, Twenty Ninth Physical Electronics Conference, Yale University, (March 17-19, 1969).
18. R. F. Willis, B. Feuerbacher and B. Fitton, Phys. Lett. 34A, 231 (1971).
19. G. A. Harrower, Phys. Rev. 102, 340 (1956).
20. O. Hachenberg and W. Brauer, Advan. Electronics and Electron Phys. 11, 413 (1959).

21. A. J. Dekker, Solid State Phys. 6, 251 (1958).
22. J. J. Lander, Phys. Rev. 91, 1382 (1953).
23. C. C. Chang, Surface Science 25, 53 (1971).
24. J. C. Riviere, Physics Bulletin 20, 85 (1969).
25. C. N. Berglund and W. E. Spicer, Phys. Rev. 136, 1030 (1964).
26. E. O. Kane, Phys. Rev. 159, 624 (1967).
27. O. Klemperer and J. P. G. Shepherd, Advances in Phys. 12, 355 (1963).
28. L. Marton, L. B. Leder, and H. Mendlowitz, Advances in Electronics and Electron Physics, New York, (1955).
29. E. Bauer, Z. Physik 224, 19, (1969).
30. E. Bauer, J. Vac. Sci. Technology 7, 3, (1970).
31. C. B. Duke and C. W. Tucker, Jr., J. Vac. Sci. Technology 8, 5 (1971).
32. C. W. Tucker, Jr. and C. B. Duke, Surface Sci. 29, 239 (1972).
33. C. Davisson and L. H. Germer, Phys. Rev. 30, 705 (1927).
34. J. C. Turnbull and H. E. Farnsworth, Phys. Rev. 54, 509 (1938).
35. P. P. Reichertz and H. E. Farnsworth, Phys. Rev. 75, 1902 (1949).
36. J. O. Porteus, "The Structure and Chemistry of Solid Surfaces", edited by G. Somorjai, (Wiley, New York, 1969), p. 12.
37. J. O. Porteus and W. N. Faith, Phys. Rev. B2, 1532 (1970).
38. J. O. Porteus and W. N. Faith, J. Vac. Sci. Tech. 9, 1062 (1972).
39. W. H. Weber and M. B. Webb, Phys. Rev. 177, 1103, (1969).
40. M. P. Seah, Surface Sci. 17, 161 (1969).
41. M. P. Seah, Surface Sci. 24, 357 (1971).

42. J. M. Burkstrand and F. M. Propst, Presented at International Conference on Solid Surfaces, Boston, Mass., October 1971.
43. C. B. Duke, G. E. Laramore and V. Metze, Solid State Communications 8, 1189 (1970).
44. C. B. Duke, A. J. Howsman and G. E. Laramore, J. of Vacuum Science and Technology 8, 10 (1971).
45. C. B. Duke and G. E. Laramore, Phys. Rev. B3, 3183 (1971).
46. C. B. Duke and G. E. Laramore, Phys. Rev. B3, 3198 (1971).
47. A. Bagchi, C. B. Duke, P. J. Feibelman and J. O. Porteus, Phys. Rev. Letters, 27, 998 (1971).
48. A. Bagchi and C. B. Duke, Presented at: International Conference on Solid Surfaces, Boston, Mass., October, 1971.
49. A. L. Hughes and V. Rojansky, Phys. Rev. 34, 284 (1954).
50. D. Roy and J. D. Carette, J. Appl. Phys. 42, 3601 (1971).
51. P. W. Palmberg and T. N. Rhodin, J. Appl. Phys. 39, 2425 (1968).
52. G. H. Schwuttke, J. Electrochem. Soc. 106, 315 (1959).
53. J. Freudenthal, J. Appl. Phys. 38, 4818 (1967).
54. F. Jona, IBM J. of Research and Development 9, 375 (1965).
55. J. J. Lander and J. Morrison, J. Appl. Phys. 34, 1403 (1963).
56. J. M. Chen, Ph.D. Thesis, University of Minnesota, Nov. 1967.
57. M. P. Seah, Surface Sci. 17, 181 (1969).
58. R. J. Reid, Surface Sci. 29, 603 (1972).
59. C. W. Tucker, Jr. and C. B. Duke, Surface Sci. 24, 31 (1971).
60. E. G. McRae and C. W. Caldwell, Jr., Surface Sci. 2 509 (1964).

61. K. Zeppenfeld and H. Raether, Z. Physik 193, 471 (1966).
62. H. R. Philipp and H. Ehrenreich, Phys. Rev. 129, 1550 (1963).
63. F. Herman, R. L. Kortum, C. D. Kuglin and J. P. Van Dyke, Methods in Computational Phys. 8, 193 (1968).
64. D. L. Greenaway and G. Harbeke, Optical Properties and Band Structure of Semiconductors, Pergamon Press (1968).
65. E. O. Kane, Phys. Rev. 146, 558 (1966).
66. L. H. Jenkins and M. F. Chung, Surface Sci. 26, 151 (1971).
67. D. E. Edwards, Jr., Ph.D. Thesis, University of Illinois (1970).
68. M. P. Seah, Surface Sci. 17, 132 (1969).
69. D. Brust and E. O. Kane, Phys. Rev. 176, 894 (1968).
70. H. Frohlich and R. L. Platzman, Phys. Rev. 92, 1152 (1953).
71. H. Frohlich and H. Pelzer, Proc. Phys. Soc. A68 525 (1955).
72. J. M. Ziman, Principles of the Theory of Solids, Cambridge University Press (1964).

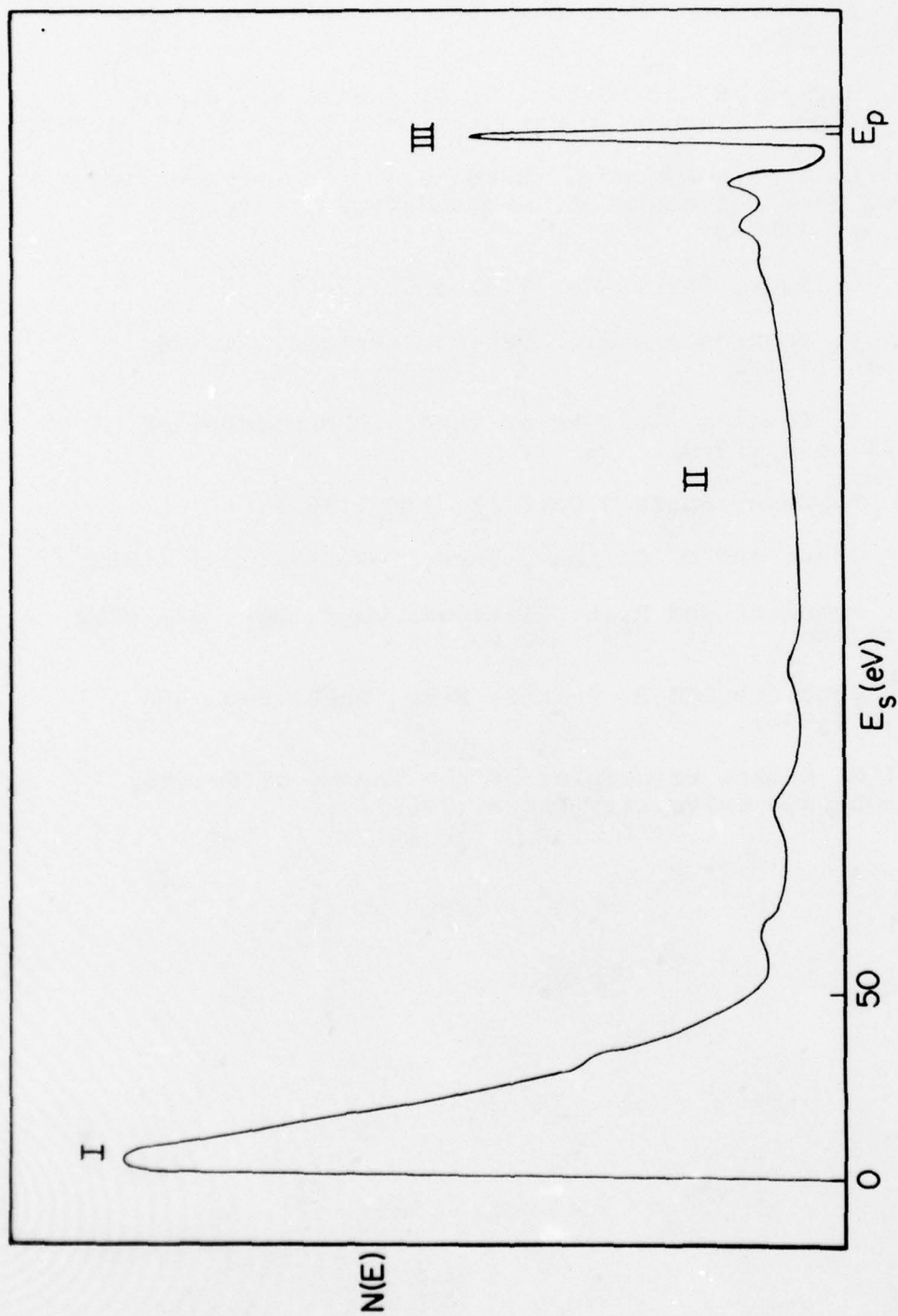


Figure 1 Typical secondary electron energy distribution

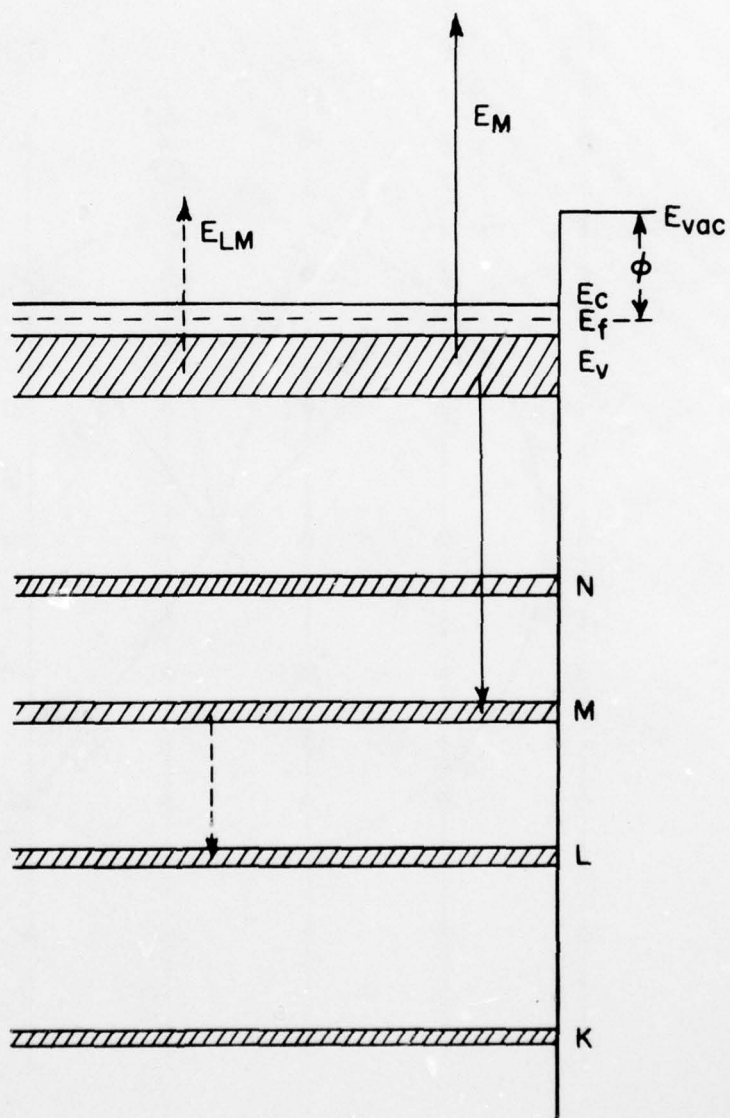


Figure 2 Possible bulk Auger transitions

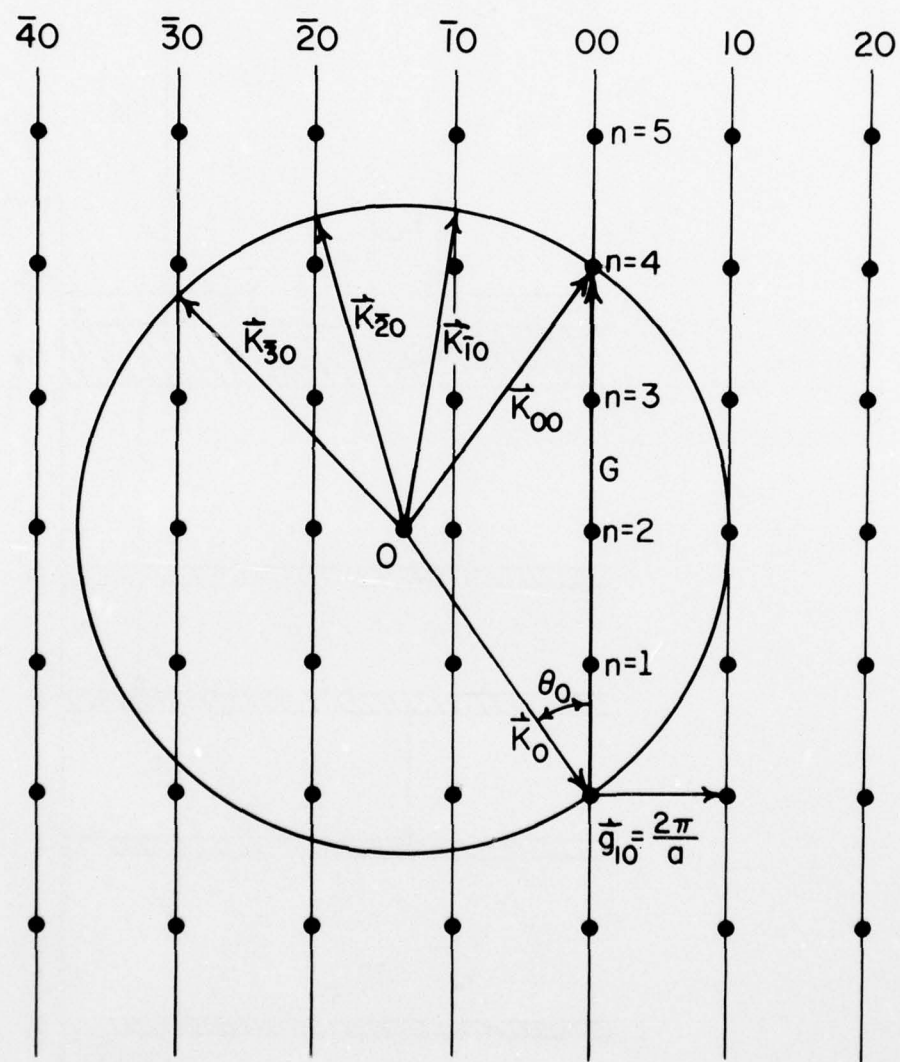


Figure 3 Ewald sphere construction in K -space

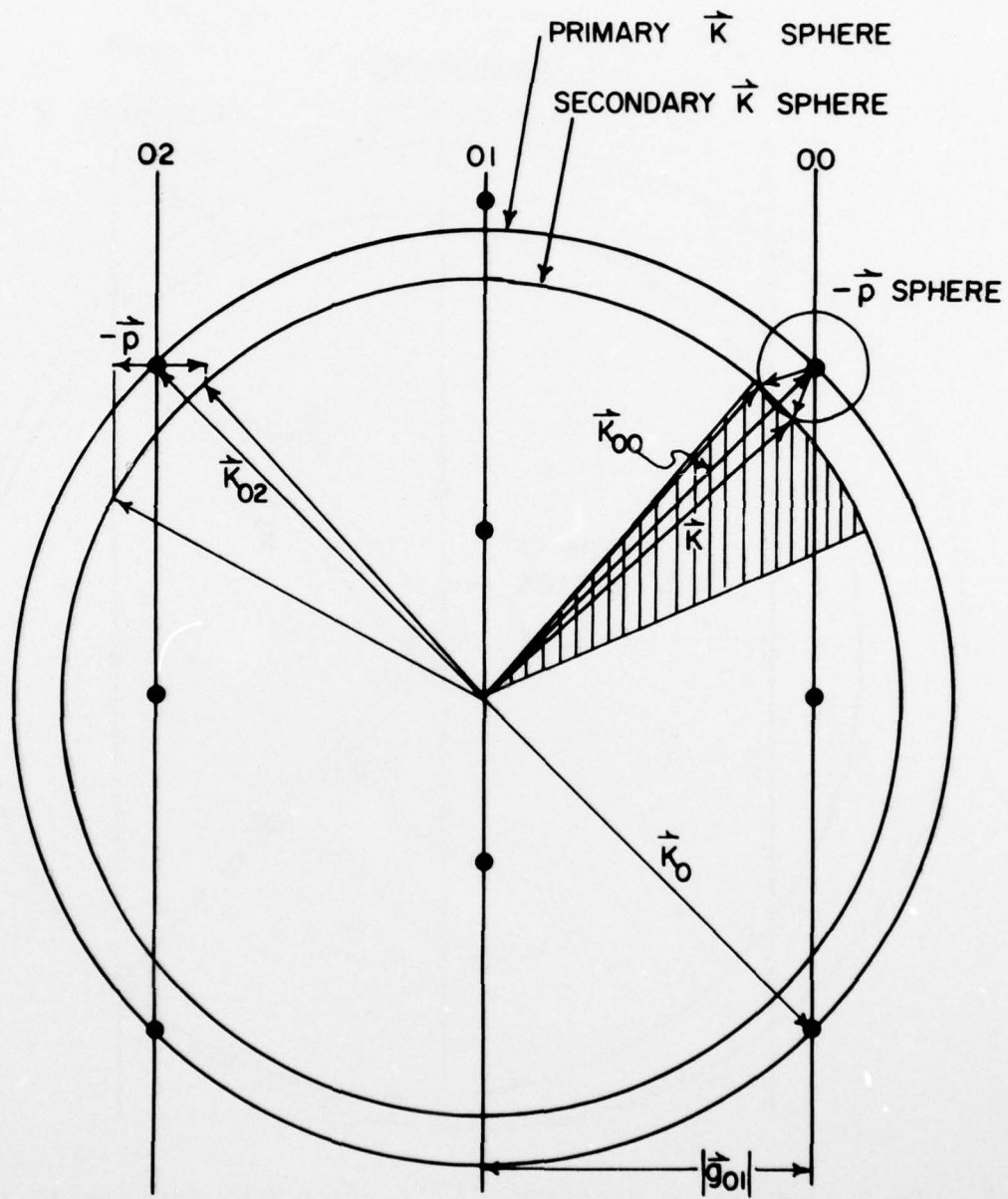


Figure 4 Inelastic electron diffraction diagram

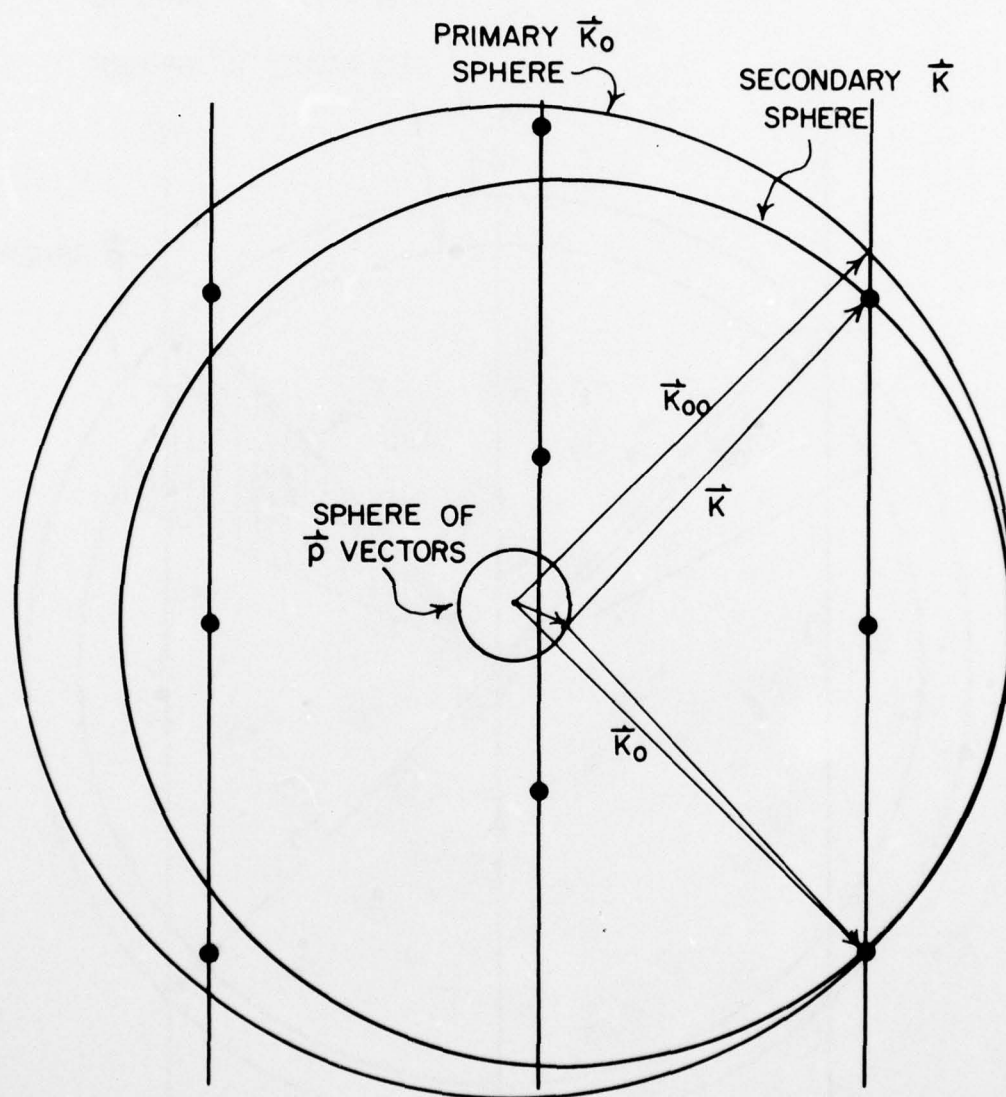


Figure 5 Inelastic electron diffraction diagram for IE process

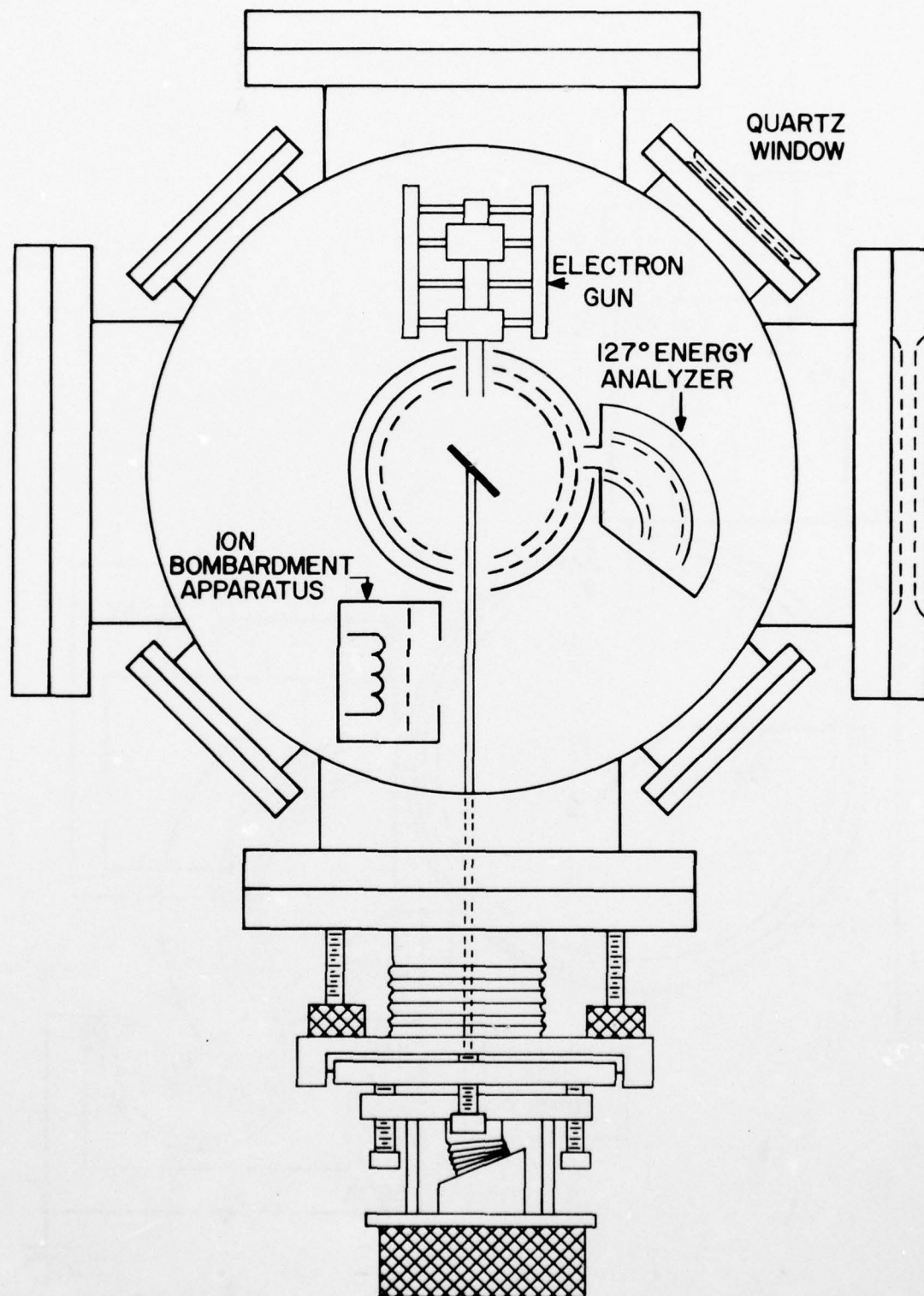
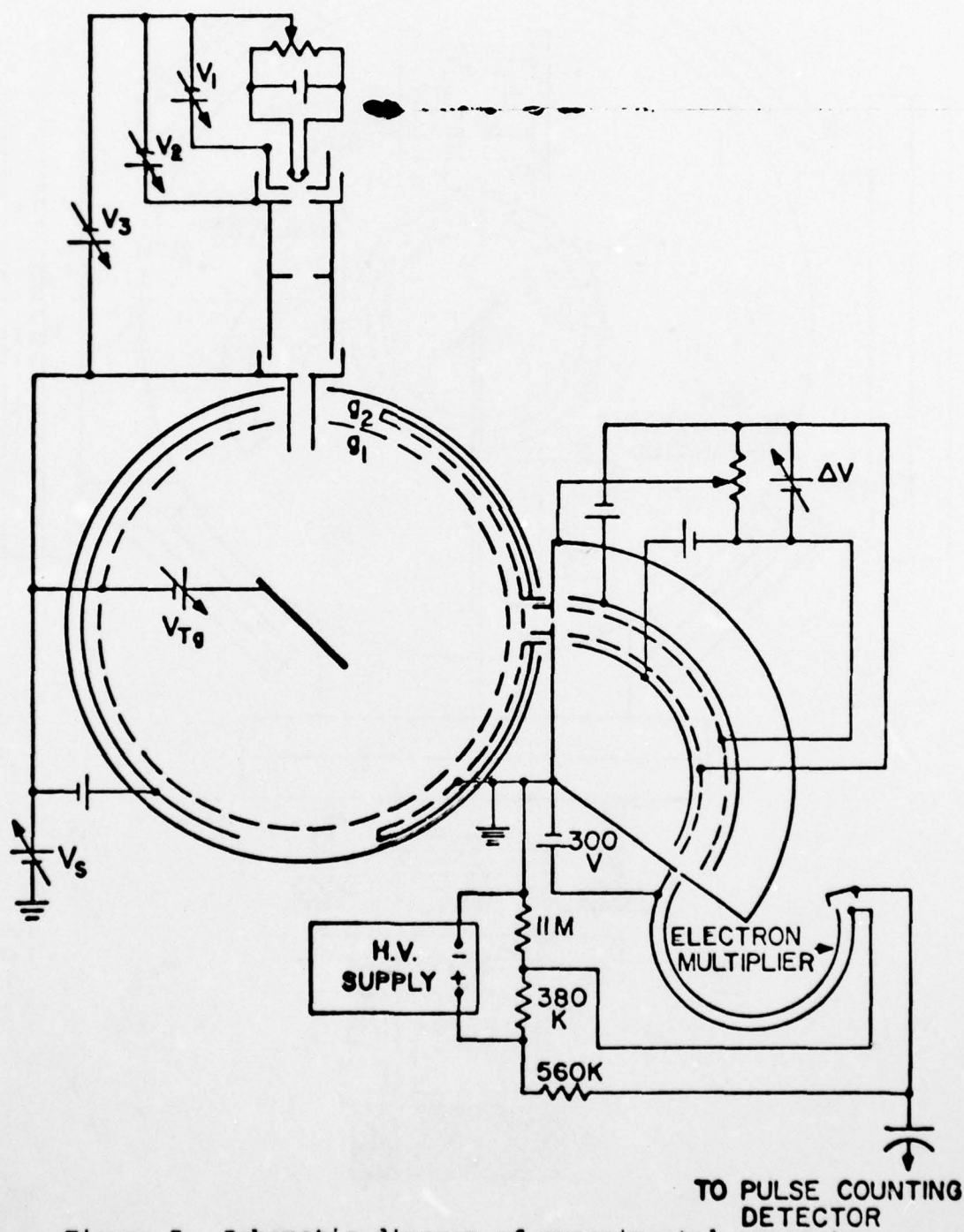


Figure 6 Schematic diagram of vacuum chamber



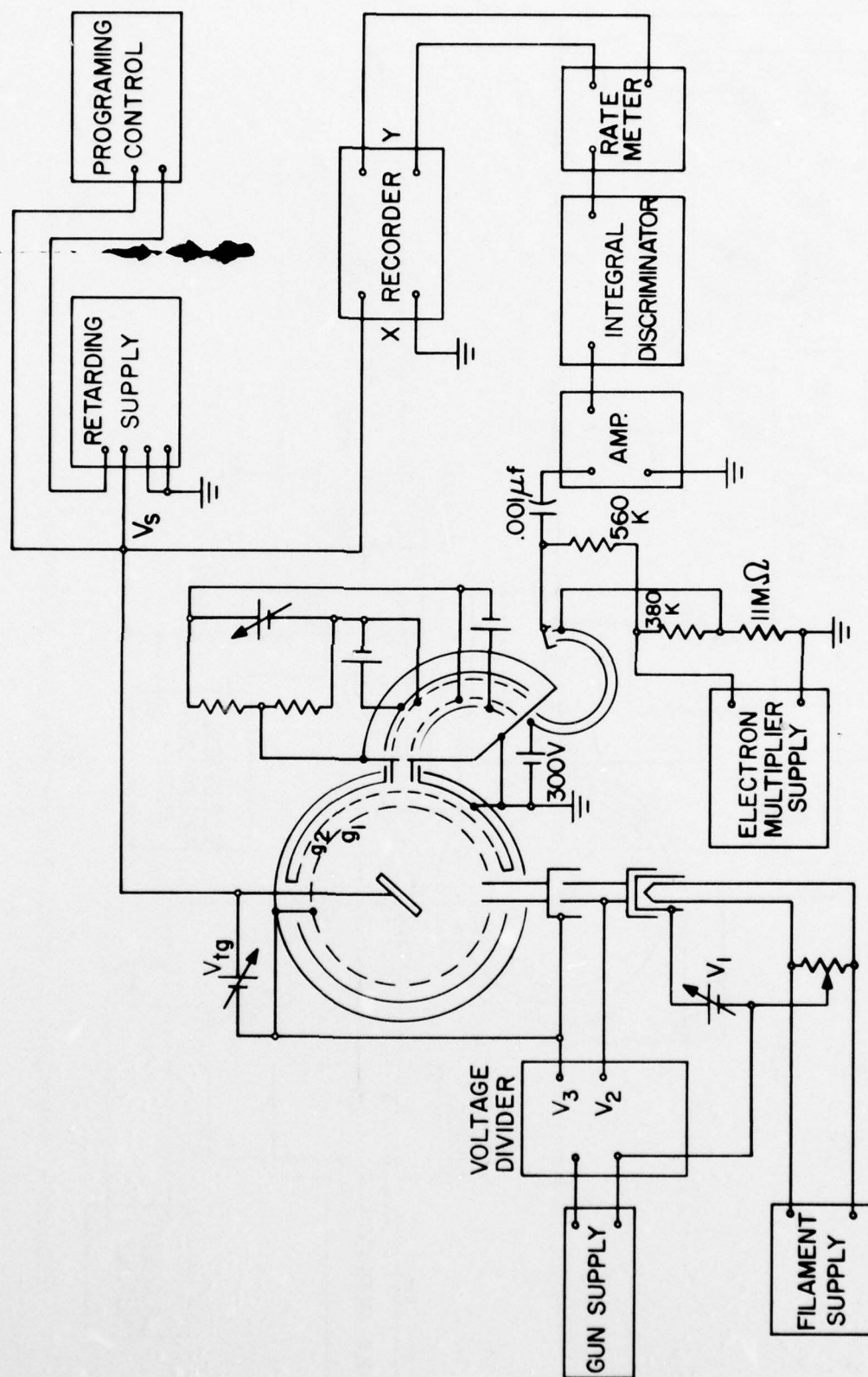


Figure 8 Schematic diagram of apparatus for secondary electron measurements

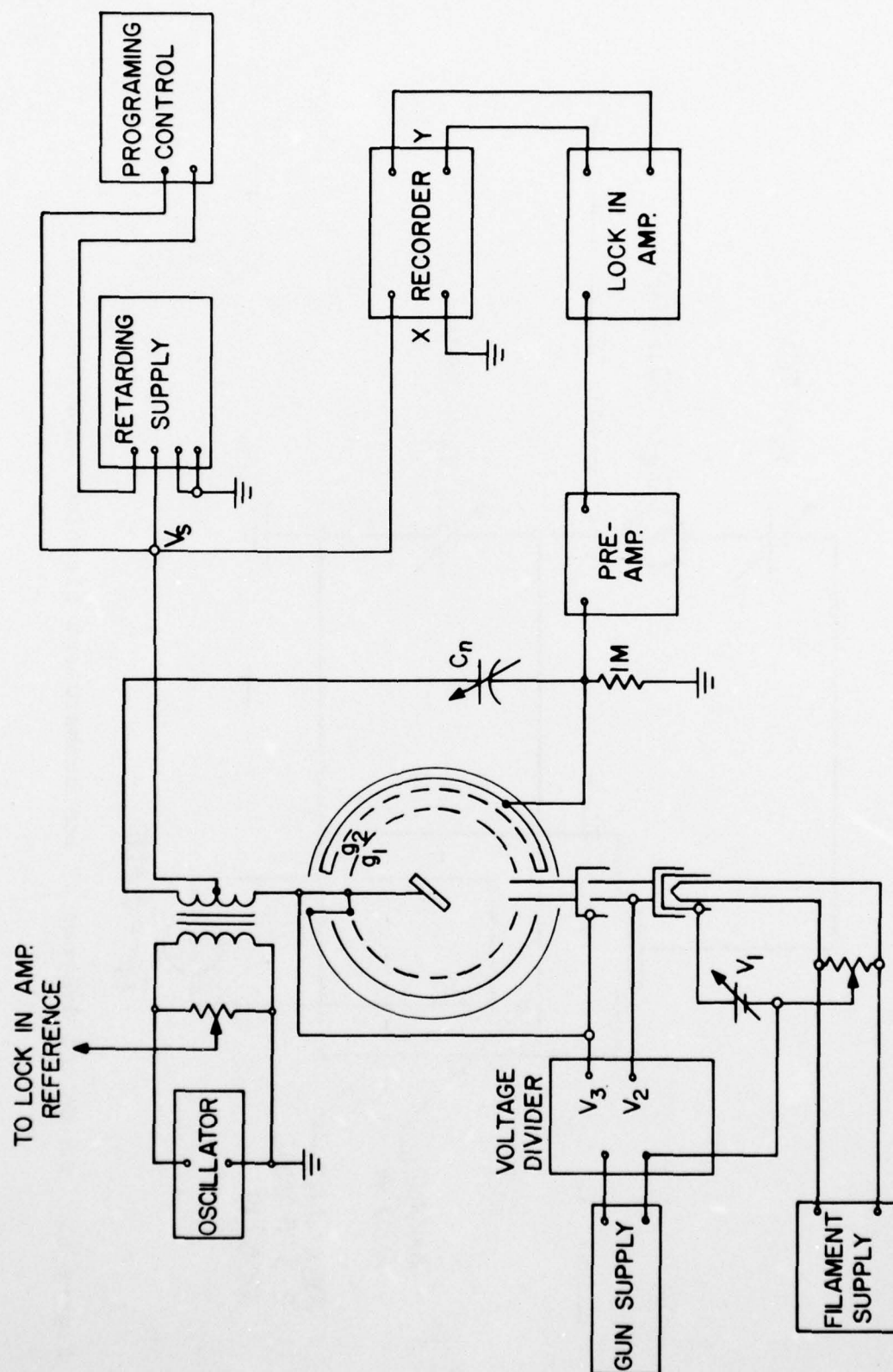


Figure 10 Schematic diagram of apparatus for Auger measurements

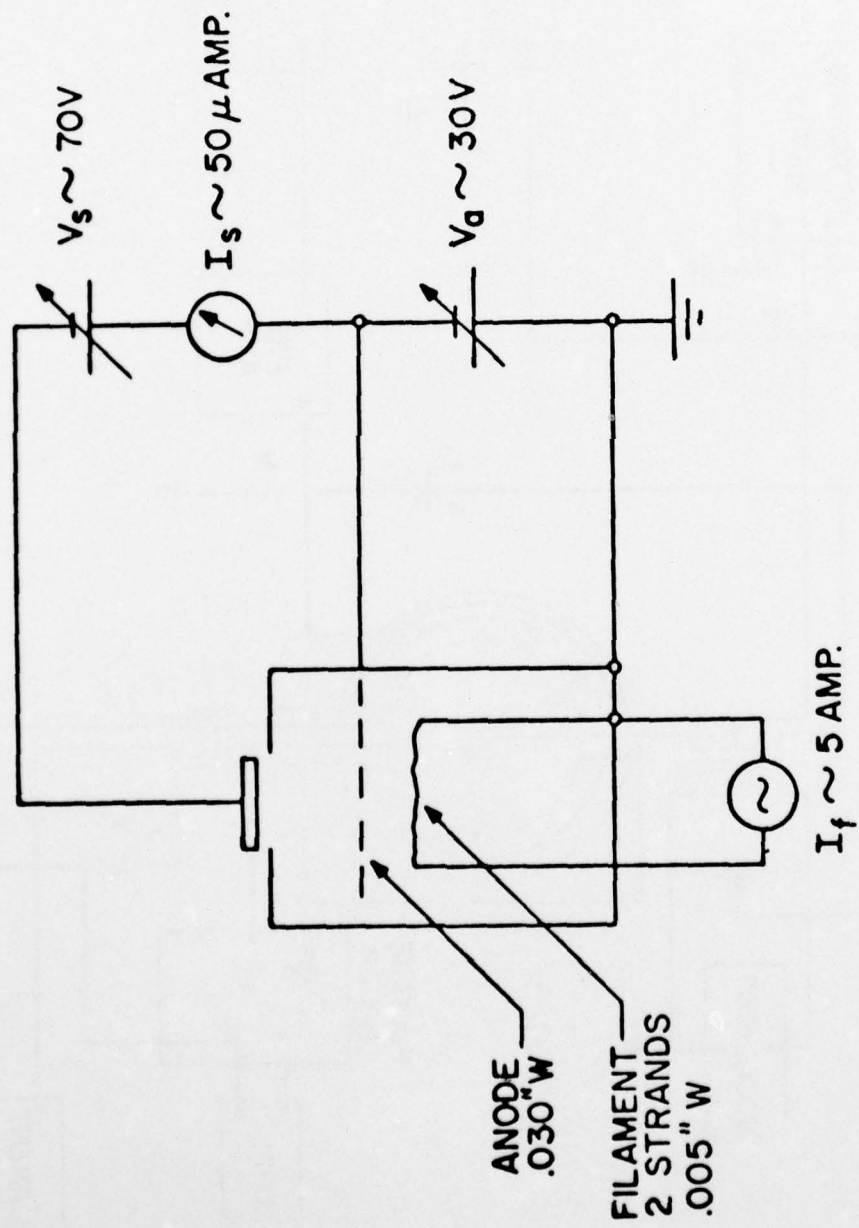


Figure 11 Schematic diagram of ion bombardment cleaning apparatus

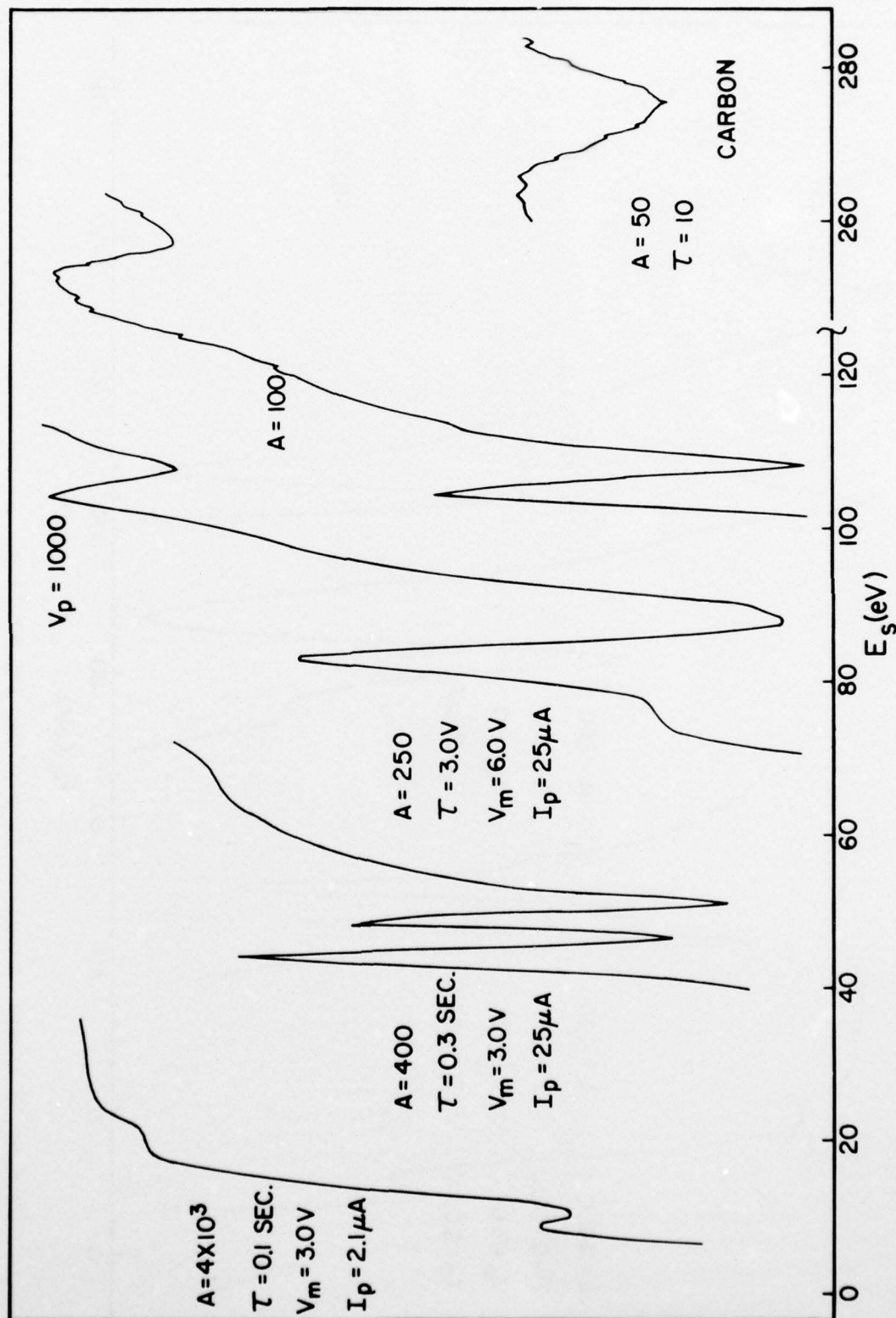


Figure 12 Auger spectrum from carbon contaminated Ge surface

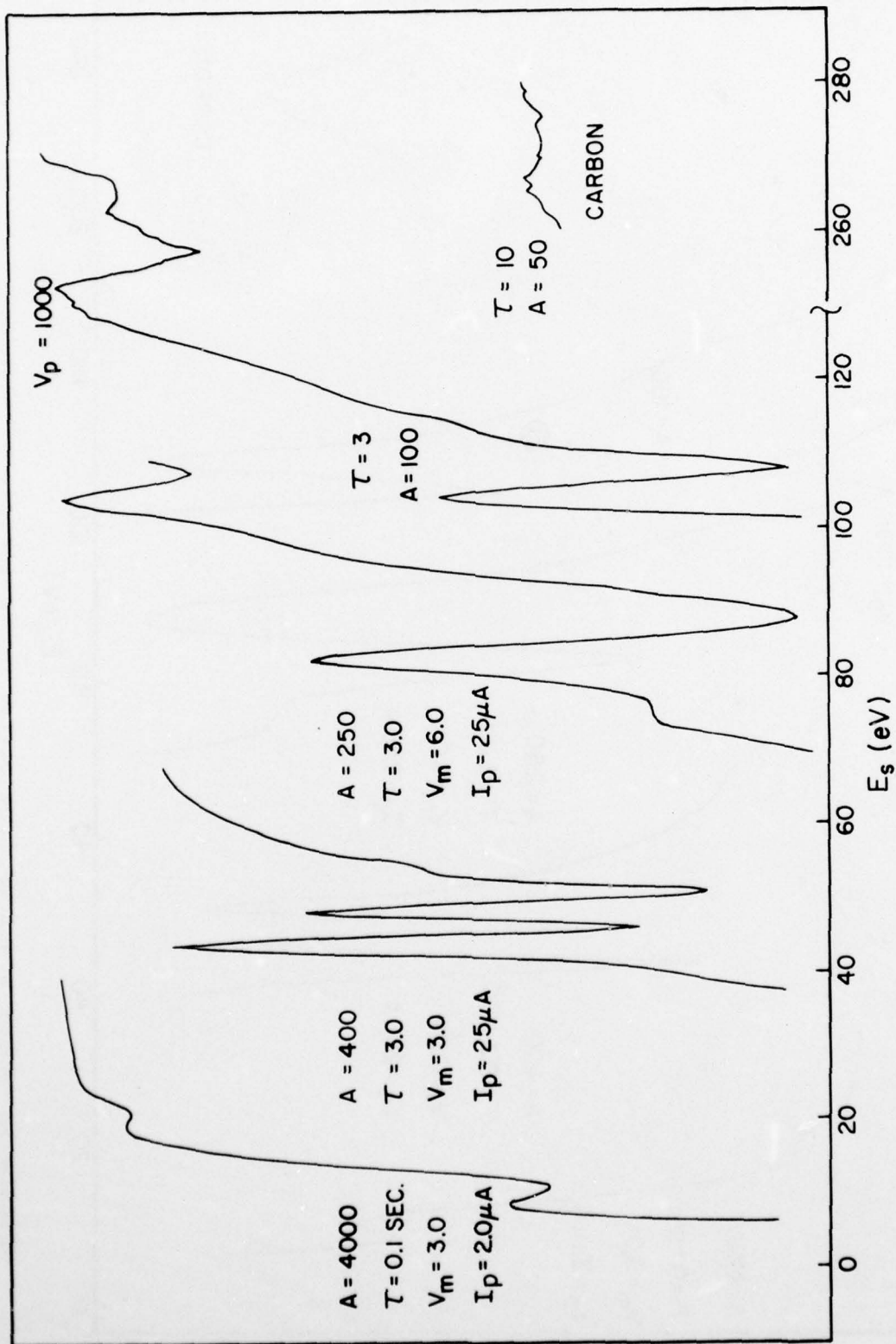


Figure 13 Auger spectrum from clean Ge surface

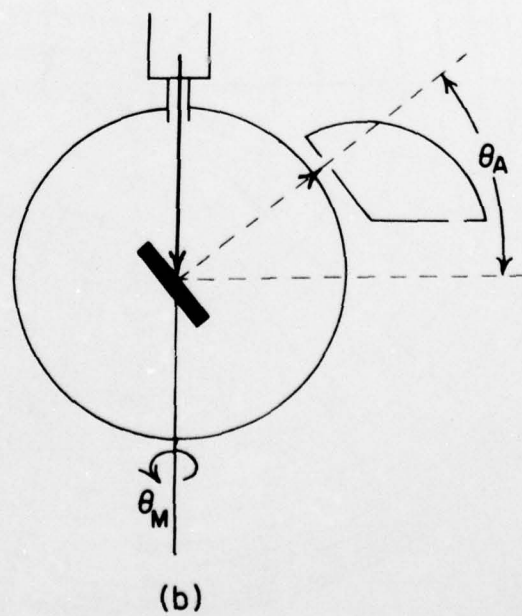
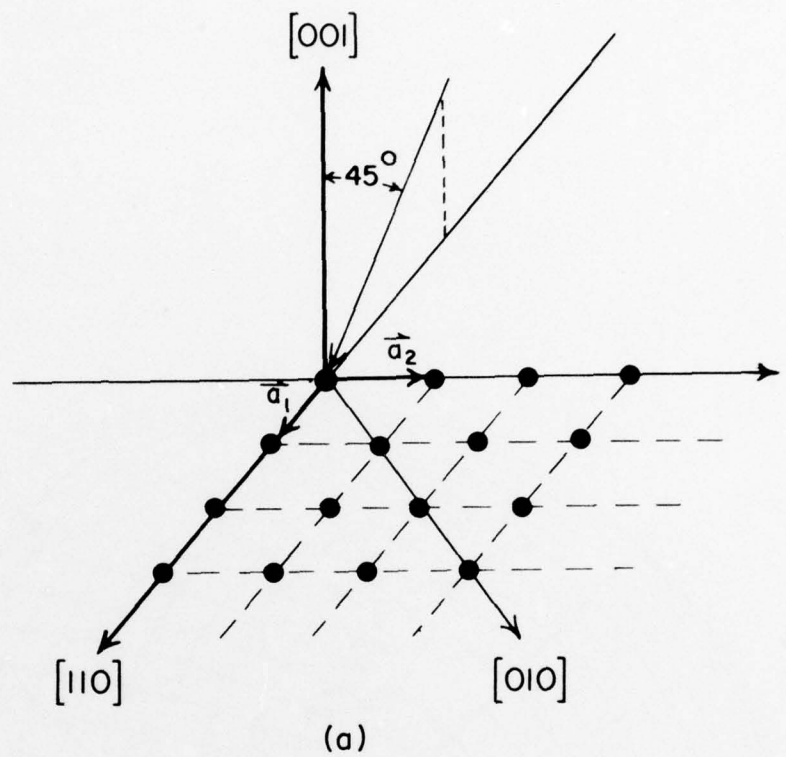


Figure 14 (a) Primary electron beam orientation with crystal axes. (b) Experimentally controlled angular variables.

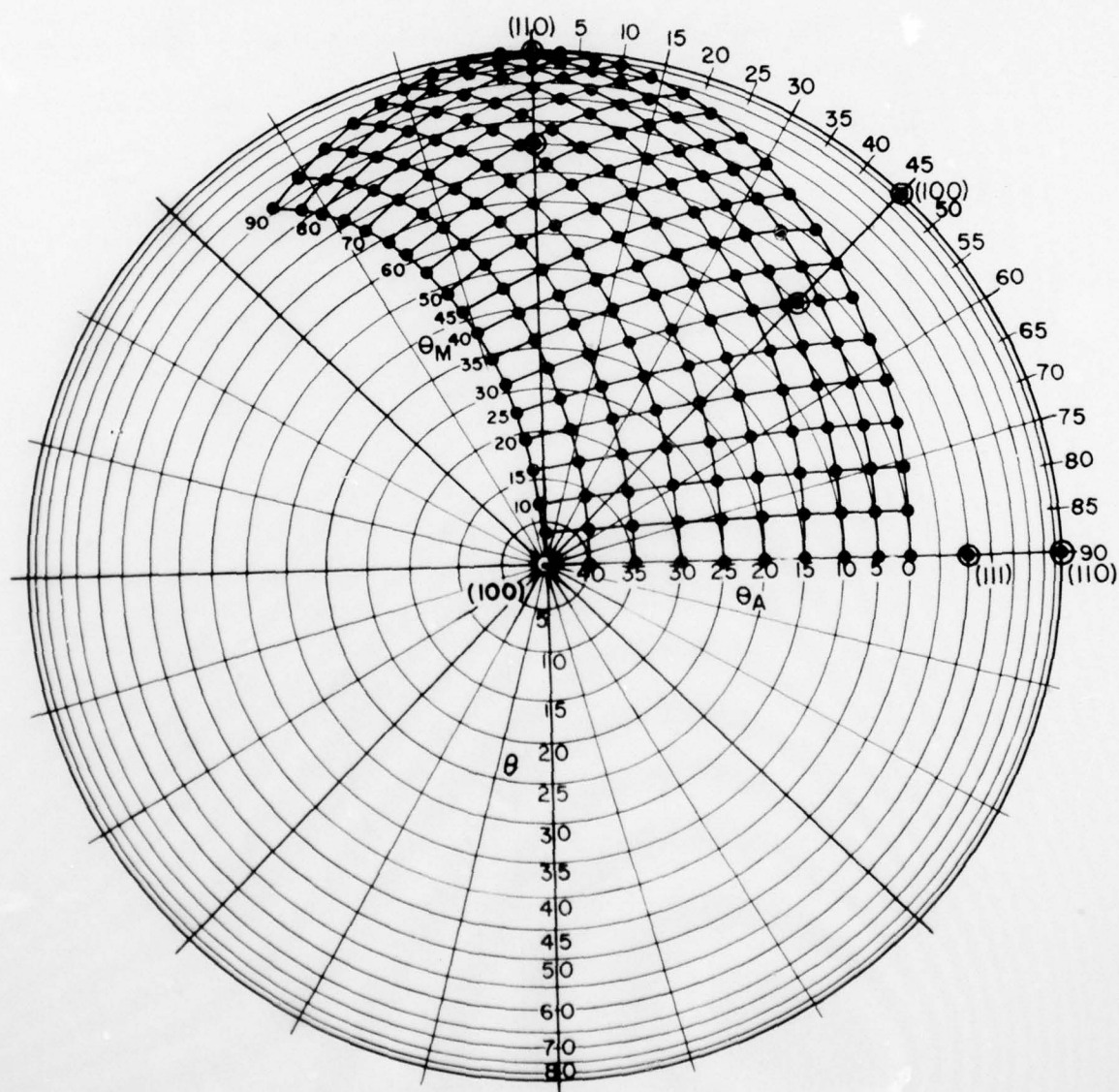


Figure 15 Graphical construction for determining scattering angles

AD-A042 189

MINNESOTA UNIV MINNEAPOLIS DEPT OF ELECTRICAL ENGIN--ETC F/G 20/8
A STUDY OF ELECTRON SCATTERING FROM GERMANIUM (100). (U)
APR 77 R L ERICKSON

UNCLASSIFIED

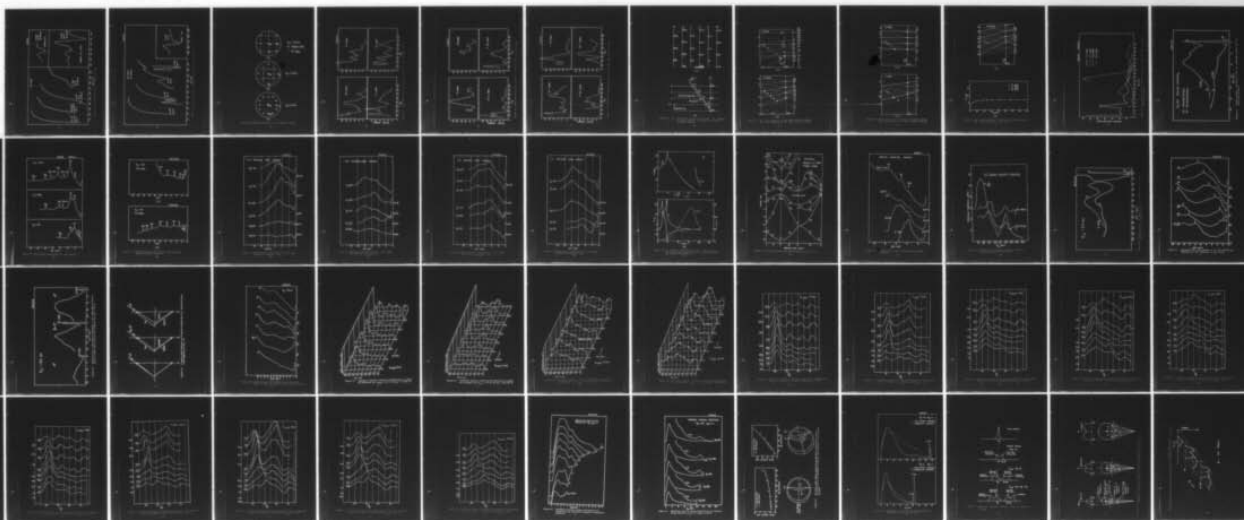
AFAL-TR-76-36

F33615-72-C-2105

NL

2 OF 2

AD
A042189



END

DATE

FILMED

8-77

268018

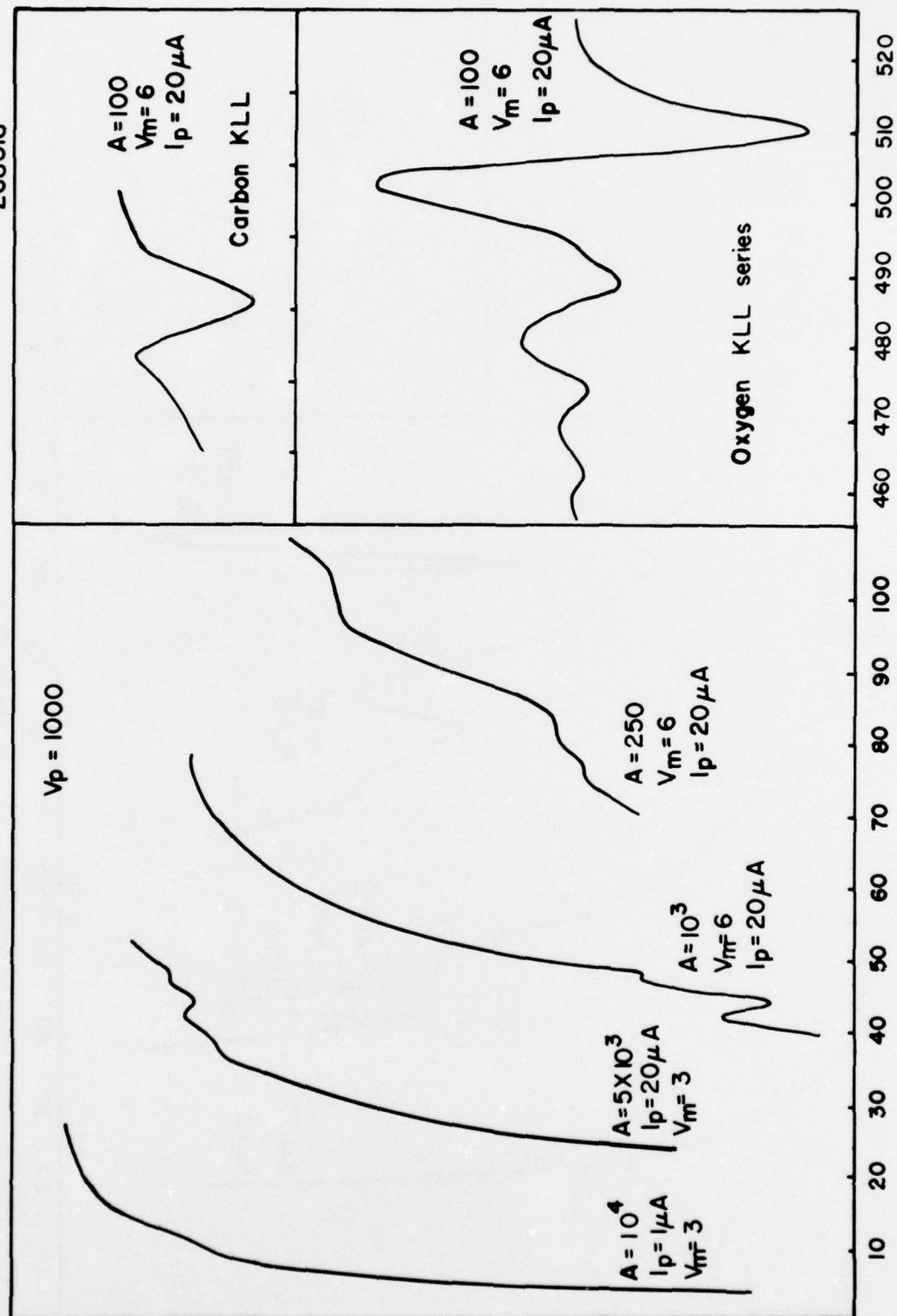


Figure 16 Auger spectrum of oxidized Ge surface

268021

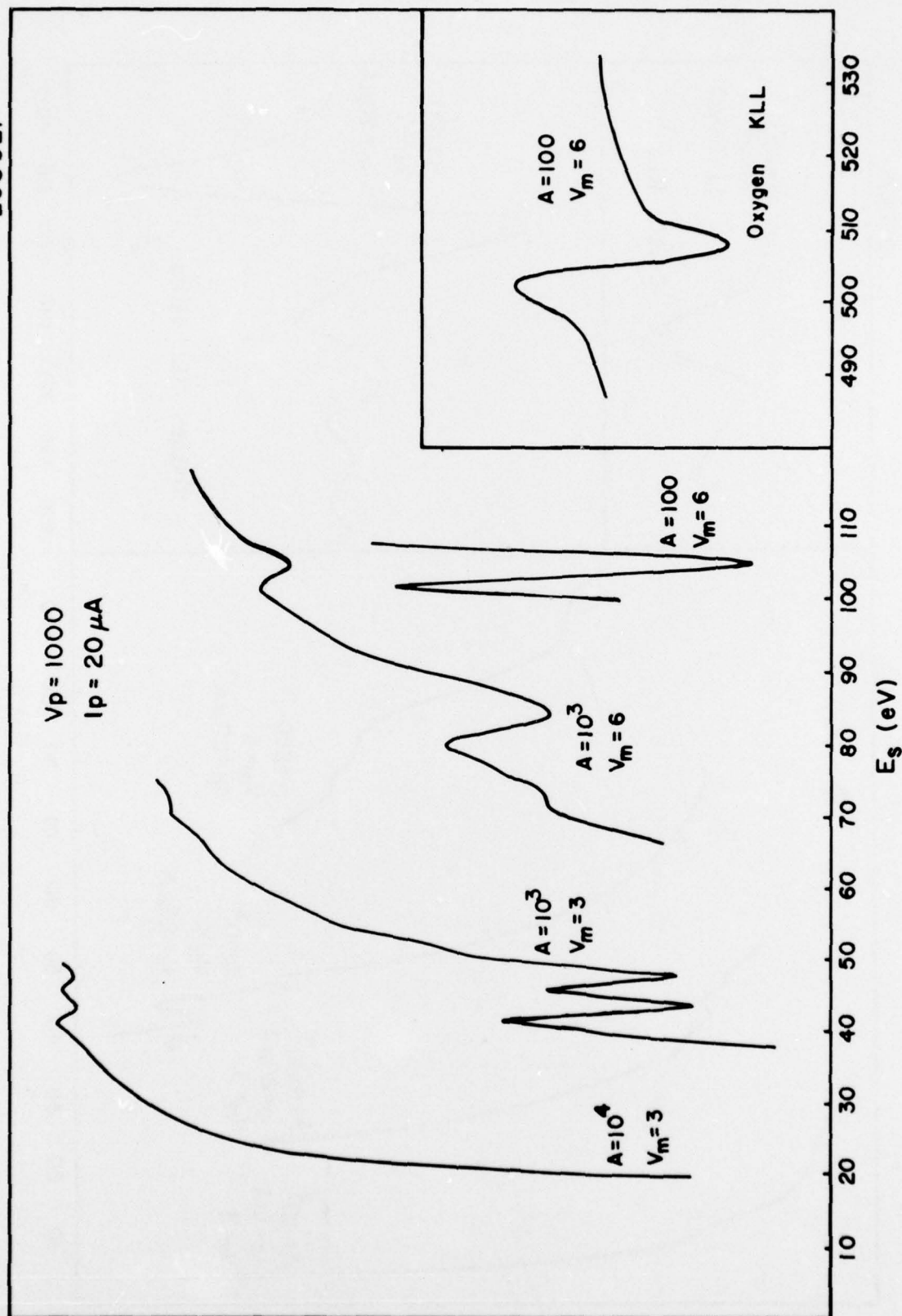
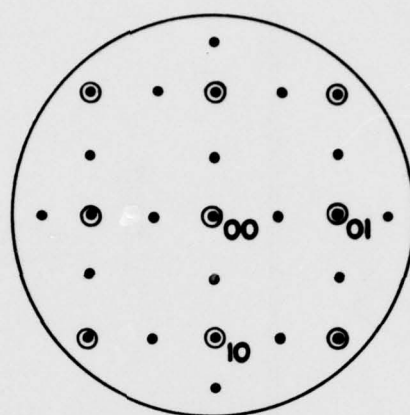


Figure 17 Auger spectrum of oxidized Ge surface after sputtering

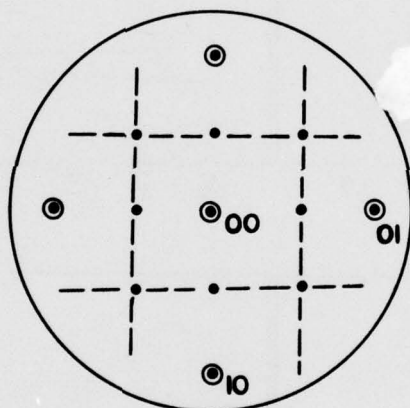


$E_p \approx 40 \text{ eV}$

● integral order

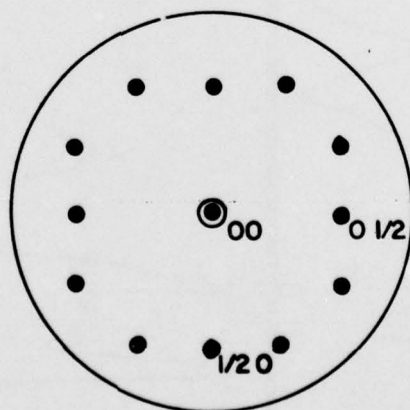
• 1/2-order

(a)



$E_p \approx 20 \text{ eV}$

(b)



$E_p \approx 4 \text{ eV}$

(c)

Figure 18 LEED patterns for clean Ge(100) surface

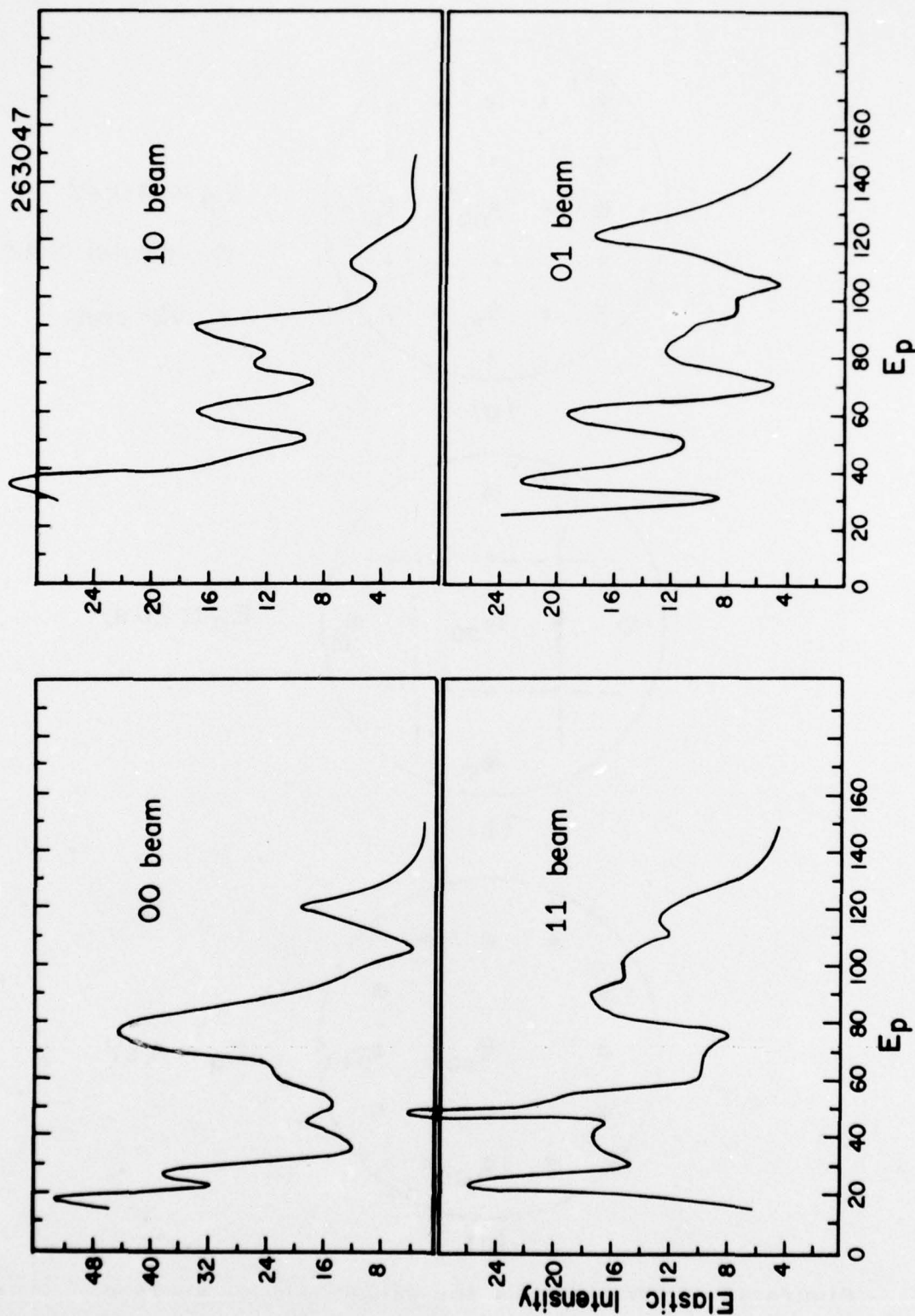


Figure 19 LEED beam intensity plots for (00), (10), (11) and (01) beams

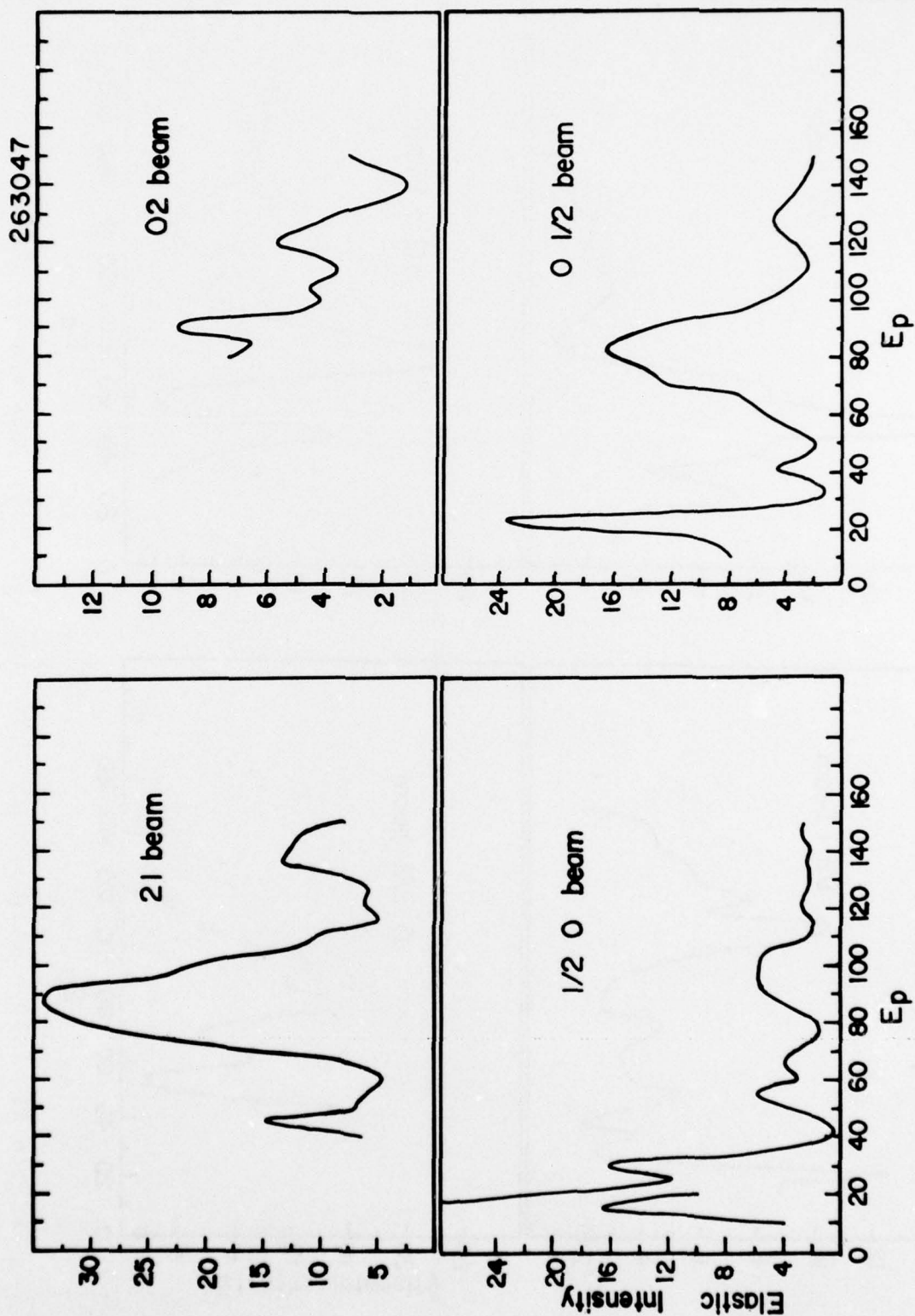


Figure 20 LEED beam intensity plots for (21) , (02) , $(\frac{1}{2}0)$ and $(0\frac{1}{2})$ beams

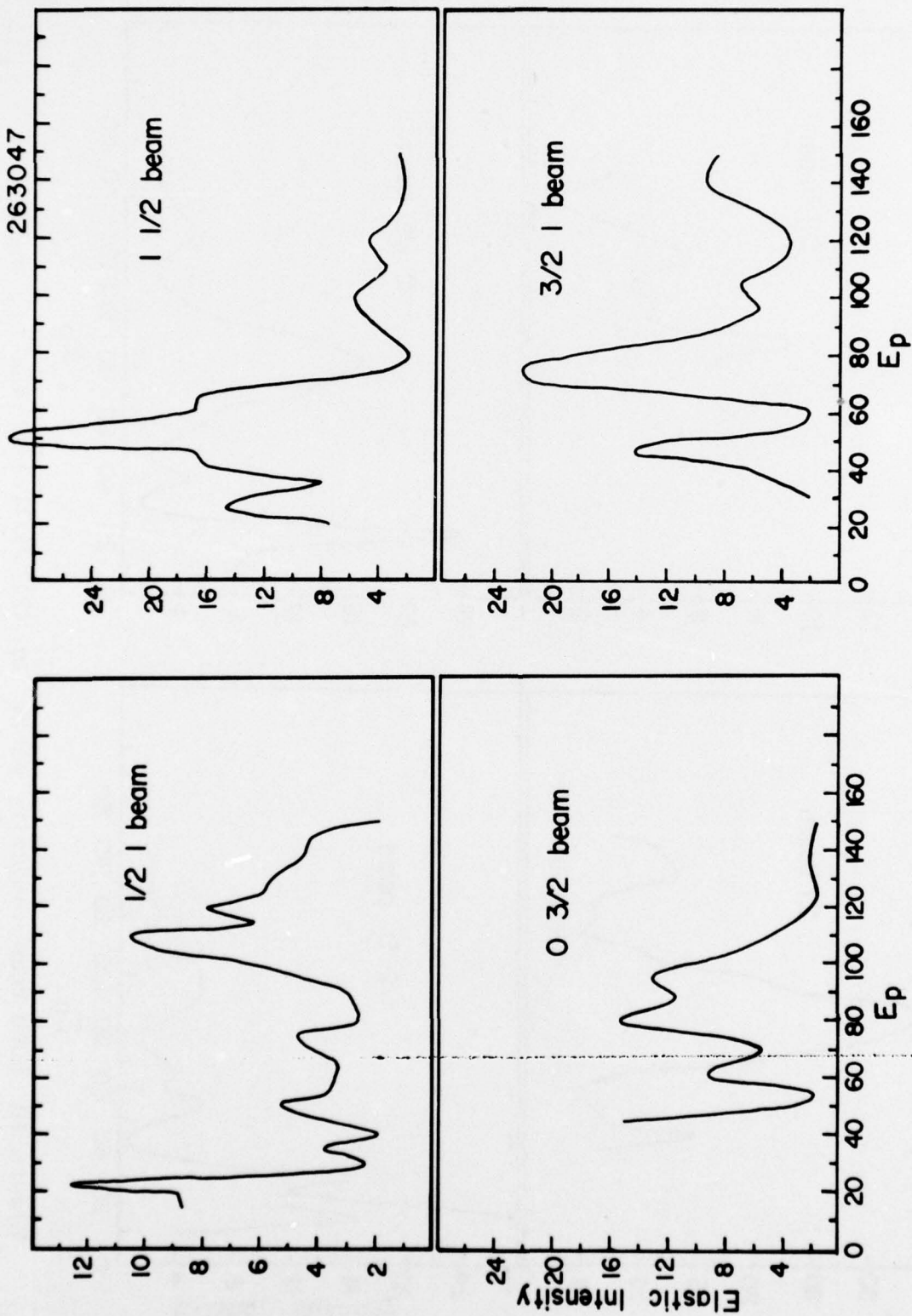
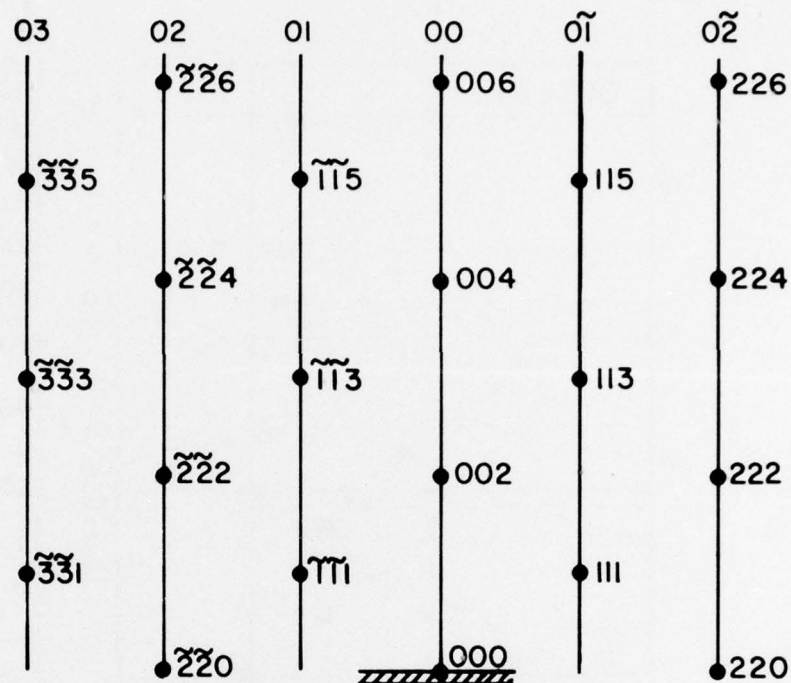
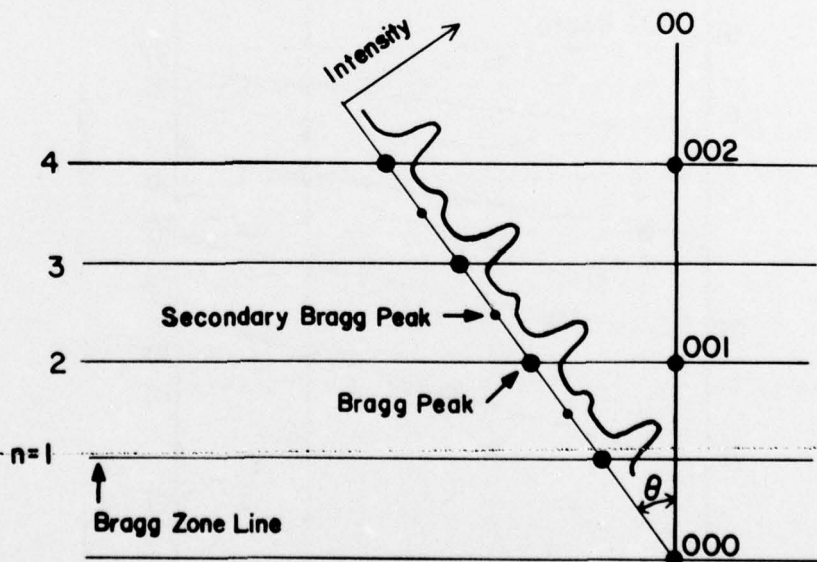


Figure 21 LEED beam intensity plots for $(\frac{1}{2}1)$, $(1\frac{1}{2})$, $(0\frac{3}{2})$ and $(\frac{3}{2}1)$ beams

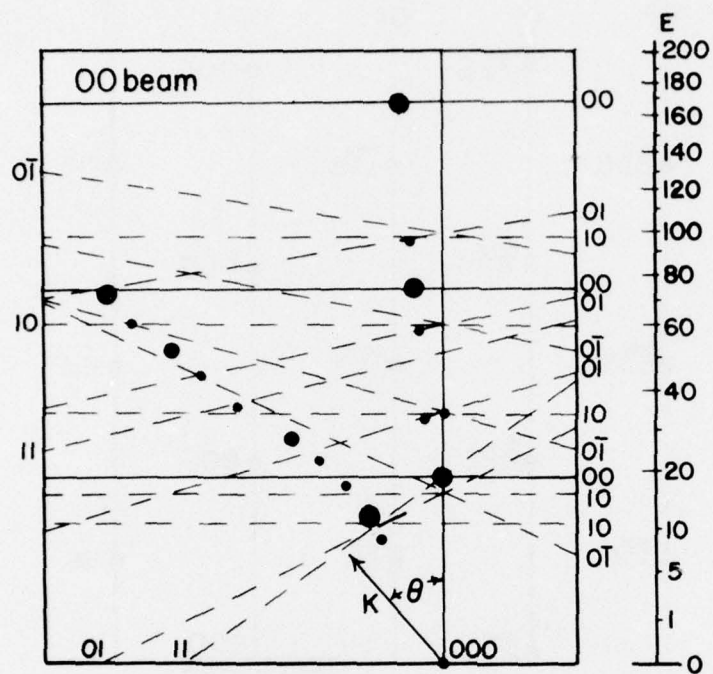


(a)

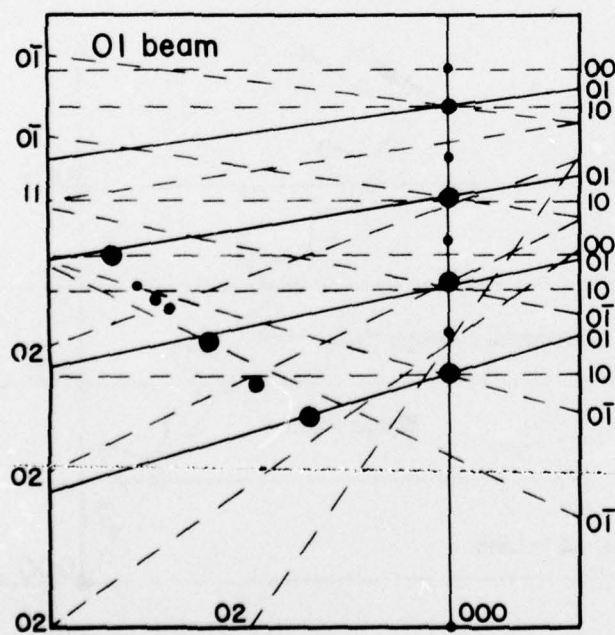


(b)

Figure 22 (a) Reciprocal lattice for Ge(100) (b) Example of point plotting in K-space for elastic intensity maxima.

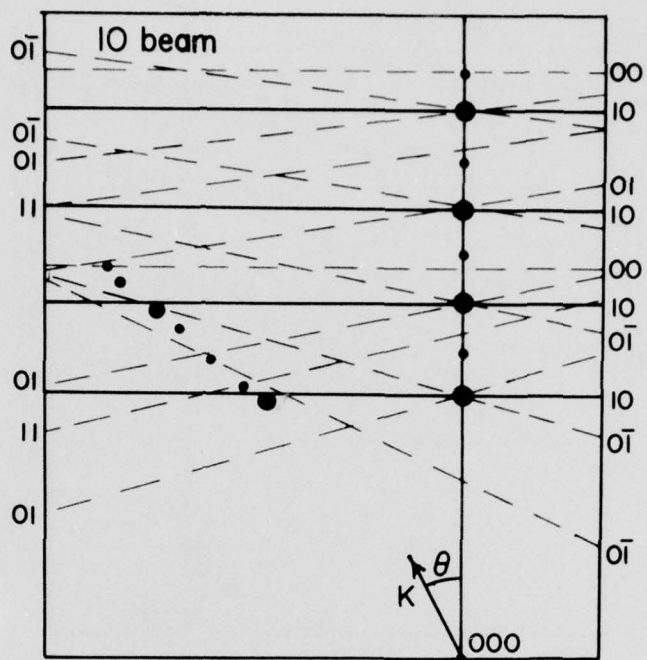


(a)

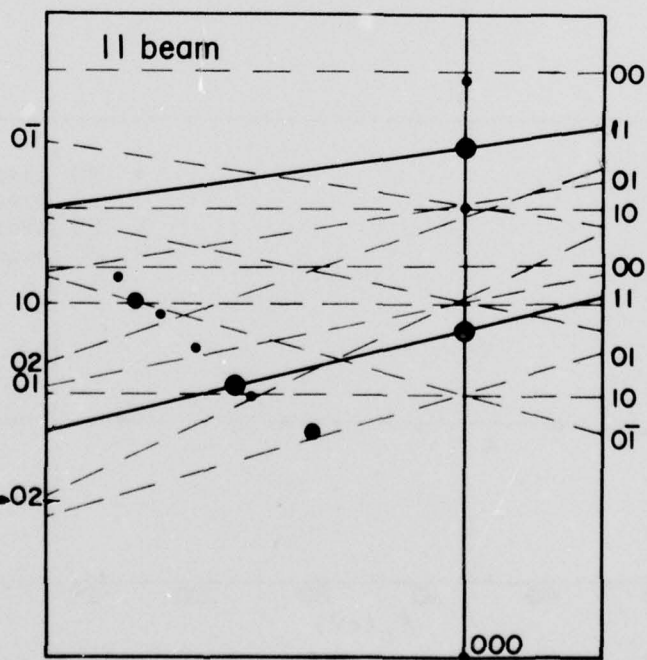


(b)

Figure 23 (a) Point plotting of (00) beam intensity maxima
(b) Point plotting of (01) beam intensity maxima

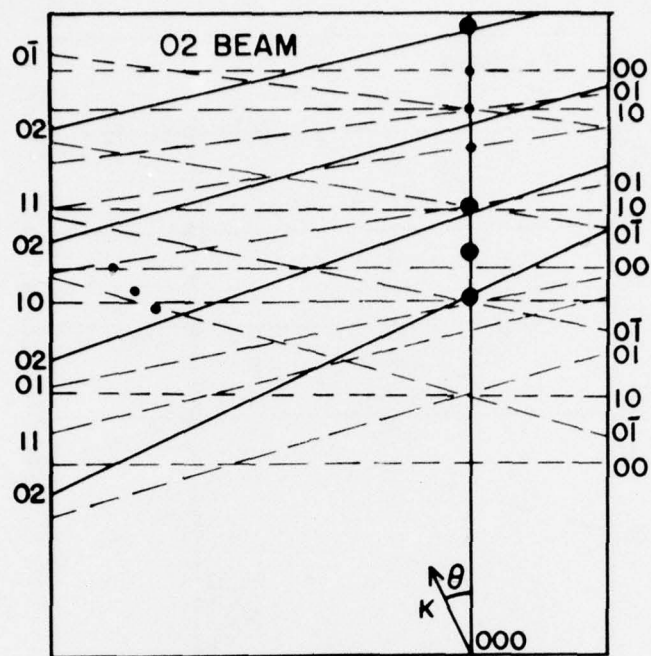


(a)



(b)

Figure 24 Point plotting of (10) beam intensity maxima
Point plotting of (11) beam intensity maxima



(a)

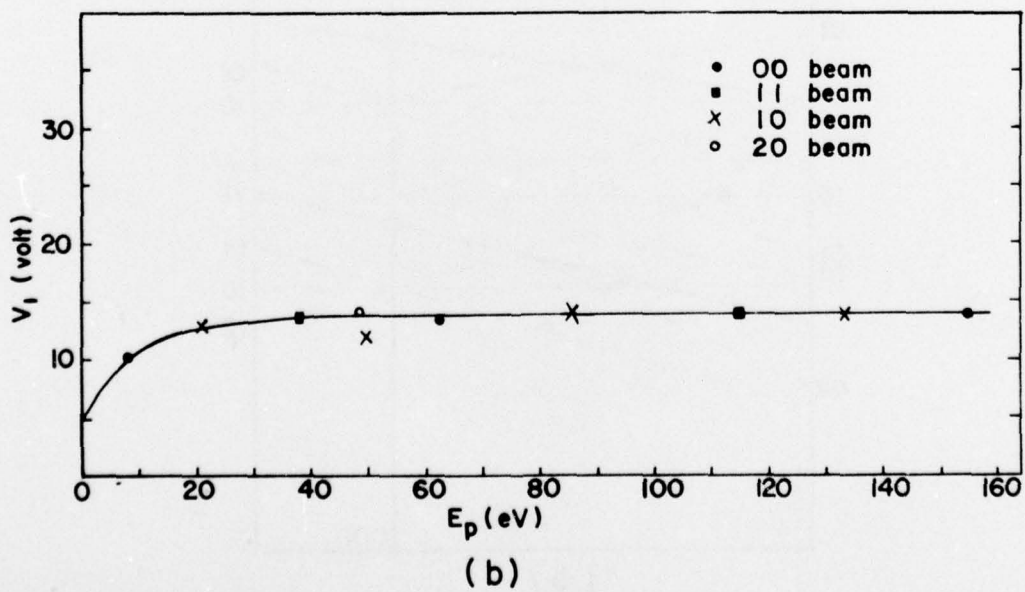


Figure 25 (a) Point plotting of (02) beam intensity maxima
(b) Inner potential curve for Ge

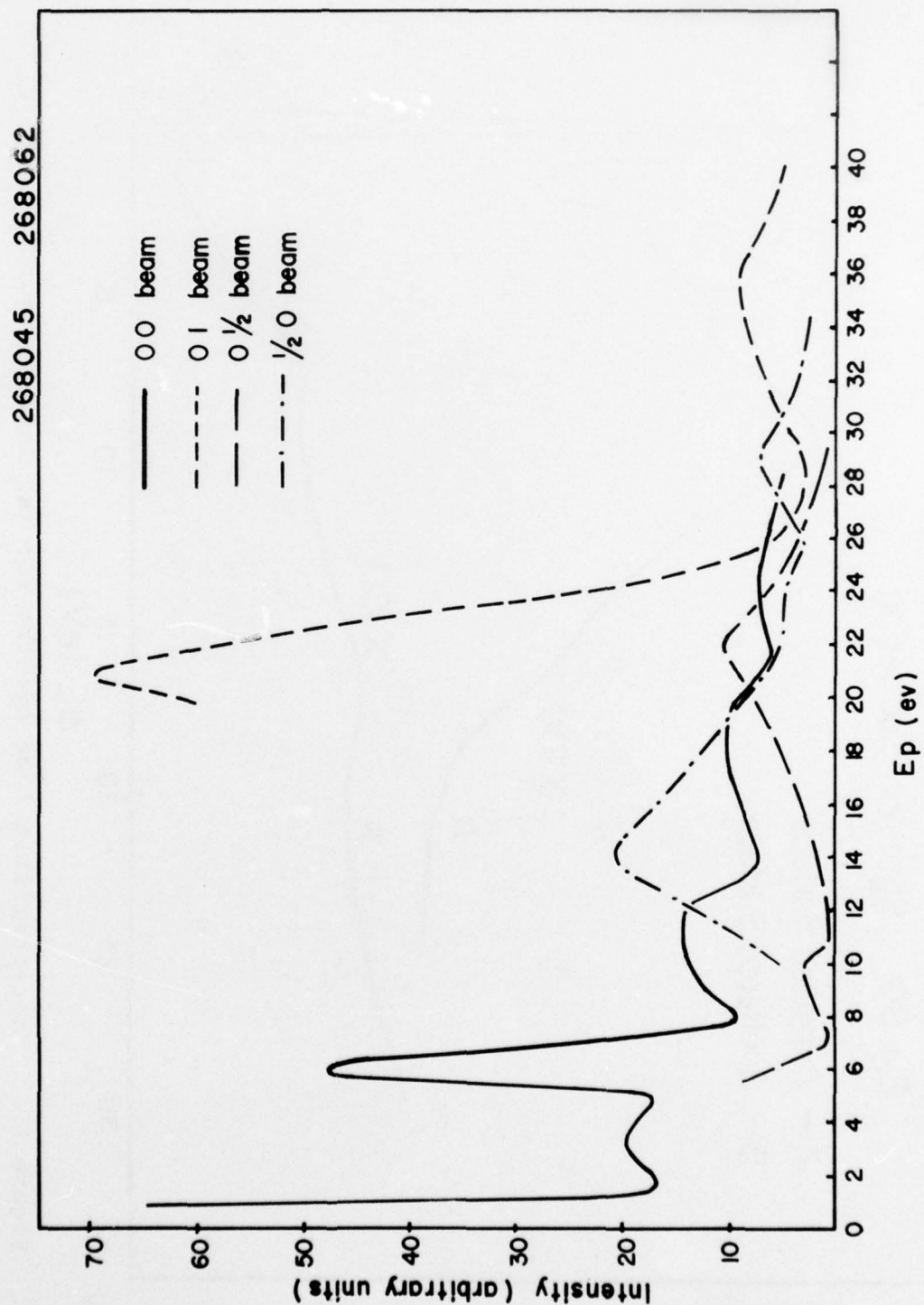


Figure 26 Low energy elastic intensity plots for (00), (01), (0 $\frac{1}{2}$) and ($\frac{1}{2}$ 0) diffraction beams

263074

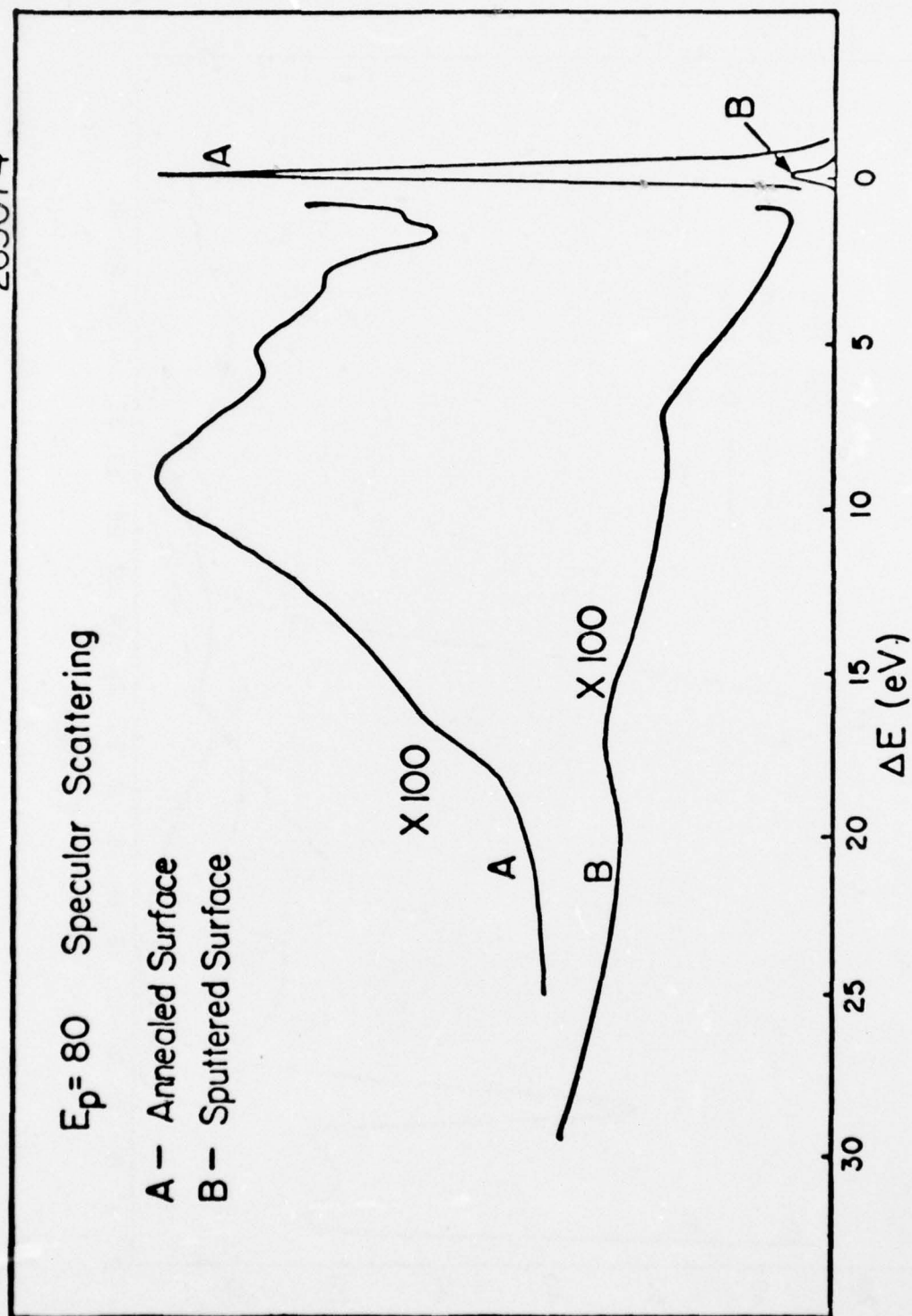


Figure 27 Characteristic loss spectra for (a) annealed surface and (b) sputtered surface

260029

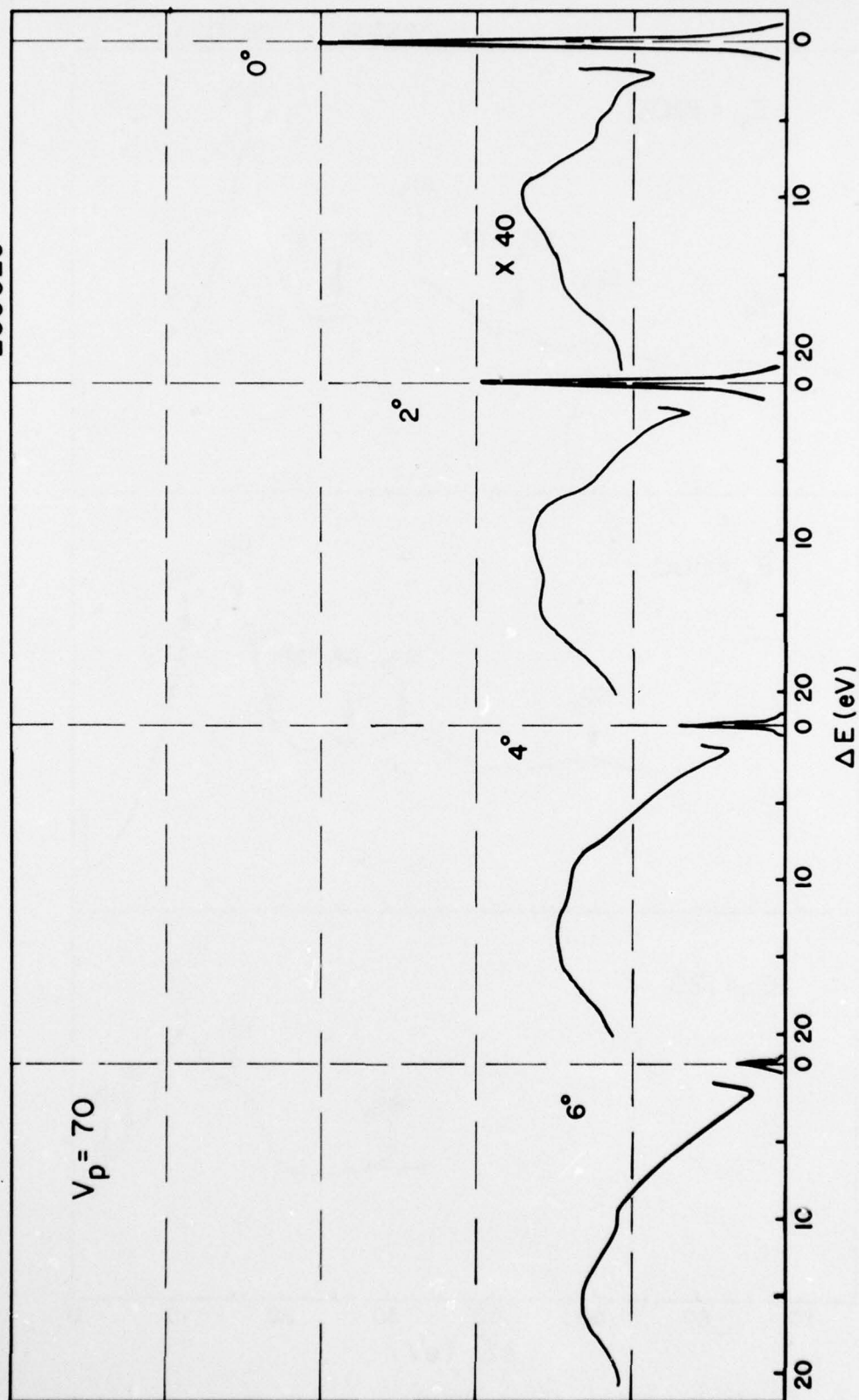


Figure 28 Characteristic loss spectra vs. scattering angle transverse to plane of incidence about the (00) diffraction beam

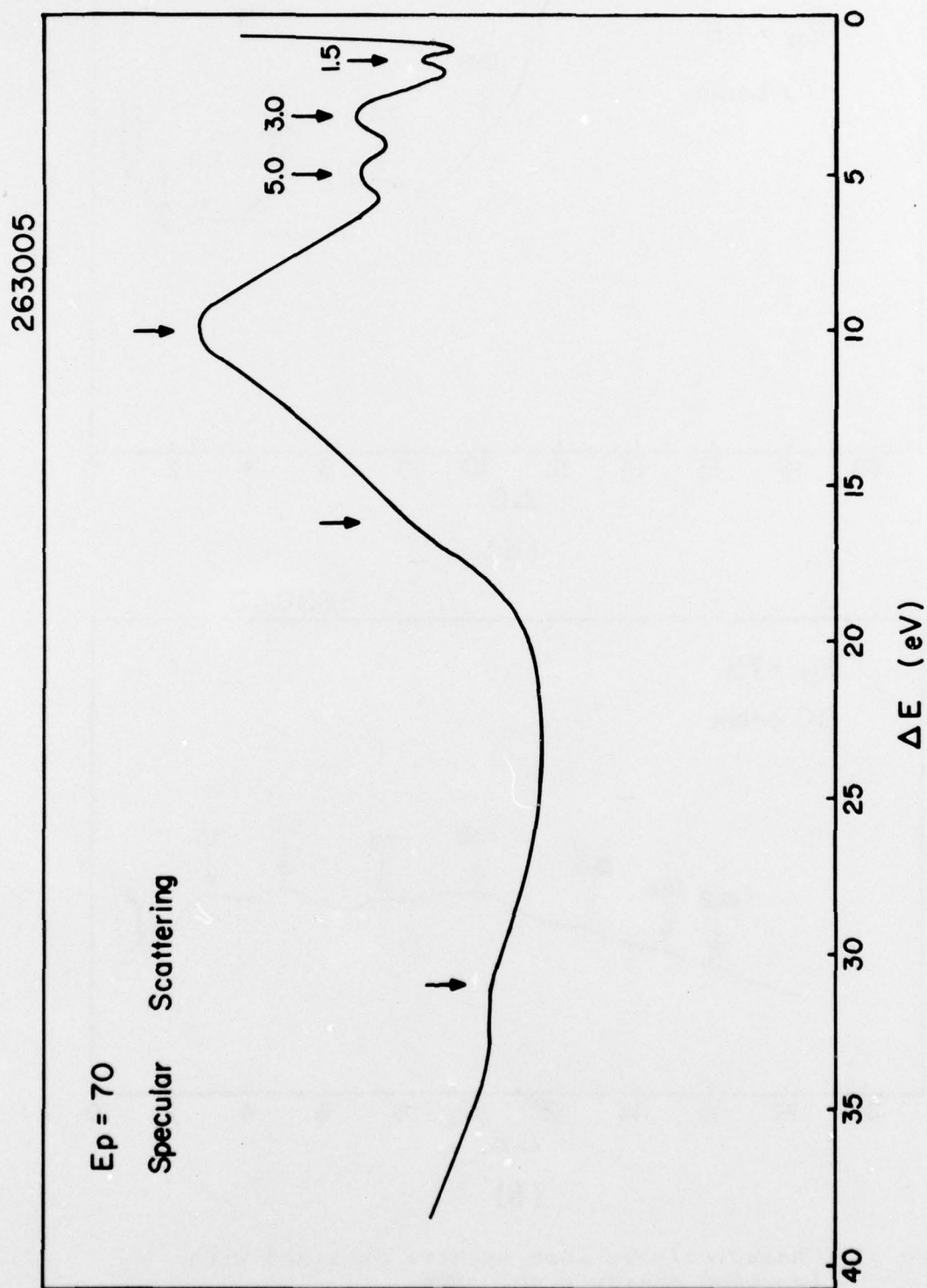


Figure 30 Typical low energy characteristic loss spectrum for specular scattering

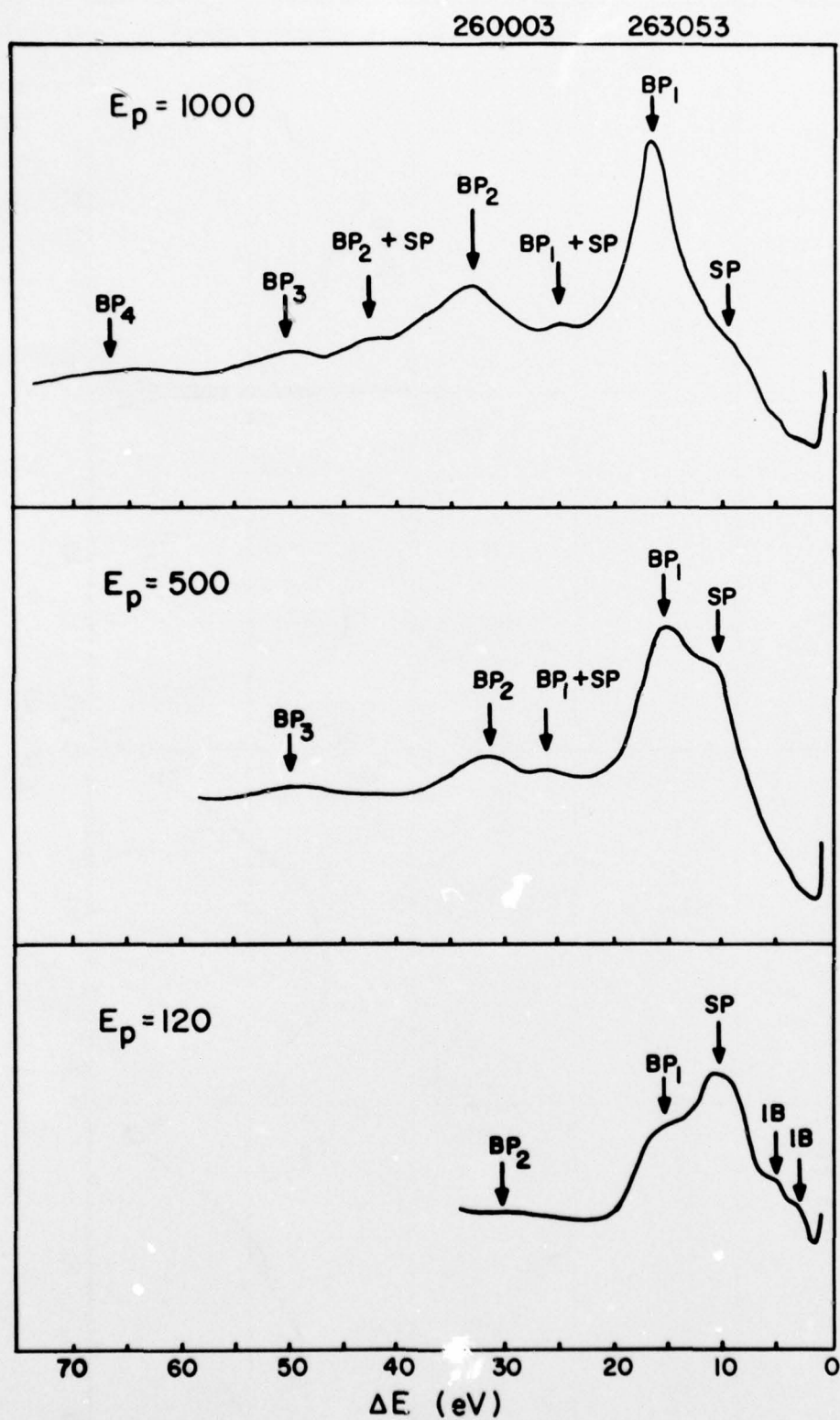
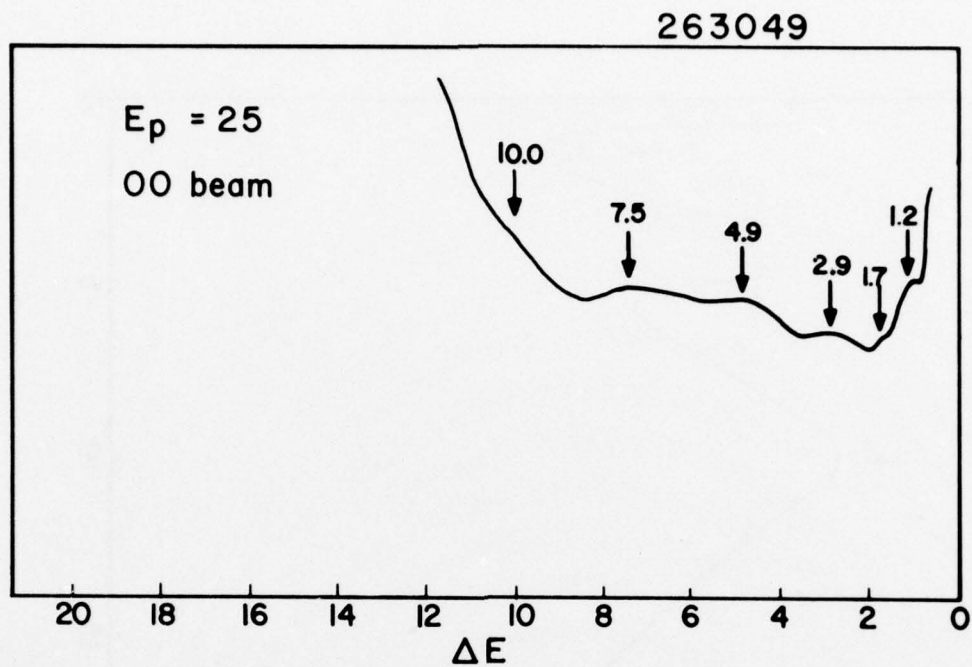
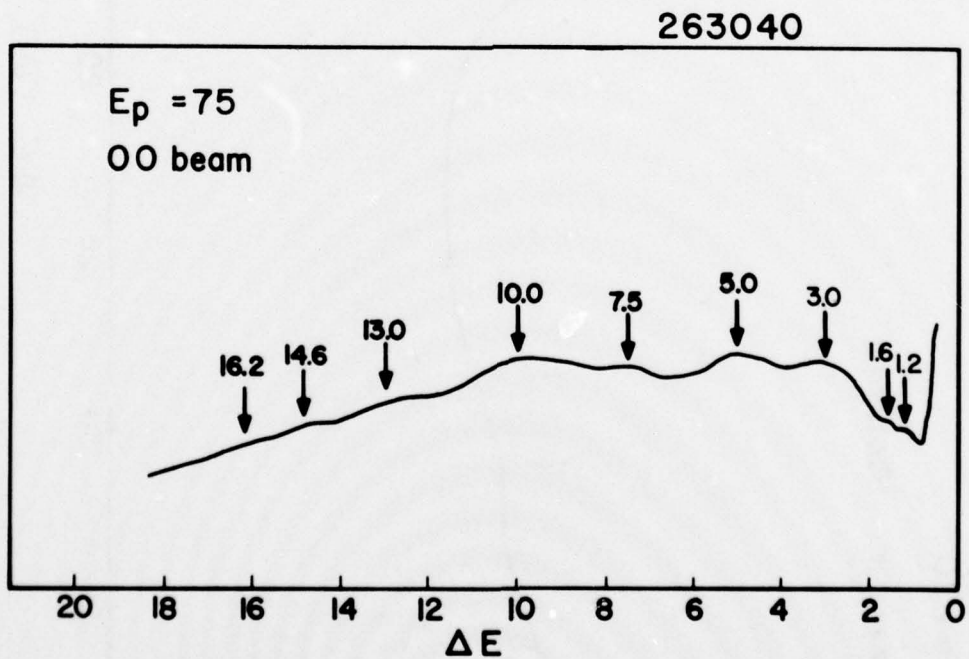


Figure 29 High energy characteristic loss spectra



(a)



(b)

Figure 31 Characteristic loss spectra obtained with improved energy resolution

263056

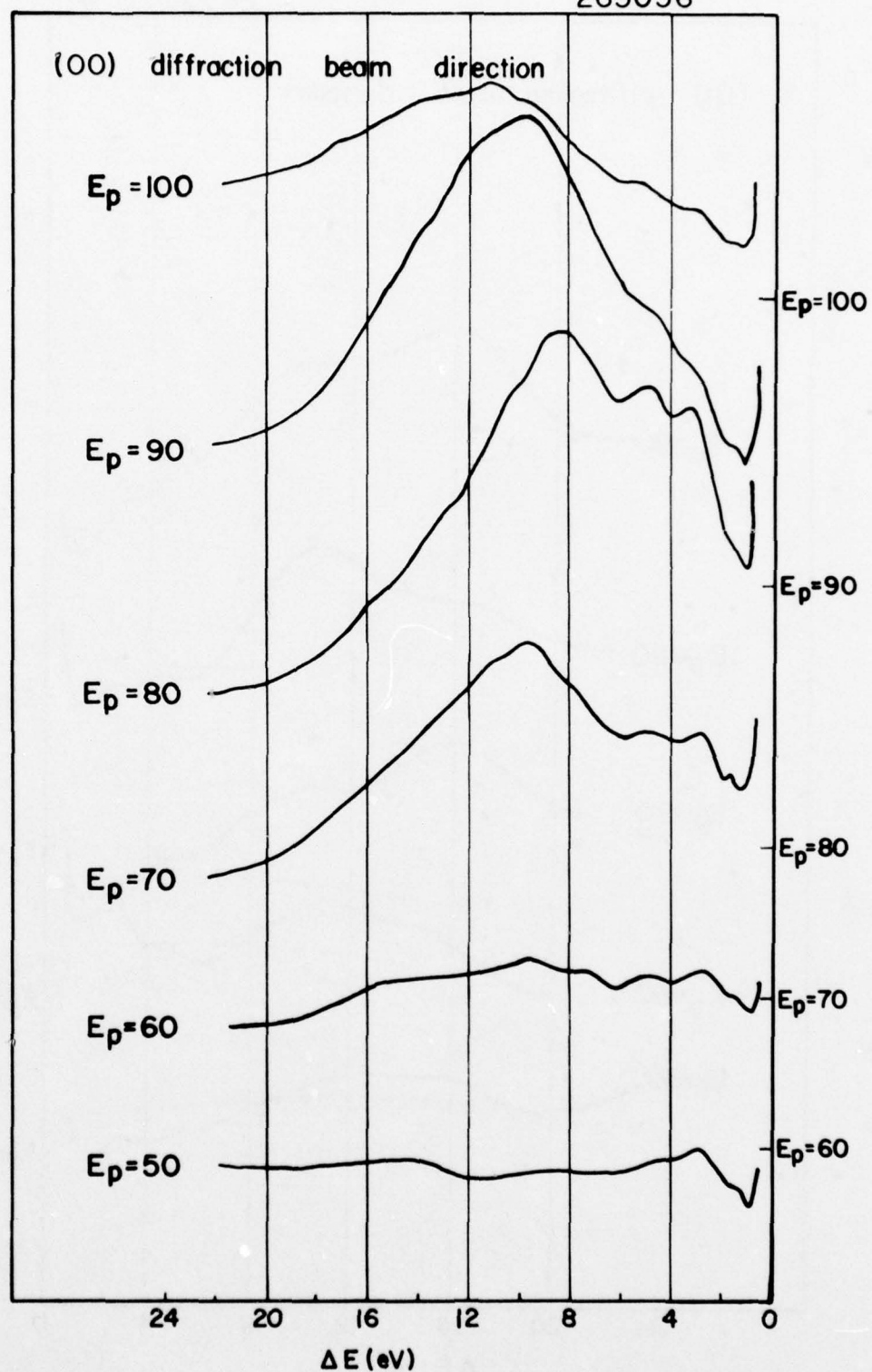


Figure 32 Characteristic loss spectra in (00) beam direction as function of E_p

263056

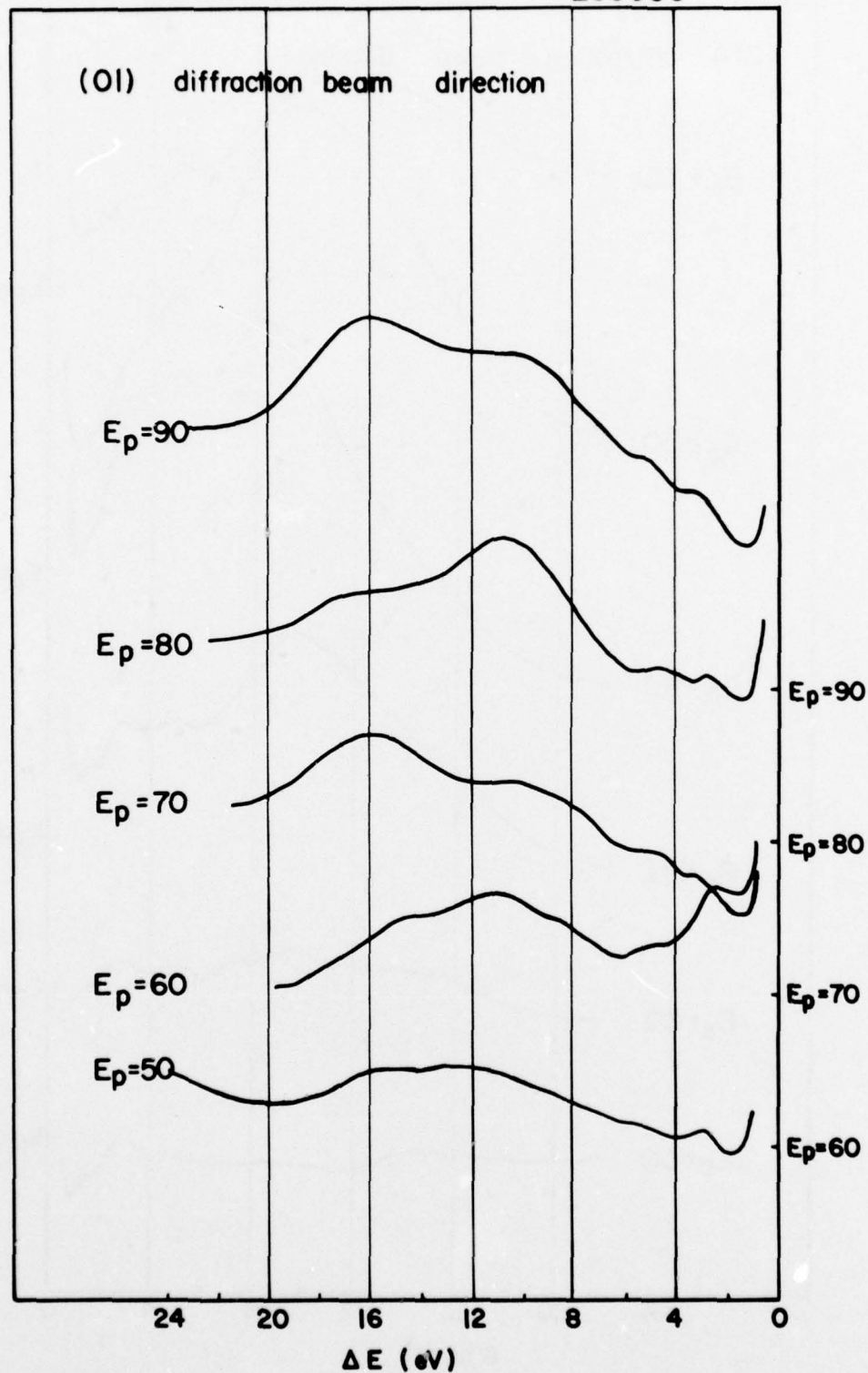


Figure 33 Characteristic loss spectra in (01) beam direction as function of E_p

263054

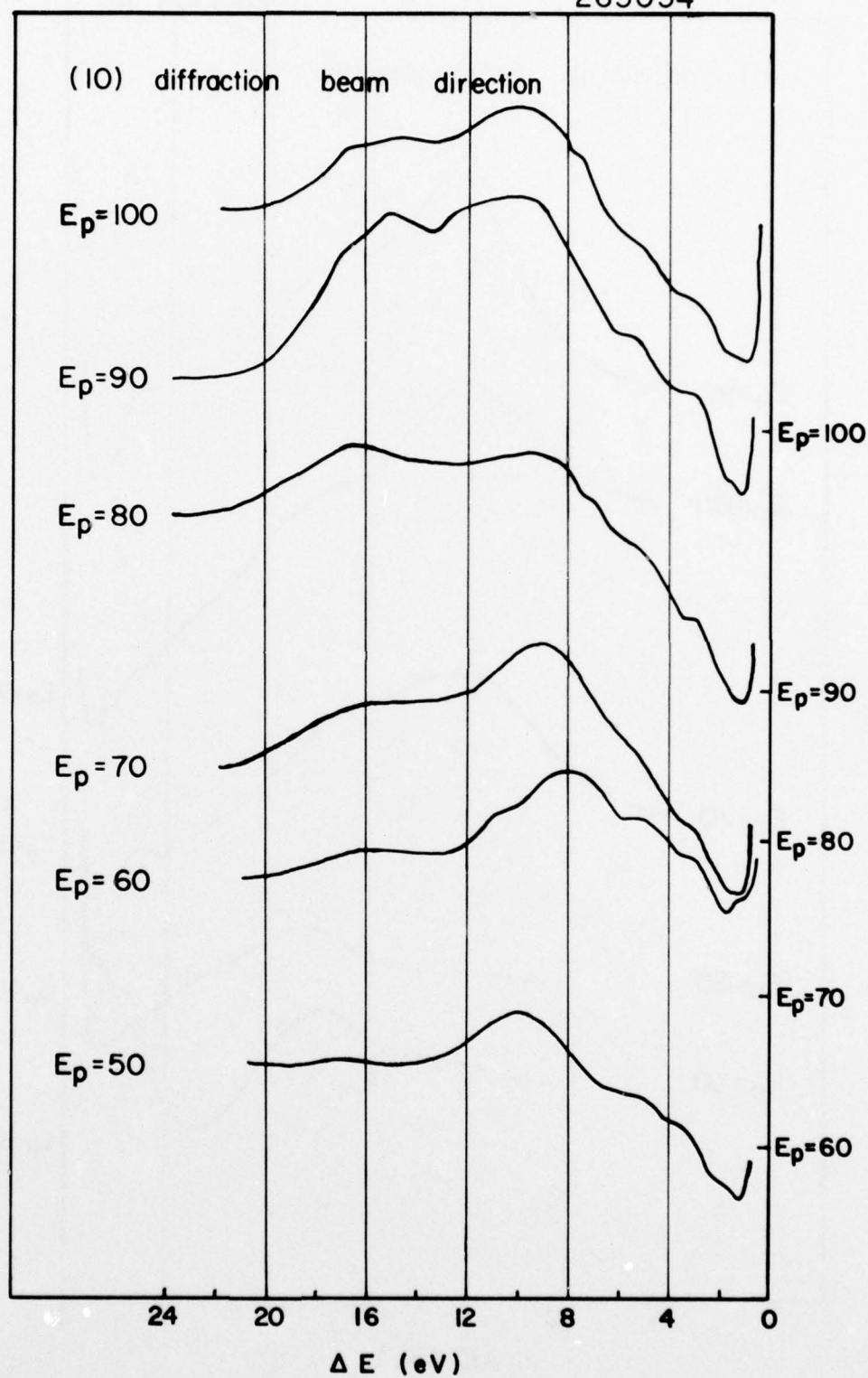


Figure 34 Characteristic loss spectra in (10) beam direction as function of E_p

263054

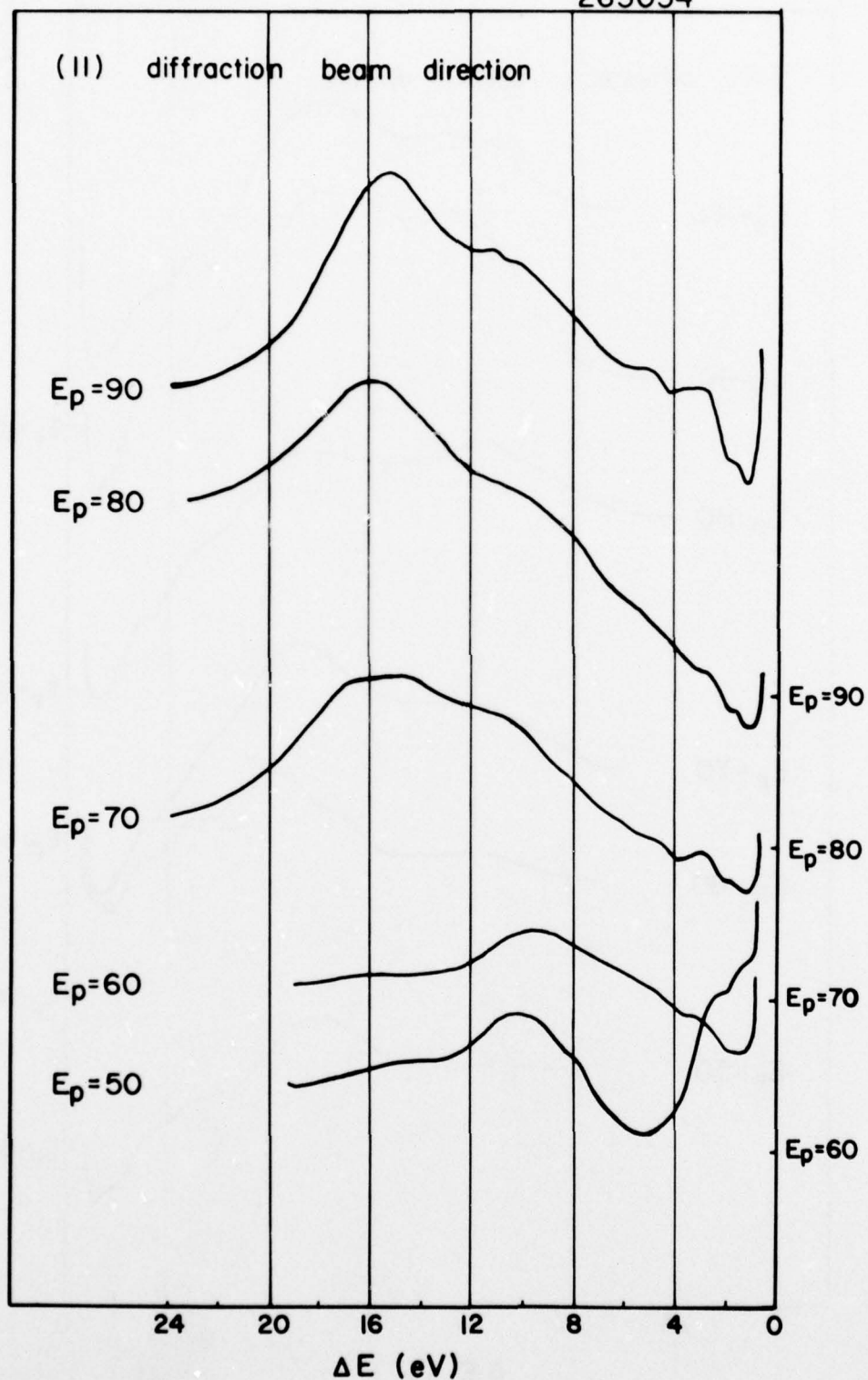


Figure 35 Characteristic loss spectra in (11) beam direction as function of E_p

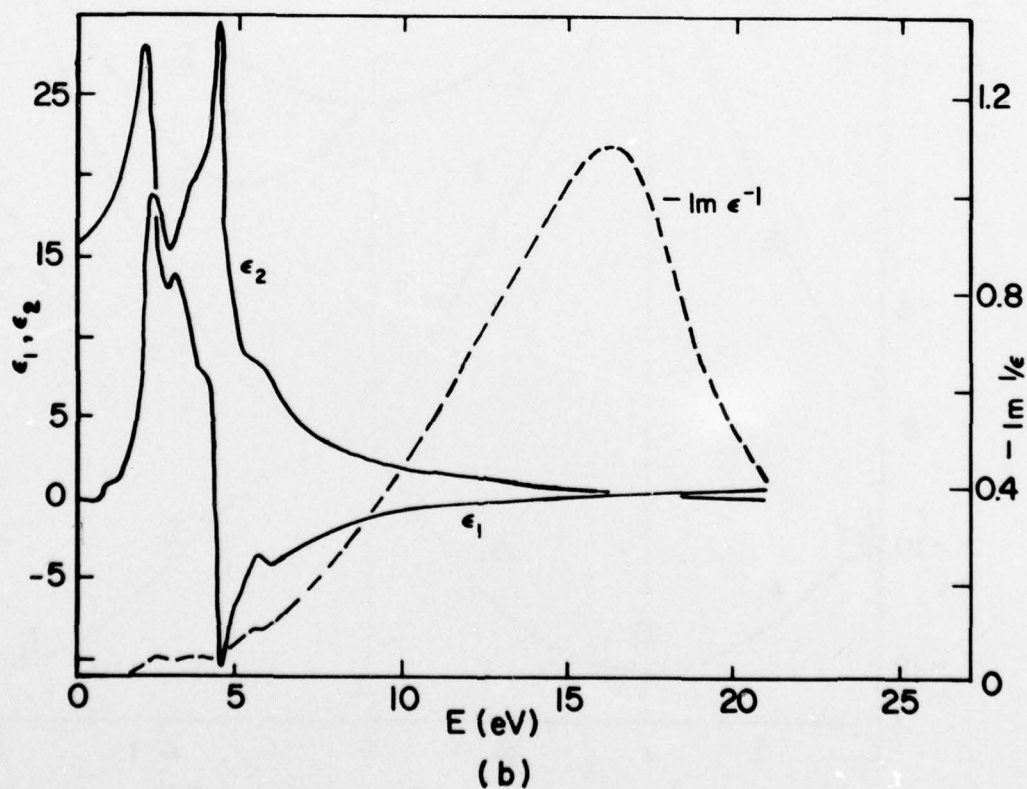
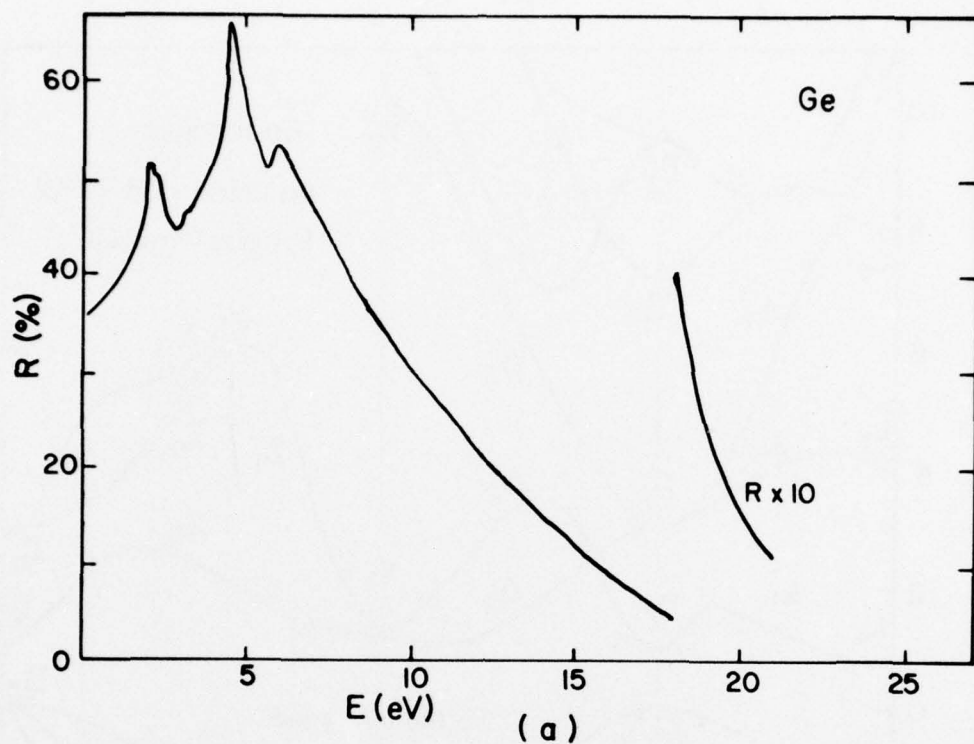


Figure 36 (a) Optical reflectivity for Ge. (b) $\epsilon_1(\omega)$, $\epsilon_2(\omega)$ and energy loss function, $\text{Im } \frac{1}{\epsilon}$, vs. photon energy for Ge (from reference 62).

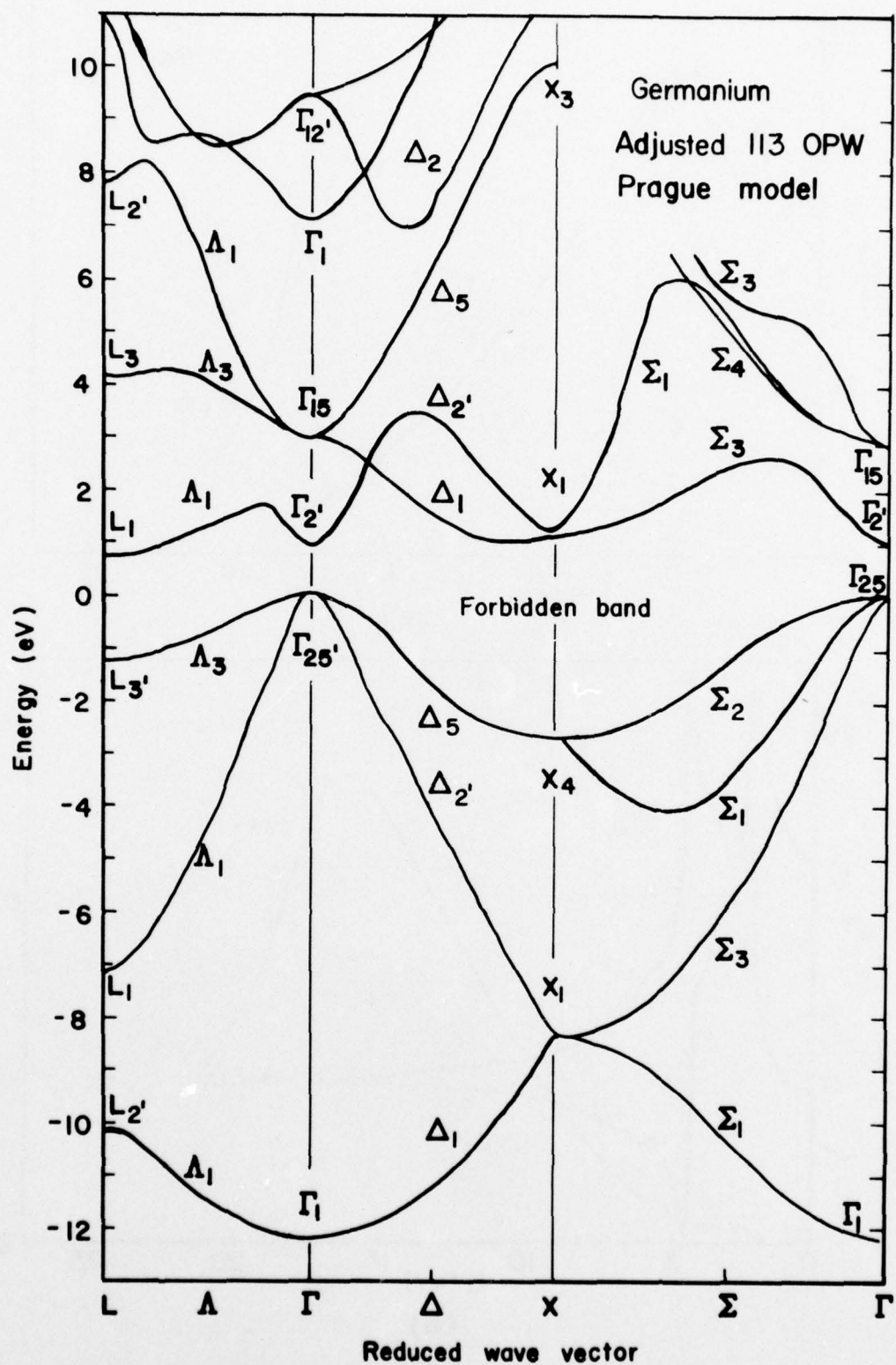


Figure 37 Calculated electron energy bands (from ref. 63)

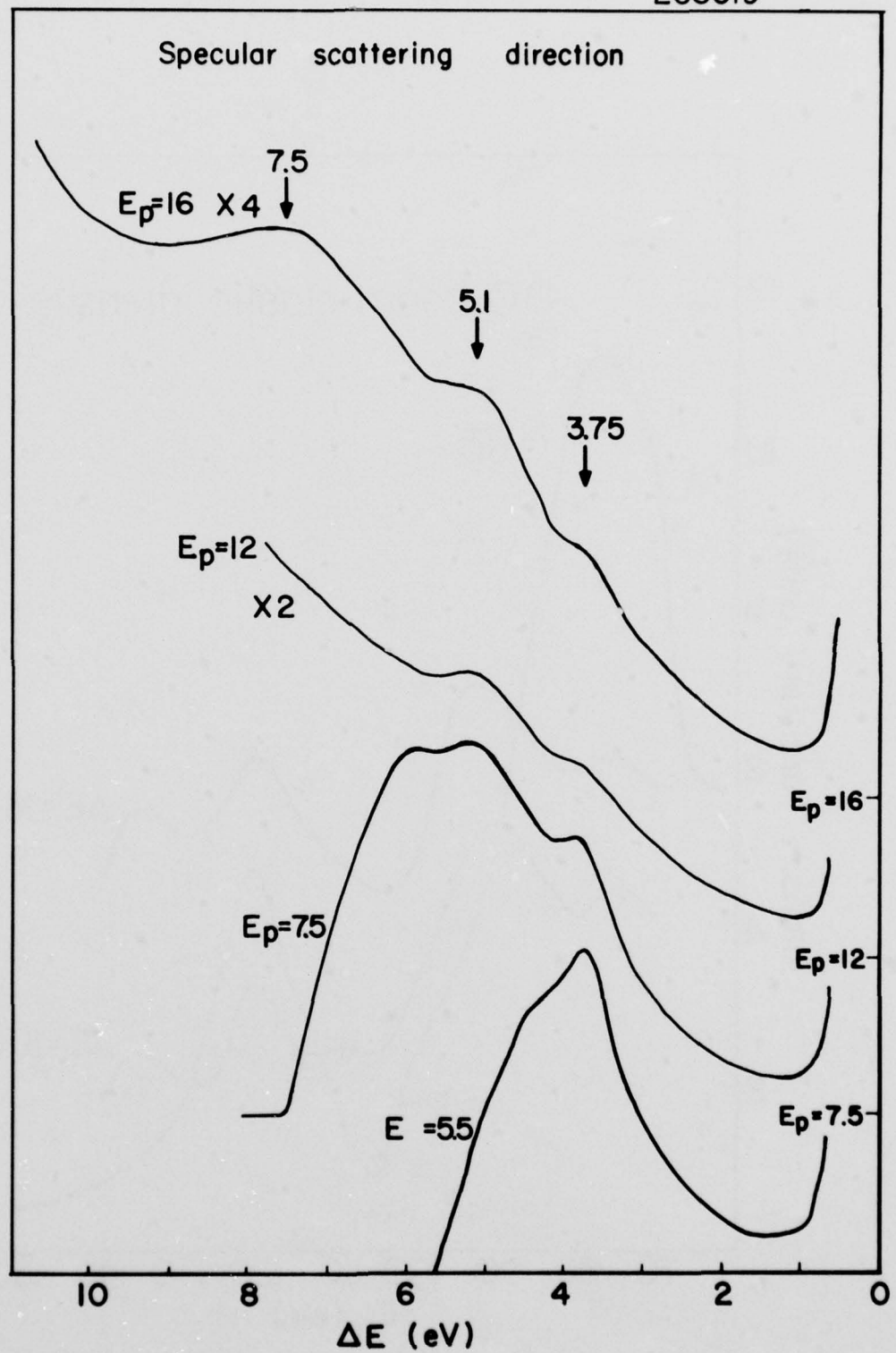


Figure 38 Characteristic loss spectra from oxidized Ge surface

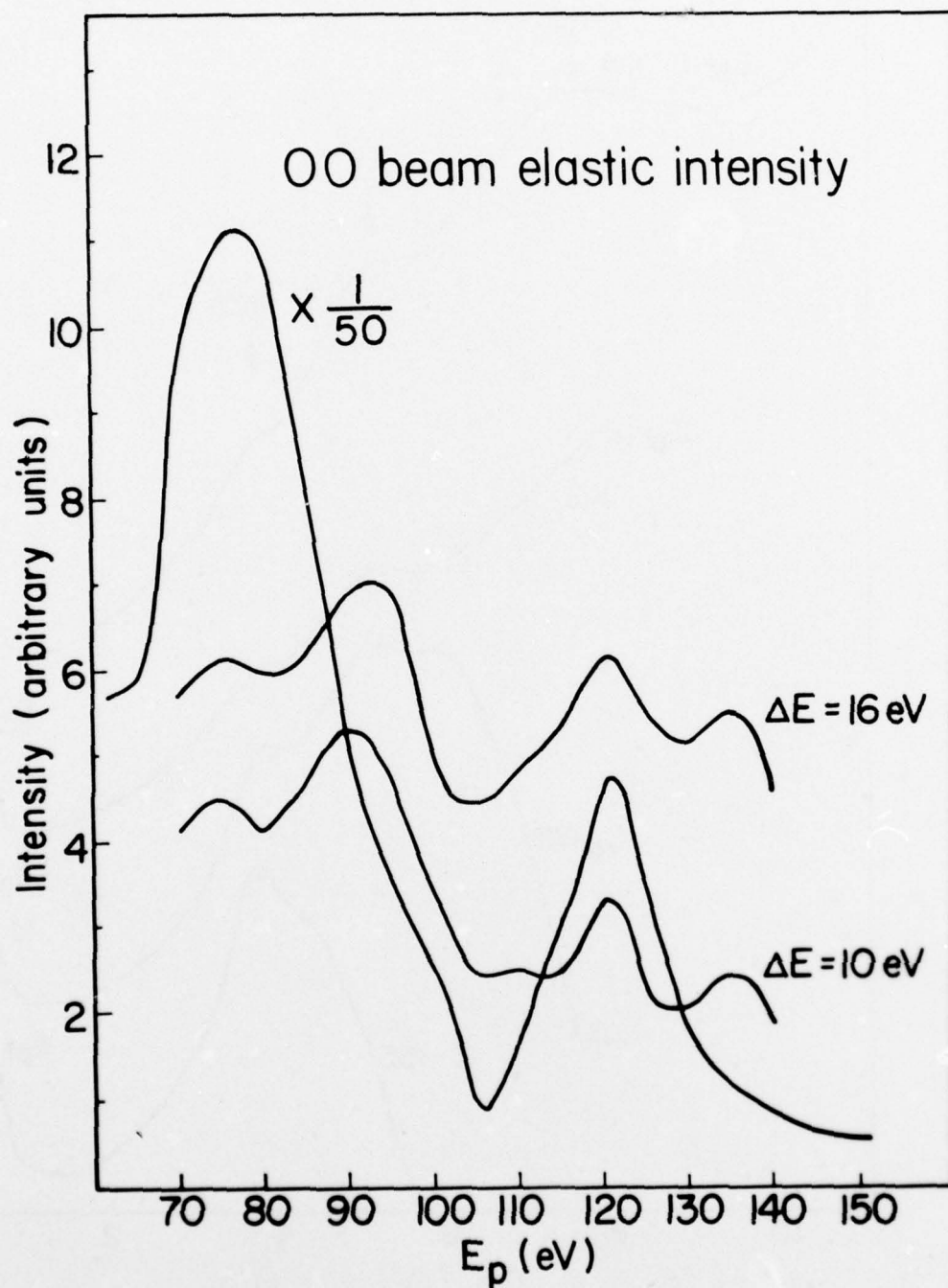


Figure 39 Elastic and inelastic intensity plots in specular scattering direction

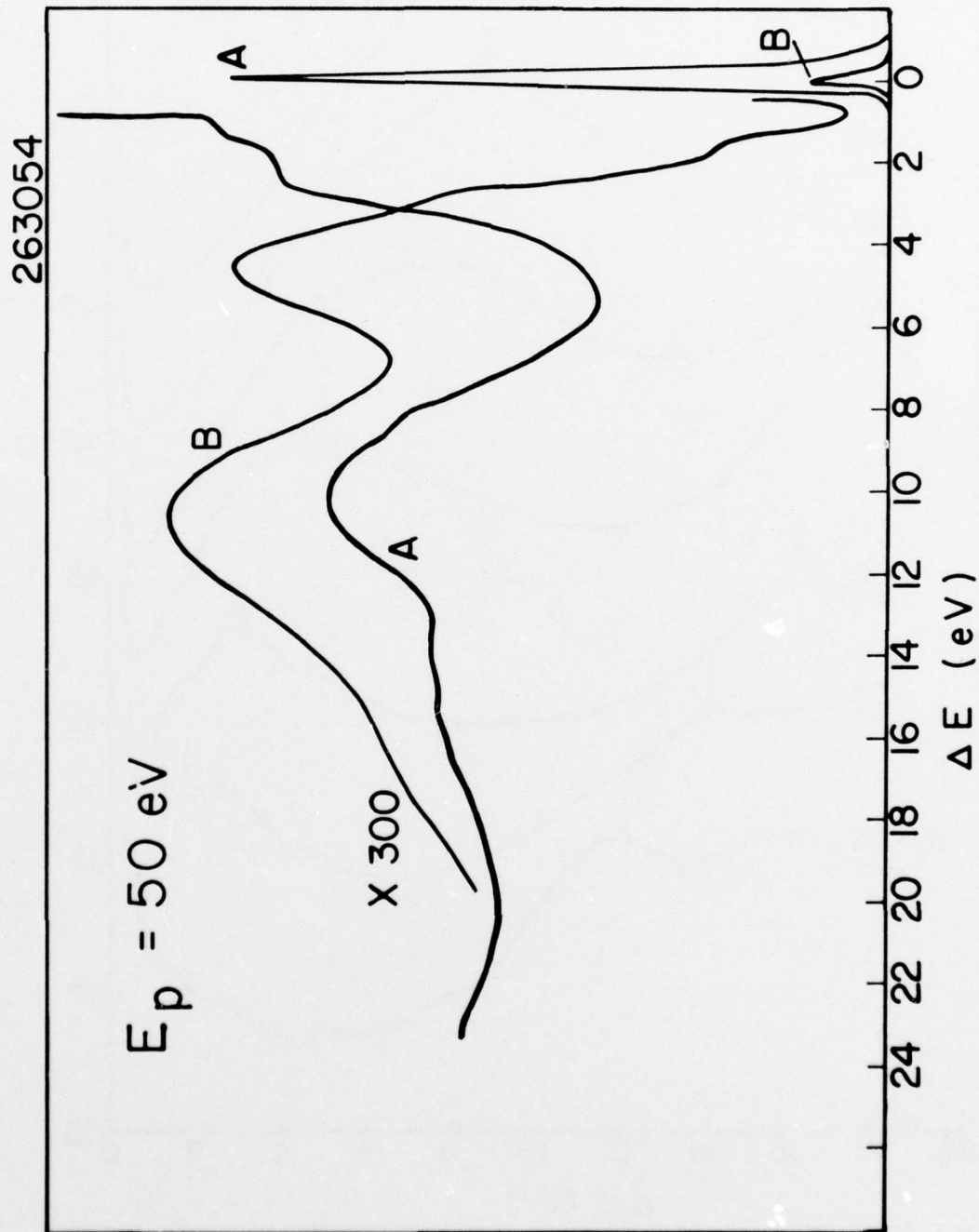


Figure 40 Characteristic loss spectra for (11) beam direction (curve A) and 2° off of (11) beam curve (B)

263042

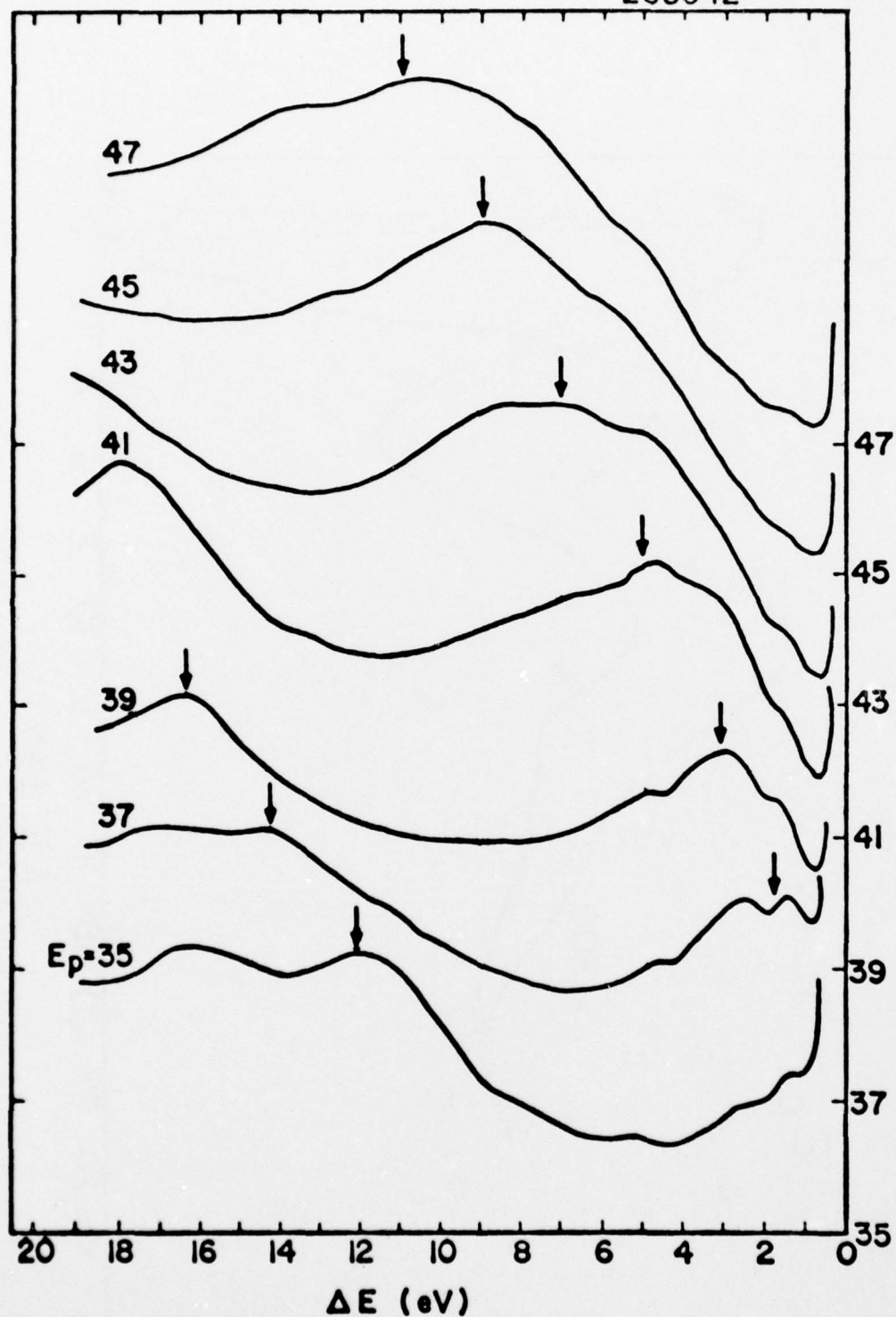


Figure 41 Characteristic loss spectra vs. E_p for scattering direction of (01) LEED beam at $E_p^p = 36$ eV

268034

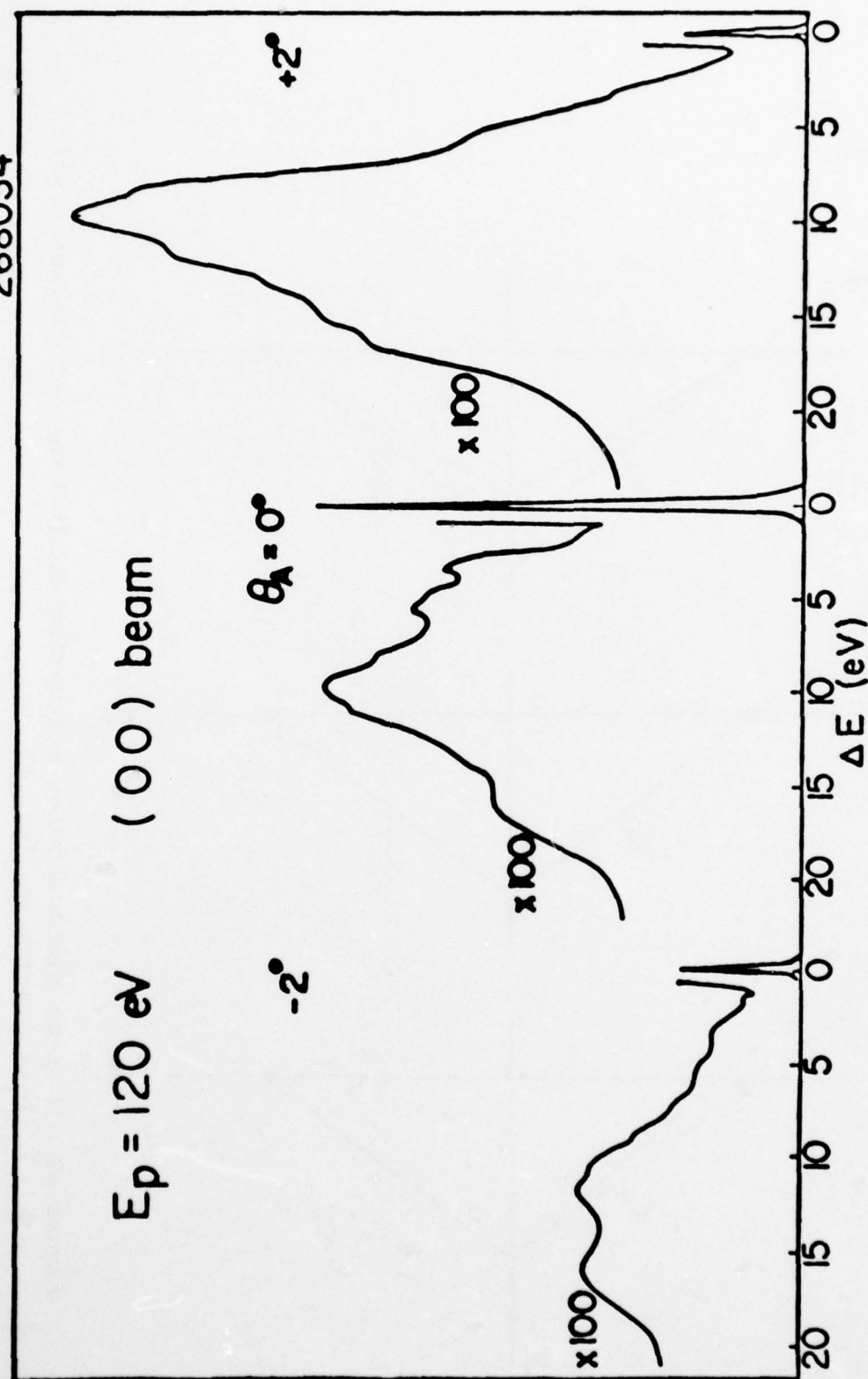


Figure 42 Characteristic loss spectra measured in (00) LEED beam direction and 2° either side in plane of incidence for $E_p = 120$ eV

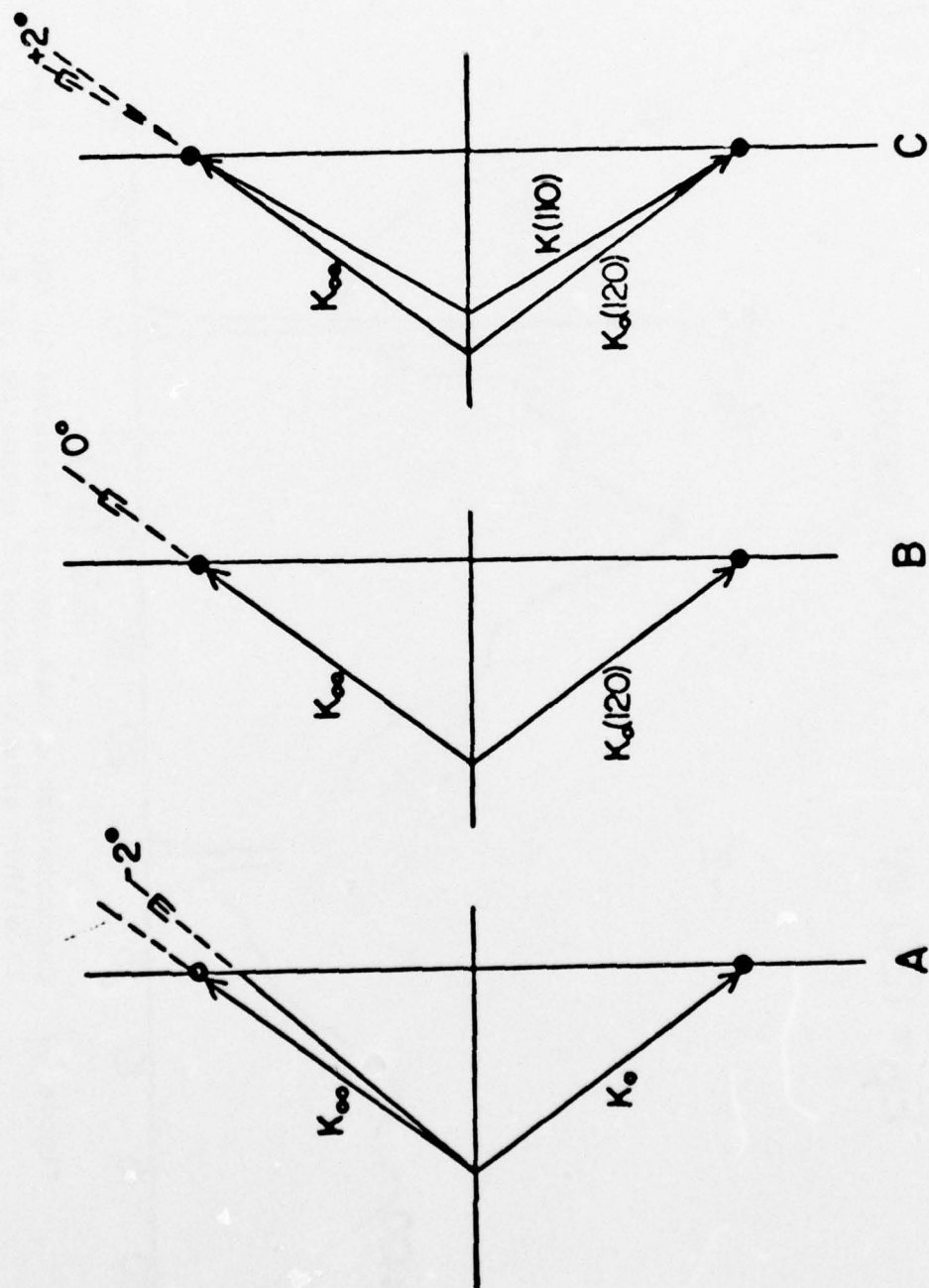


Figure 43. K-space plots showing scattering conditions for characteristic loss spectra of fig. 42

268034

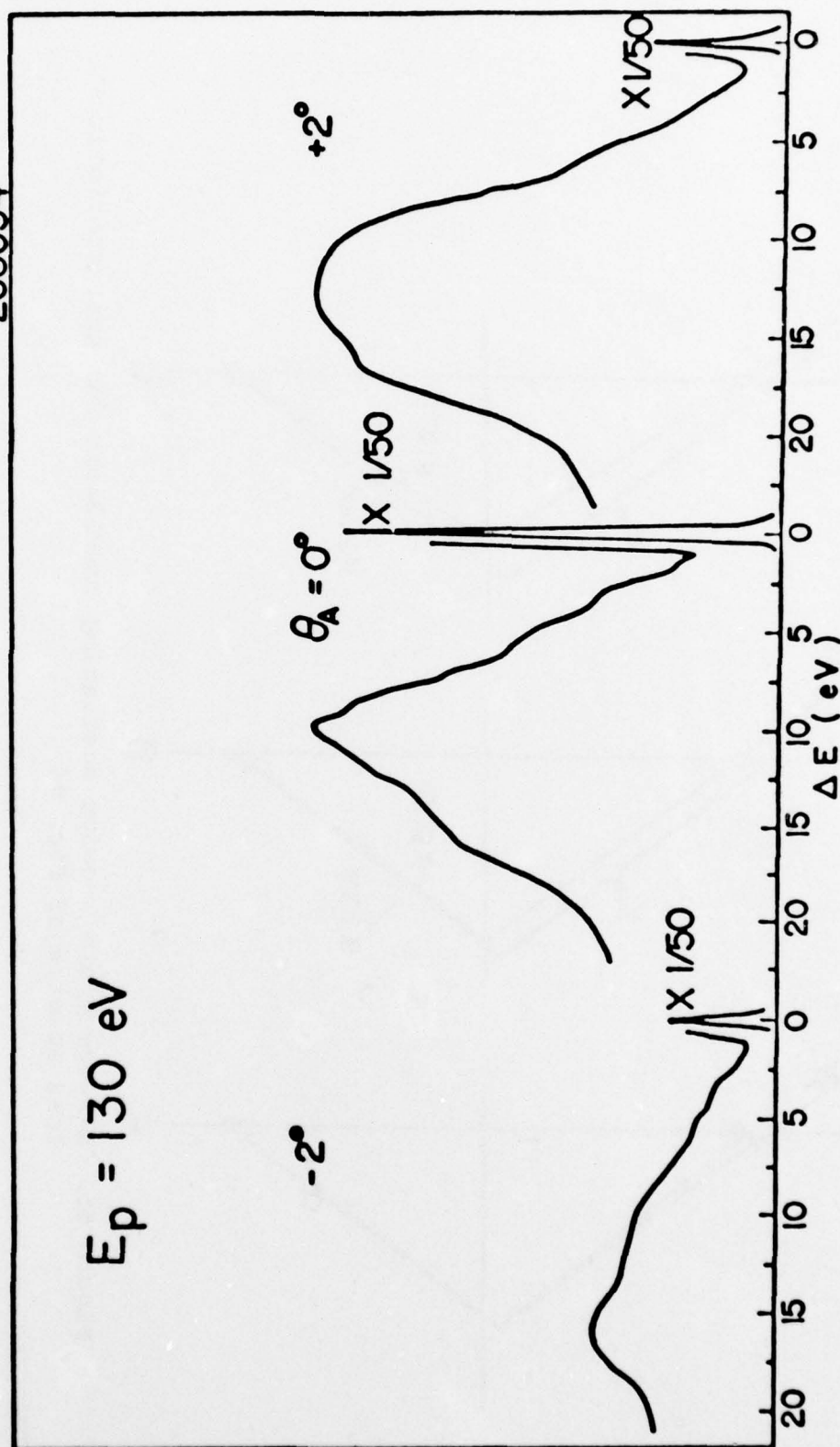


Figure 44 Characteristic loss spectra measured in (00) LEED beam direction and 2° either side in plane of incidence for $E_p = 130$ eV

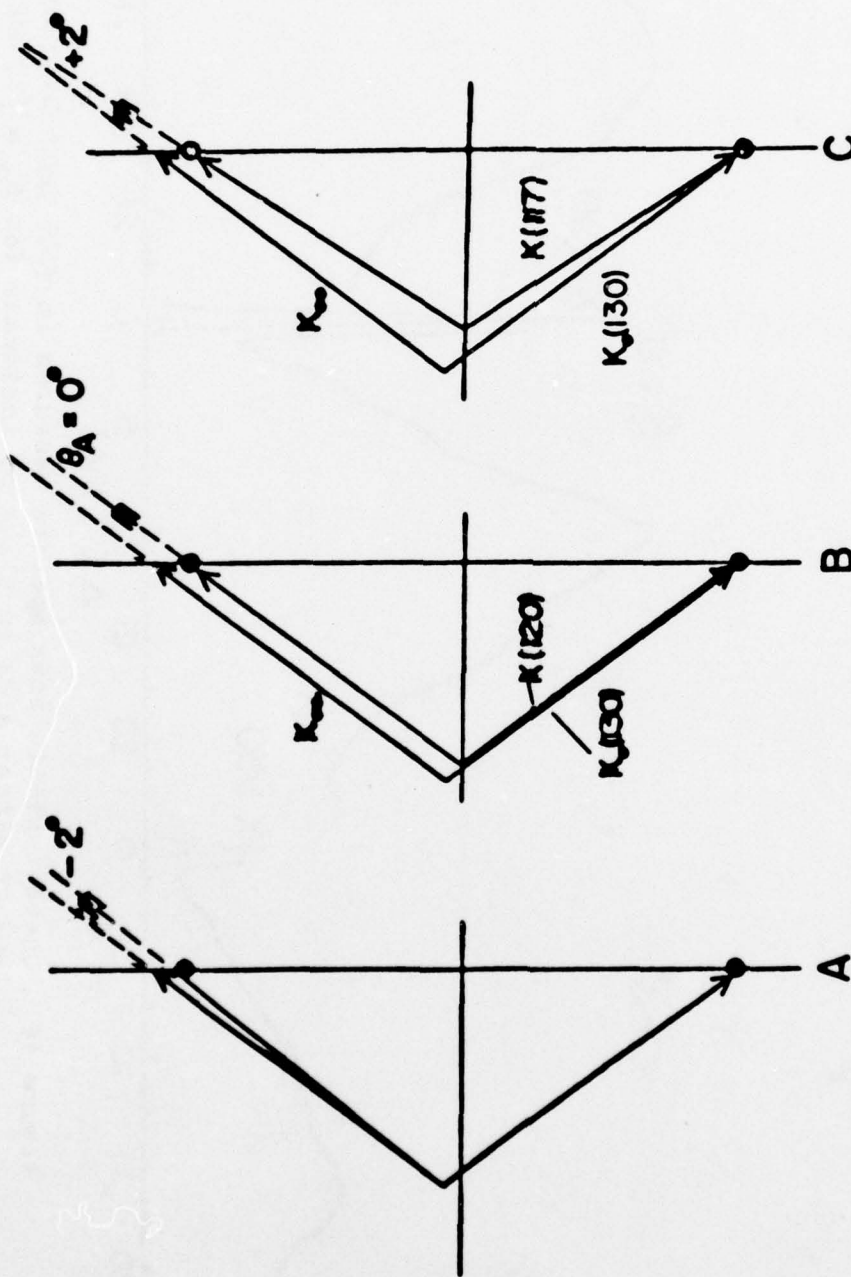


Figure 45 K-space plots showing scattering conditions for characteristic loss spectra of fig. 44

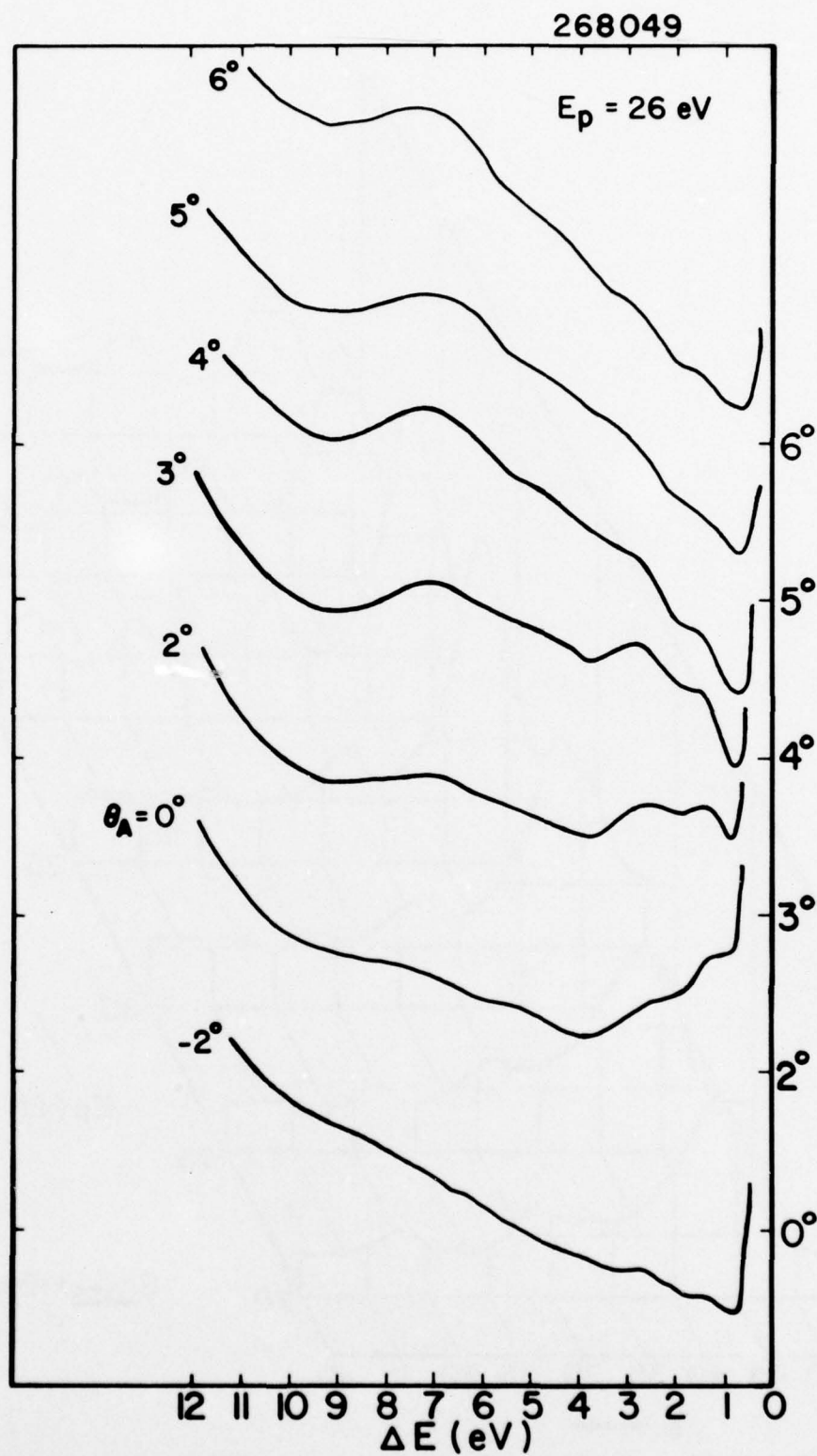


Figure 46 Characteristic loss spectra vs. scattering angle in plane of incidence about (00) diffraction

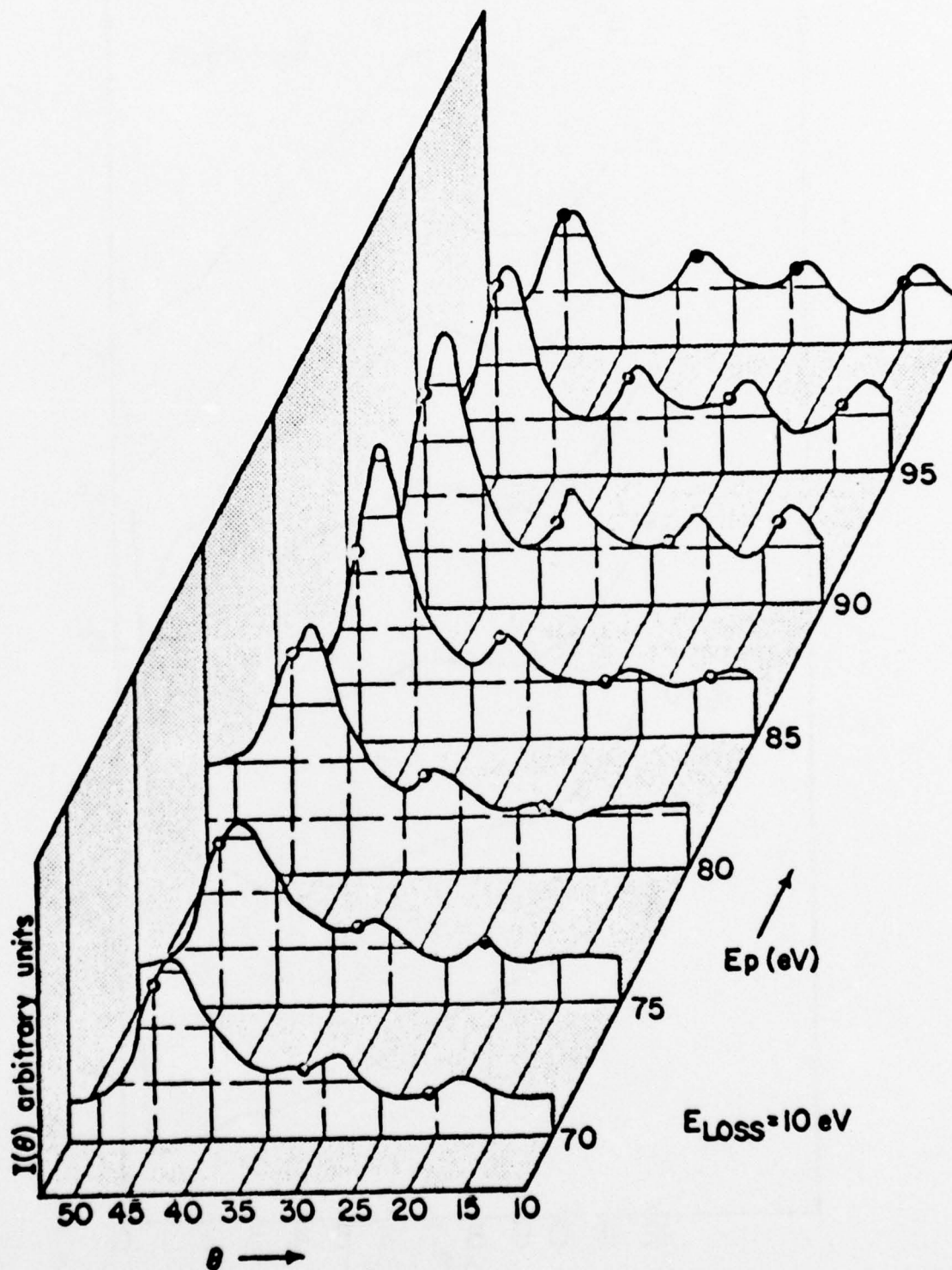


Figure 47 Inelastic angular intensity distributions in plane of incidence for $E_{\text{Loss}} = 10 \text{ eV}$ and $E_p = 70\text{-}100 \text{ eV}$

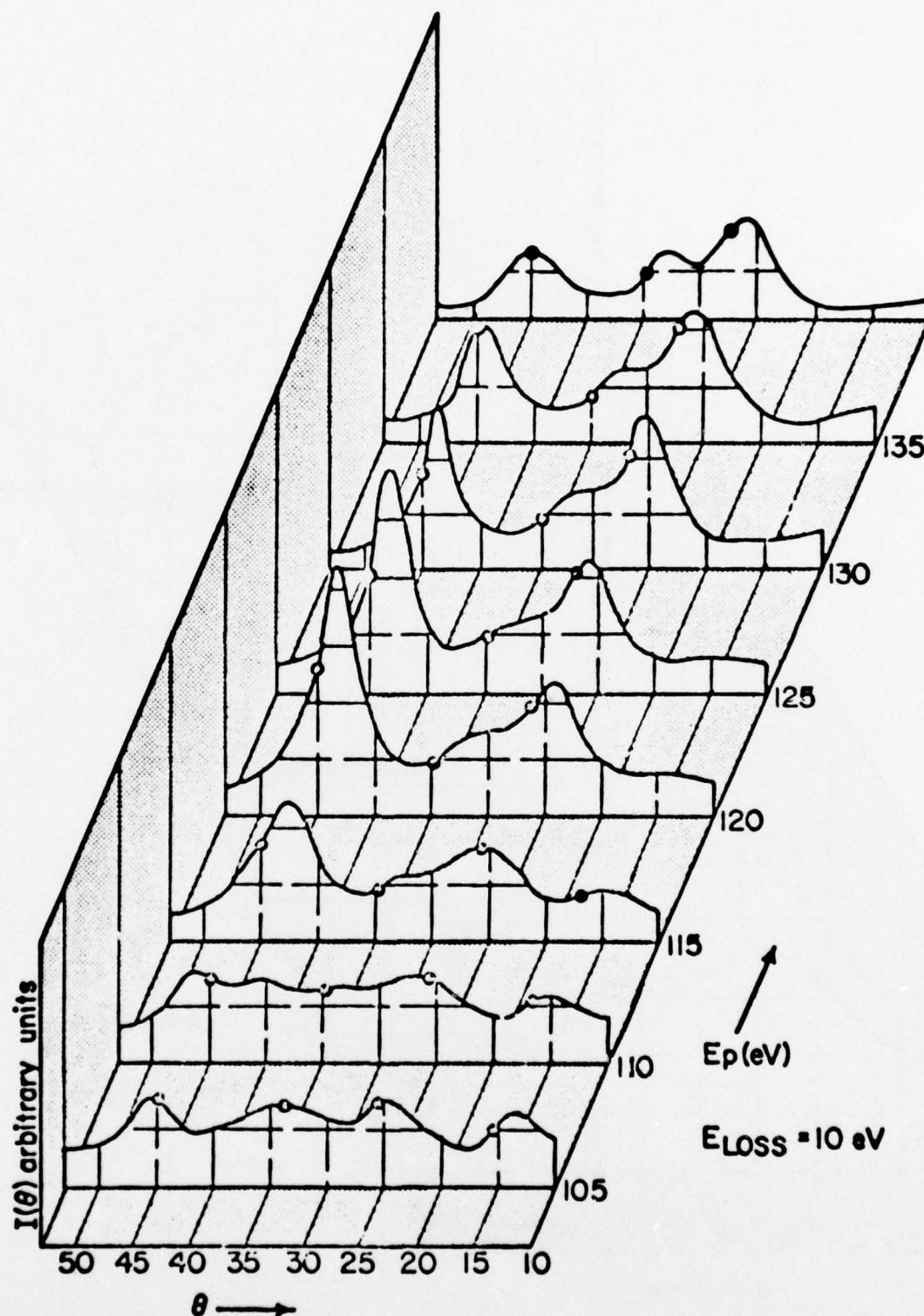


Figure 48 Inelastic angular intensity distributions in plane of incidence for $E_{\text{LOSS}} = 10 \text{ eV}$ and $E_p = 105\text{--}140 \text{ eV}$

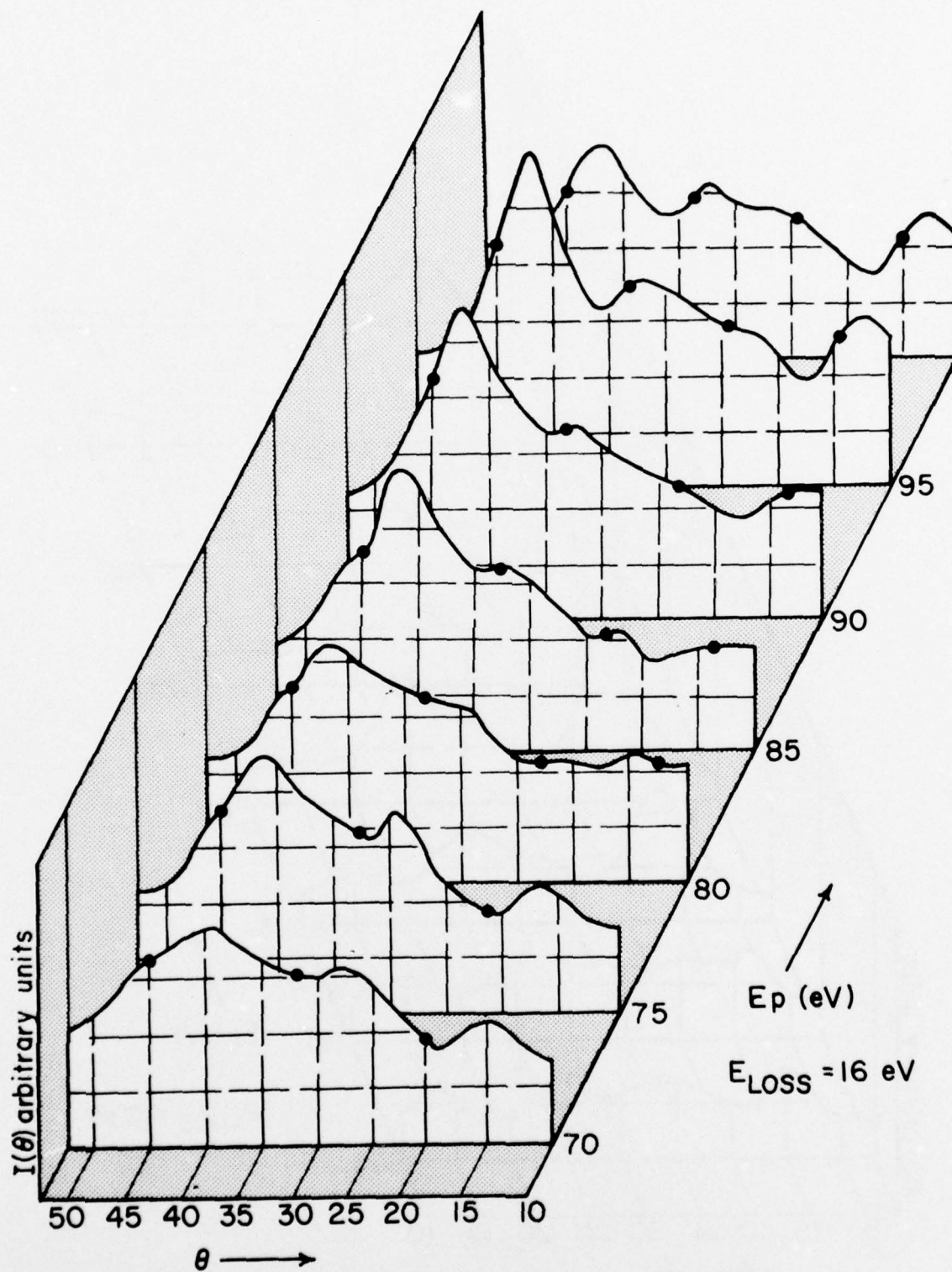


Figure 49 Inelastic angular intensity distributions in plane of incidence for $E_{\text{Loss}} = 16 \text{ eV}$ and $E_p = 70\text{-}100 \text{ eV}$

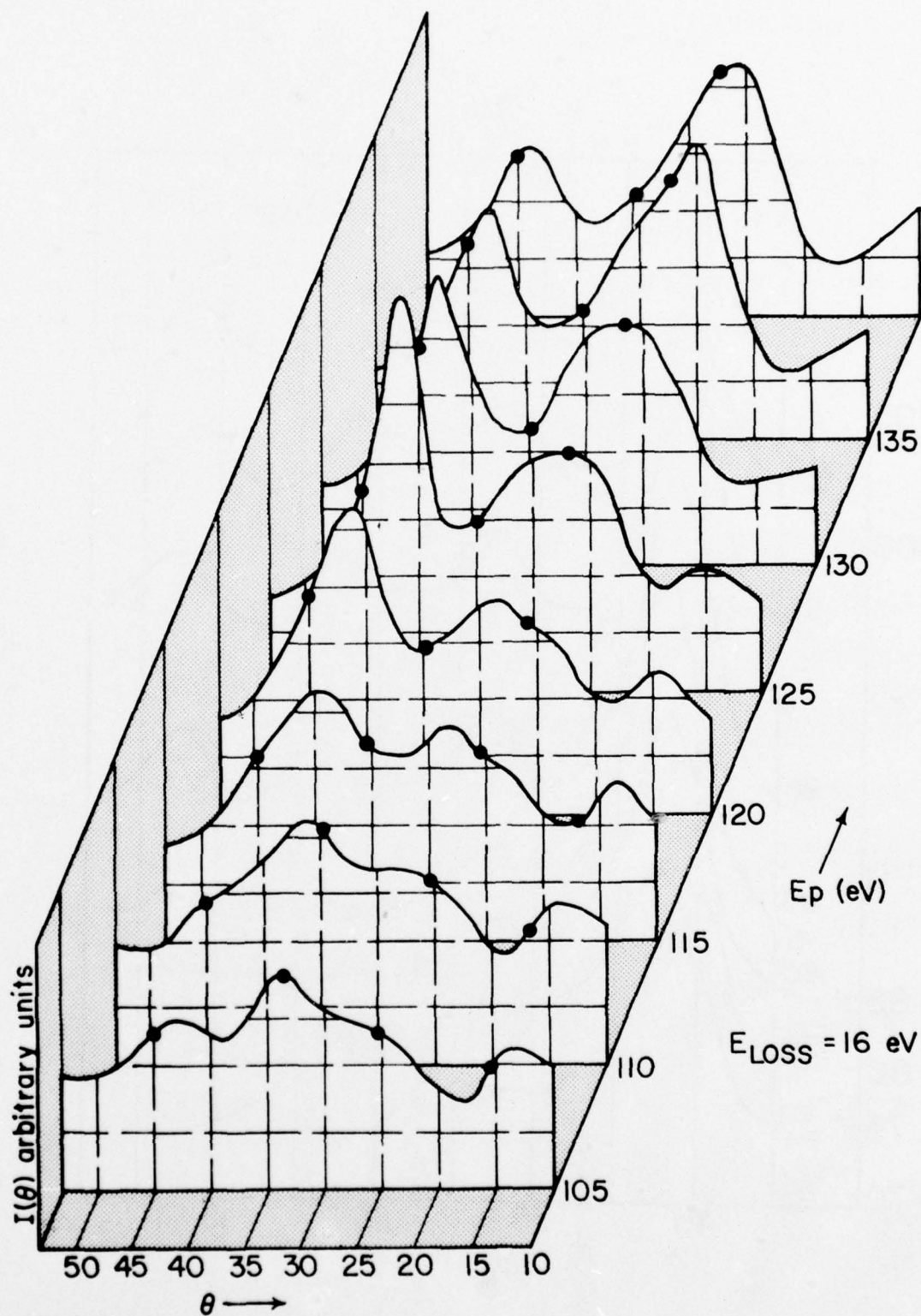


Figure 50 Inelastic angular intensity distributions on plane of incidence for $E_{\text{LOSS}} = 16 \text{ eV}$ and $E_p = 105-140 \text{ eV}$

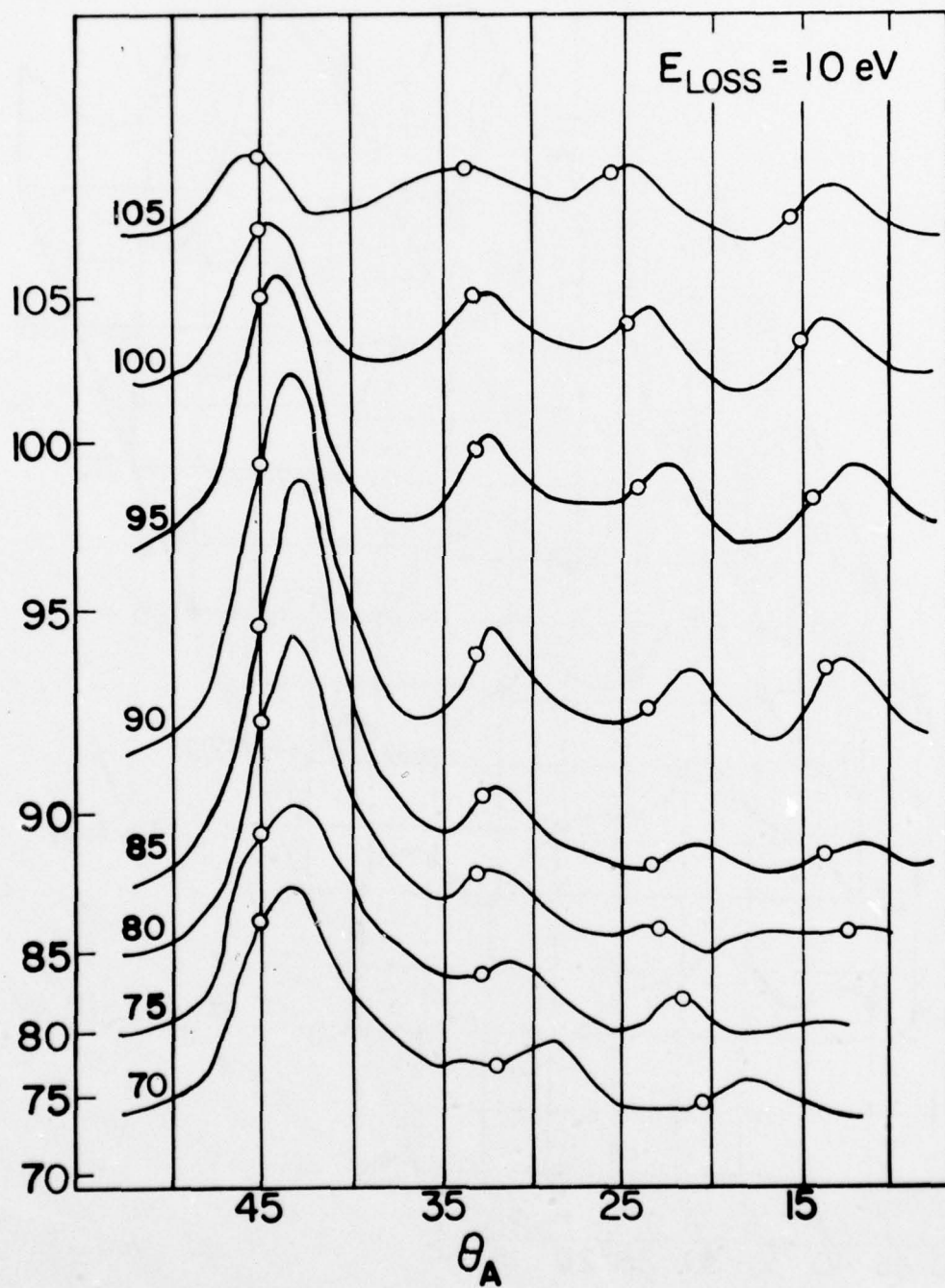


Figure 51 Inelastic angular intensity distribution as function of E_p , for plane of incidence and $E_{\text{loss}} = 10 \text{ eV}$

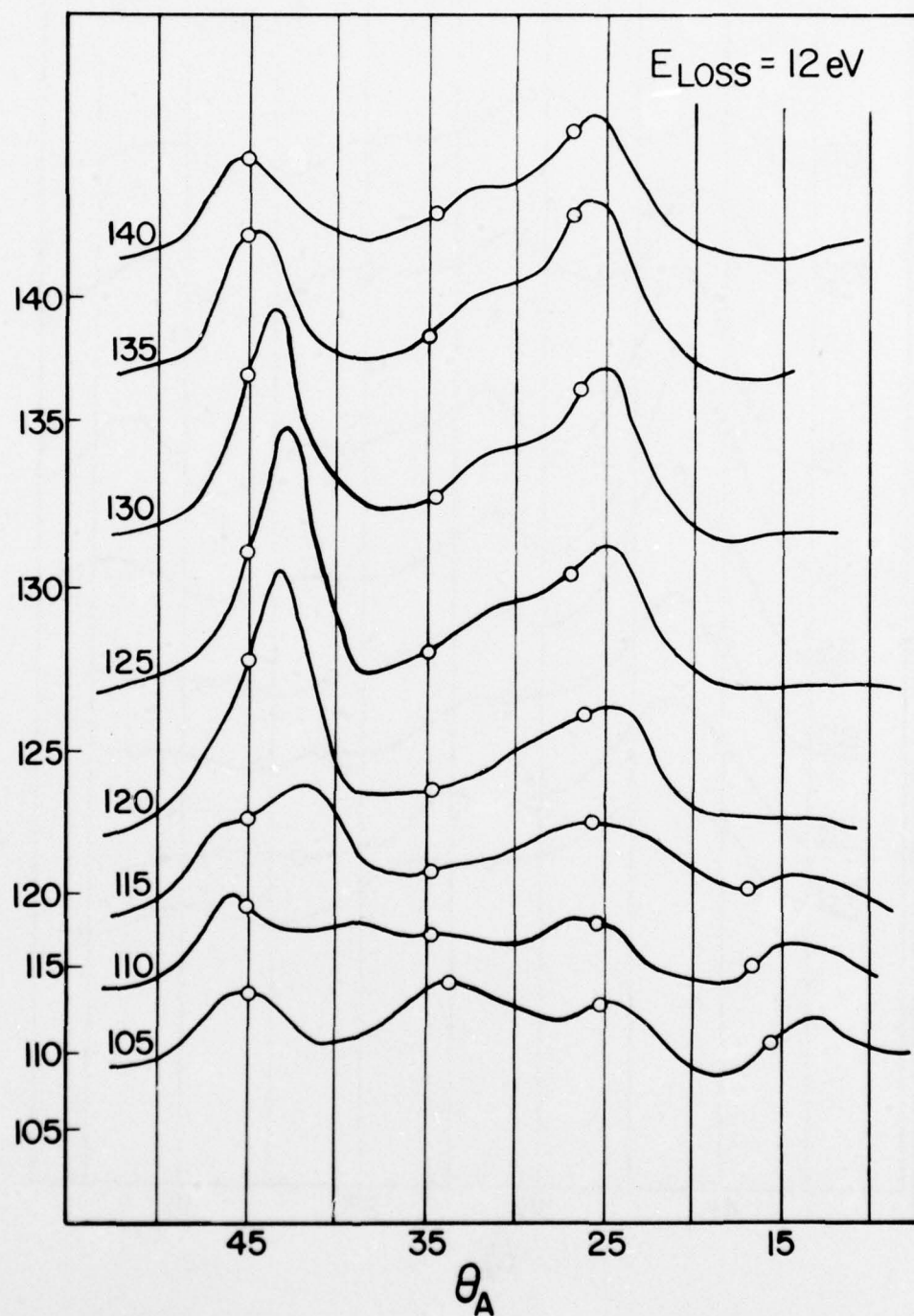


Figure 52 Inelastic angular intensity distributions as function of E_p' , for plane of incidence and $E_{\text{loss}} = 12 \text{ eV}$

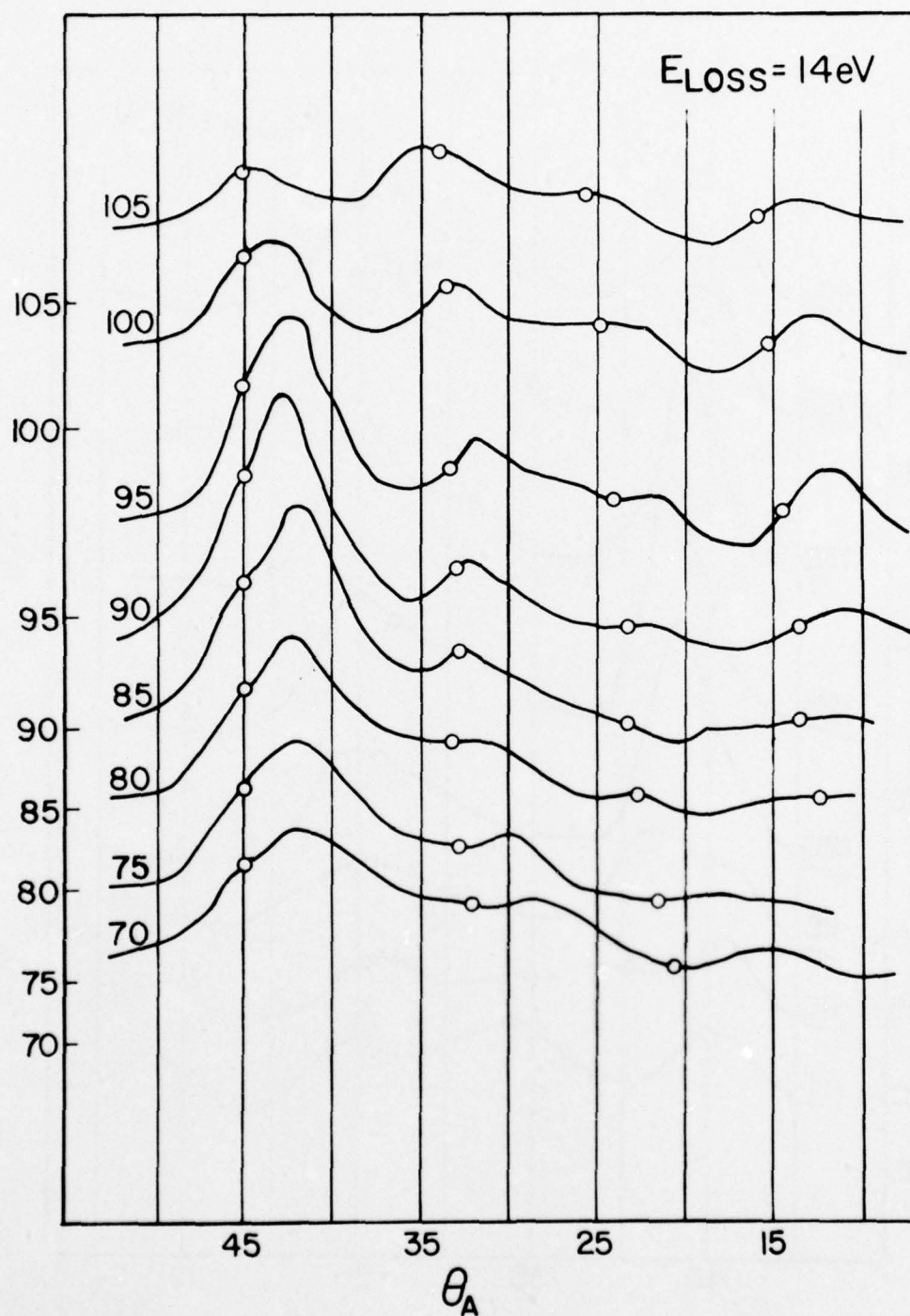


Figure 53 Inelastic angular intensity distributions as function of E_p , for plane of incidence and $E_{\text{loss}} = 14 \text{ eV}$

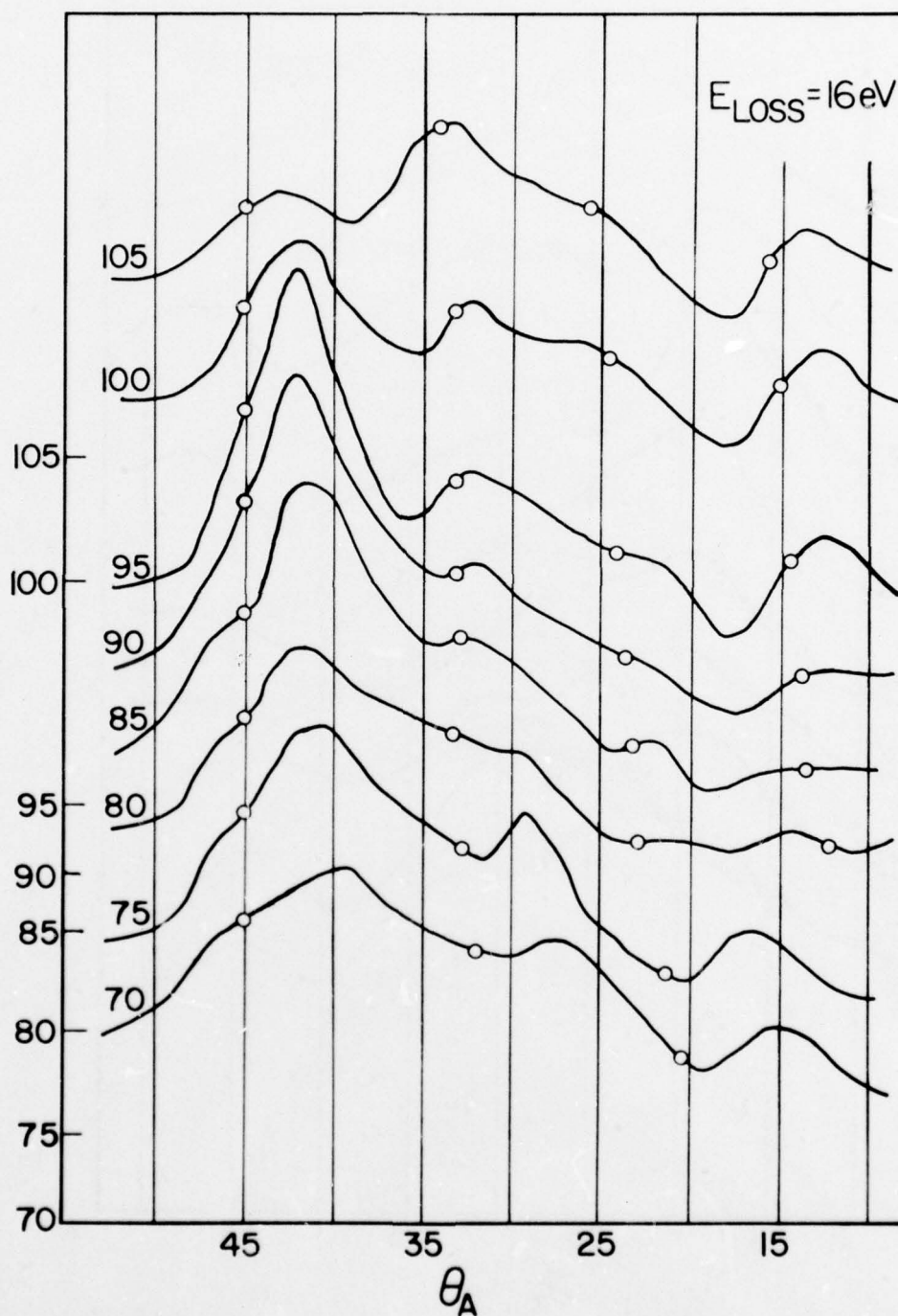


Figure 54 Inelastic angular intensity distributions as function of E_p , for plane of incidence and $E_{\text{loss}} = 16 \text{ eV}$

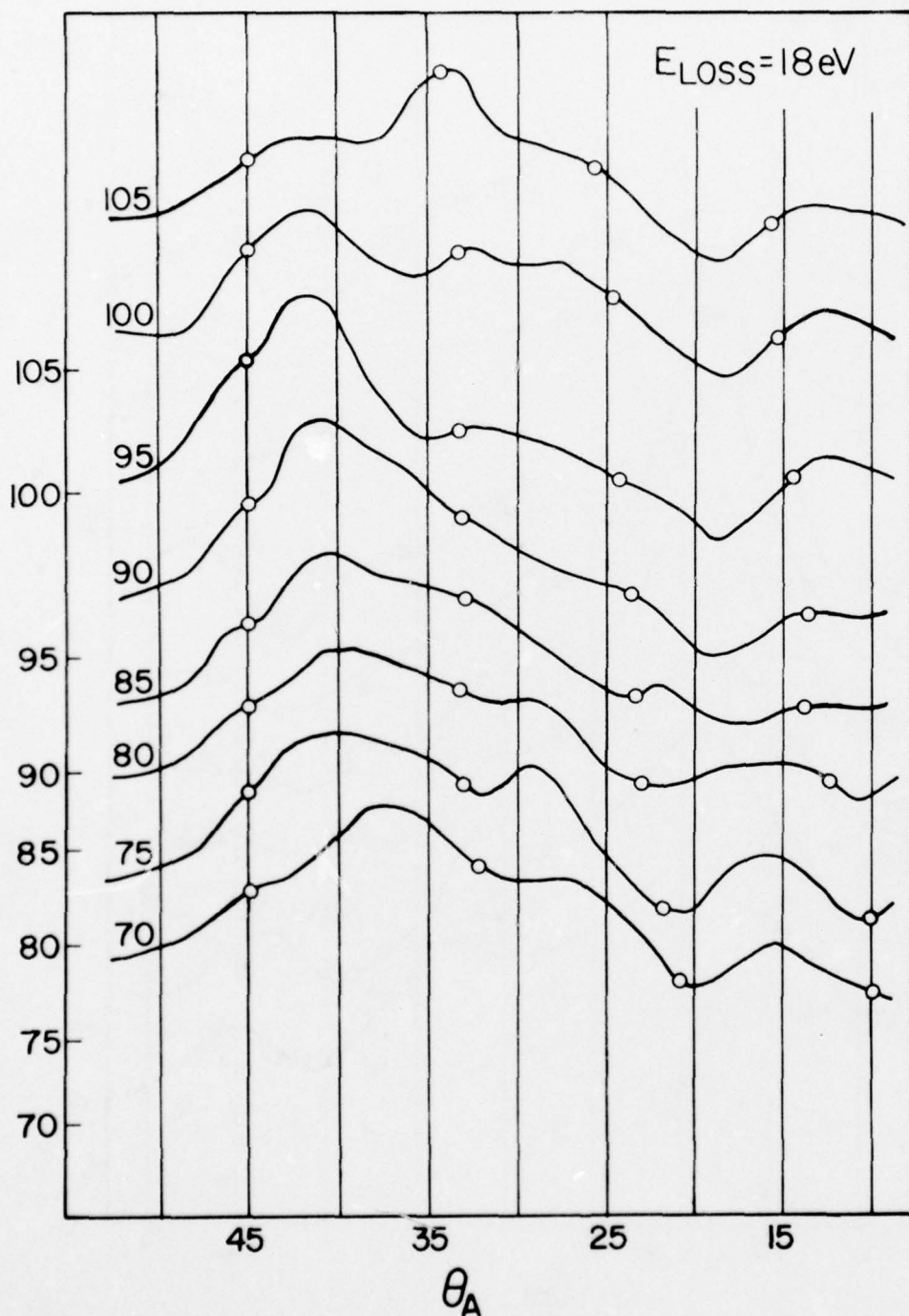


Figure 55 Inelastic angular intensity distributions as function of E_p , for plane of incidence and $E_{\text{loss}} = 18 \text{ eV}$

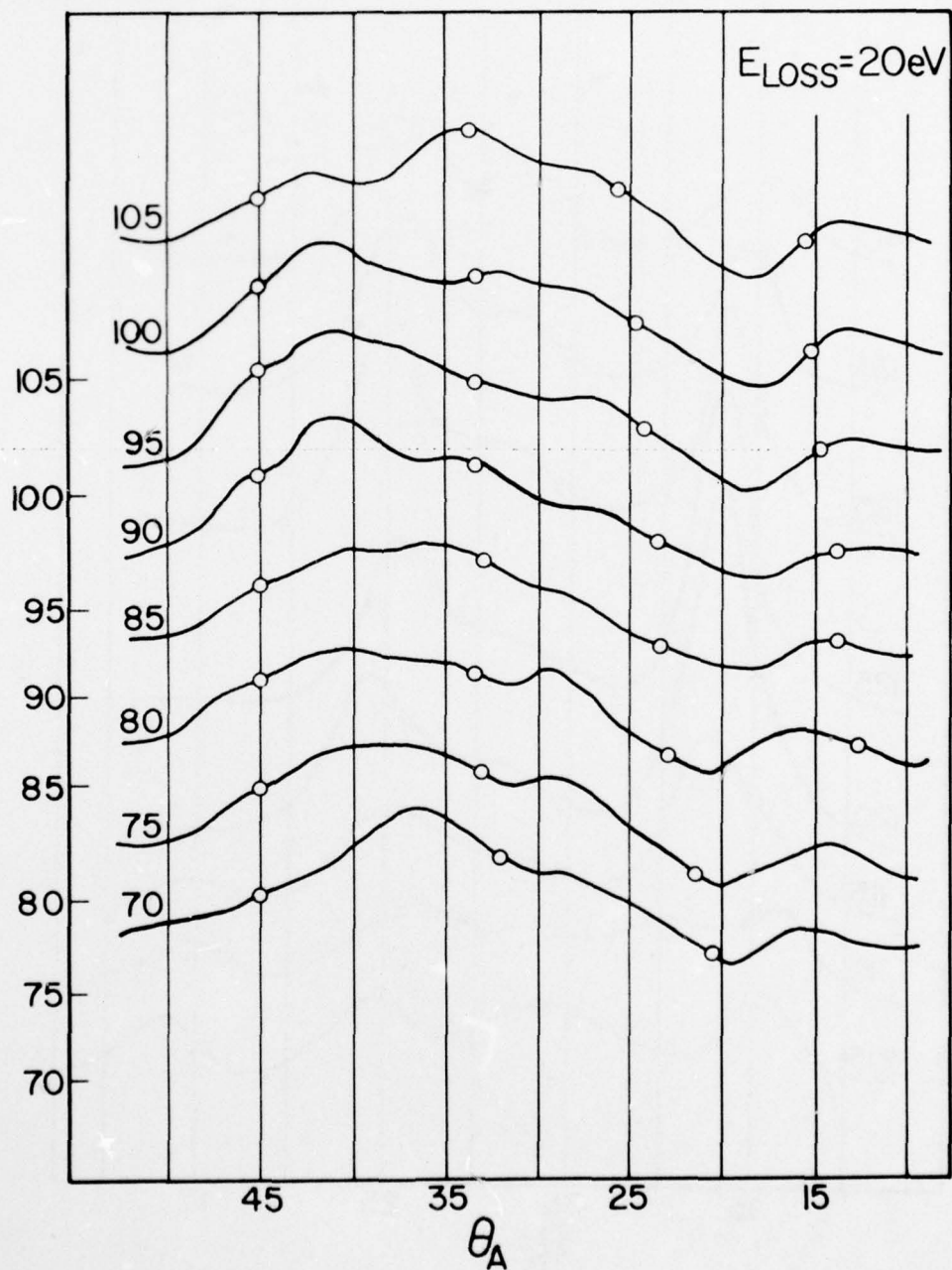


Figure 56 Inelastic angular intensity distribution as function of E_p , for plane of incidence and $E_{\text{loss}} = 20 \text{ eV}$

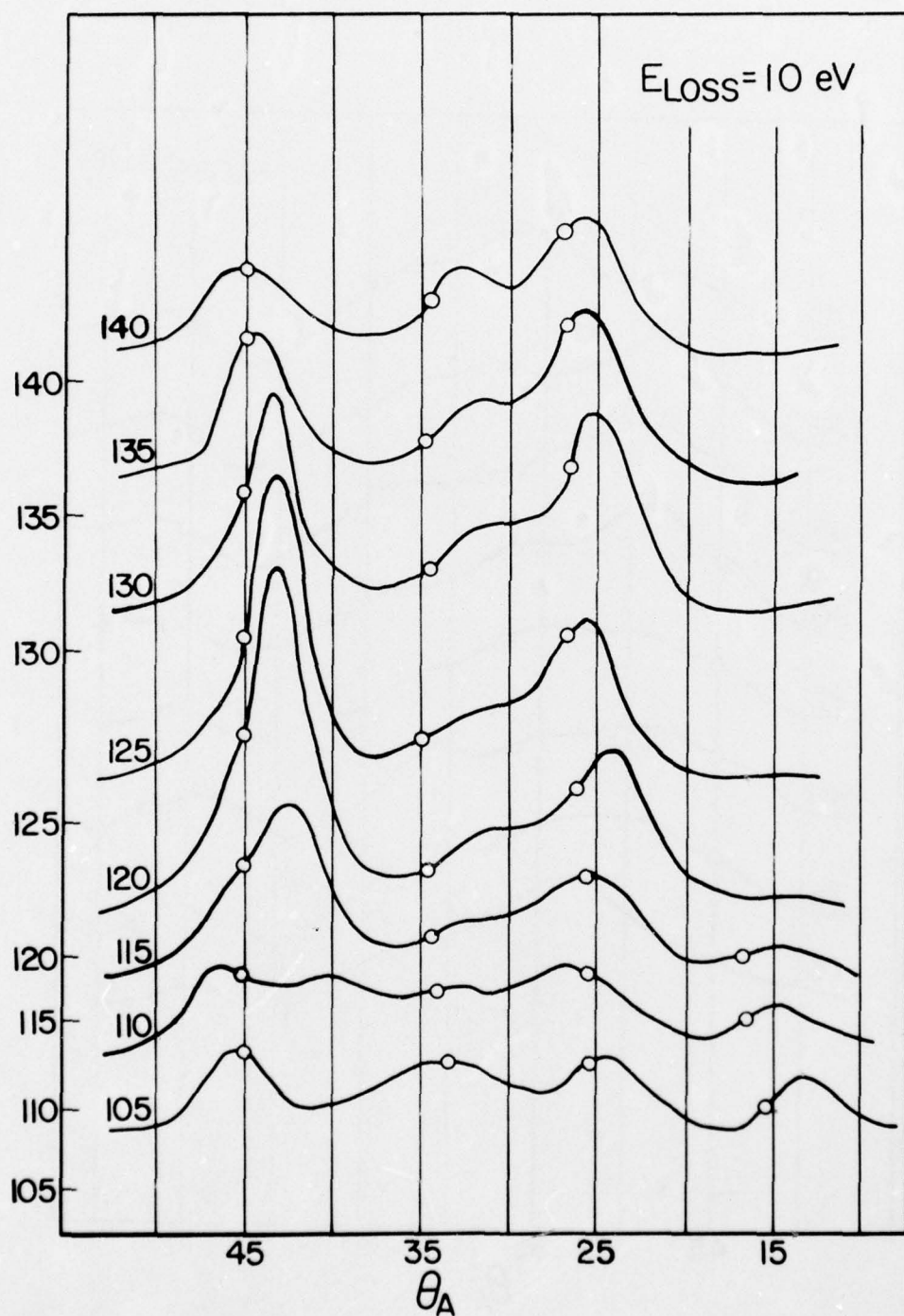


Figure 57 Inelastic angular intensity distributions as function of E_p , for plane of incidence and $E_{\text{loss}} = 10 \text{ eV}$

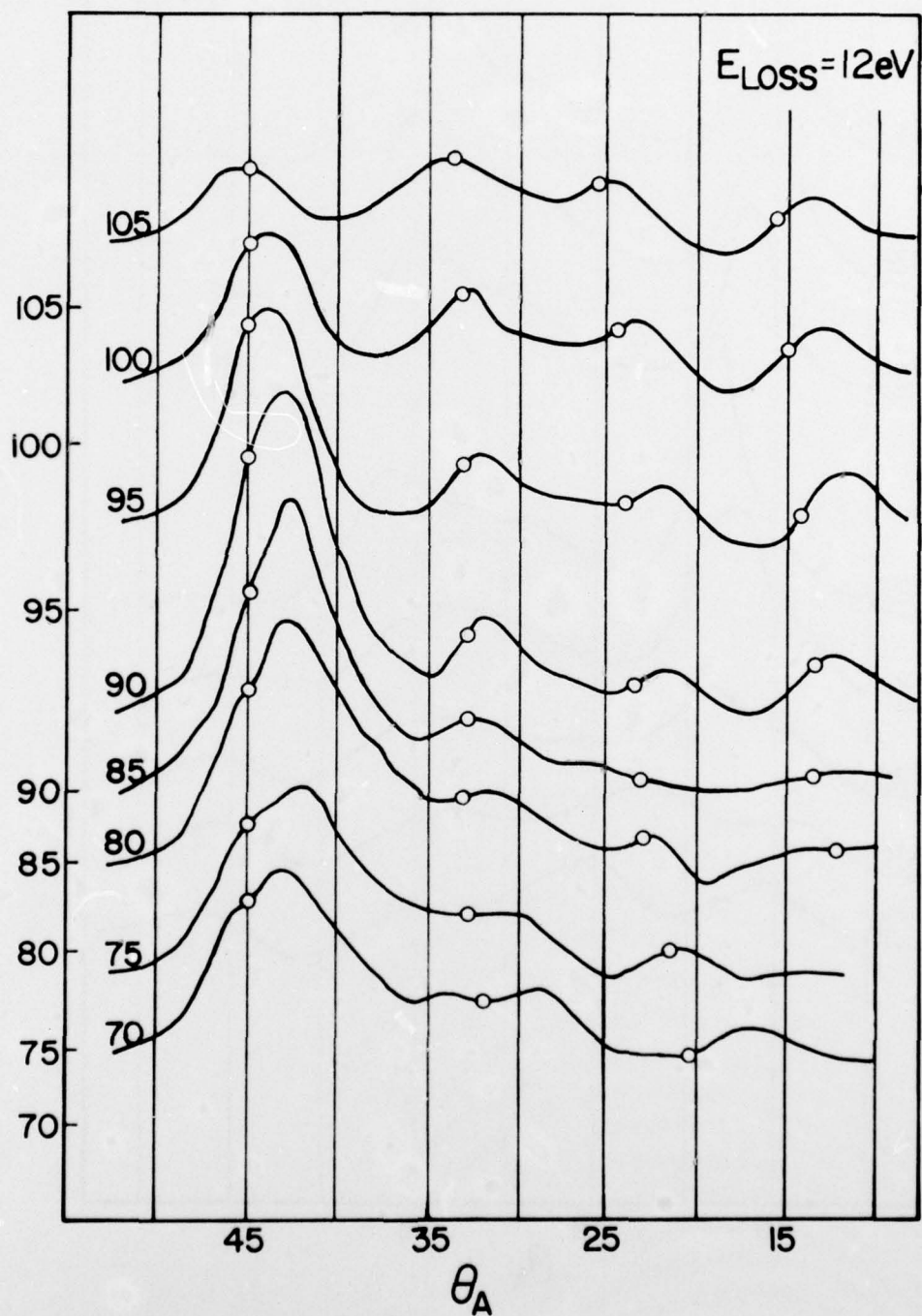


Figure 58 Inelastic angular intensity distributions as function of E_p , for plane of incidence and $E_{\text{loss}} = 12 \text{ eV}$

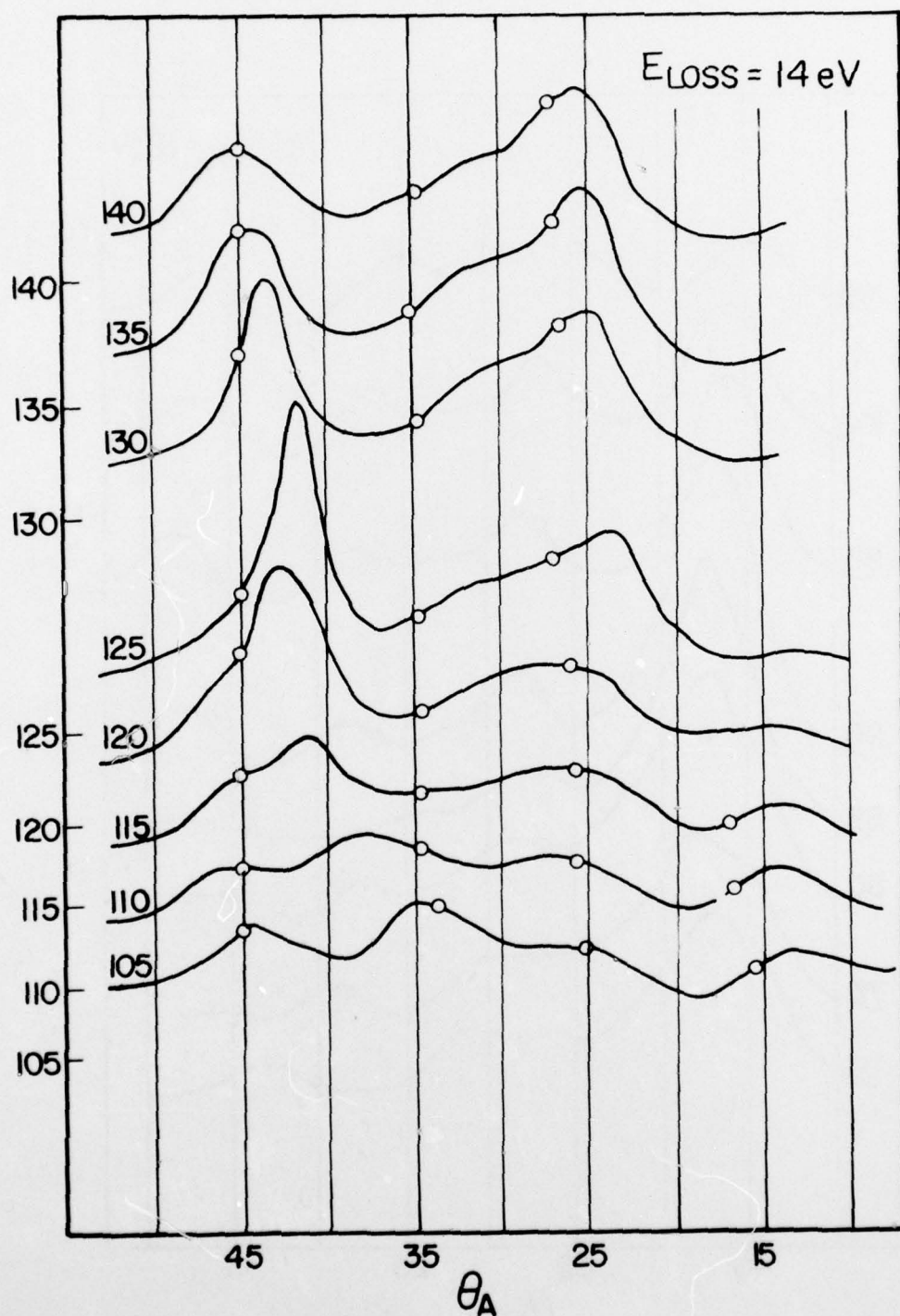


Figure 59 Inelastic angular intensity distributions as function of E_p , for plane of incidence and $E_{\text{loss}} = 14 \text{ eV}$

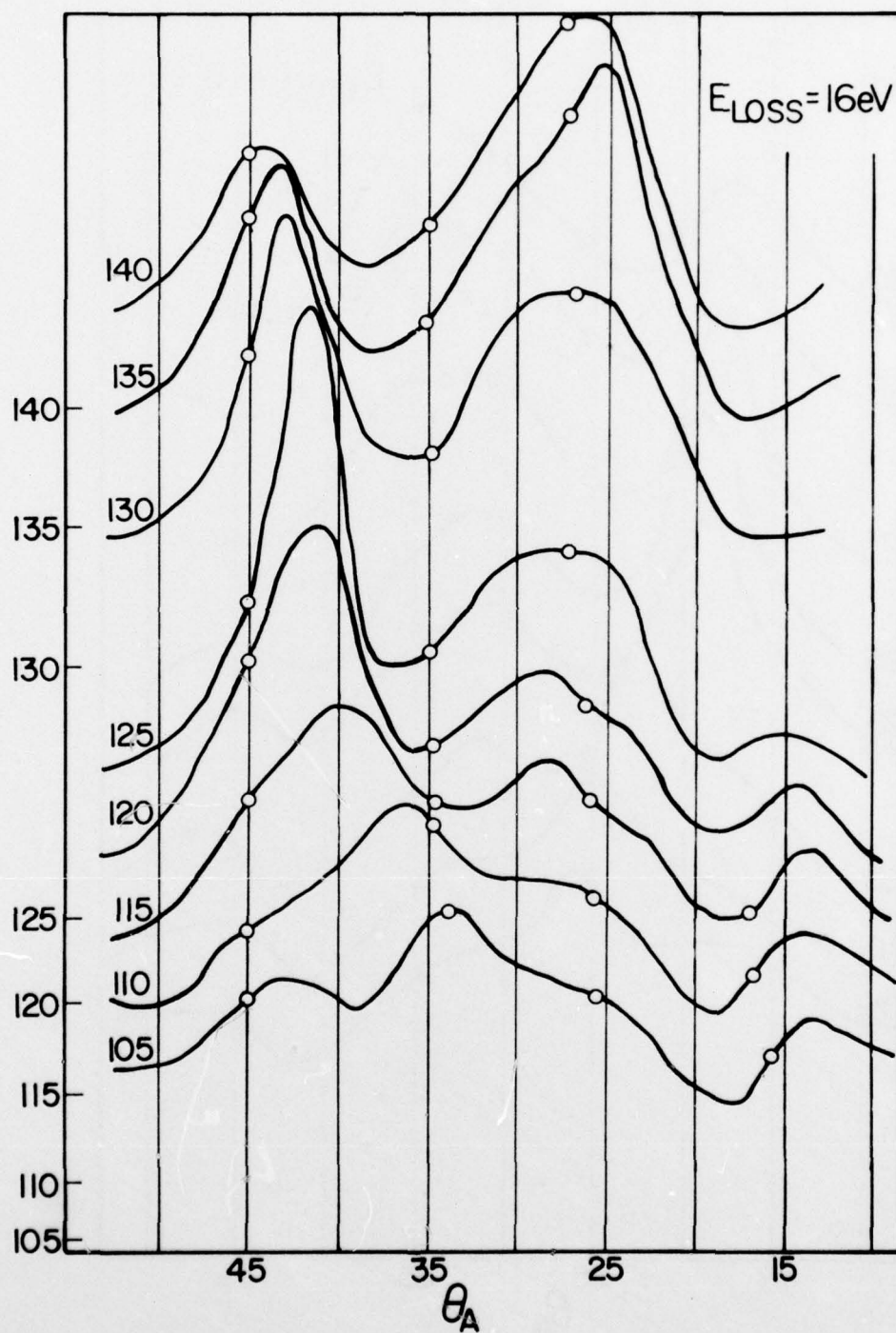


Figure 60 Inelastic angular intensity distributions as function of E_p , for plane of incidence and $E_{\text{loss}} = 16 \text{ eV}$

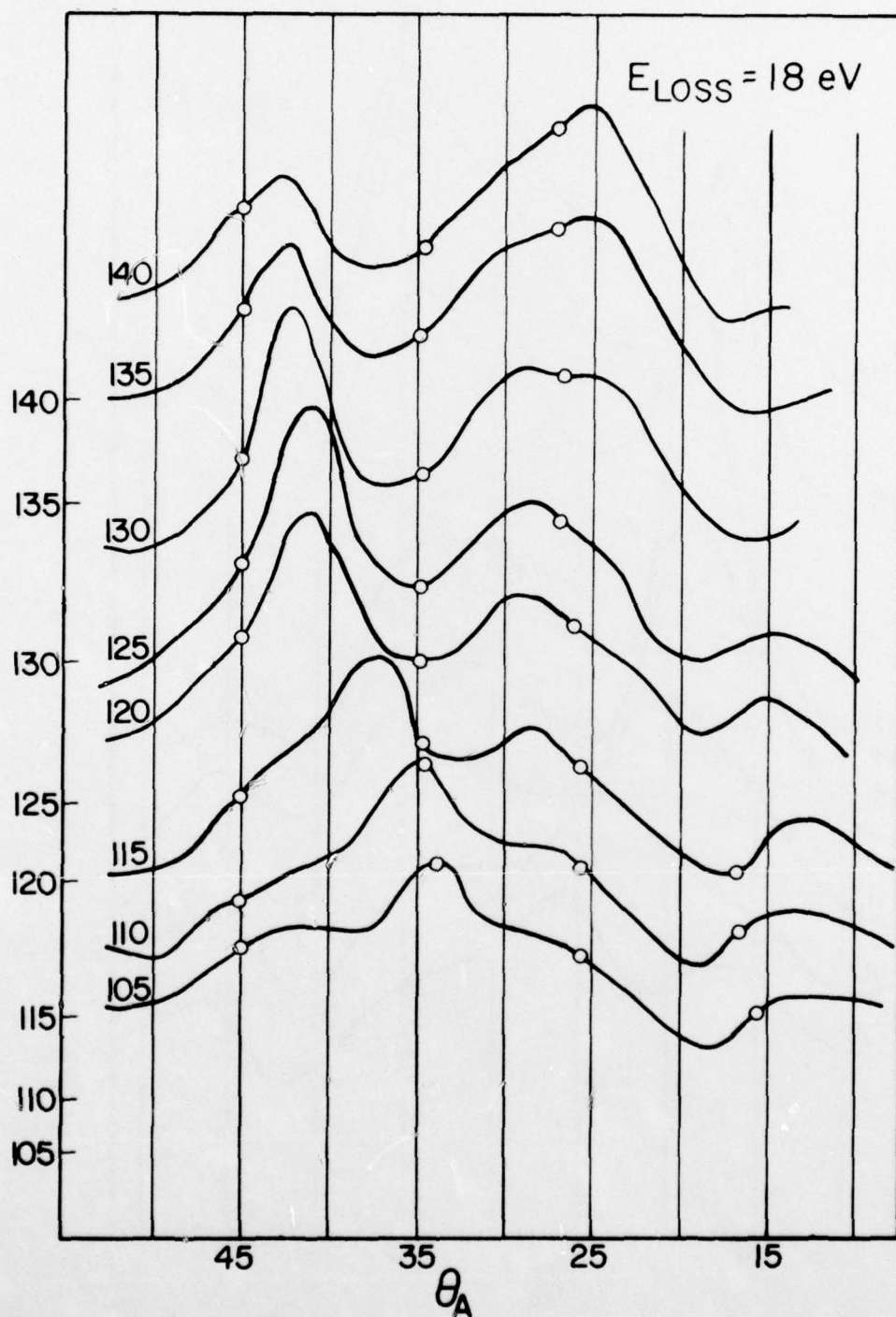


Figure 61 Inelastic angular intensity distributions as function of E_p , for plane of incidence and $E_{\text{loss}} = 18 \text{ eV}$

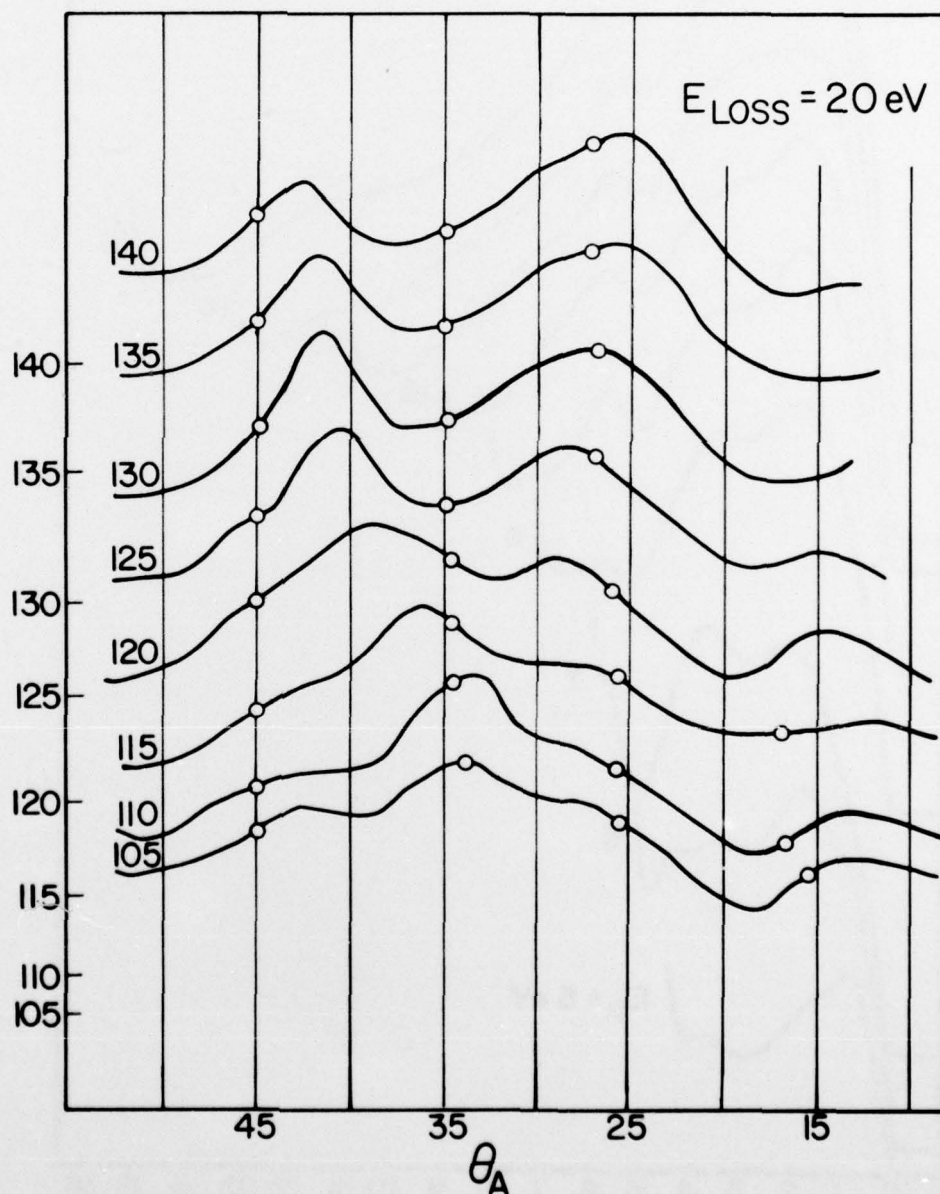


Figure 62 Inelastic angular intensity distributions as function of E_p , for plane of incidence and $E_{\text{loss}} = 20 \text{ eV}$

268058

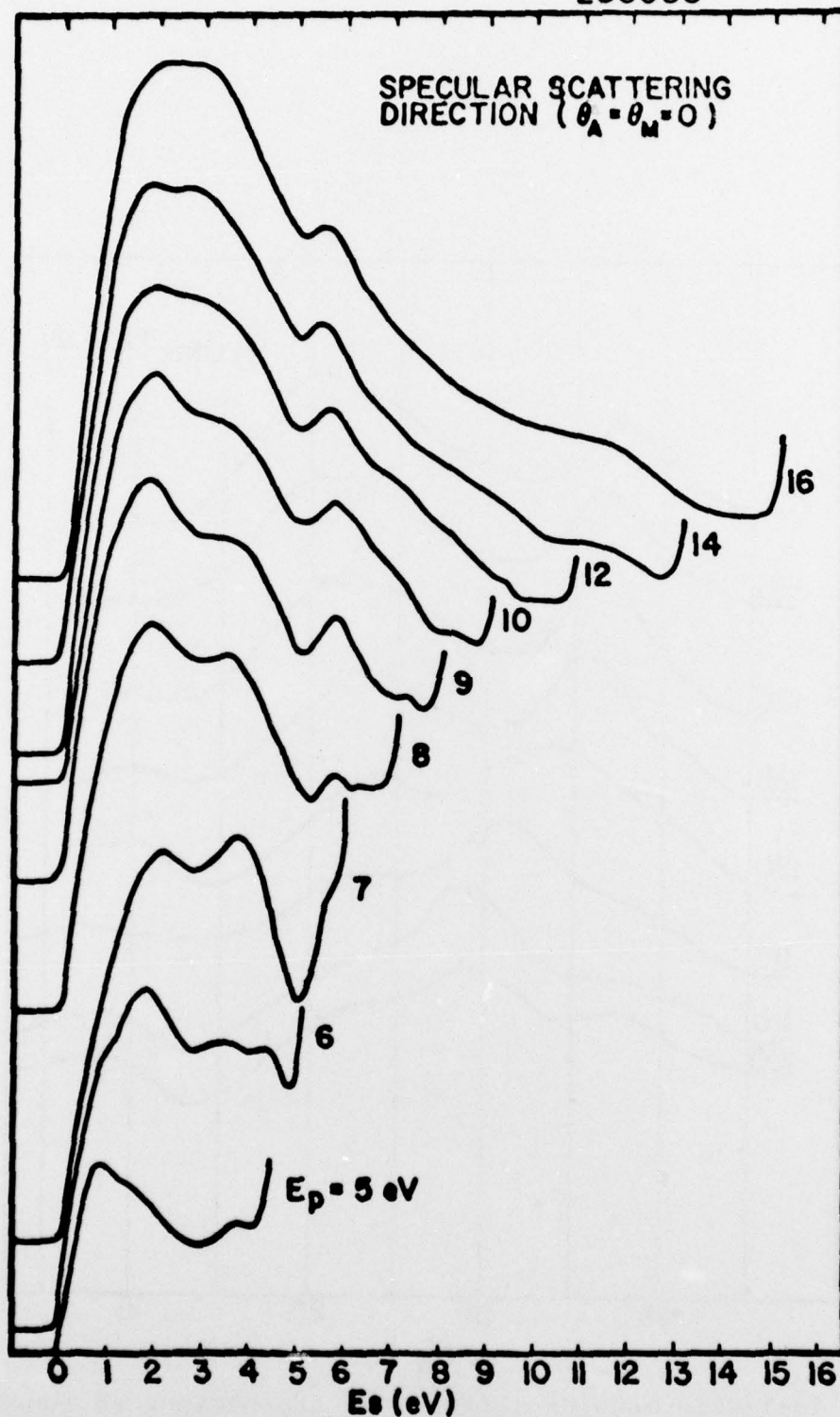


Figure 63. Secondary electron energy distributions as function of E_p , measured in specular scattering direction

268013

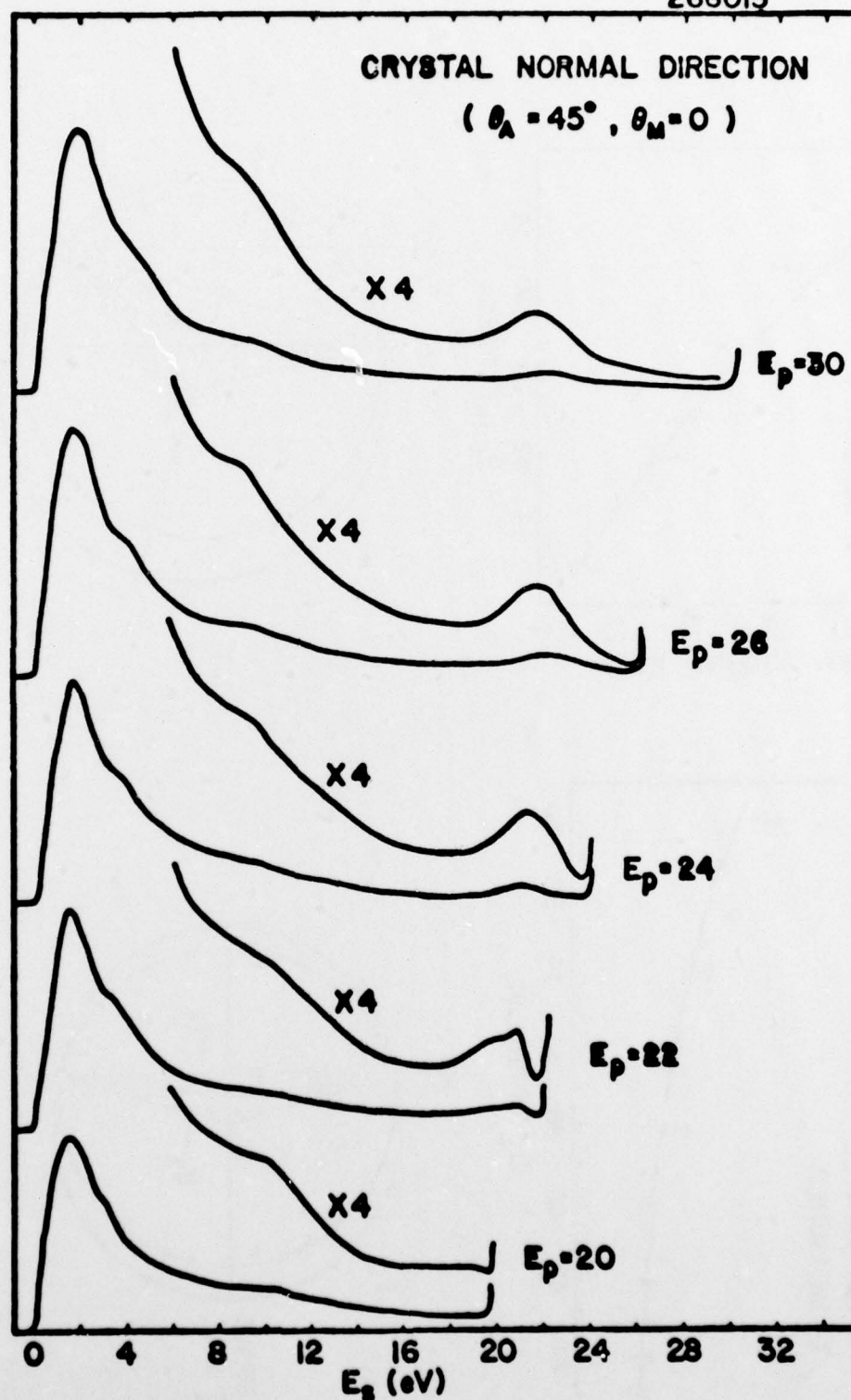


Figure 64 Secondary electron energy distribution as function of E_p , measured normal to sample surface

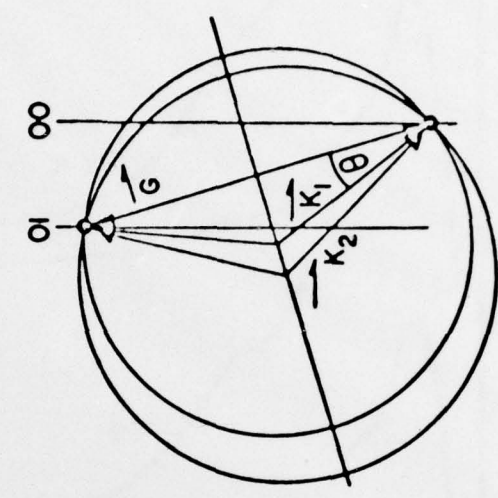
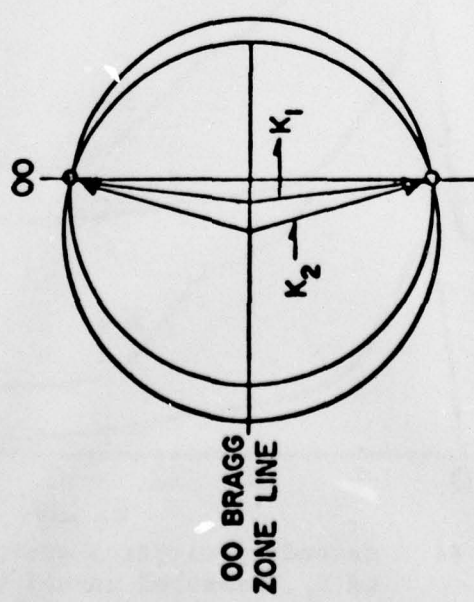
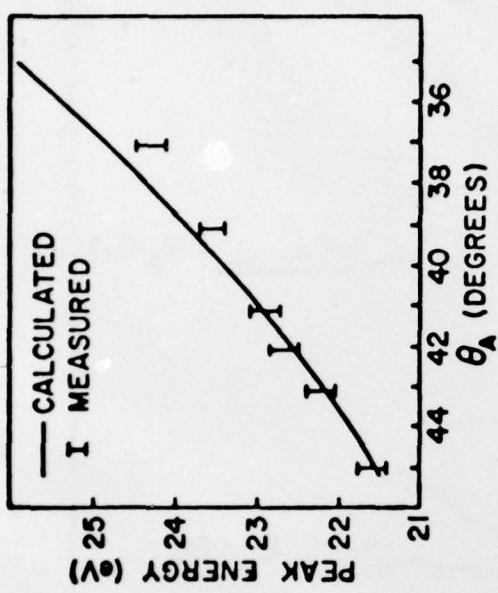
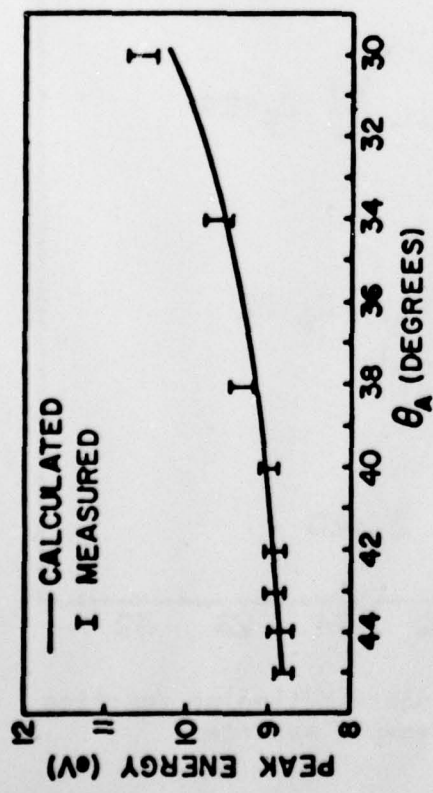


Figure 65 Secondary peak energy variation as function of scattering angle for diffraction of secondary electron; with descriptive wave vector diagrams

268057

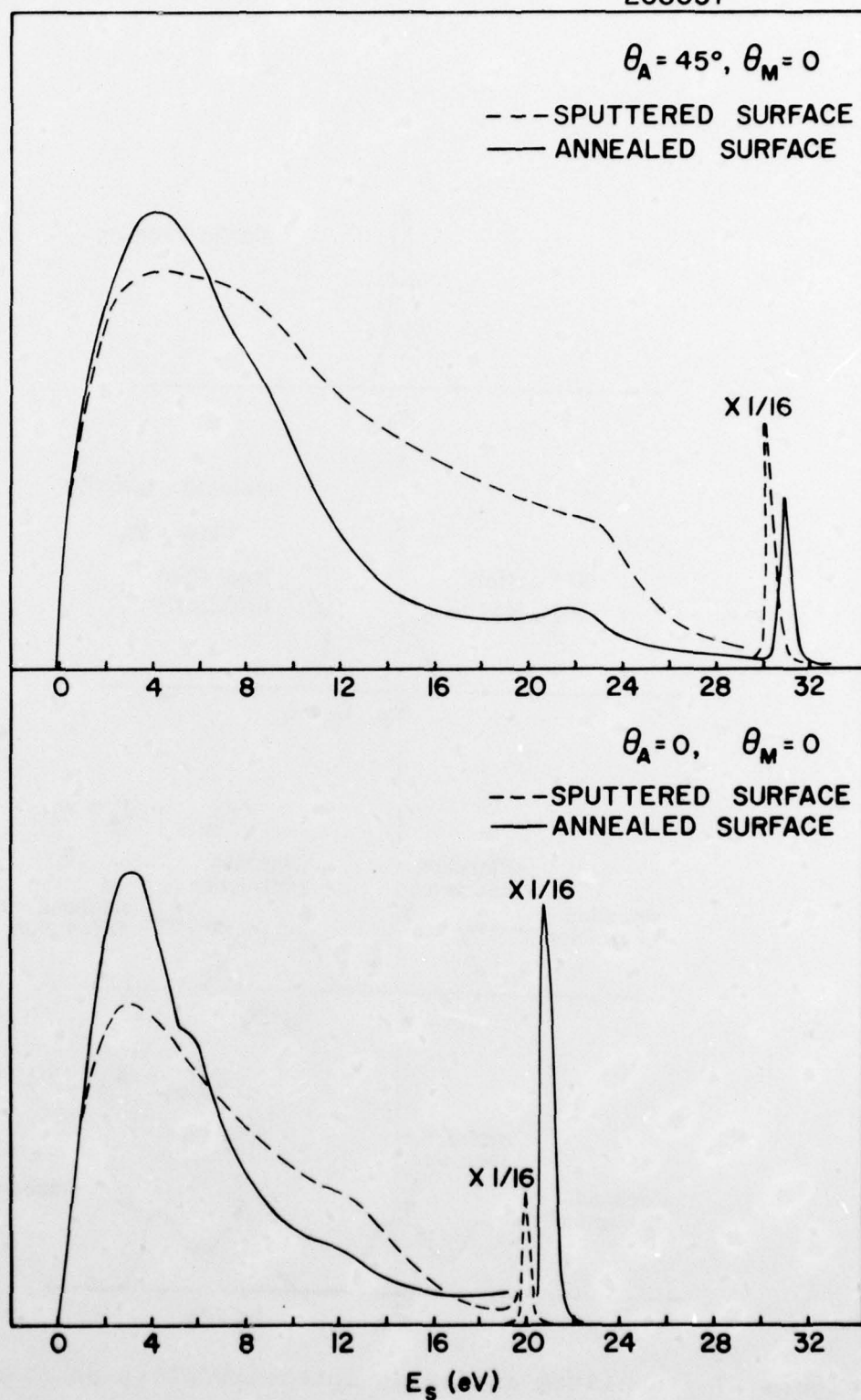


Figure 66 Secondary electron energy distributions for sputtered and annealed surfaces

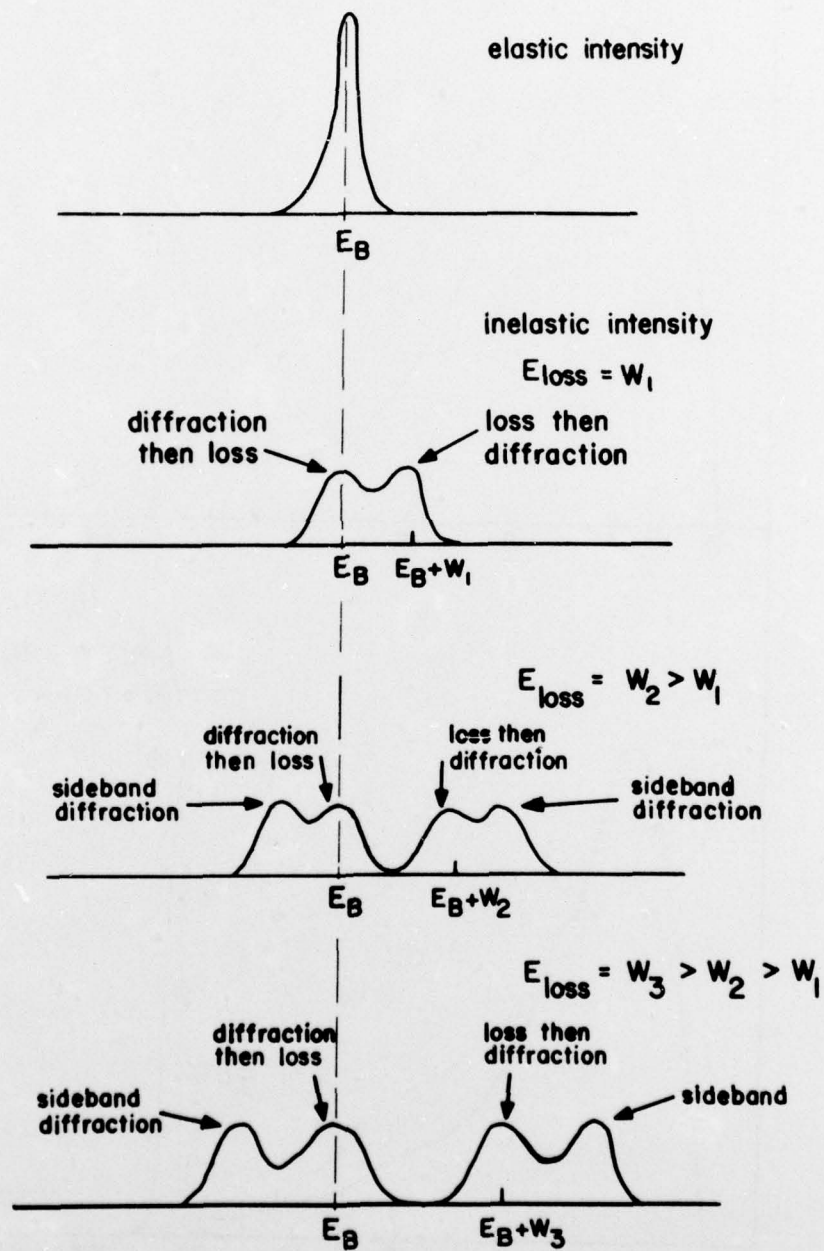


Figure 67 Idealized inelastic intensity plots as function of E_{loss}

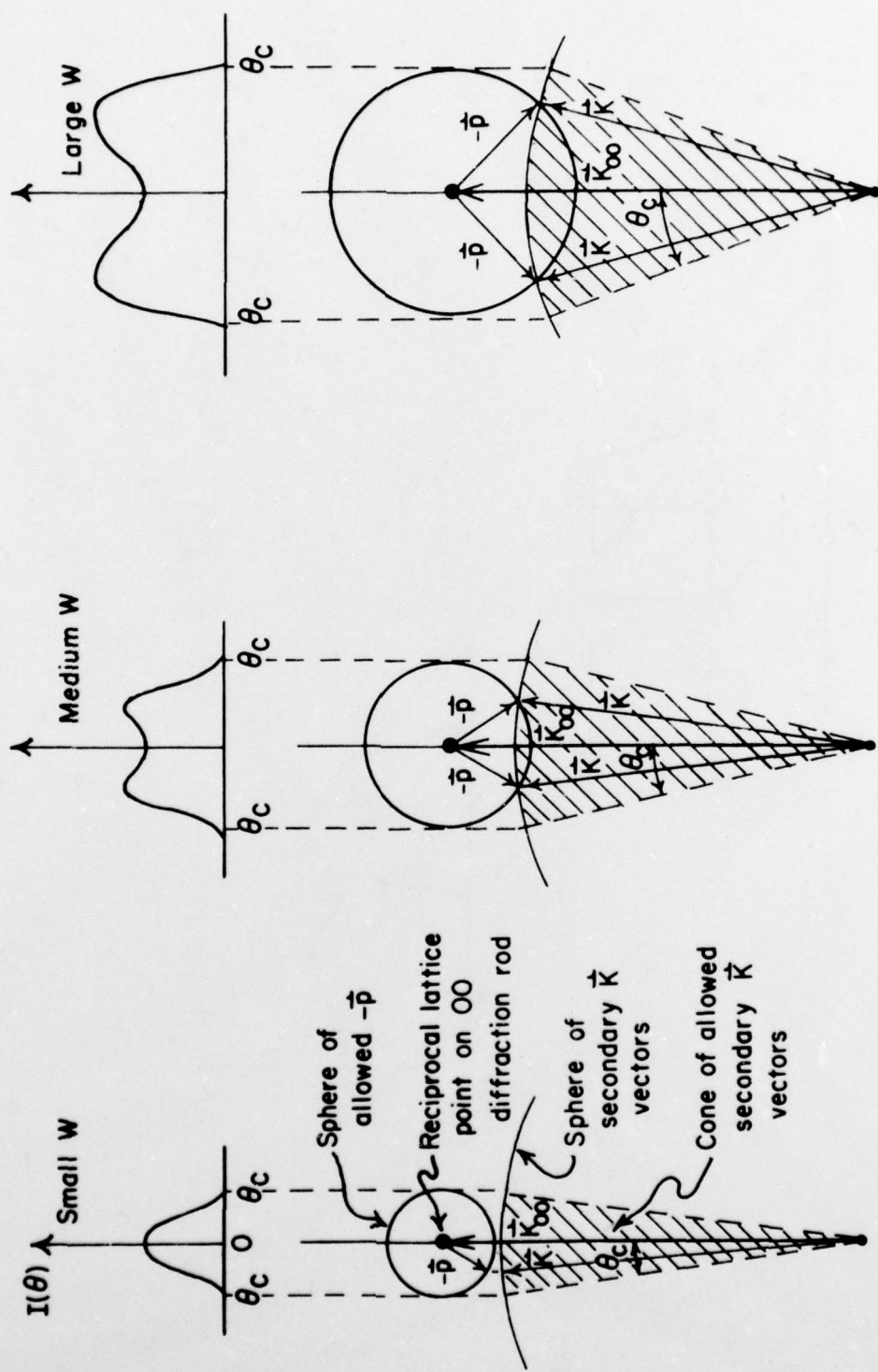


Figure 68 Idealized wave vector plots describing angular variation of inelastic intensity; depicting sideband diffraction conditions

$$\text{Energy loss} = W$$

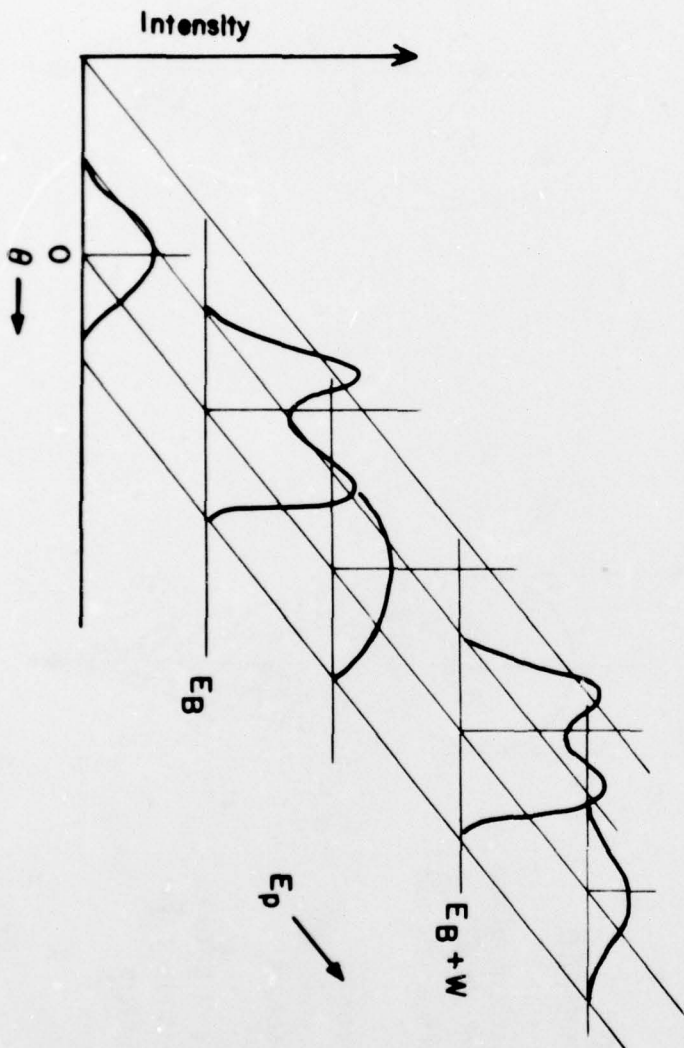
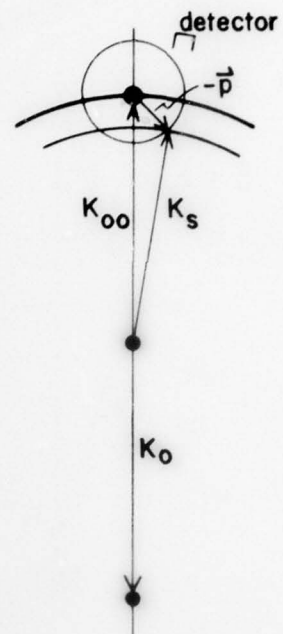
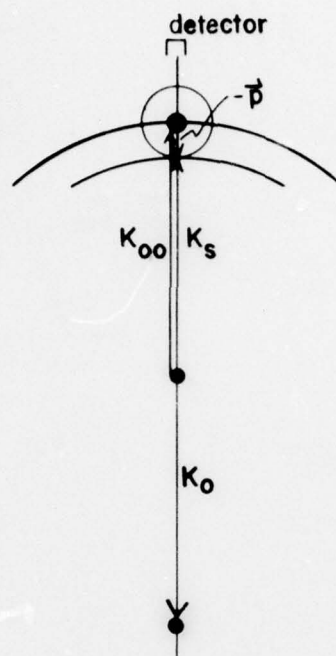
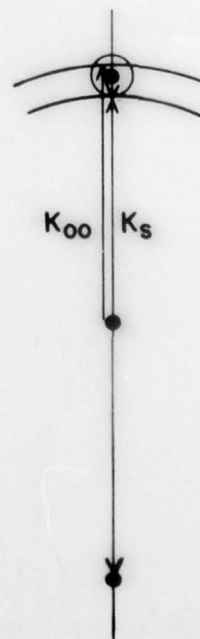
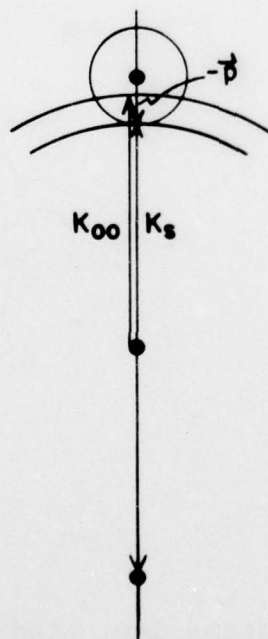


Figure 69 Idealized inelastic angular intensity variation as function of E_p near a Bragg energy



(a)



(b)

Figure 70 (a) Changes in wave vector for sideband diffraction with changes in detector angle
(b) Changes in wave vector for sideband diffraction with changes in E_p

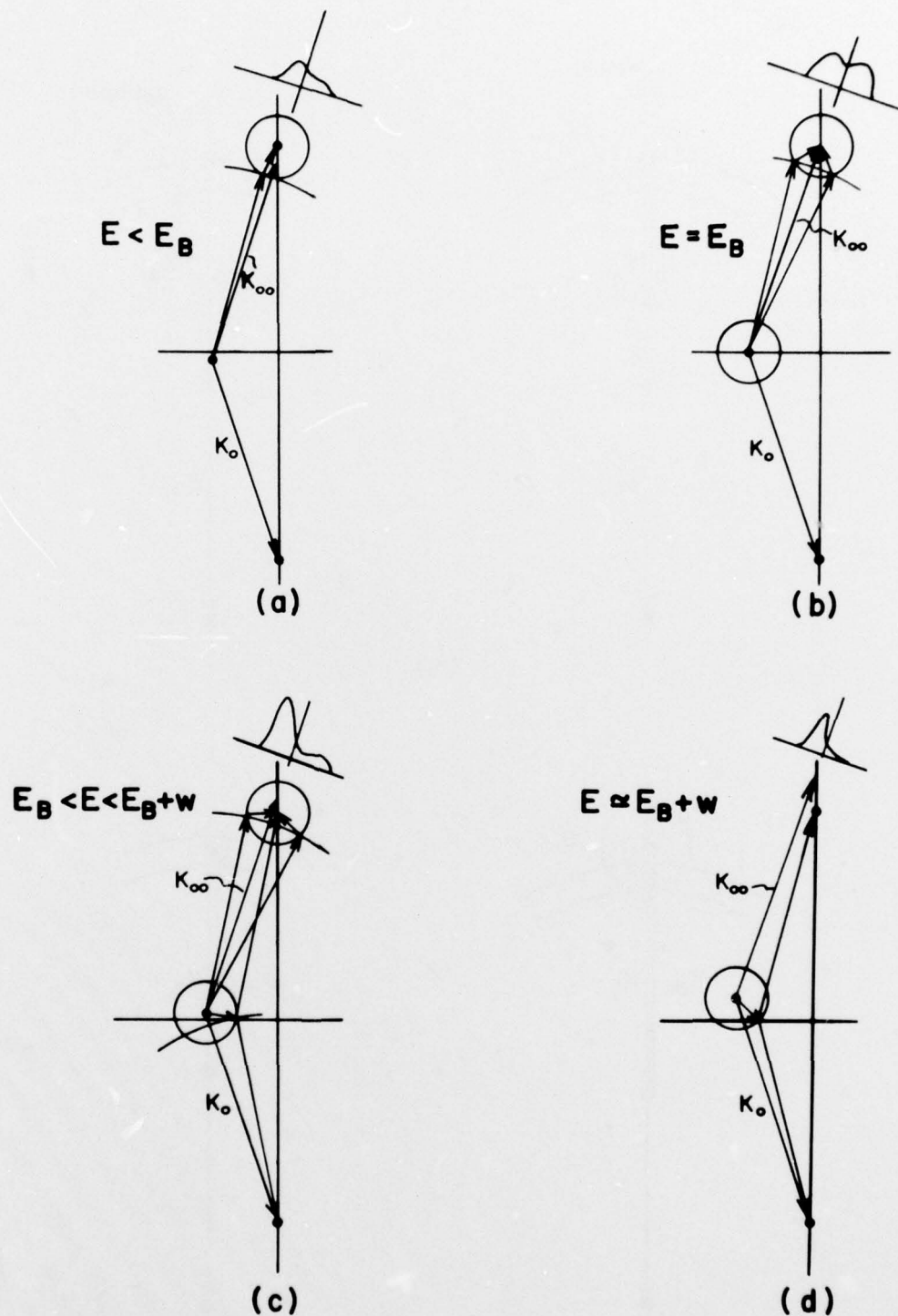


Figure 71 Idealized wave vector diagrams depicting changes in inelastic angular intensity as function of E_p near Bragg energy